DOCTOR OF PHILOSOPHY

Information geometry in the analysis and control of dynamical systems

Guel-Cortez, A.-J.

Award date:
2023

Awarding institution:
Coventry University

Information geometry in the analysis and control of dynamical systems

By

Adrián Josué Guel Cortez

PhD

May 2023

Information geometry in the analysis and control of dynamical systems

By

Adrián Josué Guel Cortez

A thesis submitted in partial fulfilment of the University's requirements for the Degree of Doctor of Philosophy

May 2023

To my family, in particular, to my beloved mother. Your hard work, unwavering love, and endless support have been instrumental in helping me achieve this significant milestone in my life. Without your sacrifices, I would not have been able to pursue my dream of obtaining a PhD.

To my wife, whose love and support have been the cornerstone of my success. During the COVID-19 pandemic period, your presence was especially vital. Your unwavering encouragement helped me navigate the challenges and uncertainties of this unprecedented time. Your support allowed me to stay focused and productive, even in the face of significant obstacles.

Acknowledgments

I want to express my deep gratitude to my advisor, Professor Eun-jin Kim, for her guidance, patience, and support throughout my research. Your expertise has been invaluable in shaping my ideas and helping me to develop as a scholar.

I would also like to thank Cesar Mendez-Barrios, Karl Friston, Charo I. del Genio, Harold R. Chamorro, Mohamed W. Mehrez, and Mario Sandoval for their insightful comments and feedback on my work, which have helped me to refine and strengthen my arguments.

Finally, I want to thank my peers at the Centre for Fluid and Complex Systems for their collegiality, intellectual exchange, and support throughout my studies.

Contents

I

Introduction

In physics, a complex system is a set of dynamical systems that is characterized by the presence of a large number of interconnected components that interact with each other[1]. Complex systems may arise and evolve through self-organization (a dynamical process by which a system spontaneously forms non-trivial macroscopic structures and/or behaviours over time), such that they are neither completely regular nor random[2], permitting the development of emergent behaviours at macroscopic scales [2].

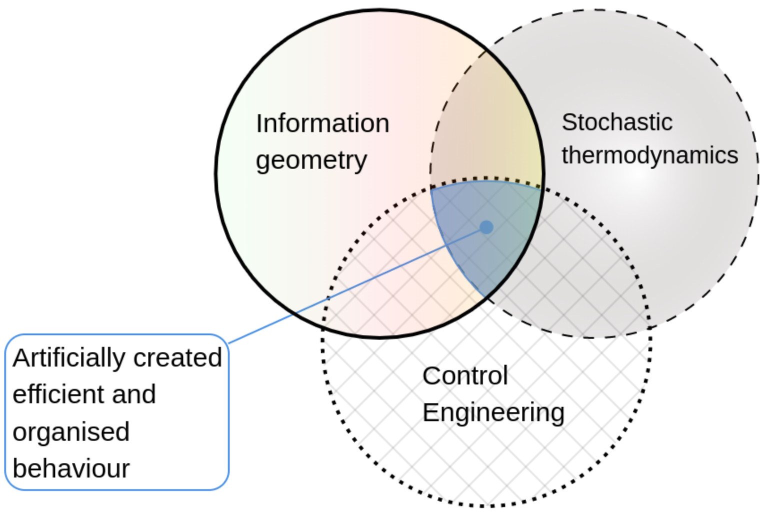

Figure I.1: Venn diagram describing the research areas that this thesis covers and tries to merge in order to study and control complex systems. The main goal of our research is to elucidate the interconnection between information geometry, stochastic thermodynamics, and control engineering to obtain efficient and organised behaviours in complex systems.

Since emergent behaviours in complex systems can be interpreted as the resistance of entropic decay and dissipation, similar to controlled systems (for instance, see [3]) that maintain their states around set-points despite perturbations from the environment [4; 5], our hypothesis is that:

> We can mimic emergent behaviours principles to artificially construct organised (controlled) complex systems. Furthermore, by interpreting entropy as a level of ignorance via information-theoretic constructs, we can diagnose abrupt changes, describe causal relations, or control the level of ignorance we have on the system dynamics.

In this regard, the present work aims to develop a set of tools to understand and control a set of complex systems through the interconnection of the fields of information geometry, stochastic thermodynamics, and

[1] While these interactions often exhibit nonlinearity, it is important to note that this is not a necessary condition for a system to be considered complex. Rather, the defining characteristic of a complex system lies in the emergent behavior that arises from the interactions among its components, which can exhibit surprising and unpredictable patterns [1].
[2] In this work, randomness refers to the degree of uncertainty or unpredictability associated with the occurrence of an event. Hence, a regular event is one whose level of uncertainty is minimum.

control engineering (see Figure I.1). From information geometry, we establish a metric that helps us quantify variability in the given complex systems subject to randomness. From control engineering, we recover the concept of "feedback" to inform, in this manner, a suitable control algorithm that will organise the system dynamics. Since efficiency is usually defined thermodynamically, Stochastic thermodynamics gives us the effects of the proposed regulator on the entropy production linked to Helmholtz free energy. Additionally, information geometry and stochastic thermodynamics give us tools to detect abrupt events and correlations between the variables in stochastic dynamics.

Specifically, this thesis contains the following results[3]

- **Chapters II and III:** The analysis of complex systems described by linear and non-linear stochastic differential equations (Langevin equations) via the so-called Laplace assumption, their corresponding Fokker-Planck equation, information geometry and stochastic thermodynamics.
- **Chapter IV:** Study the effects of information flow between the variables in the dynamical system, referring to some sort of causality.
- **Chapter IV:** Detection of "ongoing" abrupt changes (perturbations) in stochastic dynamics.
- **Chapter V:** Creating organised behaviour (with minimum statistical variability) when the system is clearly subject to randomness.
- **Chapter VI:** Development of integrated techniques to study complex systems described via time series.
- **Chapters IV, V, and VI:** Presentation of different case studies, including the analysis of classical Brownian motion and an electrical power system.

These results have also been previously published in the following journals (some of them currently under review)

List of published and submitted journal papers:

[6] Guel-Cortez, Adrian-Josue, and Eun-jin Kim. "Information length analysis of linear autonomous stochastic processes." Entropy 22.11 (2020): 1265.

[7] Guel-Cortez, Adrian-Josue, and Eun-jin Kim. "Information geometric theory in the prediction of abrupt changes in system dynamics." Entropy 23.6 (2021): 694.

[8] Chamorro, Harold R., Guel-Cortez, Adrian-Josue, et al. "Information length quantification and forecasting of power systems kinetic energy." IEEE Transactions on Power Systems 37.6 (2022): 4473-4484. Harold R. Chamorro and Adrian-Josue Guel-Cortez contributed equally to this work.

[3] Throughout the thesis, each chapter contains an abstract discussing the chapter's goal and, depending on the nature of the chapter, an introduction with the challenges and proposed solutions.

[9] Guel-Cortez, Adrian-Josue, and Eun-Jin Kim. "Relations between entropy rate, entropy production and information geometry in linear stochastic systems." Journal of Statistical Mechanics: Theory and Experiment 2023.3 (2023): 033204.

[10] Guel-Cortez, Adrian-Josue, Eun-jin Kim, and Mohamed W. Mehrez. "Minimum Information Variability in Linear Langevin Systems Via Model Predictive Control." Available at SSRN 4214108 (2022).

Throughout the development of this thesis, the author also participated in different international events and collaborations, some of which included the publication of an article. The following summarises such results

List of published and submitted conference papers:

[11] Guel-Cortez, Adrian-Josue, and Eun-jin Kim. "Information Geometry Control under the Laplace Assumption." Physical Sciences Forum. Vol. 5. No. 1. Multidisciplinary Digital Publishing Institute, 2022.

[12] Guel-Cortez, Adrian-Josue, and Eun-jin Kim. "A Fractional-Order Model of the Cardiac Function." 13th Chaotic Modeling and Simulation International Conference 13. Springer International Publishing, 2021.

[13] Guel-Cortez, Adrian-Josue, and Eun-jin Kim. "Model reduction and control design of a multi-agent line formation of mobile robots." Recent Trends in Sustainable Engineering: Proceedings of the 2nd International Conference on Applied Science and Advanced Technology. Springer International Publishing, 2022. Received the first place award in the conference best-submitted paper contest.

[14] Guel-Cortez, Adrián-Josué, et al. "Further Remarks on Irrational Systems and Their Applications." Computer Sciences & Mathematics Forum. Vol. 4. No. 1. MDPI, 2022.

[15] Guel-Cortez, Adrian-Josue, et. al. "Parameter Estimation of Fractional-Order Systems via Evolutionary Algorithms and the Extended Fractional Kalman Filter." The International Conference on Fractional Differentiation and its Applications (ICFDA 2023)At: Ajman University, 14-16 March, 2023.

List of published journal papers that come from collaborations:

[16] Kim, Eun-jin, and Adrian-Josue Guel-Cortez. "Causal information rate." Entropy 23.8 (2021): 1087.

[3] Guel-Cortez, Adrian-Josue, et al. "Fractional-order controllers for irrational systems." IET Control Theory & Applications 15.7 (2021): 965-977.

List of presentations given for international conferences or research groups:

- "Minimum information variability control" talk at Thermodynamics 2.0, Online, July 18, 2022.
- "Information geometry under the Laplace assumption" talk at International Workshop on Bayesian Inference and Maximum Entropy Methods in Science and Engineering, IHP, Paris, July 18-22, 2022.
- "Information Length in Dynamical Systems" seminar at the Wellcome Centre for Human Neuroimaging, London. 17 January 2022. Link to video
- "Information Length Analysis of Linear Autonomous Stochastic Processes" at the The British Mathematical Colloquium (BMC) and the British Applied Mathematics Colloquium (BAMC). From 6 Apr. 2021 to 9 Apr. 2021. Link to poster
- "Model reduction and control design of a multi-agent line formation of mobile robots" at The 2021 International Conference on Applied Science and Advanced Technology. 3 Jun. 2021.
- "System dynamics simulation using Processing and Python" Workshop instructor at The 2021 International Conference on Applied Science and Advanced Technology. 3 Jun. 2021.
- "Fractional order model of the cardiac function" at Chaotic Modelling & Simulation Web Conference. 22-24 October 2020. Online.

II

Preliminaries

Chapter summary

In this chapter, we review the basic theoretical concepts and results that have been applied throughout this dissertation. When introducing the theoretical results, specially the ones which can be found in many published textbooks, the discussion does not intend to be a formal or complete presentation but rather to act as a gentle descriptive/conceptual guide to them. The section also contains various links to codes made by the author that may serve as a practical introduction to future employed algorithms. We also highlight that not all the concepts we use may be introduced within this section. If the discussion requires it, we also introduce new concepts in the subsequent chapters as we make use of them in our results.

This chapter includes material that has been published by the author in [6], [9], and [11].

keywords: Stochastic dynamics; Stochastic thermodynamics; Fokker-Planck equation; Entropy

II.1 Stochastic systems

A stochastic system is a process characterised by the presence of randomness. In such dynamical systems[1], we commonly use $x(t)$ to describe the current state at time t and identify a corresponding probability p of $x(t)$ to occur. In continuous time, we denote $p(x,t)$ the probability density function (PDF) of finding the system in $x(t)$ at time t.

From the PDF, we can obtain the so-called statistical moments. For example, the expected value[2] defined by

$$\mu(t) = \langle x(t) \rangle = \int_{\mathbb{R}} x(t) p(x,t) \, \mathrm{d}x. \tag{II.2}$$

The expected value parameterises the random variable $x(t)$, as well as its higher moments $\langle x^n \rangle$ and its moments about the mean $\langle (x-\mu)^n \rangle$. From the latter, we recover the definition of the variance of the random state $x(t)$ as[3]

$$\Sigma = \langle (x-\mu)^2 \rangle. \tag{II.3}$$

We can also study stochastic systems by analysing their trajectories, denoted by

$$\boldsymbol{\mathcal{X}} = [x(t)]. \tag{II.4}$$

Here, $\boldsymbol{\mathcal{X}}$ identifies the whole function $x(t)$ over a given time interval, i.e. the stochastic system trajectory. For instance, Figure II.1 shows the three-dimensional space describing the evolution of x and its probability over time. In red, we see a trajectory $\boldsymbol{\mathcal{X}}$. In blue, the shape of the PDF at different instants of time (denoted here as P_k where $k = 0, 1, 2, 3, \ldots$).

[1] A dynamical system can be defined as a system in which a function describes the time dependence of a point in space. For instance, a particle whose state varies over time is governed by differential equations (for further details, see [17]).

[2] The discrete version of the expected value is given by

$$\langle X \rangle = \sum_i x_i P(x_i), \tag{II.1}$$

where $P(x_i)$ is called the probability mass function (PMF) which describes the probability of observing outcome x_i of the random variable X [18] and the sum is over all the distinct possible outcomes of X.

[3] The variance is sometimes denoted by σ^2 instead of Σ, and $\sqrt{\sigma^2} = \sigma$ is called the standard deviation of x.

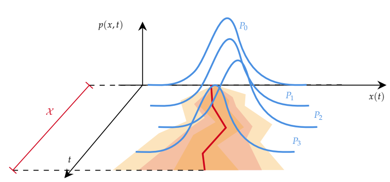

Figure II.1: Graphical description of stochastic dynamics. The behaviour of a stochastic process can be analysed by the system trajectory $\boldsymbol{\mathcal{X}}$ or the time-varying probability density function $p(x,t)$.

Figure II.1 also shows a typical kind of PDF $p(x,t)$ called "Normal" or Gaussian. The Gaussian distributions are a type of continuous PDFs defined as

$$p(x) = \frac{1}{\sqrt{2\pi\Sigma}} e^{-\frac{1}{2}\frac{(x-\mu)^2}{\Sigma}}. \tag{II.5}$$

As we can see from Equation (II.5), Gaussian distributions are completely parametrised if we fix only the first two moments about the mean μ of the random variable x (for instance, see Figure II.2). When we refer to a variable that follows a normal distribution, we use the notation $x \sim \mathcal{N}(\mu, \Sigma)$.

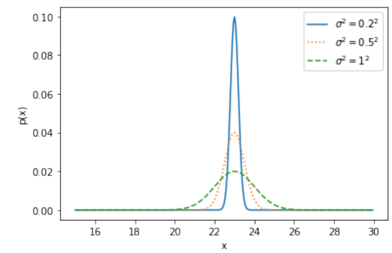

Figure II.2: Plots of Gaussian distributions with different values of variance σ^2 and mean $\mu = 23$ `https://github.com/AdrianGuel/PhDThesis/blob/main/Chapter1/Gaussianplots.py`

II.1.1 Stochastic calculus

The analysis of dynamical systems subject to probabilities is described via stochastic differential equations (SDEs). In mathematics and finance SDE are written as follows [19]

$$\mathrm{d}X_t = \mu(X_t, t)\,\mathrm{d}t + \sigma(X_t, t)\,\mathrm{d}W_t, \tag{II.6}$$

where W_t denotes a Wiener process[4]. The terms $\mu(X_t, t)$ and $\sigma(X_t, t)$ are called the drift and diffusion terms of the SDE, respectively. Equation (II.6) can be rewritten using the corresponding integral equation

$$X_{t+s} - X_t = \int_t^{t+s} \mu(X_u, u)\,\mathrm{d}u + \int_t^{t+s} \sigma(X_u, u)\,\mathrm{d}W_u. \tag{II.7}$$

If we consider the integral from of the SDE given by (II.7), we come up with the problem of defining the integral of the rightmost term. But, before discussing the solution to stochastic integrals, let us introduce a commonly used SDE in the field of Physics called the Langevin equation.

[4] Properties of the Wiener process:

1. $W_0 = 0$
2. $\forall t > 0$, the future increments $W_{t+u} - W_t, u \geq t$ are independent of the past values $W_s, s \leq t$.
3. $W_{t+u} - W_t \sim \mathcal{N}(0, u)$.
4. W_t is continuous in t.

II.1.2 Langevin equation

In physics, a basic application of SDEs lies in the description of the so-called Brownian motion, a motion associated with the random motion of particles suspended in a medium (a liquid or a gas) [5].

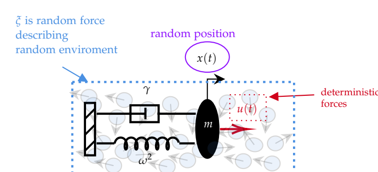

Figure II.3: Example of a typical application of the Langevin equations. The Langevin equation is used to describe the position of a particle under a random environment.

As an example of Brownian motion mathematical modelling, Figure II.3 shows a particle of mass m modelled as a mass-spring-damper system subject to a deterministic force and a random force describing the random environment to avoid the many-body interactions problem. Additionally, in this scenario, we assume that the environment is at thermal equilibrium and it is defined by a given temperature.

[5] Einstein described Brownian motion as a phenomenon where bodies of microscopic size suspended in a liquid perform random movements that can be perceived via a microscope. [20]

The description of the trajectories of a Brownian particle with drift $\mu(x,t)$ and diffusion $D(x,t)$ coefficients are solutions of[6] the Langevin equation

$$\frac{\mathrm{d}x}{\mathrm{d}t} = \mu(x,t) + \sigma(x,t)\xi(t), \tag{II.8}$$

[6] For simplicity, in this work, we commonly will avoid writing the term $\sigma(x,t)$ in Equation (II.8), as our analysis will rely completely on the value of $D(x,t)$.

where $\sigma(x,t) = \sqrt{2D(x,t)}$, $\xi(t)$ is a random quantity considered unbiased, $\langle \xi(t) \rangle = 0 \; \forall t$, and with uncorrelated displacements in non-overlapping time intervals, i.e. $\langle \xi(t)\xi(t') \rangle = 0$ for t and t' sufficiently far apart. Assuming that the latter holds, it is useful to rewrite the second moment as $\langle \xi(t)\xi(t') \rangle = 2D(x,t)\delta(t-t')$. When the random variable ξ satisfies these properties, we call it "white noise".

The solution of the Langevin equation requires the evaluation of a stochastic integral of the form[7]

$$\int_{t_0}^{t_f} \mathrm{d}t \xi(t) \sigma(x(t),t) = \int_{t_0}^{t_f} \mathrm{d}W(t) \sigma(x(t),t), \tag{II.9}$$

where $\sigma(x,t)$ is any given function. The solution of stochastic integrals can be obtained by the Stratonovich or Itô conventions[8].

[7] Like the rightmost term of Equation (II.7) but written following the Langevin equation notation

[8] A more formal and complete study of both conventions can be found in [21; 22]

Itô convention The Itô integration is defined as follows [23]

$$I_I = \lim_{\mathrm{d}t \to 0} \sum_{k=0}^{N} \left[W(t_k + \mathrm{d}t) - W(t_k) \right] \sigma(x(t_k), t_k), \tag{II.10}$$

where $t_k = t_0 + k\,\mathrm{d}t$ and $N = \frac{t_f - t_0}{\mathrm{d}t}$. Note that in this convention, $\sigma(x(t),t)$ is evaluated at the beginning of each infinitesimal time interval $[t_k, t_k + \mathrm{d}t]$. When written in the continuos time domain, the Itô integral is denoted by a dot product symbol

$$I_I = \int_{t_0}^{t_f} \mathrm{d}W \cdot \sigma(x(\tau), \tau). \tag{II.11}$$

Stratonovich convention The Stratonovich integral is defined by

$$\begin{aligned} I_S &= \lim_{\mathrm{d}t \to 0} \sum_{k=0}^{N} \left[W(t_k + \mathrm{d}t) - W(t_k) \right] \sigma\left(\frac{x(t_k + \mathrm{d}t) + x(t_k)}{2}, t_k + \frac{\mathrm{d}t}{2} \right) \\ &= \lim_{\mathrm{d}t \to 0} \sum_{k=0}^{N} \left[W(t_k + \mathrm{d}t) - W(t_k) \right] \frac{1}{2} \left[\sigma(x(t_k + \mathrm{d}t), t_k + \mathrm{d}t) + \sigma(x(t_k), t_k) \right]. \end{aligned} \tag{II.12}$$

From (II.12), we see that $\sigma(x(t),t)$ is evaluated at the midpoint of each infinitesimal interval $[t_k, t_k + \mathrm{d}t]$ in the Stratonovich integral. In continuos time , we denote the Stratonovich convention by a circle product symbol as follows

$$I_S = \int_{t_0}^{t_f} \mathrm{d}W \circ \sigma(x(\tau), \tau). \tag{II.13}$$

To decide which convention to use, we consider the following result

Proposition II.1: Stratonovich to Ito transformation [23]

The relationship between the Stratonovich and Ito integral is given by

$$\int_{t_0}^{t_f} \mathrm{d}W \circ \sigma(x(\tau), \tau) = \frac{1}{2} \int_{t_0}^{t_f} \frac{\mathrm{d}\sigma(x(\tau), \tau)}{\mathrm{d}x} \sigma(x(\tau), \tau)\, \mathrm{d}t + \int_{t_0}^{t_f} \mathrm{d}W \cdot \sigma(x(\tau), \tau). \tag{II.14}$$

From Proposition II.1, it becomes clear that both conventions are the same if σ does not depend on the random variable x. Here, we highlight that, throughout this work, we only consider additive noises, i.e., σ is always independent of x, giving us the freedom to write any stochastic integral using either notation. From now on, we will consider the Ito convention and avoid the symbol $\cdot$ for simplicity.

II.1.3 Numerical methods

The following are the most common numerical methods to solve SDEs of the type (II.6).

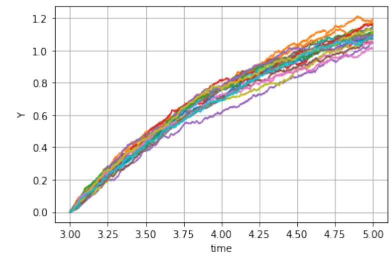

Figure II.4: Simulation of an SDE with $\mu(X_t, t) = \theta(\mu - X_t)$ and $\sigma(X_t, t) = \Sigma$ where θ, μ and Σ are some constant parameters using the Euler-Maruyama method. Code available at `https://github.com/AdrianGuel/PhDThesis/blob/main/Chapter1/eulermaruyama.ipynb`.

Euler–Maruyama method

Given the SDE (II.6), we wish to solve it at some interval of time $[0, T]$. To develop an approximate solution, we partition the interval $[0, T]$ into N equal subintervals of width $\Delta t > 0$

$$0 = \tau_0, \tau_1, \tau_2, \ldots, \tau_N = T \quad s.t. \quad \Delta t = \frac{T}{N}. \tag{II.15}$$

Then, we set the initial random value $Y_0 = x_0$ where x_0 comes from, for instance, $N(\mu_0, \sigma_0)$ such that μ_0 and σ_0 are the moments describing the initial PDF. Now, recursively define

$$Y_{n+1} = Y_n + \mu(Y_n, \tau_n)\Delta t + \sigma(Y_n, \tau_n)\Delta W_n, \tag{II.16}$$

where $\Delta W_n = W_{\tau_{n+1}} - W_{\tau_n}$. Each random number ΔW_n is computed as [24]

$$\Delta W_n = z_n\sqrt{\Delta t} \quad s.t. \quad z_n \sim N(0, 1). \tag{II.17}$$

Algorithm 1 and Figure II.4 show the description of the Euler-Maruyama method and a plot with the solution of an SDE implementing the Euler-Maruyama method, respectively.

Algorithm 1: Euler-Maruyama method.

Data: Consider the simulation time $t = T \in \mathbb{R}$, the number of points in the solution $N \in \mathbb{N}$ and the probability distribution described by the parameters $\mu_0 \in \mathbb{R}$, and $\sigma_0 \in \mathbb{R}^+$.
Result: The vector $\mathbf{Y} := [Y_0, Y_1, \ldots, Y_N] \in \mathbb{R}^N$ containing the approximate solution to the SDE (II.6).

```
/* The function randn(μ,σ) generates a random number from normal distribution with
   mean μ and variance σ.  */
Y_0=randn(μ_0,σ_0)
Δt = T/N
n = 0
while n < T do
    ΔW_n=randn(0,Δt)
    Y_{n+1} = Y_n + μ(Y_n,τ_n)Δt + σ(Y_n,τ_n)ΔW_n
    n = n + 1
end
return Y
```

Milstein method

Similarly to the Euler-Maruyama method, the Milstein method is an approximate solution to the SDE (II.6) obtained by doing the same time partition (II.15) but employing the following recursive solution update

$$Y_{n+1} = Y_n + \mu(Y_n, \tau_n)\Delta t + \sigma(Y_n, \tau_n)\Delta W_n + \frac{1}{2}\sigma(Y_n, \tau_n)\sigma'(Y_n, \tau_n)\left((\Delta W_n)^2 - \Delta t\right)\Bigg(\tag{II.18}$$

where σ' denotes the derivative of $\sigma(X_t, t)$ with respect to X_t. ΔW_n is defined as in (II.17). Note that when $\sigma' = 0$ (the diffusion term does not depend on X_t); this method is equivalent to the Euler–Maruyama method.

Runge–Kutta method

Runge-Kutta methods are a family of numerical methods used to obtain more accurate solutions to ordinary differential equations. Regarding SDE, these methods can become complex as their order of approximation increases [25]. The simplest Runge-Kutta scheme was introduced by [26], in this method, the solution of the SDE (II.6) is solved via the following recursive equation

$$Y_{n+1} = Y_n + \frac{1}{2}\left(K_1 + K_2\right), \tag{II.19}$$

where

$$K_1 = \mu(Y_n, \tau_n)\Delta t + \left(\Delta W_n - S_n\sqrt{\Delta t}\right)\sigma(Y_n, \tau_n), \tag{II.20}$$

$$K_2 = \mu(Y_n + K_1, \tau_{n+1})\Delta t + \left(\Delta W_n + S_n\sqrt{\Delta t}\right)\sigma(Y_n + K_1, \tau_{n+1}), \tag{II.21}$$

$S_n = \pm 1$, each alternative chosen with probability $\frac{1}{2}$, and ΔW_n as in (II.17) [9].

II.2 The Fokker-Plack equation

As it was mentioned in Section II.1, the behaviour of dynamics subject to probability can also be described in terms of PDFs. A classical approach to determine the system PDF at every instant of time corresponds to the multiple solutions of the dynamics via the numerical solution of its SDE (see Figure II.5).

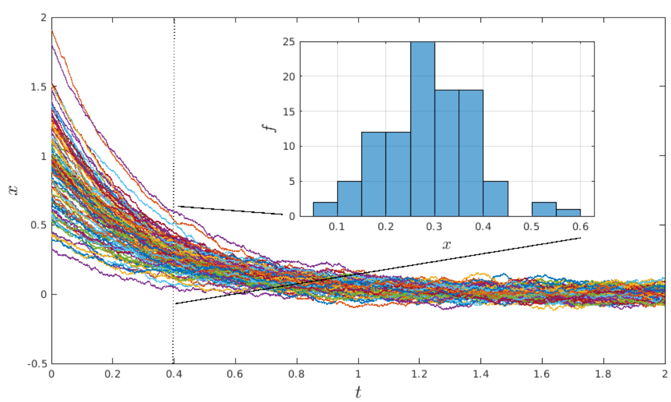

Figure II.5: PDF estimation via stochastic numerical simulations. A given SDE is solved multiple times in parallel to create samples at every time t. Then, we create a histogram representing the statistical behaviour of the system at every t. For instance, in the Figure we have a histogram of x at time $t = 0.4$ of the numerical solution of the linear Langevin equation $\dot{x} = -3x + \xi$, $\langle x(0)\rangle = 1$ and $\langle (x - \langle x(0)\rangle)^2\rangle = 0.1$.

In this method, the multiple numerical solutions to the SDE generate a sample at every t, which can be used to estimate a PDF. If we plot every histogram, we obtain the time evolution of the statistics associated with the stochastic process. In Figure II.6, we show an example of such methodology. In the example, we see that every histogram is used to fit a probability distribution function $p(x, t)$, again, used to describe the probability of finding x in a given value at time t.

[9] Code example of the Runge-Kutta method to solve a first-order SDE `https://github.com/AdrianGuel/PhDThesis/blob/main/Chapter1/RKmethod.py`

This method requires large amount of computational memory. Furthermore, it becomes more complicated to estimate the PDF in high-dimensional spaces. Thus, it is sometimes important to look for a different approach allowing us to describe the PDF time-evolution of the stochastic dynamics. A popular method consists of the so-called "Fokker-Planck equation", a differential equation describing the time-evolution of the system's PDF. The idea behind the Fokker-Planck equation relies on the following reasoning.

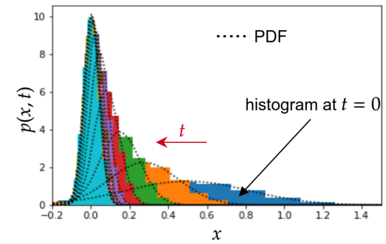

Figure II.6: PDF estimation via stochastic numerical simulations and histograms.

First, we describe the expectation of an arbitrary function $f(x)$ at time t as

$$\langle f(x)\rangle = \int \mathrm{d}x f(x) p(x;t), \tag{II.22}$$

and its time rate of change

$$\frac{\mathrm{d}\langle f(x)\rangle}{\mathrm{d}t} = \int \mathrm{d}x f(x) \frac{\partial}{\partial t} p(x;t). \tag{II.23}$$

Then, we can use the Chapman-Kolmogorov[10] equation to describe the expectation of f at the next instant of time $t + \Delta t$[11]

$$\langle f(x)\rangle_{t+\Delta t} = \int \mathrm{d}\Delta x \int \mathrm{d}x f(x+\Delta x) p(x+\Delta x; t+\Delta t | x; t) p(x;t). \tag{II.24}$$

Now, assuming the Δx is small, we expand $f(x + \Delta x)$ in a Taylor series to second order to obtain

$$\begin{aligned} \langle f(x)\rangle_{t+\Delta t} \approx & \int \mathrm{d}\Delta x \int \mathrm{d}x \left[f(x) + \Delta x \frac{\partial f(x)}{\partial x} + \frac{\Delta x^2}{2} \frac{\partial^2 f(x)}{\partial x^2} \right] \\ & \times p(x+\Delta x; t+\Delta t | x; t) p(x;t), \\ & = \int \mathrm{d}x \left[f(x) + \langle \Delta x\rangle_x \frac{\partial f(x)}{\partial x} + \frac{\langle \Delta x^2\rangle_x}{2} \frac{\partial^2 f(x)}{\partial x^2} \right] p(x;t). \end{aligned} \tag{II.25}$$

Here, we define $\langle \cdots \rangle_x = \int \mathrm{d}\Delta x \cdots p(x+\Delta x; t+\Delta t | x; t)$. Rearranging (II.25)

$$\begin{aligned} \langle f\rangle_{t+\Delta t} - \langle f\rangle_t = & \int \mathrm{d}x \left[\frac{\partial}{\partial x} \left(\langle \Delta_x\rangle_x f(x, p(x;t)) \right) - \frac{\partial}{\partial x} \left(\langle \Delta_x\rangle_x p(x;t) \right) f(x) \right] \\ & + \int \mathrm{d}x \left[\frac{\partial}{\partial x} \left(\frac{1}{2} \langle \Delta x^2\rangle_x p(x;t) \frac{\partial}{\partial x} f(x) \right) - \frac{\partial}{\partial x} \left(\frac{\partial}{\partial x} \left\{ \frac{1}{2} \langle \Delta x^2\rangle_x p(x;t) \right\} \frac{\partial}{\partial x} f(x) \right) \right. \\ & \left. + \frac{\partial^2}{\partial x^2} \left(\frac{1}{2} \langle \Delta x^2\rangle_x p(x;t) \right) f(x) \right] \\ = & \int \mathrm{d}x f(x) \left[-\frac{\partial}{\partial x} \left(\langle \Delta x\rangle_x p(x;t) \right) + \frac{\partial^2}{\partial x^2} \left(\frac{1}{2} \langle \Delta x^2\rangle_x p(x;t) \right) \right] \end{aligned} \tag{II.26}$$

Considering that Δt in (II.25) is also small (a condition that Brownian motion satisfies), the following Δt-limit can be operated in (II.26)

$$\lim_{\Delta t \to 0} \frac{\langle f\rangle_{t+\Delta t} - \langle f\rangle_t}{\Delta t} = \int \mathrm{d}x f(x) \left[-\frac{\partial}{\partial x} \left(\lim_{\Delta t \to 0} \frac{\langle \Delta x\rangle_x}{\Delta t} p(x;t) \right) + \frac{\partial^2}{\partial x^2} \left(\lim_{\Delta t \to 0} \frac{\langle \Delta x^2\rangle_x}{2\Delta t} p(x;t) \right) \right] \tag{II.27}$$

[10] The Chapman-Kolmogorov equation is an expression indicating the decomposition of the transition probability into the state-space integral of products of probabilities to and from a location in state space (for further details, see [27; 28]).
[11] The symbol | in Equation (II.24) refers to the conditional probability. The conditional probability is a measure of the probability of an event occurring, given that another event has already occurred [29].

Then, defining the drift $\mu(x,t)$ and diffusion coefficient $D(x,t)$ of the associated Langevin equation II.8, respectively, by the following expressions

$$\mu(x,t) = \lim_{\Delta t\to 0} \frac{\langle \Delta x\rangle_x}{\Delta t}, \tag{II.28}$$

$$D(x,t) = \lim_{\Delta t\to 0} \frac{\langle \Delta x^2\rangle_x}{2\Delta t}, \tag{II.29}$$

we have

$$\lim_{\Delta t\to 0} \frac{\langle f\rangle_{t+\Delta t} - \langle f\rangle_t}{\Delta t} = \int \mathrm{d}x f(x) \left[\left(-\frac{\partial}{\partial x}\left(\mu(x,t)p(x;t)\right) + \frac{\partial^2}{\partial x^2}\left(D(x,t)p(x;t)\right)\right]\right(\tag{II.30}$$

Finally, comparing (II.23) with (II.30), it becomes clear that

$$\frac{\partial}{\partial t}p(x;t) = -\frac{\partial}{\partial x}\left(\mu(x,t)p(x;t)\right) + \frac{\partial^2}{\partial x^2}\left(D(x,t)p(x;t)\right), \tag{II.31}$$

which describes the **Fokker-Planck equation** for $p(x;t)$.

In the following, we give some useful examples of finding the Fokker-Planck equation associated with different Langevin equations. In addition, we derive the Fokker-Planck equation associated with a multi-dimensional non-linear type of Langevin equation, which will be of core importance to many results in the coming Chapters. To simplify the notation, we use the Euler's notation $\partial_x, \partial^2_{x^2}$ for $\frac{\partial}{\partial x}$ and $\frac{\partial^2}{\partial x^2}$, respectively. Also, ∂_t to denote the time derivative, sometimes also written using the dot notation $\dot{x}$.

II.2.1 *The Fokker-Planck equation for some Langevin equations*

Example II.1 (Ornstein-Uhlenbeck (O-U) process)**.** *The Ornstein-Uhlenbeck (O-U) process is a first-order differential equation named after Leonard Ornstein and George Eugene Uhlenbeck and whose application describes the velocity of a Brownian particle under the influence of friction. The O-U process is governed by the following Langevin equation*

$$\frac{dx}{dt} = F(x) + \xi. \tag{II.32}$$

Where, ξ is a white noise with a short correlation time with the following property:

$$\langle \xi(t)\xi(t')\rangle = 2D\delta(t-t'). \tag{II.33}$$

Proposition II.2: The linear O-U Fokker-Planck equation

The Fokker-Planck equation corresponding to (II.32) for $F(x) = -\gamma x$ and (II.33) is

$$\frac{\partial}{\partial t}p(x,t) = \frac{\partial}{\partial x}\left[\gamma x + D\frac{\partial}{\partial x}\right] p(x,t). \tag{II.34}$$

Proof. Following the procedure presented in chapter 4 of [30], consider the generating function [12] $\tilde{p} = e^{-\mathrm{i}\lambda x(t)}$ where $\lambda \in \mathbb{R}$ and $\mathrm{i} = \sqrt{-1}$. Then, by definition

$$\langle \tilde{p}\rangle = \int\left(_{-\infty}^{\infty} e^{-\mathrm{i}\lambda x(t)} p(x,t)\mathrm{d}x, \tag{II.35}$$

[12] A moment-generating function is a function to compute a distribution's moments (for a formal definition see [31]).

this means that by applying the Inverse Fourier Transform (IFT)[13] to $\langle \tilde{p} \rangle$, we can obtain the value of the probability density function

$$p(x,t) = \frac{1}{2\pi} \int_{-\infty}^{\infty} e^{\mathrm{i}\lambda x(t)} \langle \tilde{p} \rangle \mathrm{d}\lambda. \tag{II.36}$$

We start our proof by finding the time derivative of $\tilde{p}$

$$\partial_t \tilde{p} = -\mathrm{i}\lambda \dot{x} e^{-\mathrm{i}\lambda x(t)} = -\mathrm{i}\lambda \dot{x} \tilde{p}, \tag{II.37}$$

substituting (II.32) in (II.37)

$$\partial_t \tilde{p} = -\mathrm{i}\lambda \left(-\gamma x + \xi\right) e^{-\mathrm{i}\lambda x} = -\gamma \mathrm{i}\lambda \partial_{\mathrm{i}\lambda} \tilde{p} - \mathrm{i}\lambda \xi \tilde{p}. \tag{II.38}$$

Applying the IFT to (II.38), we get the following

$$\begin{aligned}
\mathcal{F}^{-1}\left[\partial_t \tilde{p}\right] &= \mathcal{F}^{-1}\left[-\gamma \mathrm{i}\lambda \partial_{\mathrm{i}\lambda} \tilde{p}\right] + \mathcal{F}^{-1}\left[-\mathrm{i}\lambda \xi \tilde{p}\right] \\
\frac{1}{2\pi} \int_{-\infty}^{\infty} e^{\mathrm{i}\lambda x} \left(\partial_t \tilde{p}\right) \mathrm{d}\lambda &= \frac{1}{2\pi} \int_{-\infty}^{\infty} e^{\mathrm{i}\lambda x} \left(-\gamma \mathrm{i}\lambda \partial_{\mathrm{i}\lambda} \tilde{p}\right) \mathrm{d}\lambda + \frac{1}{2\pi} \int_{-\infty}^{\infty} e^{\mathrm{i}\lambda x} \left(-\mathrm{i}\lambda \xi \tilde{p}\right) \mathrm{d}\lambda \\
\partial_t \left(\frac{1}{2\pi} \int_{-\infty}^{\infty} e^{\mathrm{i}\lambda x} \tilde{p} \mathrm{d}\lambda\right) &= \frac{-\gamma}{2\pi} \int_{-\infty}^{\infty} \partial_x e^{\mathrm{i}\lambda x} \partial_{\mathrm{i}\lambda} \tilde{p} \mathrm{d}\lambda + \frac{1}{2\pi} \int_{-\infty}^{\infty} e^{\mathrm{i}\lambda x} \left(-\mathrm{i}\lambda \xi \tilde{p}\right) \mathrm{d}\lambda \\
\partial_t \left(\frac{1}{2\pi} \int_{-\infty}^{\infty} e^{\mathrm{i}\lambda x} \tilde{p} \mathrm{d}\lambda\right) &= \frac{-\gamma}{2\pi} \partial_x \left(\int_{-\infty}^{\infty} e^{\mathrm{i}\lambda x} \partial_{\mathrm{i}\lambda} \tilde{p} \mathrm{d}\lambda\right) + \frac{1}{2\pi} \int_{-\infty}^{\infty} e^{\mathrm{i}\lambda x} \left(-\mathrm{i}\lambda \xi \tilde{p}\right) \mathrm{d}\lambda \\
\partial_t \left(\frac{1}{2\pi} \int_{-\infty}^{\infty} e^{\mathrm{i}\lambda x} \tilde{p} \mathrm{d}\lambda\right) &= \frac{-\gamma}{2\pi} \partial_x \left(\int_{-\infty}^{\infty} \left[\partial_{\mathrm{i}\lambda} \left(e^{\mathrm{i}\lambda x} \tilde{p}\right) - x e^{\mathrm{i}\lambda x} \tilde{p}\right] \mathrm{d}\lambda\right) + \frac{1}{2\pi} \int_{-\infty}^{\infty} e^{\mathrm{i}\lambda x} \left(-\mathrm{i}\lambda \xi \tilde{p}\right) \mathrm{d}\lambda \\
\partial_t \left(\frac{1}{2\pi} \int_{-\infty}^{\infty} e^{\mathrm{i}\lambda x} \tilde{p} \mathrm{d}\lambda\right) &= \frac{i\gamma}{2\pi} \partial_x \left[e^{\mathrm{i}\lambda x} \tilde{p}\right]_{-\infty}^{\infty} + \frac{\gamma x}{2\pi} \partial_x \left(\int_{-\infty}^{\infty} e^{\mathrm{i}\lambda x} \tilde{p} \mathrm{d}\lambda\right) + \frac{1}{2\pi} \int_{-\infty}^{\infty} e^{\mathrm{i}\lambda x} \left(-\mathrm{i}\lambda \xi \tilde{p}\right) \mathrm{d}\lambda.
\end{aligned} \tag{II.39}$$

The last term of (II.39) can be solved by finding its average. We find $\tilde{p}(t)$ from (II.38) and substitute in such term to obtain the following

$$\begin{aligned}
\frac{1}{2\pi} \int_{-\infty}^{\infty} e^{\mathrm{i}\lambda x} \left(-\mathrm{i}\lambda \xi \tilde{p}\right) \mathrm{d}\lambda &= \frac{1}{2\pi} \int_{-\infty}^{\infty} e^{\mathrm{i}\lambda x} \left(-\mathrm{i}\lambda \xi \left(\tilde{p}(0) - \gamma \mathrm{i}\lambda \partial_{\mathrm{i}\lambda} \int_0^t \tilde{p}(\tau) \mathrm{d}\tau - \mathrm{i}\lambda \int_0^t \xi(\tau) \tilde{p}(\tau) \mathrm{d}\tau\right)\right) \mathrm{d}\lambda \\
&= \frac{1}{2\pi} \int_{-\infty}^{\infty} e^{\mathrm{i}\lambda x} \left(-\mathrm{i}\lambda \xi \tilde{p}(0) - \gamma \partial_{\mathrm{i}\lambda} \int_0^t \lambda^2 \xi(t) \tilde{p}(\tau) \mathrm{d}\tau \right. \\
&\quad \left. - \int_0^t \lambda^2 \xi(t) \xi(\tau) \tilde{p}(\tau) \mathrm{d}\tau\right) \mathrm{d}\lambda.
\end{aligned} \tag{II.40}$$

We can now find the average of expression (II.39) and use expressions (II.36) and (II.33) as follows

$$\begin{aligned}
\partial_t \left(\frac{1}{2\pi} \int_{-\infty}^{\infty} e^{\mathrm{i}\lambda x} \langle \tilde{p} \rangle \mathrm{d}\lambda\right) &= \frac{i\gamma}{2\pi} \partial_x \left[e^{\mathrm{i}\lambda x} \langle \tilde{p} \rangle\right]_{-\infty}^{\infty} + \frac{\gamma x}{2\pi} \partial_x \left(\int_{-\infty}^{\infty} e^{\mathrm{i}\lambda x} \langle \tilde{p} \rangle \mathrm{d}\lambda\right) \\
&\quad + \frac{1}{2\pi} \int_{-\infty}^{\infty} e^{\mathrm{i}\lambda x} \left(-\mathrm{i}\lambda \langle \xi \rangle \tilde{p}(0) - \gamma \partial_{\mathrm{i}\lambda} \int_0^t \lambda^2 \langle \xi(t) \rangle \tilde{p}(\tau) \mathrm{d}\tau - \int_0^t \lambda^2 \langle \xi(t) \xi(\tau) \rangle \tilde{p}(\tau) \mathrm{d}\tau\right) \mathrm{d}\lambda \\
\partial_t p(x,t) &= \gamma \partial_x x p(x,t) + \frac{1}{2\pi} \int_{-\infty}^{\infty} e^{\mathrm{i}\lambda x} \left(-\int_0^t \lambda^2 \langle \xi(t) \xi(\tau) \rangle \tilde{p}(\tau) \mathrm{d}\tau\right) \mathrm{d}\lambda \\
\partial_t p(x,t) &= \gamma \partial_x x p(x,t) + \frac{1}{2\pi} \int_{-\infty}^{\infty} e^{\mathrm{i}\lambda x} \left(-\lambda^2 \int_0^t 2D\delta(t-\tau) \tilde{p}(\tau) \mathrm{d}\tau\right) \mathrm{d}\lambda
\end{aligned}$$

[13] The Fourier transform of a function f defined on $\mathbb{R}$ is the function $\tilde{f}$ defined on $\mathbb{R}$ by the integral $\tilde{f} = \int_{-\infty}^{\infty} f(x) e^{-\mathrm{i}x\lambda \mathrm{d}x}$. On the other hand, the IFT is defined as $f(x) = \frac{1}{2\pi} \int_{-\infty}^{-\infty} \tilde{f}(\lambda) e^{\mathrm{i}x\lambda} \mathrm{d}\lambda$ (for further details about the Fourier transform, please see [32; 33]).

$$\partial_t p(x,t) = \gamma\partial_x xp(x,t) + \frac{1}{2\pi}\int_{-\infty}^{\infty} e^{\mathrm{i}\lambda x}\left(-2D\lambda^2\frac{1}{2}\tilde{p}(\mathrm{i}\lambda)\right)\mathrm{d}\lambda$$
$$\partial_t p(x,t) = \gamma\partial_x xp(x,t) + D\frac{1}{2\pi}\int_{-\infty}^{\infty} e^{\mathrm{i}\lambda x}\left(-\lambda^2\tilde{p}(\mathrm{i}\lambda)\right)\mathrm{d}\lambda$$
$$\partial_t p(x,t) = \gamma\partial_x xp(x,t) + D\partial^2_{x^2}p(x,t) \quad \text{(II.41)}$$

■

Example II.2 (Stochastic logistic equation)**.** *In some scenarios, it is also possible to express the Fokker-Planck equation for systems with multiplicative noise. As an example, consider the following result.*

Proposition II.3

Given the stochastic logistic equation

$$\dot{x} = \gamma x - \epsilon x^2 + \xi x + \eta, \quad \text{(II.42)}$$

where

$$\begin{aligned}
\langle\xi\rangle &= \langle\eta\rangle = 0, && \text{(II.43)}\\
\langle\xi(t)\xi(\tau)\rangle &= 2D_{\xi\xi}\delta(t-\tau), && \text{(II.44)}\\
\langle\xi(t)\eta(\tau)\rangle &= 2D_{\xi\eta}\delta(t-\tau), && \text{(II.45)}\\
\langle\eta(t)\eta(\tau)\rangle &= 2D_{\eta\eta}\delta(t-\tau). && \text{(II.46)}
\end{aligned}$$

The Fokker-Planck equation of (II.42) is

$$\begin{aligned}
\partial_t p(x,t) = &-\gamma\partial_x\left(xp(x,t)\right) + \epsilon\partial_x\left(x^2p(x,t)\right) - D_{\xi\xi}\partial_x\left(xp(x,t)\right)\\
&+ D_{\xi\xi}\partial^2_{x^2}\left(x^2p(x,t)\right) - D_{\xi\eta}\partial_x p(x,t) + 2D_{\xi\eta}\partial^2_{x^2}\left(xp(x,t)\right) + D_{\eta\eta}\partial^2_{x^2}p(x,t) \quad \text{(II.47)}
\end{aligned}$$

Proof. To proof this statement, we proceed in the same manner as in the proof of Proposition II.2 by finding the time derivate of the generating function $\tilde{p} = e^{-\mathrm{i}\lambda x(t)}$ and substituting (II.42) in the result. This gives the following

$$\partial_t\tilde{p} = -\mathrm{i}\lambda(\gamma x - \epsilon x^2 + \xi x + \eta)\tilde{p} = \mathrm{i}\lambda\gamma\partial_{\mathrm{i}\lambda}\tilde{p} + \mathrm{i}\lambda\epsilon\partial^2_{\mathrm{i}\lambda^2}\tilde{p} + \mathrm{i}\lambda\xi\partial_{\mathrm{i}\lambda}\tilde{p} - \mathrm{i}\lambda\eta\tilde{p}, \quad \text{(II.48)}$$

with a solution

$$\begin{aligned}
\tilde{p}(t) &= \tilde{p}(0) + \int_0^t \left[\mathrm{i}\lambda\gamma\partial_{\mathrm{i}\lambda}\tilde{p}(\tau) + \mathrm{i}\lambda\epsilon\partial^2_{\mathrm{i}\lambda^2}\tilde{p}(\tau) + \mathrm{i}\lambda\xi(\tau)\partial_{\mathrm{i}\lambda}\tilde{p}(\tau) - \mathrm{i}\lambda\eta\tilde{p}(\tau)\right]\mathrm{d}\tau\\
&= \tilde{p}(0) + \mathrm{i}\lambda\gamma\partial_{\mathrm{i}\lambda}\int_0^t \tilde{p}(\tau)\mathrm{d}\tau + \mathrm{i}\lambda\epsilon\partial^2_{\mathrm{i}\lambda^2}\int_0^t \tilde{p}(\tau)\mathrm{d}\tau + \mathrm{i}\lambda\partial_{\mathrm{i}\lambda}\int_0^t \xi(\tau)\tilde{p}(\tau)\mathrm{d}\tau - \mathrm{i}\lambda\int_0^t \eta(\tau)\tilde{p}(\tau)\mathrm{d}\tau. \quad \text{(II.49)}
\end{aligned}$$

Now we find the average of the IFT of (II.48) when substituting (II.49) in its last 2 terms. First, we write

$$\partial_t\left(\frac{1}{2\pi}\int_{-\infty}^{\infty} e^{\mathrm{i}\lambda x}\langle\tilde{p}\rangle\mathrm{d}\lambda\right) = \left\langle\underbrace{\frac{1}{2\pi}\int_{-\infty}^{\infty}\left[\mathrm{i}\lambda\gamma\partial_{\mathrm{i}\lambda}\tilde{p} + \mathrm{i}\lambda\epsilon\partial^2_{\mathrm{i}\lambda^2}\tilde{p}\right]e^{\mathrm{i}\lambda x}\mathrm{d}\lambda}_{(\star)}\right\rangle + \left\langle\underbrace{\frac{1}{2\pi}\int_{-\infty}^{\infty}\left[\mathrm{i}\lambda\xi\partial_{\mathrm{i}\lambda}\tilde{p} - \mathrm{i}\lambda\eta\tilde{p}\right]e^{\mathrm{i}\lambda x}\mathrm{d}\lambda}_{(*)}\right\rangle, \quad \text{(II.50)}$$

then $(\star)$ gives

$$
\begin{aligned}
\left\langle \frac{1}{2\pi}\int_{-\infty}^{\infty}\left[\mathrm{i}\lambda\gamma\partial_{\mathrm{i}\lambda}\tilde{p}+\mathrm{i}\lambda\epsilon\partial^2_{\mathrm{i}\lambda^2}\tilde{p}\right]e^{\mathrm{i}\lambda x}\mathrm{d}\lambda\right\rangle &= \left\langle \frac{1}{2\pi}\int_{-\infty}^{\infty}\left[\gamma\partial_x e^{\mathrm{i}\lambda x}\partial_{\mathrm{i}\lambda}\tilde{p}+\epsilon\partial_x e^{\mathrm{i}\lambda x}\partial^2_{\mathrm{i}\lambda^2}\tilde{p}\right]\mathrm{d}\lambda\right\rangle \\
&= \left\langle \frac{1}{2\pi}\partial_x\int_{-\infty}^{\infty}\left[\gamma e^{\mathrm{i}\lambda x}\partial_{\mathrm{i}\lambda}\tilde{p}+\epsilon e^{\mathrm{i}\lambda x}\partial^2_{\mathrm{i}\lambda^2}\tilde{p}\right]\mathrm{d}\lambda\right\rangle \\
= \left\langle \frac{1}{2\pi}\partial_x\int_{-\infty}^{\infty}\left[\gamma\left(\partial_{\mathrm{i}\lambda}\left(e^{\mathrm{i}\lambda x}\tilde{p}\right)-xe^{\mathrm{i}\lambda x}\tilde{p}\right)\right.\right. &\left.\left.+\epsilon\left(\partial^2_{\mathrm{i}\lambda^2}\left(e^{\mathrm{i}\lambda x}\tilde{p}\right)-x\partial_{\mathrm{i}\lambda}\left(e^{\mathrm{i}\lambda x}\tilde{p}\right)-xe^{\mathrm{i}\lambda x}\partial_{\mathrm{i}\lambda}\tilde{p}\right)\right]\mathrm{d}\lambda\right\rangle \\
&= -\gamma\partial_x x p(x,t)+\epsilon\partial_x x^2 p(x,t), \qquad \text{(II.51)}
\end{aligned}
$$

and for $(*)$ we have

$$
\begin{aligned}
&\left\langle \frac{1}{2\pi}\int_{-\infty}^{\infty}\left[\mathrm{i}\lambda\xi\partial_{\mathrm{i}\lambda}\left(\tilde{p}(0)+\mathrm{i}\lambda\gamma\partial_{\mathrm{i}\lambda}\int_0^t\tilde{p}(\tau)\mathrm{d}\tau+\mathrm{i}\lambda\epsilon\partial^2_{\mathrm{i}\lambda^2}\int_0^t\tilde{p}(\tau)\mathrm{d}\tau+\mathrm{i}\lambda\partial_{\mathrm{i}\lambda}\int_0^t\xi(\tau)\tilde{p}(\tau)\mathrm{d}\tau-\mathrm{i}\lambda\int_0^t\eta(\tau)\tilde{p}(\tau)\mathrm{d}\tau\right)\right.\right. \\
&\left.\left.-\mathrm{i}\lambda\eta\left(\tilde{p}(0)+\mathrm{i}\lambda\gamma\partial_{\mathrm{i}\lambda}\int_0^t\tilde{p}(\tau)\mathrm{d}\tau+\mathrm{i}\lambda\epsilon\partial^2_{\mathrm{i}\lambda^2}\int_0^t\tilde{p}(\tau)\mathrm{d}\tau+\mathrm{i}\lambda\partial_{\mathrm{i}\lambda}\int_0^t\xi(\tau)\tilde{p}(\tau)\mathrm{d}\tau-\mathrm{i}\lambda\int_0^t\eta(\tau)\tilde{p}(\tau)\mathrm{d}\tau\right)\right]e^{\mathrm{i}\lambda x}\mathrm{d}\lambda\right\rangle \\
&= \frac{1}{2\pi}\int_{-\infty}^{\infty}\left[\mathrm{i}\lambda\partial_{\mathrm{i}\lambda}\left(\cancelto{0}{\langle\tilde{p}(0)\xi(t)\rangle}+\mathrm{i}\lambda\gamma\partial_{\mathrm{i}\lambda}\int_0^t\cancelto{0}{\langle\xi(t)\tilde{p}(\tau)\rangle}\mathrm{d}\tau\right.\right. \\
&\left.+\mathrm{i}\lambda\epsilon\partial^2_{\mathrm{i}\lambda^2}\int_0^t\cancelto{0}{\langle\xi(t)\tilde{p}(\tau)\rangle}\mathrm{d}\tau+\mathrm{i}\lambda\partial_{\mathrm{i}\lambda}\int_0^t\underbrace{\langle\xi(t)\xi(\tau)\rangle}_{2D_{\xi\xi}\delta(\tau-t)}\tilde{p}(\tau)\mathrm{d}\tau-\mathrm{i}\lambda\int_0^t\underbrace{\langle\xi(t)\eta(\tau)\rangle}_{2D_{\xi\eta}\delta(\tau-t)}\tilde{p}(\tau)\mathrm{d}\tau\right) \\
&-\mathrm{i}\lambda\left(\cancelto{0}{\langle\tilde{p}(0)\eta(t)\rangle}+\mathrm{i}\lambda\gamma\partial_{\mathrm{i}\lambda}\int_0^t\cancelto{0}{\langle\eta(t)\tilde{p}(\tau)\rangle}\mathrm{d}\tau\right. \\
&\left.\left.+\mathrm{i}\lambda\epsilon\partial^2_{\mathrm{i}\lambda^2}\int_0^t\cancelto{0}{\langle\eta(t)\tilde{p}(\tau)\rangle}\mathrm{d}\tau+\mathrm{i}\lambda\partial_{\mathrm{i}\lambda}\int_0^t\underbrace{\langle\eta(t)\xi(\tau)\rangle}_{2D_{\xi\eta}\delta(\tau-t)}\tilde{p}(\tau)\mathrm{d}\tau-\mathrm{i}\lambda\int_0^t\underbrace{\langle\eta(t)\eta(\tau)\rangle}_{2D_{\eta\eta}\delta(\tau-t)}\tilde{p}(\tau)\mathrm{d}\tau\right)\right]e^{\mathrm{i}\lambda x}\mathrm{d}\lambda \\
&= \frac{1}{2\pi}\int_{-\infty}^{\infty}\left[\mathrm{i}\lambda\partial_{\mathrm{i}\lambda}\left(\mathrm{i}\lambda\partial_{\mathrm{i}\lambda}\int_0^t 2D_{\xi\xi}\delta(\tau-t)\tilde{p}(\tau)\mathrm{d}\tau-\mathrm{i}\lambda\int_0^t 2D_{\xi\eta}\delta(\tau-t)\tilde{p}(\tau)\mathrm{d}\tau\right)\right. \\
&\left.-\mathrm{i}\lambda\left(\mathrm{i}\lambda\partial_{\mathrm{i}\lambda}\int_0^t 2D_{\xi\eta}\delta(\tau-t)\tilde{p}(\tau)\mathrm{d}\tau-\mathrm{i}\lambda\int_0^t 2D_{\eta\eta}\delta(\tau-t)\tilde{p}(\tau)\mathrm{d}\tau\right)\right]e^{\mathrm{i}\lambda x}\mathrm{d}\lambda \\
&\overset{\text{(AII.141)}}{=} \frac{1}{2\pi}\int_{-\infty}^{\infty}\left[\mathrm{i}\lambda\partial_{\mathrm{i}\lambda}\left(\mathrm{i}\lambda\partial_{\mathrm{i}\lambda}(D_{\xi\xi}\tilde{p}(\mathrm{i}\lambda))-\mathrm{i}\lambda(D_{\xi\eta}\tilde{p}(\mathrm{i}\lambda))\right)-\mathrm{i}\lambda\left(\mathrm{i}\lambda\partial_{\mathrm{i}\lambda}(D_{\xi\eta}\tilde{p}(t))-\mathrm{i}\lambda(D_{\eta\eta}\tilde{p}(t))\right)\right]e^{\mathrm{i}\lambda x}\mathrm{d}\lambda
\end{aligned}
$$

$$
\begin{aligned}
&\frac{1}{2\pi}\int_{-\infty}^{\infty}\left[\mathrm{i}\lambda\partial_{\mathrm{i}\lambda}\left(\mathrm{i}\lambda D_{\xi\xi}\partial_{\mathrm{i}\lambda}\tilde{p}(\mathrm{i}\lambda)-\mathrm{i}\lambda D_{\xi\eta}\tilde{p}(\mathrm{i}\lambda)\right)-\mathrm{i}\lambda\left(\mathrm{i}\lambda D_{\xi\eta}\partial_{\mathrm{i}\lambda}\tilde{p}(\mathrm{i}\lambda)-\mathrm{i}\lambda D_{\eta\eta}\tilde{p}(\mathrm{i}\lambda)\right)\right]e^{\mathrm{i}\lambda x}\mathrm{d}\lambda \\
&= D_{\xi\xi}\frac{1}{2\pi}\int_{-\infty}^{\infty}\left[\mathrm{i}\lambda\partial_{\mathrm{i}\lambda}\tilde{p}-\lambda^2\partial^2_{\mathrm{i}\lambda^2}\tilde{p}\right]e^{\mathrm{i}\lambda x}\mathrm{d}\lambda+D_{\xi\eta}\frac{1}{2\pi}\int_{-\infty}^{\infty}\left[-\mathrm{i}\lambda\tilde{p}+\lambda^2\partial_{\mathrm{i}\lambda}\tilde{p}\right]e^{\mathrm{i}\lambda x}\mathrm{d}\lambda+D_{\xi\eta}\frac{1}{2\pi}\int_{-\infty}^{\infty}\left[\lambda^2\partial_{\mathrm{i}\lambda}\tilde{p}\right]e^{\mathrm{i}\lambda x}\mathrm{d}\lambda \\
&\qquad+D_{\eta\eta}\frac{1}{2\pi}\int_{-\infty}^{\infty}\left[-\lambda^2\tilde{p}\right]e^{\mathrm{i}\lambda x}\mathrm{d}\lambda \\
&= D_{\xi\xi}\frac{1}{2\pi}\left[\partial_x\int_{-\infty}^{\infty}e^{\mathrm{i}\lambda x}\partial_{\mathrm{i}\lambda}\tilde{p}\mathrm{d}\lambda+\partial^2_{x^2}\int_{-\infty}^{\infty}e^{\mathrm{i}\lambda x}\partial^2_{\mathrm{i}\lambda^2}\tilde{p}\mathrm{d}\lambda\right]-D_{\xi\eta}\frac{1}{2\pi}\left[\partial_x\int_{-\infty}^{\infty}e^{\mathrm{i}\lambda x}\tilde{p}\mathrm{d}\lambda+2\partial^2_{x^2}\int_{-\infty}^{\infty}e^{\mathrm{i}\lambda x}\partial_{\mathrm{i}\lambda}\tilde{p}\mathrm{d}\lambda\right] \\
&\qquad+D_{\eta\eta}\frac{1}{2\pi}\left[\partial^2_{x^2}\int_{-\infty}^{\infty}e^{\mathrm{i}\lambda x}\tilde{p}\mathrm{d}\lambda\right]
\end{aligned}
$$

$$\overset{(\text{AII.137})-(\text{AII.140})}{=} -D_{\xi\xi}\partial_x\left(xp(x,t)\right)+D_{\xi\xi}\partial^2_{x^2}\left(x^2p(x,t)\right)-D_{\xi\eta}\partial_x p(x,t)+2D_{\xi\eta}\partial^2_{x^2}\left(xp(x,t)\right)+D_{\eta\eta}\partial^2_{x^2}p(x,t) \tag{II.52}$$

■

II.2.2 *The Fokker-Planck equation for linear stochastic systems*

To obtain a description of the Fokker-Planck equation for a generalised set of dynamics, we start by considering the case of a generalised linear dynamical system described via the following stochastic differential equation

$$\dot{\mathbf{x}}(t)=\mathbf{A}\mathbf{x}(t)+\boldsymbol{\xi}(t), \tag{II.53}$$

where $\mathbf{x},\boldsymbol{\xi}\in\mathbb{R}^n$, $\mathbf{A}\in\mathbb{R}^{n\times n}$, and a_{ij} are the elements of the matrix $\mathbf{A}$. Besides, the input $\boldsymbol{\xi}$ contains the δ-correlated Gaussian Langevin forces

$$\langle\xi_i(t)\rangle=0,\langle\xi_i(t)\xi_j(t')\rangle=2D_{ij}\delta(t-t'),D_{ij}=D_{ji},\forall i,j=1,\ldots,n. \tag{II.54}$$

Under this context, the following result holds.

Proposition II.4

The transition probability or Fokker-Planck equation of the system (II.53) is given by the partial differential equation

$$\frac{\partial p(\mathbf{x};t)}{\partial t}=-\sum_{i=1}^{n}\sum_{j=1}^{n}\gamma_{ij}\frac{\partial}{\partial x_i}\left[x_jp(\mathbf{x};t)\right]+\sum_{i=1}^{n}\sum_{j=1}^{n}D_{ij}\frac{\partial^2 p(\mathbf{x};t)}{\partial x_i\partial x_j}, \tag{II.55}$$

Proof. Firstly, let the generating function $\tilde{p}=e^{-\mathrm{i}\boldsymbol{\lambda}^T\mathbf{x}}=e^{\mathrm{i}\sum_{i=1}^n\lambda_ix_i}$ where $\boldsymbol{\lambda}\in\mathbb{R}^n$ such that $\boldsymbol{\lambda}=[\lambda_1,\lambda_2,\ldots,\lambda_n]^\top$. Then, by definition

$$\langle\tilde{p}\rangle=\iint_{\mathbb{R}^n} e^{-\mathrm{i}\boldsymbol{\lambda}^T\mathbf{x}}p(\mathbf{x};t)\,\mathrm{d}^n\lambda. \tag{II.56}$$

This means that by applying the Inverse Fourier Transform (IFT)[14] to $\langle\tilde{p}\rangle$ we can obtain the value of the probability density function

$$p(\mathbf{x};t)=\frac{1}{(2\pi)^n}\iint_{\mathbb{R}^n} e^{\mathrm{i}\sum_{i=1}^n\lambda_ix_i}\langle\tilde{p}\rangle\,\mathrm{d}^n\lambda. \tag{II.57}$$

We start our proof by finding the partial time derivative of $\tilde{p}$

$$\begin{aligned}\partial_t\tilde{p} &= -\mathrm{i}\sum_{i=1}^n\lambda_i\dot{x}_ie^{-\mathrm{i}\sum_{i=1}^n\lambda_ix_i}\\ &= -\mathrm{i}\sum_{i=1}^n\lambda_i\left[\sum_{j=1}^n\gamma_{ij}x_j+\xi_i\right]\tilde{p}\\ &= -\mathrm{i}\sum_{i=1}^n\sum_{j=1}^n\lambda_i\gamma_{ij}x_j\tilde{p}-\mathrm{i}\sum_{i=1}^n\lambda_i\xi_i\tilde{p}.\end{aligned} \tag{II.58}$$

Now finding the average of the IFT of (II.58) we obtain

[14] See [34] for a definition of the multi-dimensional Fourier transform.

$$
\begin{aligned}
\partial_t\left[\frac{1}{(2\pi)^n}\int_{\mathbb{R}^n} e^{\mathrm{i}\lambda^T\mathbf{x}}\langle\tilde{p}\rangle\,\mathrm{d}^n\lambda\right] &= \left\langle\left(\frac{1}{(2\pi)^n}\int_{\mathbb{R}^n} e^{\mathrm{i}\lambda^T\mathbf{x}} \quad -\mathrm{i}\sum_{i=1}^{n}\sum_{j=1}^{n}\lambda_i\gamma_{ij}x_j\tilde{p}\right)\mathrm{d}^n\lambda\right\rangle \\
&\quad + \left\langle\left(\frac{1}{(2\pi)^n}\int_{\mathbb{R}^n} e^{\mathrm{i}\lambda^T\mathbf{x}} \quad -\mathrm{i}\sum_{i=1}^{n}\lambda_i\xi_i\tilde{p}\right)\mathrm{d}^n\lambda\right\rangle\Bigg(\\
\partial_t p(\mathbf{x};t) &= \left\langle\left(\frac{1}{(2\pi)^n}\int_{\mathbb{R}^n} \quad -\sum_{i=1}^{n}\sum_{j=1}^{n}\gamma_{ij}\partial_{x_i}e^{\mathrm{i}\lambda^T\mathbf{x}}x_j\tilde{p}\right)\mathrm{d}^n\lambda\right\rangle \\
+\left\langle\frac{1}{(2\pi)^n}\int_{\mathbb{R}^n} e^{\mathrm{i}\lambda^T\mathbf{x}} \quad -\mathrm{i}\sum_{i=1}^{n}\lambda_i\xi_i\right.&\left.\left\{\tilde{p}(0)-\mathrm{i}\sum_{j=1}^{n}\sum_{k=1}^{n}\int_0^t\lambda_j\gamma_{jk}x_k\tilde{p}(\tau)\,\mathrm{d}\tau-\mathrm{i}\sum_{j=1}^{n}\int_0^t\lambda_j\xi_j(\tau)\tilde{p}(\tau)\,\mathrm{d}\tau\right\}\right)\mathrm{d}^n\lambda\right\rangle \\
\partial_t p(\mathbf{x};t) &= -\sum_{i=1}^{n}\sum_{j=1}^{n}\gamma_{ij}\partial_{x_i}x_j\frac{1}{(2\pi)^n}\int_{\mathbb{R}^n}\left(e^{\mathrm{i}\lambda^T\mathbf{x}}\langle\tilde{p}\rangle\right)\mathrm{d}^n\lambda \\
&\quad + \left\langle\left(\frac{1}{(2\pi)^n}\int_{\mathbb{R}^n} e^{\mathrm{i}\lambda^T\mathbf{x}} \quad -\mathrm{i}\sum_{i=1}^{n}\lambda_i\xi_i(t)\left\{-\mathrm{i}\sum_{j=1}^{n}\int_0^t\lambda_j\xi_j(\tau)\tilde{p}(\tau)\,\mathrm{d}\tau\right\}\right)\mathrm{d}^n\lambda\right\rangle \\
\partial_t p(\mathbf{x};t) = -\sum_{i=1}^{n}\sum_{j=1}^{n}\gamma_{ij}\partial_{x_i}\left(x_j p(\mathbf{x};t)\right) &+ \sum_{i=1}^{n}\sum_{j=1}^{n}\partial_{x_i}\partial_{x_j}\left(\frac{1}{(2\pi)^n}\int_{\mathbb{R}^n} e^{\mathrm{i}\lambda^T\mathbf{x}}\left\{\int_0^t\langle\xi_i(t)\xi_j(\tau)\tilde{p}(\tau)\rangle\,\mathrm{d}\tau\right\}\mathrm{d}^n\lambda\right) \\
\partial_t p(\mathbf{x};t) = -\sum_{i=1}^{n}\sum_{j=1}^{n}\gamma_{ij}\partial_{x_i}\left(x_j p(\mathbf{x};t)\right) &+ \sum_{i=1}^{n}\sum_{j=1}^{n}\partial_{x_i}\partial_{x_j}\left(\frac{1}{(2\pi)^n}\int_{\mathbb{R}^n} e^{\mathrm{i}\lambda^T\mathbf{x}}\left\{\int_0^t 2D_{ij}\delta(t-\tau)\langle\tilde{p}\rangle\,\mathrm{d}\tau\right\}\mathrm{d}^n\lambda\right) \\
\partial_t p(\mathbf{x};t) &= -\sum_{i=1}^{n}\sum_{j=1}^{n}\gamma_{ij}\partial_{x_i}\left(x_j p(\mathbf{x};t)\right) + D_{ij}\sum_{i=1}^{n}\sum_{j=1}^{n}\partial_{x_i}\partial_{x_j}\left(\frac{1}{(2\pi)^n}\int_{\mathbb{R}^n} e^{\mathrm{i}\lambda^T\mathbf{x}}\langle\tilde{p}\rangle\,\mathrm{d}^n\lambda\right) \\
\partial_t p(\mathbf{x};t) &= -\sum_{i=1}^{n}\sum_{j=1}^{n}\gamma_{ij}\partial_{x_i}\left(x_j p(\mathbf{x};t)\right) + D_{ij}\sum_{i=1}^{n}\sum_{j=1}^{n}\partial_{x_i}\partial_{x_j}p(\mathbf{x};t) \qquad \text{(II.59)}
\end{aligned}
$$

■

Dynamics described by (II.53) exhibit important features that permit us to solve its corresponding Fokker-Planck equation. For instance, through the superposition principle[15], we can assure that if the PDF at time $t = 0$ is Gaussian, it will be maintained Gaussian at all t. This assertion is proved by the following result

Proposition II.5: Solution from [36]

Given that the value of the PDF at time $t = 0$ is Gaussian, the time-varying PDF of the linear stochastic system (II.53) is given by

$$
p(\mathbf{x},t|\mathbf{x}_0,t_0) = \frac{(2\pi)^{-\frac{n}{2}}}{\sqrt{\det(\boldsymbol{\Sigma}(t-t_0))}}e^{-\frac{1}{2}(\mathbf{x}-\boldsymbol{\mu}(t-t_0)\mathbf{x}_0)^T\boldsymbol{\Sigma}^{-1}(t-t_0)(\mathbf{x}-\boldsymbol{\mu}(t-t_0)\mathbf{x}_0)}, \qquad \text{(II.60)}
$$

where $\boldsymbol{\Sigma} \in \mathbb{R}_+^{n\times n}$ and $\boldsymbol{\mu} \in \mathbb{R}^n$ are the covariance matrix and mean value vector of the random variable vector $\mathbf{x}$.

[15] A system whose output can be described as a linear combination of all its inputs is a system that satisfies the superposition principle [35].

Proof. Applying the Fourier Transform to (II.55) with respect to every variable in the vector $\mathbf{x}$, we obtain

$$\frac{\partial \tilde{p}}{\partial_t} = \gamma_{ij}\lambda_i \frac{\partial \tilde{p}}{\partial \lambda_j} - D_{ij}\lambda_i\lambda_j\tilde{p}, \tag{II.61}$$

considering the initial condition $\tilde{p}(\mathbf{x}, t|\mathbf{x}_0, t_0) = e^{-\mathrm{i}\boldsymbol{\lambda}^T\mathbf{x}_0}$, the solution of (II.61) is acquired through the ansatz as follows

$$\tilde{p}(\mathbf{x}, t|\mathbf{x}_0, t_0) = e^{-\mathrm{i}\lambda^T\boldsymbol{\mu}(t-t_0)-\frac{1}{2}\lambda^T\boldsymbol{\Sigma}(t-t_0)\lambda}. \tag{II.62}$$

Applying the inverse Fourier transform to (II.62), we finish our proof

$$\begin{aligned} p(\mathbf{x}, t|\mathbf{x}_0, t_0) &= \frac{1}{(2\pi)^n}\int_{\mathbb{R}^n} e^{\mathrm{i}\lambda^T\mathbf{x}-\mathrm{i}\lambda^T\boldsymbol{\mu}(t-t_0)-\frac{1}{2}\lambda^T\boldsymbol{\Sigma}(t-t_0)\lambda}\,\mathrm{d}\boldsymbol{\lambda} \\ &= \frac{1}{(2\pi)^n}\int_{\mathbb{R}^n} e^{-\frac{1}{2}\lambda^T\boldsymbol{\Sigma}(t-t_0)\lambda+\lambda^T(\mathrm{i}\mathbf{x}-\mathrm{i}\boldsymbol{\mu}(t-t_0))}\,\mathrm{d}\boldsymbol{\lambda} \\ &= \sqrt{\left(\frac{(2\pi)^n}{\det(\boldsymbol{\Sigma}(t-t_0))}\right.} e^{-\frac{1}{2}(\mathbf{x}-\boldsymbol{\mu}(t-t_0))^T\boldsymbol{\Sigma}^{-1}(t-t_0)(\mathbf{x}-\boldsymbol{\mu}(t-t_0))}. \end{aligned} \tag{II.63}$$

The last integral was solved by using results explained in [37] ∎

II.2.3 *The Fokker-Planck equation for a generalised process*

Let us now consider the case where the dynamics are non-linear. In this scenario, we focus on processes modelled by the following set of Langevin equations

$$\frac{d\zeta_i}{dt} = f_i(\boldsymbol{\zeta}, t) + \xi_i(t) = -\frac{\partial}{\partial x_i}V(\boldsymbol{\zeta}, t) + \xi_i(t). \tag{II.64}$$

Such that $f_i : \mathbb{R}^n \to \mathbb{R}$ is any function that maps the variables of the vector $\boldsymbol{\zeta} \in \mathbb{R}^n := \{\zeta_1, \zeta_2, \ldots, \zeta_n\}$ to a real value at a given time $t \in \mathbb{R}$. Besides, ξ_i is a random variable with $\langle \xi_i(t) \rangle = 0$, and $\langle \xi_i(t)\xi_j(t') \rangle = 2D_{ij}\delta(t - t')$ with $D_{ij} \geq 0 \forall i, j$. Finally, $V(\boldsymbol{\zeta}, t) : \mathbb{R}^n \to \mathbb{R}$ is a function involving an internal potential.

The associated Fokker-Planck equation to the Langevin equation (II.64) is given by

$$\frac{\partial p(\mathbf{x}; t)}{\partial t} = -\sum_i \frac{\partial}{\partial x_i}\left(f_i(\mathbf{x}, t)p(\mathbf{x}; t)\right) + \sum_i\sum_j D_{ij}\frac{\partial^2 p(\mathbf{x}; t)}{\partial x_i \partial x_j}. \tag{II.65}$$

Equation (II.65) gives the time evolution of the probability distribution $p(\mathbf{x}; t) : \mathbb{R}^n \to \mathbb{R}_+$ with $\mathbf{x} := \{x_1, x_2, \ldots, x_n\}$ for system (II.64). Sometimes, it is convenient to rewrite Equation (II.65) as follows

$$\frac{\partial p(\mathbf{x}; t)}{\partial t} = -\sum_i \frac{\partial}{\partial x_i} J_i(\mathbf{x}; t), \tag{II.66}$$

where J_i is the i-th component of the current probability/flow J, defined by

$$J_i(\mathbf{x}; t) = f_i(\mathbf{x}, t)p(\mathbf{x}; t) - \sum_j D_{ij}\frac{\partial}{\partial x_j}p(\mathbf{x}; t). \tag{II.67}$$

Figure II.7 shows an example of the application of models (II.53) and (II.64) to a set of Brownian particles in one-dimension subject to forces due to the interactions between them.

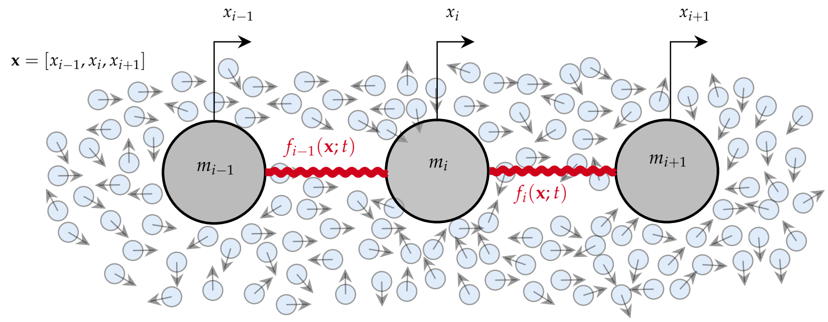

Figure II.7: A set of Brownian particles moving in one-dimension. The displacements are described via the state vector $\mathbf{x}$ and the forces due to interactions via the non-linear function $f(\mathbf{x}:t)$.

II.3 Statistical properties of a type of generalised Langevin equations

According to Proposition II.5, in a linear stochastic system with an initial Gaussian PDF, we can have the value of the PDF at every instant of time if we give the corresponding mean value $\boldsymbol{\mu}(t)$ and covariance matrix $\boldsymbol{\Sigma}(t)$. Hence, in many applications, it is useful to explicitly describe the time evolution of the statistical moments of the stochastic process to construct its corresponding PDF. In the following, and under certain conditions, we show how these values are obtained for both linear and non-linear dynamics.

II.3.1 Linear Non-Autonomous Stochastic Processes

A linear non-autonomous process is given by

$$\dot{\mathbf{x}}(t) = \mathbf{A}\mathbf{x}(t) + \mathbf{B}\mathbf{u}(t) + \boldsymbol{\xi}(t), \tag{II.68}$$

where $\mathbf{A}$ and $\mathbf{B}$ are $n \times n$ and $n \times p$ constant real matrices, respectively; $\mathbf{u} \in \mathbb{R}^p$ is a (bounded smooth) time dependent external input vector, $\boldsymbol{\xi} \in \mathbb{R}^n$ is a Gaussian stochastic noise given by an n dimensional vector of δ-correlated Gaussian noises ξ_i $(i = 1, 2, ...n)$, with the following statistical property

$$\langle \xi_i(t) \rangle = 0, \langle \xi_i(t)\xi_j(t_1) \rangle = 2D_{ij}(t)\delta(t - t_1), D_{ij}(t) = D_{ji}(t), \forall i, j = 1, \ldots, n. \tag{II.69}$$

By assuming an initial Gaussian probability density function (PDF), the PDF remains Gaussian for all time, the following holds.

Proposition II.6: Joint probability [6]

The value of the joint PDF of system (II.68)-(II.69) at any time t is given by

$$p(\mathbf{x};t) = \frac{1}{\sqrt{\det(2\pi\boldsymbol{\Sigma})}} e^{-\frac{1}{2}(\mathbf{x}-\boldsymbol{\mu}(t))^T\boldsymbol{\Sigma}^{-1}(\mathbf{x}-\boldsymbol{\mu}(t))}, \tag{II.70}$$

where

$$\boldsymbol{\mu}(t) = e^{\mathbf{A}t}\boldsymbol{\mu}(0) + \int_0^t e^{\mathbf{A}(t-\tau)}\mathbf{B}\mathbf{u}(\tau)d\tau, \tag{II.71}$$

$$\boldsymbol{\Sigma}(t) = e^{\mathbf{A}t}\left\langle \delta\mathbf{x}(0)\delta\mathbf{x}(0)^T\right\rangle e^{\mathbf{A}^Tt} + 2\int_0^t e^{\mathbf{A}(t-\tau)}\mathbf{D}e^{\mathbf{A}^T(t-\tau)}d\tau, \tag{II.72}$$

and $\mathbf{D} \in \mathbb{R}_+^{n\times n}$ is a matrix with elements $D_{ij}(t)$. Here, $\boldsymbol{\mu}(t)$ is the mean value of $\mathbf{x}(t)$ while $\boldsymbol{\Sigma}$ is the covariance matrix.

Proof. For a Gaussian PDF of $\mathbf{x}$, all we need to calculate are the mean and covariance of $\mathbf{x}$ and substitute them in the general expression for multi-variable Gaussian distribution (II.70). To this end, we first write down the solution of Equation (II.68) as follows

$$\mathbf{x}(t) = e^{\mathbf{A}t}\mathbf{x}(0) + \int_0^t e^{\mathbf{A}(t-t_1)}\boldsymbol{\xi}(t_1)\,\mathrm{d}t_1. \tag{II.73}$$

By taking the average of Equation (II.73), we find the mean value of $\mathbf{x}(t)$ of (II.73) as follows

$$\langle\mathbf{x}(t)\rangle = \langle e^{\mathbf{A}t}\mathbf{x}(0)\rangle + \int_0^t e^{\mathbf{A}(t-t_1)}\langle\boldsymbol{\xi}(t_1)\rangle\,\mathrm{d}t_1 = e^{\mathbf{A}t}\boldsymbol{\mu}(0), \tag{II.74}$$

which is Equation (II.71). On the other hand, to find covariance $\boldsymbol{\Sigma}(t)$, we let $\mathbf{x} = \langle\mathbf{x}\rangle + \delta\mathbf{x}$, and use the property $\langle\delta\mathbf{x}(0)\boldsymbol{\xi}(t)\rangle = 0$ to find

$$\begin{aligned}
\boldsymbol{\Sigma}(t) &= \left\langle \delta\mathbf{x}\delta\mathbf{x}^T\right\rangle \\
&= \left\langle \left(e^{\mathbf{A}t}\delta\mathbf{x}(0) + \int_0^t e^{\mathbf{A}(t-t_2)}\langle\boldsymbol{\xi}(t_2)\rangle\,\mathrm{d}t_2\right)\left(e^{\mathbf{A}t}\delta\mathbf{x}(0) + \int_0^t e^{\mathbf{A}(t-t_1)}\langle\boldsymbol{\xi}(t_1)\rangle\,\mathrm{d}t_1\right)^T\right\rangle \\
&= \left\langle \left(e^{\mathbf{A}t}\delta\mathbf{x}(0) + \int_0^t e^{\mathbf{A}(t-t_2)}\boldsymbol{\xi}(t_2)\,\mathrm{d}t_2\right)\left(\delta\mathbf{x}(0)^T e^{\mathbf{A}^Tt} + \int_0^t \boldsymbol{\xi}(t_1)^T\left(e^{\mathbf{A}(t-t_1)}\right)^T\mathrm{d}t_1\right)\right\rangle \\
&= e^{\mathbf{A}t}\left\langle \delta\mathbf{x}(0)\delta\mathbf{x}(0)^T\right\rangle e^{\mathbf{A}^Tt} + \left\langle\left(\int_0^t e^{\mathbf{A}(t-t_2)}\boldsymbol{\xi}(t_2)\,\mathrm{d}t_2\right)\left(\int_0^t \boldsymbol{\xi}(t_1)^T e^{\mathbf{A}^T(t-t_1)}\,\mathrm{d}t_1\right)\right\rangle \\
&= e^{\mathbf{A}t}\left\langle \delta\mathbf{x}(0)\delta\mathbf{x}(0)^T\right\rangle e^{\mathbf{A}^Tt} + \int_0^t\int_0^t e^{\mathbf{A}(t-t_2)}\langle\boldsymbol{\xi}(t_2)\boldsymbol{\xi}(t_1)^T\rangle e^{\mathbf{A}^T(t-t_1)}\,\mathrm{d}t_2\,\mathrm{d}t_1 \\
&= e^{\mathbf{A}t}\left\langle \delta\mathbf{x}(0)\delta\mathbf{x}(0)^T\right\rangle e^{\mathbf{A}^Tt} + 2\int_0^t e^{\mathbf{A}(t-t_1)}\mathbf{D}e^{\mathbf{A}^T(t-t_1)}\,\mathrm{d}t_1.
\end{aligned} \tag{II.75}$$

Here $\delta\mathbf{x}(0) = \delta\mathbf{x}(t=0)$ is the initial fluctuation at $t = 0$. Equation (II.75) thus proves Equation (II.72). Substitution of Equations (II.71) and (II.72) in Equation (II.70) thus gives us a joint PDF $p(\mathbf{x};t)$ ■

We recall that in Proposition II.6, the computation of the exponential matrix $e^{\mathbf{A}t}$ can be done by using the following result [38]

$$e^{\mathbf{A}t} = \mathscr{L}^{-1}\left[(s\mathbf{I}-\mathbf{A})^{-1}\right] \tag{II.76}$$

Here, $\mathscr{L}^{-1}$ stands for the inverse Laplace transform[16] of the complex variable s. Equations (II.71) and (II.72) can be rewritten in terms of its time derivatives as follows [19]

$$\dot{\boldsymbol{\mu}}(t) = \mathbf{A}\boldsymbol{\mu}(t) + \mathbf{B}\mathbf{u}(t), \tag{II.77}$$

$$\dot{\boldsymbol{\Sigma}}(t) = \mathbf{A}\boldsymbol{\Sigma}(t) + \boldsymbol{\Sigma}(t)\mathbf{A}^\top + 2\mathbf{D}(t). \tag{II.78}$$

As we will describe in Chapter V, the application of Equations (II.77)-(II.78) will permit us to derive a general framework for controlling stochastic systems as they describe stochastic dynamics in terms of deterministic equations of motion.

II.3.2 Non-linear stochastic processes under the Laplace assumption

In the case of non-linear dynamics, we certainly can no longer assure the existence of a Gaussian PDF at every instant of time. Yet, we can describe an uncertain number of statistical moments depending on the nature of the problem. Such computation creates plenty of practical and technical issues that can be eased if we saturate the estimation to the first two moments via the so-called "Laplace assumption". In other words, we describe the solution of (II.65) through a fixed multivariable Gaussian distribution given by [41]

$$p(\mathbf{x};t) = \frac{1}{\sqrt{|2\pi\boldsymbol{\Sigma}|}} e^{\frac{1}{2}Q(\mathbf{x};t)}, \tag{II.79}$$

where $Q(\mathbf{x};t) = -\frac{1}{2}\left(\mathbf{x} - \boldsymbol{\mu}(t)\right)^\top \boldsymbol{\Sigma}^{-1}(t)\left(\mathbf{x} - \boldsymbol{\mu}(t)\right)$; $\boldsymbol{\mu}(t) \in \mathbb{R}^n$ and $\boldsymbol{\Sigma}(t) \in \mathbb{R}^{n\times n}$ are the mean and covariance value of the random variable $\mathbf{x}$. The value of the mean $\boldsymbol{\mu}(t)$ and covariance matrix $\boldsymbol{\Sigma}(t)$ can be obtained from the following result.

Proposition II.7: The Laplace assumption [11]

Under the Laplace assumption, the dynamics of the mean $\boldsymbol{\mu}$ and covariance $\boldsymbol{\Sigma}$ at any time t of a non-linear stochastic differential system (II.64) are governed by the following differential equations

$$\dot{\boldsymbol{\mu}} = \left[f_1(\boldsymbol{\mu},t) + \frac{1}{2}\mathrm{Tr}\left(\boldsymbol{\Sigma}\mathbf{H}_{f_1}\right), f_2(\boldsymbol{\mu},t) + \frac{1}{2}\mathrm{Tr}\left(\boldsymbol{\Sigma}\mathbf{H}_{f_2}\right), \ldots, f_n(\boldsymbol{\mu},t) + \frac{1}{2}\mathrm{Tr}\left(\boldsymbol{\Sigma}\mathbf{H}_{f_n}\right)\right]^\top, \tag{II.80}$$

$$\dot{\boldsymbol{\Sigma}} = \mathbf{J}_f\boldsymbol{\Sigma} + \boldsymbol{\Sigma}\mathbf{J}_f^\top + \mathbf{D} + \mathbf{D}^\top, \tag{II.81}$$

where $\mathbf{H}_{f_i}$ is the Hessian matrix of the function $f_i(\mathbf{x},t)$ and $\mathbf{J}_f$ is the Jacobian of the function $f(\mathbf{x},t)$.

Proof. We start by defining the first two moments of the ensemble density $p(\mathbf{x})$. This is given as follows

$$\dot{\mu}_i = \int_{\mathbb{R}^n} x_i \dot{p}(\mathbf{x};t)\,\mathrm{d}^n x, \tag{II.82}$$

[16] Given a function F of the complex variable s that is analytic throughout the finite complex plane except for a finite number of isolated singularities, a new function f of the real variable t (time) is defined for positive values of t by the following equation

$$f(t) = \frac{1}{2\pi}\lim_{R\to\infty}\int_{L_r} e^{st}F(s)\,\mathrm{d}s \quad (t > 0),$$

where L_R denotes a vertical line segment from $s = \sigma - \mathrm{i}R$ to $s = \sigma + \mathrm{i}R$ such that the constant σ is positive and large enough that the singularities of F all lie to the left of that segment. Furthermore, the function f is the inverse Laplace transform of the function

$$F(s) = \int_0^\infty e^{-st}f(t)\,\mathrm{d}t.$$

For further details, see chapter 7 of [39] and [40].

$$\dot{\Sigma}_{ij} = \int_{\mathbb{R}^n} \overline{x}_i \overline{x}_j \dot{p}(\mathbf{x};t)\, \mathrm{d}^n x. \tag{II.83}$$

Here, $\overline{x}_i = x_i - \mu_i$. Using (II.82)-(II.83) and (II.65) while avoiding the arguments for simplicity, we have

$$\begin{aligned}
\dot{\mu}_i &= \int_{\mathbb{R}^n} x_i \left[-\sum_{i=1}^{n} \partial_{x_i}(f_i p) + \sum_{i,j=1}^{n} \left(\partial_{x_i} D_{ij} \partial_{x_j}\right) p \right] \mathrm{d}^n x \\
&= -\int_{\mathbb{R}^n} x_i \partial_{x_i}(f_i p)\, \mathrm{d}^n x + \int_{\mathbb{R}^n} x_i \partial_{x_i} \left(\sum_{j=1}^{n} D_{ij} \partial_{x_j} p \right) \mathrm{d}^n x \\
&= \int_{\mathbb{R}^n} f_i p \, \mathrm{d}^n x = \langle f_i \rangle.
\end{aligned} \tag{II.84}$$

$$\begin{aligned}
\dot{\Sigma}_{ij} &= \int_{\mathbb{R}^n} \overline{x}_i \overline{x}_j \left[-\sum_{i=1}^{n} \partial_{x_i}(f_i p) + \sum_{i,j=1}^{n} \left(\partial_{x_i} D_{ij} \partial_{x_j}\right) p \right] \mathrm{d}^n x \\
&= -\int_{\mathbb{R}^n} \overline{x}_i \overline{x}_j \partial_{x_i}(f_i p)\, \mathrm{d}^n x - \int_{\mathbb{R}^n} \overline{x}_i \overline{x}_j \partial_{x_j}(f_j p)\, \mathrm{d}^n x + \int_{\mathbb{R}^n} \overline{x}_i \left(\sum_{j=1}^{n} D_{ij} \partial_{x_j} p \right) \mathrm{d}^n x + \int_{\mathbb{R}^n} \overline{x}_j \left(\sum_{i=1}^{n} D_{ji} \partial_{x_i} p \right) \mathrm{d}^n x \\
&= \langle \overline{x}_j f_i + \overline{x}_i f_j \rangle + D_{ij} + D_{ji}.
\end{aligned} \tag{II.85}$$

A closed-form solution to (II.84)-(II.85) can be obtained by exploiting the Laplace assumption, i.e., we recover the sufficient statistics (II.82)-(II.83) of system (II.64) through the first three terms the non-linear flow $f_i(\mathbf{x}, t)$ Taylor expansion around the expected state $\boldsymbol{\mu}$. This is given as follows

$$f_i(\mathbf{x}, t) = f_i(\boldsymbol{\mu}, t) + \sum_{j=1}^{n} \frac{\partial f_i(\boldsymbol{\mu}, t)}{\partial x_j} \overline{x}_j + \frac{1}{2} \sum_{j,k=1}^{n} \frac{\partial^2 f_i(\boldsymbol{\mu}, t)}{\partial_{x_j} \partial_{x_k}} \overline{x}_j \overline{x}_k + \dots \tag{II.86}$$

Under Gaussian assumptions, $\langle \overline{x}_i \rangle = 0$ and $\langle \overline{x}_i \overline{x}_j \rangle = \Sigma_{ij}$ and applying (II.86) to (II.84)-(II.85) we have

$$\begin{aligned}
\dot{\mu} &= \left\langle f_i(\boldsymbol{\mu}, t) + \sum_{j=1}^{n} \frac{\partial f_i(\boldsymbol{\mu}, t)}{\partial x_j} \overline{x}_j + \frac{1}{2} \sum_{j,k=1}^{n} \frac{\partial^2 f_i(\boldsymbol{\mu}, t)}{\partial_{x_j} \partial_{x_k}} \overline{x}_j \overline{x}_k \right\rangle \\
&= f_i(\boldsymbol{\mu}, t) + \frac{1}{2} \sum_{j,k=1}^{n} \frac{\partial^2 f_i(\boldsymbol{\mu}, t)}{\partial_{x_j} \partial_{x_k}} \Sigma_{jk}.
\end{aligned} \tag{II.87}$$

$$\begin{aligned}
\dot{\Sigma}_{ij} &= \left\langle (\overline{x}_j + \overline{x}_i) \left(f_i(\boldsymbol{\mu}, t) + \sum_{k=1}^{n} \frac{\partial f_i(\boldsymbol{\mu}, t)}{\partial x_k} \overline{x}_k \right) \right\rangle + D_{ij} + D_{ji} \\
&= \sum_{k=1}^{n} \frac{\partial f_i(\boldsymbol{\mu}, t)}{\partial x_k} \Sigma_{jk} + \sum_{k=1}^{n} \frac{\partial f_i(\boldsymbol{\mu}, t)}{\partial x_k} \Sigma_{ik} + D_{ij} + D_{ji}.
\end{aligned} \tag{II.88}$$

Equations (II.87)-(II.88) are the expansion of the equations shown in Proposition II.7. This finishes the proof. ■

Example II.3. *To illustrate the application of Proposition II.7, consider the following Langevin form of the Duffing equation*

$$\begin{aligned}
\dot{x}(t) &= v(t) + \xi_1(t) \\
\dot{v}(t) &= -\delta v(t) - \alpha x(t) - \beta x(t)^3 + \gamma \cos(\omega t) + \xi_2(t)
\end{aligned} , \tag{II.89}$$

where $x(t)$ is the displacement at time t, $v(t) = \dot{x}(t)$ is the first derivative of x with respect to time, i.e. velocity, ξ is a delta correlated noise and the values $\delta, \alpha, \beta, \gamma$, and ω are given constants.

Figure II.8 shows a simulation of (II.89) using the deterministic equations of the mean vector $\boldsymbol{\mu} = [\langle x \rangle, \langle v \rangle]^\top$ and covariance matrix $\boldsymbol{\Sigma}$ as described by Proposition II.7. Specifically, Figure II.8 includes the time evolution of the random variables x and v with its phase portrait, and the time evolution of Σ_{11}, Σ_{12}, and Σ_{22}. In the plot, time is scaled by the factor $T = 2\pi/\omega$.

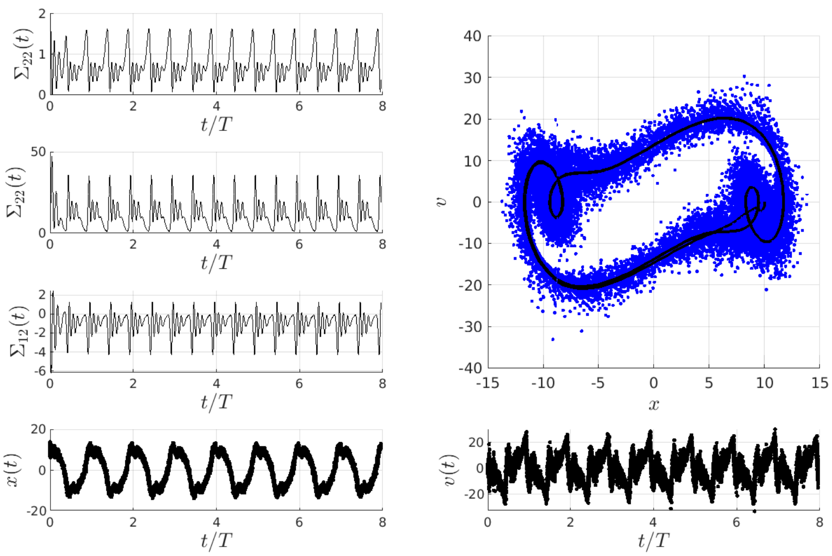

Figure II.8: Time evolution of the stochastic Duffing equation (II.89). The plot includes the time evolution of the values in the covariance matrix $\boldsymbol{\Sigma}$ and the random states x and $\dot{x}$ [11].

II.4 *Thermodynamics*

Another set of preliminary concepts and results that we will need to understand before we continue with our discussion comes from the area of thermodynamics. Again, we highlight that the following is not a deep presentation of the subject but rather a short introduction to useful concepts in the field.

As thermodynamics deals with the study of relations between heat, work, temperature, and energy, it has the following useful system's classifications (see Figure II.9) [42]

- **Isolated systems**. Systems that exchange no fluxes of energy or matter with the environment.

- **Closed systems**. Systems that share energy fluxes with the environment but not matter.

- **Open systems**. Systems that share both energy and matter with the environment.

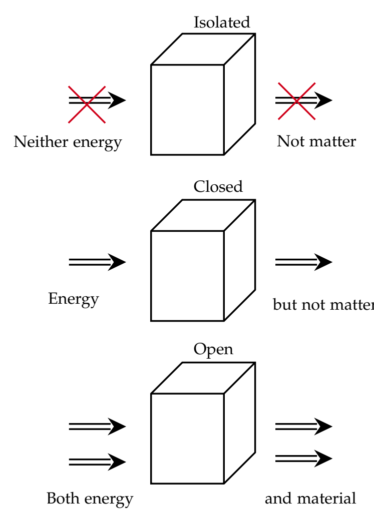

Figure II.9: Types of systems according to thermodynamics.

Within this framework, the field of thermodynamics also establishes the following two widely accepted fundamental laws

1st law In a closed system, the change in internal energy of the system ΔU is equal to the difference between the heat supplied to the system Q and the work W performed by the system on its surroundings, i.e.,

$$\Delta U = Q - W. \tag{II.90}$$

2nd law If two isolated systems in thermal equilibrium are allowed to interact, they will reach to a mutual thermodynamic equilibrium but with a higher so-called entropy S (see Section II.5 for a more detailed discussion about entropy).

The first and second laws of thermodynamics give us important information about the nature of any system. For instance, the second law explains that while energy remains constant, there is something else changing. As we will see in Section II.5, a possible interpretation would be that energy is transformed in terms of its quality. Such a change is only in one direction, resulting in energy being unable to perform work.

II.4.1 Stochastic thermodynamics

Recently, the literature presents a renewed approach to thermodynamics called "stochastic thermodynamics" [23; 43]. Such a field presents a thermodynamic theory for mesoscopic[17], non-equilibrium physical systems interacting with equilibrium heat reservoirs (closed systems).

Since we are interested in dynamical systems described via stochastic differential equations, stochastic thermodynamics is the optimal framework for our work. Stochastic thermodynamics fits well for applications such as mesoscopic systems which can be driven out of equilibrium via optical tweezers.

[17] Mesoscopic systems are systems characterised by energy differences among its states on the order of the thermal energy $k_B T$, where k_B is the Boltzmann constant, and T is the temperature.

II.5 Entropy

Since entropy is an important concept in this work, it is necessary to expand our discussion about it. Entropy, as a mathematical contrivance [44], can be related to the following interpretations [45]

Entropy as irreversibility In steam engines, the creation of heat is a less useful form of energy as this spreads out the energy among all the atoms, and not all of it can be retrieved back to do useful work. Note that the spreading of such energy is an irreversible process. It was Carnot who realised that irreversibility should be avoided to produce the most efficient possible engine. In principle, a reversible heat engine would be able to run forward, generating work by transferring heat from the hot to the cold bath and then run backward using the same work to pump heat back into the hot bath. For instance, let us consider Carnot's prototype of a heat engine shown in Figure II.10, which consists of a piston with external pressure P, two heat baths at a hot temperature T_1 and a cold temperature T_2, and some type of gas inside the piston. During one cycle of his engine heat Q_1 flows out of the hot bath, heat Q_2 flows into our cold bath, and net work $W = Q_1 - Q_2$ is done by the piston on the outside world. To make his engine reversible Carnot must avoid friction, letting hot things touch cold things, letting systems at high pressure expand into systems at low pressure, and moving the walls of the container too quickly (emitting sound or shock waves).

In his cycle, and hence in any reversible engine, the following law is satisfied

$$\frac{Q_1}{T_1} = \frac{Q_2}{T_2}. \tag{II.91}$$

If entropy is considered to be defined as [46; 45]

$$\Delta S_{\text{thermo}} = \frac{Q}{T}, \tag{II.92}$$

where Q is the heath flow at a fixed temperature T, we have that an engine is reversible if no entropy is created or destroyed. This is of course an idealisation as any real engine will create net entropy during a cycle and no engine can reduce the net amount of entropy in the universe.

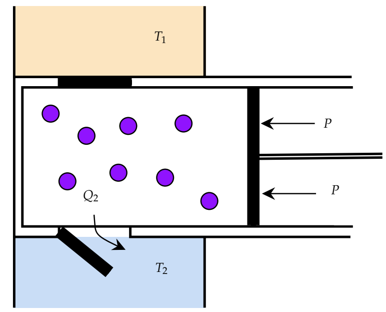

Figure II.10: Carnot's prototype of a heat engine. A piston with external pressure P, two heat baths at a hot temperature T_1 and a cold temperature T_2, and some type of gas inside the piston.

Entropy as disorder The notion of entropy as a measure of disorder is an interpretation that can be understood if we consider the Boltzmann entropy which creates a relation between the thermodynamic entropy and the microscopic properties of matter. Such a value is defined as follows

$$S = k \ln \Omega, \tag{II.93}$$

where k is some constant and Ω is the number of possible microstates (different arrangements of a system) corresponding to the macroscopic state of the system [47].

According to Equation (II.93), if we consider a vessel divided into two sections (see Figure II.11) where we prepare a first state Ω_1 by placing two indistinguishable particles only in one section, meaning $\Omega_1 = 1$, and a second state where we assume that the particles can move freely in the vessel reaching three possible configurations, i.e. $\Omega_2 = 3$, the second state will show higher entropy as compared with the first state. Such a result agrees with the second law of thermodynamics: an isolated system changes from some prepared state to the equilibrium state and entropy increases.

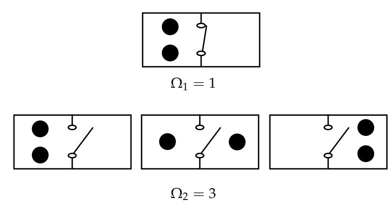

Figure II.11: Simple model explaining the concept of microstates. A vessel divided into two sections, we prepare a first state Ω_1, and a second state Ω_2 where we assume that the particles can move freely in the vessel reaching three possible configurations.

When analysing examples like the one in Figure II.11, we give rise to an opinion that entropy is related to a notion of "disorder". Yet, we have to be cautious when we describe what we mean by the disorder. For the general public, the order is estimated only in the spatial three-dimensional space while not considering the interaction between the elements in the system. For physicists, the order considers the coordinate-momentum $6N$-dimensional phase space and the interactions [48].

Entropy as ignorance Entropy can also be interpreted as a measure of our ignorance about a system as it was presumably first proposed by Edwin Jaynes in 1957 [49]. An advantage of this interpretation is that it poses entropy as a measure of our knowledge about the system rather than as a property of the system.

Remark II.4. *Throughout this work, we pragmatically make use of entropy as a measure of irreversibility, disorder or ignorance. In the case that only one interpretation is preferred, we state it in our analysis.*

This interpretation is also closely related to the concept of entropy created by Shannon in the field of information theory. For Shannon, the entropy of a random variable is the average level of "information", "surprise", or "uncertainty" associated with the possible outcomes of the considered variable [50].

II.5.1 Entropy rate

In stochastic thermodynamics, when the system is out of equilibrium, we can compute its "entropy rate" (ER), i.e. the time derivative of the entropy S, via its time-varying PDF. In closed systems, as shown in Figure II.12, the entropy rate describes a balance between the entropy produced by internal processes Π (entropy production) and the entropy produced by external changes Φ (entropy flow) which can be written as follows

$$\dot{S}(t) = \frac{d}{dt}S(t) = \Pi - \Phi, \tag{II.94}$$

where Π is always a non-negative value. The sign of Φ represents the direction in which the entropy flows between the system and the environment (specifically, $\Phi > 0$ ($\Phi < 0$) when the entropy flows from the system (environment) to the environment (system)). The equality $\Pi = 0$ holds in an equilibrium reversible process, giving $\dot{S} = \Phi$. In comparison, when $\dot{S} = 0$, we have $\Pi = \Phi \geq 0$ [51].

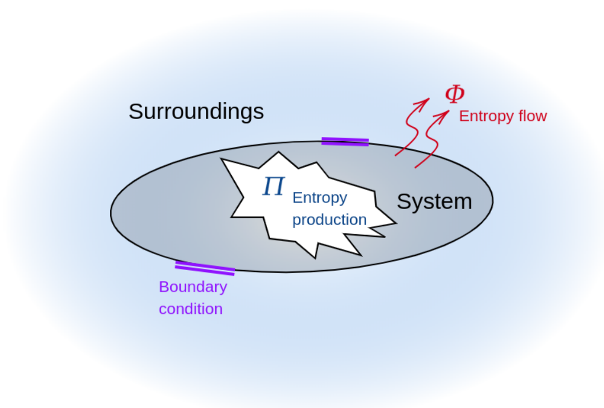

Figure II.12: In a closed system out of equilibrium, there is an entropy balance described via the entropy rate equals the difference between the entropy production (entropy produced by internal processes) and the entropy flow (entropy produced by external exchanges) [52].

Given the time-varying multivariable probability distribution $p(\mathbf{x};t)$ of a system described by the Langevin equation (II.64), we can compute its entropy rate $\dot{S}$ via the following expression [53; 54]

$$\dot{S}(t) = -\int_{\mathbb{R}^n} \dot{p}(\mathbf{x};t) \ln\left(p(\mathbf{x};t)\right) \mathrm{d}^n x. \tag{II.95}$$

Specifically, by substituting (II.66) in (II.95), we have

$$\begin{aligned} \frac{d}{dt}S(t) &= \int_{\mathbb{R}^n} \sum_i \frac{\partial}{\partial x_i} J_i(\mathbf{x};t) \Big) \ln\left(p(\mathbf{x};t)\right) \mathrm{d}\mathbf{x} \\ &= \int_{\mathbb{R}^n} \sum_i \frac{\partial}{\partial x_i} \left(J_i(\mathbf{x};t) \ln\left(p(\mathbf{x};t)\right)\right) - \int_{\mathbb{R}^n} \sum_i J_i(\mathbf{x};t) \left(\frac{\partial}{\partial x_i} \ln\left(p(\mathbf{x};t)\right)\right) \mathrm{d}^n x. \end{aligned} \tag{II.96}$$

Now, if we substitute (II.67) in the first term on the right hand side of (II.96), we obtain[18]

$$\frac{d}{dt}S(t) = -\int_{\mathbb{R}^n}\sum_i J_i(\mathbf{x};t)\left(\frac{\partial}{\partial x_i}\ln\left(p(\mathbf{x};t)\right)\right)d^n x. \tag{II.97}$$

From (II.67), the term $\frac{\partial}{\partial x_i}\ln\left(p(\mathbf{x};t)\right)$ in (II.97) becomes[19]

$$\begin{aligned}\frac{d}{dt}S(t) &= -\int_{\mathbb{R}^n}\sum_i J_i(\mathbf{x};t)\left(\frac{f_i(\mathbf{x})}{D_{ii}} - \frac{J_i(\mathbf{x};t)}{D_{ii}p(\mathbf{x};t)}\right.\\ &\quad\left. - \frac{\sum_{j\neq i} D_{ij}\frac{\partial}{\partial x_j}p(\mathbf{x};t)}{D_{ii}p(\mathbf{x};t)}\right)d\mathbf{x}.\end{aligned} \tag{II.98}$$

Taking the positive definite part on the right hand side of (II.98), we define Π as follows[20]

$$\Pi = \sum_i \Pi_{J_i} = \int_{\mathbb{R}^n}\sum_i \frac{J_i(\mathbf{x};t)^2}{D_{ii}p(\mathbf{x};t)}\,d\mathbf{x}, \tag{II.99}$$

where Π_{J_i} is the contribution to the entropy production by the current flow J_i. Therefore, the remaining terms define the entropy flow Φ as

$$\Phi = \int_{\mathbb{R}^n}\sum_i\left(\frac{J_i(\mathbf{x};t)f_i(\mathbf{x})}{D_{ii}} - \frac{\sum_{j\neq i}D_{ij}J_i(\mathbf{x};t)\frac{\partial}{\partial x_j}p(\mathbf{x};t)}{D_{ii}p(\mathbf{x};t)}\right)d\mathbf{x}, \tag{II.100}$$

In this work, we consider only the case when $D_{ij}=0$ if $i\neq j$ in (II.100)[21], which gives

$$\Phi = \sum_i \Phi_{J_i} = \int_{\mathbb{R}^n}\sum_i\left(\frac{J_i(\mathbf{x};t)f_i(\mathbf{x})}{D_{ii}}\right)d\mathbf{x}, \tag{II.101}$$

where, Φ_{J_i} is the contribution to the entropy production by the current flow J_i. Notice that when $D_{ii}=0$, (II.99)-(II.100) are undefined. In such a scenario, we can still find the values of Π and Φ by substituting $D_{ij}=0$ in (II.67) before computing the ER as follows

$$\begin{aligned}\dot{S} &= -\int_{\mathbb{R}^n}\sum_i J_i(\mathbf{x};t)\left(\frac{\partial}{\partial x_i}\ln\left(p(\mathbf{x};t)\right)\right)d^n x\\ &\overset{D_{ij}=0 \text{ in (II.67)}}{=} -\int_{\mathbb{R}^n}\sum_i\left(f_i(\mathbf{x},t)p(\mathbf{x};t)\right)\left(\frac{\partial}{\partial x_i}\ln\left(p(\mathbf{x};t)\right)\right)d^n x\end{aligned}$$

[18] Since $p(\mathbf{x};t)\to 0$ at $\pm\infty\ \forall x_i\in\mathbf{x}$, we have $\int_{\mathbb{R}^n}\sum_i\frac{\partial}{\partial x_i}\left(J_i(\mathbf{x};t)\ln\left(p(\mathbf{x};t)\right)\right)\to 0$.

[19] Clearly, according to (II.67),

$$\frac{\partial}{\partial x_i}\ln\left(p(\mathbf{x};t)\right) = \frac{1}{p(\mathbf{x};t)}\frac{\partial}{\partial x_i}p(\mathbf{x};t) = \frac{1}{D_{ii}p(\mathbf{x};t)}\left(f_i(\mathbf{x},t)p(\mathbf{x};t) - J_i(\mathbf{x}:t) - \sum_{j\neq i}D_{ij}\frac{\partial}{\partial x_i}p(\mathbf{x};t)\right)$$

[20] The positive definite part on the right hand side of (II.98) is

$$\int_{\mathbb{R}^n}\sum_i\frac{J_i(\mathbf{x};t)^2}{D_{ii}p(\mathbf{x};t)}\,d\mathbf{x}$$

since $p(\mathbf{x};t)$, D_{ii}, and $J_i(\mathbf{x};t)^2$ are, by definition, non-negative terms.

[21] In other words, we consider only the case when there is no correlation between the particles' temperature in the diffusion process. While this limits our study to a specific set of systems, it permits us to find a closed-form solution of the stochastic thermodynamics that is used to understand the effects of an optimal control protocol as discussed in Chapter V.

$$
\begin{aligned}
&= -\int_{\mathbb{R}^n} \sum_i f_i(\mathbf{x},t)\frac{\partial}{\partial x_i} p(\mathbf{x};t)\,\mathrm{d}^n x \\
&= -\sum_i \cancelto{0}{\int_{\mathbb{R}^n} \frac{\partial}{\partial x_i}\left(f_i(\mathbf{x},t)p(\mathbf{x};t)\right)\mathrm{d}^n x} + \sum_i \int_{\mathbb{R}^n} p(\mathbf{x};t)\frac{\partial}{\partial x_i} f_i(\mathbf{x},t)\,\mathrm{d}^n x.
\end{aligned} \tag{II.102}
$$

Hence, given that $D_{ij} = 0$, $\Pi = 0$ as there is no positive definite part in (II.102), and

$$
\Phi = \sum_i \Phi_{J_i} = \sum_i \left\langle \frac{\partial f_i(\mathbf{x})}{\partial x_i} \right\rangle = \sum_i a_{ii}. \tag{II.103}
$$

The specific value of entropy rate, entropy production, and entropy flow can be computed for linear and non-linear stochastic dynamics using the following results.

Proposition II.8: Stochastic thermodynamics in linear systems [9]

The value of entropy production Π and entropy flow Φ in a Gaussian process whose mean $\boldsymbol{\mu}$ and covariance $\boldsymbol{\Sigma}$ are governed by equations (II.77)-(II.78) are given by

$$
\begin{aligned}
\Pi &= \dot{\boldsymbol{\mu}}^\top \mathbf{D}^{-1}\dot{\boldsymbol{\mu}} + \mathrm{Tr}\left(\mathbf{A}^\top \mathbf{D}^{-1}\mathbf{A}\boldsymbol{\Sigma}\right) + \mathrm{Tr}\left(\boldsymbol{\Sigma}^{-1}\mathbf{D}\right) + 2\mathrm{Tr}(\mathbf{A}), && \text{(II.104)}\\
\Phi &= \dot{\boldsymbol{\mu}}^\top \mathbf{D}^{-1}\dot{\boldsymbol{\mu}} + \mathrm{Tr}\left(\mathbf{A}^\top \mathbf{D}^{-1}\mathbf{A}\boldsymbol{\Sigma}\right) + \mathrm{Tr}(\mathbf{A}). && \text{(II.105)}
\end{aligned}
$$

Recall that $\mathbf{A} \in \mathbb{R}^{n\times n}$ and $\mathbf{D} \in \mathbb{R}_+^{n\times n}$ are matrices describing the internal dynamics and noise amplitude of the linear stochastic system (II.68).

Proof. We start by applying the definition of entropy (II.99) production and entropy flow (II.101) to obtain the contribution of each current flow J_i as follows

$$
\begin{aligned}
\Pi_{J_i} &= \frac{1}{D_{ii}}\left\langle f_i(\mathbf{x},t)^2\right\rangle + D_{ii}\left\langle \left(\frac{\partial Q(\mathbf{x})}{\partial x_i}\right)^2\right\rangle + 2\left\langle \frac{\partial f_i(\mathbf{x},t)}{\partial x_i}\right\rangle, && \text{(II.106)}\\
\Phi_{J_i} &= \frac{1}{D_{ii}}\langle f_i(\mathbf{x},t)^2\rangle + \left\langle \frac{\partial f_i(\mathbf{x},t)}{\partial x_i}\right\rangle, && \text{(II.107)}
\end{aligned}
$$

where $Q(\mathbf{x};t) = -\frac{1}{2}\left(\mathbf{x}-\boldsymbol{\mu}(t)\right)^\top \boldsymbol{\Sigma}^{-1}(t)\left(\mathbf{x}-\boldsymbol{\mu}(t)\right)$. Before continuing, it is useful to note that [55]

$$
\begin{aligned}
\frac{\partial Q}{\partial x_k} &= -\frac{1}{2}\left[\sum_i \delta x_i \Sigma_{ki}^{-1} + \sum_j \delta x_j \Sigma_{jk}^{-1}\right] \\
&= -\sum_i \delta x_i \Sigma_{ki}^{-1} = -\delta\mathbf{x}^\top \boldsymbol{\Sigma}_k^{-1},
\end{aligned} \tag{II.108}
$$

where $\delta x_i = x_i - \mu_i$, $\delta\mathbf{x} := \mathbf{x} - \boldsymbol{\mu} = [\delta x_1, \ldots, \delta x_n]^\top$ and $\boldsymbol{\Sigma}_k^{-1}$ is the k-th column of the inverse matrix $\boldsymbol{\Sigma}^{-1}$ of $\boldsymbol{\Sigma}$. Besides,

$$
f_i(\mathbf{x})^2 = \mathbf{x}^\top \mathbf{A}_i^\top \mathbf{A}_i \mathbf{x} + \mathbf{u}^\top \mathbf{B}_i^\top \mathbf{B}_i \mathbf{u} + 2\mathbf{u}^\top \mathbf{B}_i^\top \mathbf{A}_i \mathbf{x}, \tag{II.109}
$$

where we recall that $\mathbf{A}_i$ and $\mathbf{B}_i$ are the i-th arrows of the matrices $\mathbf{A}$ and $\mathbf{B}$ defined according to (II.68). Therefore [55]

$$
\left\langle D_{ii}\left(\frac{\partial Q(\mathbf{x})}{\partial x_i}\right)^2\right\rangle = D_{ii}\left\langle \delta\mathbf{x}^\top \boldsymbol{\Sigma}_i^{-1}(\boldsymbol{\Sigma}_i^{-1})^\top \delta\mathbf{x}\right\rangle
$$

$$= \quad D_{ii}\operatorname{Tr}(\mathbf{\Delta}_i\mathbf{\Sigma}), \tag{II.110}$$

and

$$\frac{f_i(\mathbf{x})^2}{D_{ii}} = \frac{1}{D_{ii}}\left(\operatorname{Tr}(\mathbf{\Gamma}_i\mathbf{\Sigma}) + \boldsymbol{\mu}^\top\mathbf{\Gamma}_i\boldsymbol{\mu} + \mathbf{u}^\top\mathbf{\Omega}_i\mathbf{u} + 2\mathbf{u}^\top\boldsymbol{\varphi}_i\boldsymbol{\mu}\right), \tag{II.111}$$

where $\mathbf{\Delta}_i = \mathbf{\Sigma}_i^{-1}(\mathbf{\Sigma}_i^{-1})^\top$, $\mathbf{\Gamma}_i = \mathbf{A}_i^\top\mathbf{A}_i$, $\mathbf{\Omega}_i = \mathbf{B}_i^\top\mathbf{B}_i$, and $\boldsymbol{\varphi}_i = \mathbf{B}_i^\top\mathbf{A}_i$. Furthermore, we have that

$$\frac{\partial f_i(\mathbf{x})}{\partial x_i} = a_{ii}.$$

Then

$$\begin{aligned}
\Pi_{J_i} &= \frac{1}{D_{ii}}\left(\operatorname{Tr}(\mathbf{\Gamma}_i\mathbf{\Sigma}) + \boldsymbol{\mu}^\top\mathbf{\Gamma}_i\boldsymbol{\mu} + \mathbf{u}^\top\mathbf{\Omega}_i\mathbf{u} + 2\mathbf{u}^\top\boldsymbol{\varphi}_i\boldsymbol{\mu}\right) \\
&\quad + D_{ii}\operatorname{Tr}(\mathbf{\Delta}_i\mathbf{\Sigma}) + 2a_{ii}, \qquad\qquad \text{(II.112)} \\
\Phi_{J_i} &= \frac{1}{D_{ii}}\left(\operatorname{Tr}(\mathbf{\Gamma}_i\mathbf{\Sigma}) + \boldsymbol{\mu}^\top\mathbf{\Gamma}_i\boldsymbol{\mu} + \mathbf{u}^\top\mathbf{\Omega}_i\mathbf{u} + 2\mathbf{u}^\top\boldsymbol{\varphi}_i\boldsymbol{\mu}\right) + a_{ii}.
\end{aligned}$$

Finally, since elements in (II.112) like

$$\begin{aligned}
\sum_i^n \frac{\boldsymbol{\mu}^\top\mathbf{\Gamma}_i\boldsymbol{\mu}}{D_{ii}} &= \boldsymbol{\mu}^\top\left(\frac{\mathbf{A}_1^\top\mathbf{A}_1}{D_{11}} + \cdots + \frac{\mathbf{A}_n^\top\mathbf{A}_n}{D_{nn}}\right)\boldsymbol{\mu} \\
&= \boldsymbol{\mu}^\top\mathbf{A}^\top\mathbf{D}^{-1}\mathbf{A}\boldsymbol{\mu}, \qquad\qquad \text{(II.113)} \\
\sum_i^n \frac{\operatorname{Tr}(\mathbf{\Delta}_i\mathbf{\Sigma})}{D_{ii}} &= \operatorname{Tr}\left(\left(\frac{\mathbf{\Sigma}_1^{-1}(\mathbf{\Sigma}_1^{-1})^\top}{D_{11}} + \cdots + \frac{\mathbf{\Sigma}_n^{-1}(\mathbf{\Sigma}_n^{-1})^\top}{D_{nn}}\right)\mathbf{\Sigma}\right) \\
&= \operatorname{Tr}\left(\mathbf{\Sigma}^{-1}\mathbf{D}^{-1}(\mathbf{\Sigma}^{-1})^\top\mathbf{\Sigma}\right), \qquad\qquad \text{(II.114)}
\end{aligned}$$

we can apply the same reasoning to all the terms on the right hand side of (II.112) to get

$$\Pi = \dot{\boldsymbol{\mu}}^\top\mathbf{D}^{-1}\dot{\boldsymbol{\mu}} + \operatorname{Tr}\left(\mathbf{A}^\top\mathbf{D}^{-1}\mathbf{A}\mathbf{\Sigma}\right) + \operatorname{Tr}\left(\mathbf{\Sigma}^{-1}\mathbf{D}\right) + 2\operatorname{Tr}(\mathbf{A}), \tag{II.115}$$

$$\Phi = \dot{\boldsymbol{\mu}}^\top\mathbf{D}^{-1}\dot{\boldsymbol{\mu}} + \operatorname{Tr}\left(\mathbf{A}^\top\mathbf{D}^{-1}\mathbf{A}\mathbf{\Sigma}\right) + \operatorname{Tr}(\mathbf{A}), \tag{II.116}$$

$$\dot{S} = \operatorname{Tr}\left(\mathbf{\Sigma}^{-1}\mathbf{D}\right) + \operatorname{Tr}(\mathbf{A}) = \frac{1}{2}\operatorname{Tr}\left(\mathbf{\Sigma}^{-1}\dot{\mathbf{\Sigma}}\right), \tag{II.117}$$

which corresponds to the result given in Relation II.8. ■

Proposition II.9: Stochastic thermodynamics in non-linear systems under the Laplace assumption[11]

Under the Laplace assumption (Proposition II.7), the value of entropy rate $\dot{S}$, entropy production Π, and entropy flow Φ in a non-linear stochastic system described by (II.64) are given by

$$\dot{S} = \operatorname{Tr}\left(\mathbf{\Sigma}^{-1}\mathbf{D}\right) + \operatorname{Tr}(\mathbf{J}_f) = \frac{1}{2}\operatorname{Tr}\left(\mathbf{\Sigma}^{-1}\dot{\mathbf{\Sigma}}\right), \tag{II.118}$$

$$\Pi = \operatorname{Tr}\left(\mathbf{\Sigma}^{-1}\mathbf{D}\right) + \operatorname{Tr}\left(f(\boldsymbol{\mu},t)^\top\mathbf{D}^{-1}f(\boldsymbol{\mu},t)\right) + \operatorname{Tr}\left(\mathbf{J}_f\mathbf{D}^{-1}\mathbf{J}_f^\top\mathbf{\Sigma}\right) + 2\operatorname{Tr}(\mathbf{J}_f), \tag{II.119}$$

$$\Phi = \operatorname{Tr}\left(f(\boldsymbol{\mu},t)^\top\mathbf{D}^{-1}f(\boldsymbol{\mu},t)\right) + \operatorname{Tr}\left(\mathbf{J}_f\mathbf{D}^{-1}\mathbf{J}_f^\top\mathbf{\Sigma}\right) + \operatorname{Tr}(\mathbf{J}_f), \tag{II.120}$$

where $\mathbf{J}_f$ is the Jacobian of the function $f(\mathbf{x},t) = [f_1(\mathbf{x},t), f_2(\mathbf{x},t), \ldots, f_n(\mathbf{x},t)]^\top$.

Proof. Like in the proof of Proposition II.8, we start by applying the definition of entropy production (II.99) and entropy flow (II.100) to obtain the contribution to them by each current flow J_i. This gives us

$$\Pi_{J_i} = \frac{1}{D_{ii}}\left\langle f_i(\mathbf{x},t)^2\right\rangle + D_{ii}\left\langle\left(\frac{\partial Q(\mathbf{x})}{\partial x_i}\right)^2\right\rangle + 2\left\langle\frac{\partial f_i(\mathbf{x},t)}{\partial x_i}\right\rangle \tag{II.121}$$

$$\Phi_{J_i} = \frac{1}{D_{ii}}\langle f_i(\mathbf{x},t)^2\rangle + \left\langle\frac{\partial f_i(\mathbf{x},t)}{\partial x_i}\right\rangle \tag{II.122}$$

where $Q(\mathbf{x};t) = -\frac{1}{2}\left(\mathbf{x}-\boldsymbol{\mu}(t)\right)^\top \boldsymbol{\Sigma}^{-1}(t)\left(\mathbf{x}-\boldsymbol{\mu}(t)\right)$. Again, before continuing, it is useful to note that [55]

$$\frac{\partial Q}{\partial x_k} = -\frac{1}{2}\left[\sum_i \bar{x}_i \Sigma^{-1}_{ki} + \sum_j \bar{x}_j \Sigma^{-1}_{jk}\right] = -\sum_i \bar{x}_i \Sigma^{-1}_{ki} = -\bar{\mathbf{x}}^\top \boldsymbol{\Sigma}^{-1}_k, \tag{II.123}$$

where $\bar{x}_i = x_i - \mu_i$, $\bar{\mathbf{x}} := \mathbf{x} - \boldsymbol{\mu} = [\bar{x}_1, \ldots, \bar{x}_n]^\top$ and $\boldsymbol{\Sigma}^{-1}_k$ is the k-th column of the inverse matrix $\boldsymbol{\Sigma}^{-1}$ of $\boldsymbol{\Sigma}$. Therefore [55]

$$\left\langle D_{ii}\left(\frac{\partial Q(\mathbf{x})}{\partial x_i}\right)^2\right\rangle = D_{ii}\left\langle \bar{\mathbf{x}}^\top \boldsymbol{\Sigma}^{-1}_i (\boldsymbol{\Sigma}^{-1}_i)^\top \bar{\mathbf{x}}\right\rangle = D_{ii}\mathrm{Tr}(\boldsymbol{\Delta}_i\boldsymbol{\Sigma}). \tag{II.124}$$

Now, following the ideas of the Laplace assumption given in Proposition II.7, if we substitute the first two terms of the non-linear flow $f_i(\mathbf{x},t)$ Taylor expansion around the expected state $\boldsymbol{\mu}$ (see Equation (II.86)) in the terms $\frac{\langle f_i(\mathbf{x})^2\rangle}{D_{ii}}$ and $\left\langle\frac{\partial f_i(\mathbf{x},t)}{\partial x_i}\right\rangle$ of the right hand side of (II.121)-(II.122), we have

$$\begin{aligned}\frac{f_i(\mathbf{x})^2}{D_{ii}} &= \frac{1}{D_{ii}}\left\langle \left(f_i(\boldsymbol{\mu},t) + \sum_{j=1}^n \frac{\partial f_i(\boldsymbol{\mu},t)}{\partial x_j}\bar{x}_j\right)\left(f_i(\boldsymbol{\mu},t) + \sum_{k=1}^n \frac{\partial f_i(\boldsymbol{\mu},t)}{\partial x_k}\bar{x}_k\right)\right\rangle \\ &= \frac{1}{D_{ii}}\left(f_i(\boldsymbol{\mu},t)^2 + \sum_{j,k=1}^n \frac{\partial f_i(\boldsymbol{\mu},t)}{\partial x_j}\frac{\partial f_i(\boldsymbol{\mu},t)}{\partial x_k}\Sigma_{jk}\right) = \frac{1}{D_{ii}}\left(f_i(\boldsymbol{\mu},t)^2 + \nabla^\top f_i(\boldsymbol{\mu},t)\boldsymbol{\Sigma}\nabla f_i(\boldsymbol{\mu},t)\right),\end{aligned} \tag{II.125}$$

and

$$\left\langle\frac{\partial f_i(\mathbf{x},t)}{\partial x_i}\right\rangle = \left\langle\frac{\partial}{\partial x_i}\left(f_i(\boldsymbol{\mu},t) + \sum_{j=1}^n \frac{\partial f_i(\boldsymbol{\mu},t)}{\partial x_j}\bar{x}_j + \frac{1}{2}\sum_{j,k=1}^n \frac{\partial^2 f_i(\boldsymbol{\mu},t)}{\partial_{x_j}\partial_{x_k}}\bar{x}_j\bar{x}_k\right)\right\rangle = \frac{\partial f_i(\boldsymbol{\mu},t)}{\partial x_i}. \tag{II.126}$$

Finally, after a lengthy process of substituting Equations (II.124) to (II.126) in (II.121)-(II.122) and summing all the current flow contributions according to the definitions of the entropy rate (II.94), entropy production (II.99) and entropy flow (II.100), we have

$$\Pi = \sum_{i=1}^n \Pi_i = \mathrm{Tr}\left(\boldsymbol{\Sigma}^{-1}\mathbf{D}\right) + \mathrm{Tr}\left(\mathbf{D}^{-1}f(\boldsymbol{\mu},t)f(\boldsymbol{\mu},t)^\top\right) + \mathrm{Tr}\left(\mathbf{J}_f\mathbf{D}^{-1}\mathbf{J}_f^\top\boldsymbol{\Sigma}\right) + 2\mathrm{Tr}(\mathbf{J}_f), \tag{II.127}$$

$$\Phi = \sum_{i=1}^n \Phi_i = \mathrm{Tr}\left(\mathbf{D}^{-1}f(\boldsymbol{\mu},t)f(\boldsymbol{\mu},t)^\top\right) + \mathrm{Tr}\left(\mathbf{J}_f\mathbf{D}^{-1}\mathbf{J}_f^\top\boldsymbol{\Sigma}\right) + \mathrm{Tr}(\mathbf{J}_f), \tag{II.128}$$

$$\dot{S} = \mathrm{Tr}\left(\boldsymbol{\Sigma}^{-1}\mathbf{D}\right) + \mathrm{Tr}(\mathbf{J}_f), \tag{II.129}$$

which corresponds to the result given in Proposition II.9. ∎

Chapter concluding remarks

In this chapter, we have reviewed the basic theoretical concepts and essential results that will be applied in the following chapters. The results include novel descriptions of the entropy rate using dynamical systems and control engineering nomenclature. The preliminaries show that the Fokker-Planck equation is a fundamental and simplified method to describe the time-varying PDF of a non-linear stochastic system with additive noise. Yet, we have included a description of the most popular numerical methods used to solve SDE and an alternative procedure to compute such a time-varying PDF. Finally, we have introduced the concept of stochastic thermodynamics and entropy rate that will be useful to analyse the proposed control protocol for creating efficient and organised behaviours.

AII Appendix Chapter II.

AII.1 Properties and Formulas

$$\int_{a-\epsilon}^{a+\epsilon} f(t)\delta(t-a)\mathrm{d}t = f(a), \quad \epsilon > 0 \tag{AII.130}$$

$$\delta(-x) = \delta(x), \tag{AII.131}$$

$$|a-b| = \max(a,b) - \min(a,b), \tag{AII.132}$$

$$|a+b| = \max(a,b) + \min(a,b), \tag{AII.133}$$

$$C_{\xi}(u) = 1 + \sum_{n=1}^{\infty} (iu)^n \frac{M_n}{n!}, \tag{AII.134}$$

$$\mathcal{W}_{\xi}(x) = \frac{1}{2\pi}\int_{-\infty}^{\infty} C_{\xi}(u) e^{-iux}\mathrm{d}u, \tag{AII.135}$$

$$\langle \xi(t_1)\xi(t_2)\cdots\xi(t_{2n})\rangle = (2D)^n \left[\sum_{P_d} \delta(t_{i_1}-t_{i_2})\delta(t_{i_3}-t_{i_4})\cdots\delta(t_{i_{2n-1}}-t_{i_{2n}})\right], \tag{AII.136}$$

$$\partial_{\mathrm{i}\lambda}\left(e^{\mathrm{i}\lambda x}\tilde{p}\right) = xe^{\mathrm{i}\lambda x}\tilde{p} + e^{\mathrm{i}\lambda x}\partial_{\mathrm{i}\lambda}\tilde{p}, \tag{AII.137}$$

$$\partial^2_{\mathrm{i}\lambda^2}\left(e^{\mathrm{i}\lambda x}\tilde{p}\right) = x\partial_{\mathrm{i}\lambda}\left(e^{\mathrm{i}\lambda x}\tilde{p}\right) + xe^{\mathrm{i}\lambda x}\partial_{\mathrm{i}\lambda}\tilde{p} + e^{\mathrm{i}\lambda x}\partial^2_{\mathrm{i}\lambda^2}\tilde{p}, \tag{AII.138}$$

$$\begin{aligned}\frac{1}{2\pi}\int_{-\infty}^{\infty} e^{\mathrm{i}\lambda x}\partial_{\mathrm{i}\lambda}\langle\tilde{p}\rangle\mathrm{d}\lambda &= \frac{1}{2\pi}\int_{-\infty}^{\infty}\left(\partial_{\mathrm{i}\lambda}\left(e^{\mathrm{i}\lambda x}\langle\tilde{p}\rangle\right) - xe^{\mathrm{i}\lambda x}\langle\tilde{p}\rangle\right)\mathrm{d}\lambda \\ &= -xp(x,t),\end{aligned} \tag{AII.139}$$

$$\begin{aligned}\frac{1}{2\pi}\int_{-\infty}^{\infty} e^{\mathrm{i}\lambda x}\partial^2_{\mathrm{i}\lambda^2}\langle\tilde{p}\rangle\mathrm{d}\lambda &= \frac{1}{2\pi}\int_{-\infty}^{\infty}\left(\partial^2_{\mathrm{i}\lambda^2}\left(e^{\mathrm{i}\lambda x}\langle\tilde{p}\rangle\right) - x\partial_{\mathrm{i}\lambda}\left(e^{\mathrm{i}\lambda x}\langle\tilde{p}\rangle\right) - xe^{\mathrm{i}\lambda x}\partial_{\mathrm{i}\lambda}\langle\tilde{p}\rangle\right)\mathrm{d}\lambda \\ &= x^2 p(x,t),\end{aligned} \tag{AII.140}$$

$$\int_0^t 2D\delta(\tau-t)\tilde{p}(\tau)\mathrm{d}\tau = D\tilde{p}(t), \tag{AII.141}$$

$$\int_{-\infty}^{\infty} e^{-x^2}\mathrm{d}x = \sqrt{\pi}, \tag{AII.142}$$

$$\int_0^t\int_0^t 2Df(t_2)\delta(t_2-t_1)\,\mathrm{d}t_2\,\mathrm{d}t_1 = \int_0^t 2Df(t_1)\,\mathrm{d}t_1. \tag{AII.143}$$

III

Information Length (IL)

Chapter summary

In this chapter, we introduce the concept of "Information length", a metric of the distance that a time-varying PDF takes over time. Since this metric is of core importance to the results presented throughout the thesis, we have created its own chapter. The chapter includes results detailing how to compute information length in linear and non-linear Langevin equations. It also considers a case study on the information length application to the Kramers equation. Finally, the chapter presents an equation relating entropy rate, entropy production and information length.

This chapter contains information that has been published by the author in [6], [8], and [7].

keywords:Information geometry; information length

III.1 Information geometry

In the chapter summary, we have verbally mentioned that "information length" is a **metric** of the distance that a given time-varying PDF takes over time. Such a metric can be introduced from information geometry, a mathematical area that combines information theory with differential geometry to create geometrical notions in statistical manifolds, and therefore, a true metric.

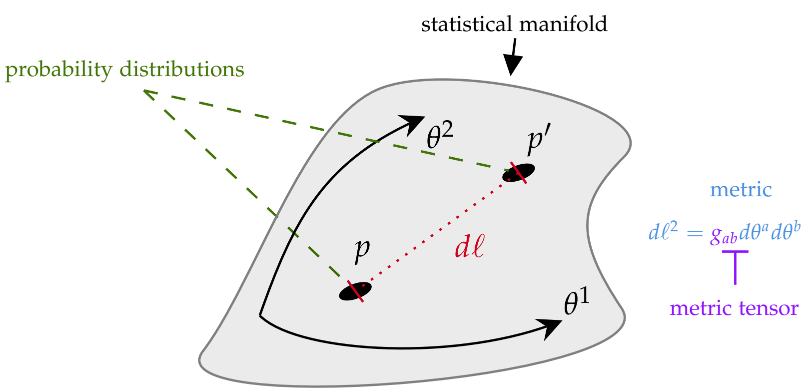

Figure III.1: Computing the distance between two probability distributions in a statistical manifold is a process that requires assumptions similarly used in differential geometry to compute distances in curved spaces.

Statistical manifolds are manifolds formed by a parametric family of probability distributions p labelled by parameters $\boldsymbol{\theta} = [\theta_1, \theta_2, \ldots, \theta_n]$. Figure III.1 shows a graphical description of an example where the statistical manifold contains probability distributions p with parameters $\boldsymbol{\theta} = [\theta_1, \theta_2]$. As each point on this space represents a unique probability distribution p, in principle, the distance $d\ell$ between two neighbouring points

p and p' with parameters $\boldsymbol{\theta}$ and $\boldsymbol{\theta} + \mathrm{d}\boldsymbol{\theta}$, respectively, would be given by the Pythagoras' theorem[1]

$$d\ell^2 = \sum_a \sum_b g_{ab} d\theta_a d\theta_b, \tag{III.1}$$

where g_{ab} is a unique metric tensor [57].

Example III.1 (Multivariable Gaussian distributions)**.** *In a multivariable Gaussian distribution with mean values $\mu_a, a = 1, 2, \ldots, n$ and variances Σ_a defined as*

$$p(\mathbf{x}; \boldsymbol{\mu}, \boldsymbol{\Sigma}) = \frac{1}{\left(2\pi \left(\prod_a \Sigma_a\right)\right)^{1/n}} e^{-\frac{1}{2}\sum_a \frac{(x_a-\mu_a)^2}{\Sigma_a}}, \tag{III.2}$$

create an (2n)-dimensional statistical manifold. Here, the coordinates would be $\boldsymbol{\theta} = [\mu_1, \ldots, \mu_n, \Sigma_1, \ldots, \Sigma_n]$;

Without much rigour, we can derive such a metric between two nearby distributions $p(\mathbf{x}; \boldsymbol{\theta})$ and $p(\mathbf{x}; \theta + \mathrm{d}\boldsymbol{\theta})$ from distinguishability (as suggested in [56; 58; 59]). We highlight that this derivation is not a proof for the metric uniqueness but it permits us to easily interpret the result.

A first approach to obtain the "distinguishability" between two distributions is via the expected value of the relative difference

$$\Delta = \frac{p(\mathbf{x}; \boldsymbol{\theta} + \mathrm{d}\boldsymbol{\theta}) - p(\mathbf{x}; \boldsymbol{\theta})}{p(\mathbf{x}; \boldsymbol{\theta})} = \sum_a \frac{\partial \log p(\mathbf{x}; \boldsymbol{\theta})}{\partial \theta_a} \, \mathrm{d}\theta_a, \tag{III.3}$$

given by

$$\langle \Delta \rangle = \int \mathrm{d}^n x p(\mathbf{x}; \boldsymbol{\theta}) \left(\sum_a \frac{\partial \log p(\mathbf{x}; \boldsymbol{\theta})}{\partial \theta_a} \, \mathrm{d}\theta_a \right) = \sum_a \mathrm{d}\theta_a \frac{\partial}{\partial \theta_a} \int \mathrm{d}^n x p(\mathbf{x}; \boldsymbol{\theta}) = 0. \tag{III.4}$$

Since this value vanishes, it is not a proper measure. On the other hand, if we compute the variance of Δ, i.e.

$$\begin{aligned} d\ell^2 = \langle \Delta^2 \rangle &= \int \mathrm{d}^n x p(\mathbf{x}; \boldsymbol{\theta}) \left(\sum_a \frac{\partial \log p(\mathbf{x}; \boldsymbol{\theta})}{\partial \theta_a} \, \mathrm{d}\theta_a \right) \left(\sum_b \frac{\partial \log p(\mathbf{x}; \boldsymbol{\theta})}{\partial \theta_b} \, \mathrm{d}\theta_b \right) &\text{(III.5)} \\ &= \int \mathrm{d}^n x p(\mathbf{x}; \boldsymbol{\theta}) \left(\sum_a \sum_b \frac{\partial \log p(\mathbf{x}; \boldsymbol{\theta})}{\partial \theta_a} \frac{\partial \log p(\mathbf{x}; \boldsymbol{\theta})}{\partial \theta_b} \, \mathrm{d}\theta_a \, \mathrm{d}\theta_b \right), &\text{(III.6)} \end{aligned}$$

the value that does not vanish. Furthermore, a small value of $d\ell^2$ means that the relative difference Δ is also small and the neighbouring points $\boldsymbol{\theta}$ and $\boldsymbol{\theta} + \mathrm{d}\boldsymbol{\theta}$ are difficult to distinguish. Additionally, $d\ell^2 = \langle \Delta^2 \rangle$ is positive definite and vanishes only when the $\mathrm{d}\theta_a$ vanish. Hence, this is a more accurate measure for distinguishability [56]. In fact, we can now introduce the matrix g_{ab} as

$$g_{ab} = \int \mathrm{d}^n p(\mathbf{x}; \boldsymbol{\theta}) \frac{\partial \log p(\mathbf{x}; \boldsymbol{\theta})}{\partial \theta_a} \frac{\partial \log p(\mathbf{x}; \boldsymbol{\theta})}{\partial \theta_b}. \tag{III.7}$$

Equation (III.7) is known as the Fisher information matrix [60].

III.2 The definition of information length

Consider the case where the probability density function evolves over time subject to some dynamics as seen in Chapter II. In this scenario, each point on the statistical manifold will also evolve over time with

[1] As suggested by [56], in an n-dimensional smooth and possibly curved manifold M that is locally like $\mathbb{R}^n$, the distance can be computed using the Euclidean metric if the probability distributions are close to each other. In addition, [56] emphasises that independently of the meaning of the probability distributions they are uniform over the space of parameters.

parameters labelled $\boldsymbol{\theta}(t)$, i.e. each point will consists of a PDF $p(\mathbf{x};\boldsymbol{\theta}(t))$ where time is implicit. Then, the distinguishability measure between two probability distributions at two close time stamps t and $t+\Delta t$ will be given by

$$d\ell^2 = \left\langle \left(\sum_a \frac{\partial \log p(\mathbf{x};t)}{\partial \theta_a} \frac{\mathrm{d}\theta_a}{\mathrm{d}t} \right)^2 \right\rangle \tag{III.8}$$

where we have omitted the parameters $\boldsymbol{\theta}(t)$ and put only the time t for brevity.

From equation (III.8), we have the fisher matrix metric

$$g_{ab} = \int \mathrm{d}^n x p(\mathbf{x};t) \left(\sum_{a,b} \frac{\partial \log p(\mathbf{x};t)}{\partial \theta_a} \frac{\partial \log p(\mathbf{x};t)}{\partial \theta_b} \right), \tag{III.9}$$

which can be used to compute the total length

$$\ell = \int_{t_0}^{t_f} \sqrt{\sum_{ab} g_{ab} \frac{\mathrm{d}\theta_a}{\mathrm{d}t} \frac{\mathrm{d}\theta_b}{\mathrm{d}t}}\, \mathrm{d}t. \tag{III.10}$$

As it will be discussed in the following chapters, Equation (III.10) turns out to be very useful specially when controlling, detecting abrupt events or measuring causality between variables in stochastic dynamics. Equation (III.10) is what we call the "Information Length". Rewriting Equation (III.10) in terms of the time-varying PDF, from now on, we define the Information Length (IL) as follows.

Definition III.1: IL from a joint distribution [6; 7]

Given a time-dependent probability density function $p(\mathbf{x};t)$ of a n-variante stochastic variable $\mathbf{x}$, the Information Length $\mathcal{L}(t)$ of its evolution from an initial time $t_0 = 0$ to a final time $t_f = t$ is defined by

$$\mathcal{L}(t) = \int_0^t \frac{\mathrm{d}\tau}{\dagger(\tau)} = \int_0^t \Gamma(\tau)\, \mathrm{d}\tau, \tag{III.11}$$

$$\Gamma(\tau) = \sqrt{\int_{\mathbb{R}^n} p(\mathbf{x};\tau) \left[\partial_\tau \log p(\mathbf{x};\tau)\right]^2 \mathrm{d}^n x}. \tag{III.12}$$

To unveil the physical meaning of equation (III.11), we note that $\dagger(t)$ is a dynamic time unit which gives the correlation time over which $p(\mathbf{x};t)$ changes [61]. $\dagger(t)$ also serves as the time unit in the statistical space. In addition, its inverse $\frac{1}{\dagger(t)}$ quantifies the (average) rate of change of information in time [62]. Hence, $\mathcal{L}$ is a dimensionless distance that quantifies the total information change in time through the information rate $\Gamma(t)$ integration [63].

Note that $\mathcal{L}(t=0) = 0$ and $\mathcal{L}$ monotonically increases with time as $\Gamma \geq 0$ and takes a constant value when $\Gamma = \partial_t p = 0$. Hence, when $p(\mathbf{x};t)$ relaxes in the long time limit $t \to \infty$ into a stationary PDF, the following limits hold $\lim_{t\to\infty} \Gamma(t) \to 0$ and $\lim_{t\to\infty} \mathcal{L}(t) \to \mathcal{L}_\infty$ where $\mathcal{L}_\infty$ is a constant that depends on the initial conditions and the SDE parameters. The value of $\mathcal{L}_\infty$ has been used to understand attractor structure in a relaxation problem (for further details see [64; 65; 66; 67]) via examining how $\mathcal{L}_\infty$ depends on the initial mean value $\boldsymbol{\mu}(0)$. Γ and $\mathcal{L}$ were also shown to help quantifying hysteresis in forward-backward processes [68], correlation and self-regulation among different players [69; 70], and predicting the occurrence of sudden events [7] and phase transitions [70]. As a graphical example, Figure III.2 depicts the time evolution of a univariate PDF $p(x,t)$ transitioning from $p(x,t_0)$ to $p(x,t_f)$. Here, $\mathcal{L}$ gives the total number of statistically

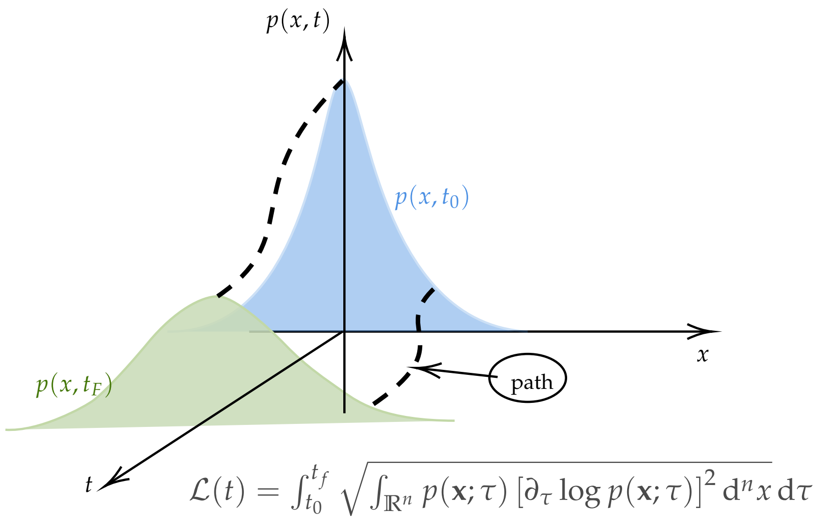

Figure III.2: Schematic of the evolution of $p(x;t)$ over time t. Computing $\mathcal{L}(t)$ gives the total amount of statistical changes on $p(x;t)$ from t_0 to t_f [8].

different states the random variable $\mathbf{x}$ passes through in time over the PDF's transitioning path [2]. Throughout this work, we will call $\Gamma(t)$ the information rate and $\Gamma^2(t)$ the information energy.

III.3 IL in Gaussian Processes

Even-though IL's value is generally computed via numerical methods, in some scenarios, we can give analytical expressions which ease the computation while permitting us to explore the significance of the metric. For instance, consider the following example.

Example III.2 (IL in the Ornstein–Uhlenbeck (O-U) process)**.** *Given the following stochastic model*

$$\frac{\mathrm{d}x}{\mathrm{d}t} = -\gamma x + \xi, \tag{III.13}$$

where ξ is a white noise with short correlation time with the following properties $\langle \xi(t) \rangle = 0$ and $\langle \xi(t)\xi(t') \rangle = 2D\delta(t-t')$. The following result holds.

Proposition III.1: Information rate

Given that the value of the PDF at time $t = 0$ is Gaussian and described as $p(x,0) = \sqrt{\frac{\beta_0}{\pi}} e^{\beta_0 (x-y(0))^2}$ where β, β_0 and y stand for the variance, variance at time $t = 0$ and the mean value of the random variable x, respectively. The information rate Γ of the O-U process (III.13) is

$$\Gamma = \frac{1}{2\beta^2}\dot{\beta}^2 + 2\beta\dot{y}^2 = \frac{2\gamma^2}{T^2}(r^2 + qT), \tag{III.14}$$

where $q = \beta_0\gamma\mu^2$, $r = 2\beta_0 D - \gamma$, and $T = 2\beta_0 D(e^{2\gamma t} - 1) + \gamma$.

[2] For an animated demonstration, see `https://openprocessing.org/sketch/1594393`

Proof. We start by recalling that, according to Proposition II.5, given that the value of the PDF at time $t = 0$ is Gaussian, the time-varying PDF of a linear stochastic system is also Gaussian at all t. Hence, the time-varying PDF of the O-U process (III.13) at all t can be written as

$$p(x,t) = \sqrt{\frac{\beta(t)}{\pi}} e^{\beta(t)(x-y(t))^2}, \tag{III.15}$$

Here, β and y are the variance and mean of the random variable x. Using (III.15) in Definition III.1, we now compute the information rate step by step as follows

$$\begin{aligned}
\partial_t p(x,t) &= \sqrt{\frac{\beta}{\pi}} e^{-\beta(x-y)^2} Q'(t) + \frac{1}{2}\frac{\dot\beta}{\pi}\left(\frac{\beta}{\pi}\right)^{-\frac{1}{2}} e^{\beta(x-y)^2}, \\
[\partial_t p(x,t)]^2 &= \frac{\beta}{\pi} e^{-2\beta(x-y)^2} Q'(t)^2 + \frac{\dot\beta^2}{4\beta\pi} e^{-2\beta(x-y)^2} + \frac{\dot\beta}{\pi} Q'(t) e^{-2\beta(x-y)^2}, \\
\frac{[\partial_t p(x,t)]^2}{p(x,t)} &= \underbrace{\sqrt{\frac{\beta}{\pi}} e^{-\beta(x-y)^2} Q'(t)^2}_{(a)} + \underbrace{\frac{\dot\beta^2}{4\pi\beta}\sqrt{\frac{\pi}{\beta}} e^{-\beta(x-y)^2}}_{(b)} + \underbrace{\frac{\dot\beta}{\pi}\sqrt{\frac{\pi}{\beta}} e^{-\beta(x-y)^2} Q'(t)}_{(c)},
\end{aligned}$$

where $Q'(t) = -\dot\beta(x-y)^2 - 2\beta(x-y)(-\dot y)$ and $Q'(t)^2 = \dot\beta^2(x-y)^4 + 4\dot\beta\beta(x-y)^3(-\dot y) + 4\beta^2(x-y)^2(-\dot y)^2$. Now, we integrate terms (a), (b) and (c) in the previous equation as follows

$$\int_{-\infty}^{\infty} \mathrm{d}x \quad (b) = \int_{-\infty}^{\infty} \mathrm{d}x \frac{\dot\beta^2}{4\pi\beta}\sqrt{\frac{\pi}{\beta}} e^{-\beta(x-y)^2} = \frac{\dot\beta^2}{4\pi\beta}\sqrt{\frac{\pi}{\beta}}\sqrt{\frac{\pi}{\beta}} = \frac{\dot\beta^2}{4\beta^2}.$$

To integrate (a) and (c) we know that

$$\int_{\mathbb{R}} x^{2n} e^{-\alpha(x+b)^2}\, \mathrm{d}x = \sqrt{\frac{\pi}{\alpha}} \frac{(2n-1)!!}{(2\alpha)^n}, \tag{III.16}$$

where !! corresponds to the double factorial operator, such that for an odd n it is defined as

$$n!! = \prod_{k=1}^{\frac{n+1}{2}} (2k-1) = n(n-2)(n-4)\cdots 3\cdot 1. \tag{III.17}$$

Hence,

$$\begin{aligned}
\int_{-\infty}^{\infty} \mathrm{d}x \quad (a) &= \int_{-\infty}^{\infty} \mathrm{d}x \sqrt{\frac{\beta}{\pi}} e^{-\beta(x-y)^2} Q'(t)^2, \\
&= \int_{-\infty}^{\infty} \mathrm{d}x \sqrt{\frac{\beta}{\pi}} e^{-\beta(x-y)^2} \left[\dot\beta^2(x-y)^4 + 4\dot\beta\beta(x-y)^3(-\dot y) + 4\beta^2(x-y)^2(-\dot y)^2\right], \\
&= \sqrt{\frac{\beta}{\pi}}\left[\sqrt{\frac{\pi}{\beta}}\frac{(3)!!}{(2\beta)^2}\dot\beta^2 + 4\beta^2\dot y^2\sqrt{\frac{\pi}{\beta}}\frac{(1)!!}{2\beta}\right] = \frac{3}{4}\frac{\dot\beta^2}{\beta^2} + \frac{4\beta\dot y^2}{2}, \\
\int_{-\infty}^{\infty} \mathrm{d}x \quad (c) &= \int_{-\infty}^{\infty} \mathrm{d}x \frac{\dot\beta}{\pi}\sqrt{\frac{\pi}{\beta}} e^{-\beta(x-y)^2} Q'(t) = \int_{-\infty}^{\infty} \mathrm{d}x \frac{\dot\beta}{\pi}\sqrt{\frac{\pi}{\beta}} e^{-\beta(x-y)^2}\left[-\dot\beta(x-y)^2 - 2\beta(x-y)(-\dot y)\right], \\
&= -\frac{\dot\beta^2}{\pi}\sqrt{\frac{\pi}{\beta}}\sqrt{\frac{\pi}{\beta}}\frac{(1)!!}{2\beta} = -\frac{\dot\beta^2}{2\beta^2}.
\end{aligned}$$

Finally,

$$\Gamma = \frac{3}{4}\frac{\dot\beta^2}{\beta^2} + \frac{4\beta\dot y^2}{2} + \frac{\dot\beta^2}{4\beta^2} - \frac{\dot\beta^2}{2\beta^2} = \frac{\dot\beta^2}{2\beta^2} + 2\beta\dot y^2, \tag{III.18}$$

which gives expression (III.14) by considering $y(t) = \mu e^{-\gamma t}$, $\frac{1}{\beta(t)} = \frac{1}{\beta_1(t)} + \frac{e^{-2\gamma t}}{\beta_0}$ and $\frac{1}{\beta_1(t)} = \frac{2D(1-e^{-2\gamma t})}{\gamma}$ and their time derivatives over time. ■

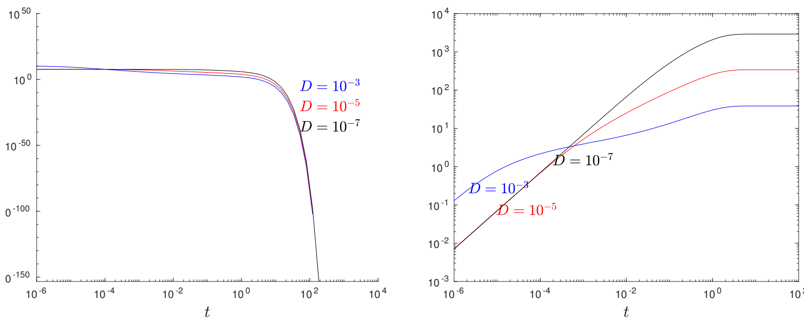

(a) Information rate Γ over time.

(b) Information length $\mathcal{L}$ over time.

Figure III.3: IL and information rate plots of O-U process (III.13).

In Fig. III.3, we show the information length of the OU process (III.13) for various values of D[3]. Note

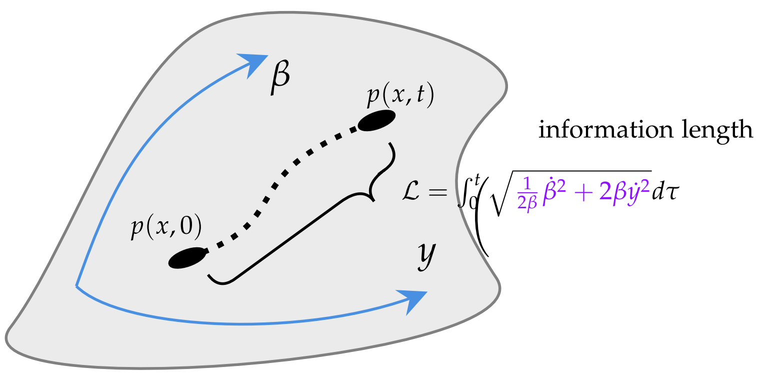

Figure III.4: Graphical representation of the statistical manifold for the O-U process (III.13). The information length measures the distance between the initial PDF at time $t = 0$ and the PDF at a given time t.

that from (III.14), the metric tensor (see Figure III.4) in the O-U process is

$$g_{ab} = \begin{bmatrix} \frac{1}{2\beta^2} & 0 \\ 0 & 2\beta, \end{bmatrix} \tag{III.19}$$

and the parameters

$$\boldsymbol{\theta} = \begin{bmatrix} \dot{\beta} \\ \dot{y} \end{bmatrix} \tag{III.20}$$

To find a generalised closed-form expression of the information rate Γ obtained from Example III.2, let us consider the computation of the IL's value for dynamics whose PDF remains Gaussian at all instants of time. Such a result is summarised in the following Theorem.

[3] Video demonstration of the change of the PDF over time using $D = \{10^{-3}, 10^{-5}, 10^{-7}\}$, $\mu = 0.7$ and $\gamma = 1$ can be seen in the following links https://youtu.be/2eUqyYLczhU, https://youtu.be/B01-xTPLykw and https://youtu.be/44DycJqCtsU

Theorem III.1: Information length in Gaussian dynamics [6; 7]

The information length of a n-variante Gaussian random variable $\mathbf{x}$ with mean $\boldsymbol{\mu} \in \mathbb{R}^n$ and covariance $\boldsymbol{\Sigma} \in \mathbb{R}^{n\times n}$ is given by the following integral

$$\mathcal{L}(t) = \int_0^t \Gamma(\tau)\,\mathrm{d}\tau, \tag{III.21}$$

$$\Gamma(\tau)^2 = \dot{\boldsymbol{\mu}}(\tau)^T \boldsymbol{\Sigma}^{-1}(\tau)\dot{\boldsymbol{\mu}}(\tau) + \frac{1}{2}\operatorname{Tr}\left(\left(\boldsymbol{\Sigma}^{-1}(\tau)\dot{\boldsymbol{\Sigma}}(\tau)\right)^2\right). \tag{III.22}$$

Proof. To prove this theorem, we use the PDF (II.70) in (III.11). First, we define

$$\mathbf{w} \equiv \delta\mathbf{x} = \mathbf{x} - \langle \mathbf{x}(t)\rangle, \;\; \mathbf{Q} = \boldsymbol{\Sigma}^{-1}$$

to simplify the analysis. Then, we compute step by step the value of

$$p(\mathbf{x};t)\,[\partial_\tau \log p(\mathbf{x};t)]^2 = \frac{[\partial_\tau p(\mathbf{x},\tau)]^2}{p(\mathbf{x},\tau)}$$

as follows:

$$\begin{aligned}\partial_\tau p(\mathbf{x},\tau) &= \frac{\partial}{\partial\tau}\left[(\det(2\pi\boldsymbol{\Sigma}))^{-\frac{1}{2}}\, e^{-\frac{1}{2}\mathbf{w}^T\mathbf{Q}\mathbf{w}}\right]\\ &= -\frac{1}{2}e^{-\frac{1}{2}\mathbf{w}^T\mathbf{Q}\mathbf{w}}(\det(2\pi\boldsymbol{\Sigma}))^{-\frac{3}{2}}\,\partial_\tau(\det(2\pi\boldsymbol{\Sigma})) - \frac{1}{2}(\det(2\pi\boldsymbol{\Sigma}))^{-\frac{1}{2}}\, e^{-\frac{1}{2}\mathbf{w}^T\mathbf{Q}\mathbf{w}}\partial_\tau\left(\mathbf{w}^T\mathbf{Q}\mathbf{w}\right),\end{aligned} \tag{III.23}$$

$$\begin{aligned}[\partial_\tau p(\mathbf{x},\tau)]^2 = {}& \frac{1}{4}e^{-\mathbf{w}^T\mathbf{Q}\mathbf{w}}(\det(2\pi\boldsymbol{\Sigma}))^{-3}\,[\partial_\tau \det(2\pi\boldsymbol{\Sigma})]^2 + \frac{1}{4}(\det(2\pi\boldsymbol{\Sigma}))^{-1}\, e^{-\mathbf{w}^T\mathbf{Q}\mathbf{w}}\left(\partial_\tau\left[\mathbf{w}^T\mathbf{Q}\mathbf{w}\right]\right)^2\\ &+\frac{1}{2}(\det(2\pi\boldsymbol{\Sigma}))^{-2}\,\partial_\tau\,[\det(2\pi\boldsymbol{\Sigma})]\,\partial_\tau\left[\mathbf{w}^T\mathbf{Q}\mathbf{w}\right] e^{-\mathbf{w}^T\mathbf{Q}\mathbf{w}},\end{aligned} \tag{III.24}$$

$$\begin{aligned}\frac{[\partial_\tau p(\mathbf{x},\tau)]^2}{p(\mathbf{x},\tau)} = {}& \frac{1}{4}(\det(2\pi\boldsymbol{\Sigma}))^{-\frac{5}{2}}\,[\partial_\tau \det(2\pi\boldsymbol{\Sigma})]^2\, e^{-\frac{1}{2}\mathbf{w}^T\mathbf{Q}\mathbf{w}} + \frac{1}{4}(\det(2\pi\boldsymbol{\Sigma}))^{-\frac{1}{2}}\, e^{-\frac{1}{2}\mathbf{w}^T\mathbf{Q}\mathbf{w}}\left(\partial_\tau\left(\mathbf{w}^T\mathbf{Q}\mathbf{w}\right)\right)^2\\ &+\frac{1}{2}(\det(2\pi\boldsymbol{\Sigma}))^{-\frac{3}{2}}\,\partial_\tau\,(\det(2\pi\boldsymbol{\Sigma}))\,\partial_\tau\left(\mathbf{w}^T\mathbf{Q}\mathbf{w}\right) e^{-\frac{1}{2}\mathbf{w}^T\mathbf{Q}\mathbf{w}}.\end{aligned} \tag{III.25}$$

Now, using Equation (III.23) in Equation (III.25), we compute the integral $\Gamma(\tau)^2 = \int_{-\infty}^{\infty}\mathrm{d}^n x\left(\frac{[\partial_\tau p(\mathbf{x},\tau)]^2}{p(\mathbf{x},\tau)}\right)$ as follows

$$\begin{aligned}\Gamma(\tau)^2 &= \int_{\mathbb{R}^n} p(\mathbf{x},\tau)\left(\frac{(\det(2\pi\boldsymbol{\Sigma}))^{-2}}{4}\,[\partial_\tau\,(\det(2\pi\boldsymbol{\Sigma}))]^2 + \frac{\left(\partial_\tau\left(\mathbf{w}^T\mathbf{Q}\mathbf{w}\right)\right)^2}{4} + \frac{\partial_\tau[\det(2\pi\boldsymbol{\Sigma})]\partial_\tau\left[\mathbf{w}^T\mathbf{Q}\mathbf{w}\right]}{2\det(2\pi\boldsymbol{\Sigma})}\right)\mathrm{d}^n x\\ &= \left\langle\left(\frac{\partial_\tau\,[\det(2\pi\boldsymbol{\Sigma})]}{2\det(2\pi\boldsymbol{\Sigma})}\right)^2\right\rangle + \left\langle\left(\frac{\partial_\tau\left[\mathbf{w}^T\mathbf{Q}\mathbf{w}\right]}{2}\right)^2\right\rangle + \left\langle\frac{\partial_\tau\,[\det(2\pi\boldsymbol{\Sigma})]\,\partial_\tau\left[\mathbf{w}^T\mathbf{Q}\mathbf{w}\right]}{2\det(2\pi\boldsymbol{\Sigma})}\right\rangle\end{aligned} \tag{III.26}$$

To calculate the three averages in (III.26), we use the following properties [37]

$$\int_{\mathbb{R}^n} e^{-\frac{1}{2}\mathbf{w}^T\mathbf{Q}\mathbf{w}}\,\mathrm{d}^n w = \sqrt{\det(2\pi\boldsymbol{\Sigma})},$$

$$
\begin{aligned}
\partial_\tau\left[e^{-\frac{1}{2}\mathbf{w}^T\mathbf{Q}\mathbf{w}}\right] &= -\frac{1}{2}e^{-\frac{1}{2}\mathbf{w}^T\mathbf{Q}\mathbf{w}}\partial_\tau\left[\mathbf{w}^T\mathbf{Q}\mathbf{w}\right],\\
\partial^2_{\tau^2}\left[e^{-\frac{1}{2}\mathbf{w}^T\mathbf{Q}\mathbf{w}}\right] &= -\frac{1}{2}\partial^2_{\tau^2}\left[\mathbf{w}^T\mathbf{Q}\mathbf{w}\right]e^{-\frac{1}{2}\mathbf{w}^T\mathbf{Q}\mathbf{w}} + \frac{1}{4}e^{-\frac{1}{2}\mathbf{w}^T\mathbf{Q}\mathbf{w}}\left(\partial_\tau\left[\mathbf{w}^T\mathbf{Q}\mathbf{w}\right]\right)^2.
\end{aligned}
$$

Then,

$$
\begin{aligned}
\Gamma(\tau)^2 &= \left(\frac{\partial_\tau[\det(2\pi\boldsymbol{\Sigma})]}{2\det(2\pi\boldsymbol{\Sigma})}\right)^2 + \iint_{\mathbb{R}^n} p(\mathbf{x},\tau)\left(\frac{\partial_\tau[\mathbf{w}^T\mathbf{Q}\mathbf{w}]}{2}\right)^2 \mathrm{d}^n x + \frac{\partial_\tau[\det(2\pi\boldsymbol{\Sigma})]}{2\det(2\pi\boldsymbol{\Sigma})}\iint_{\mathbb{R}^n} p(\mathbf{x},\tau)\partial_\tau\left[\mathbf{w}^T\mathbf{Q}\mathbf{w}\right]\mathrm{d}^n x\\
&= \frac{1}{4}\left(\frac{\partial_\tau\left[\det(2\pi\boldsymbol{\Sigma})\right]}{\det(2\pi\boldsymbol{\Sigma})}\right)^2 + \frac{1}{4\left(\det(2\pi\boldsymbol{\Sigma})\right)^{\frac{1}{2}}}\iint_{\mathbb{R}^n}\left[4\partial^2_{\tau^2}e^{-\frac{1}{2}\mathbf{w}^T\mathbf{Q}\mathbf{w}} + 2\partial^2_{\tau^2}\left[\mathbf{w}^T\mathbf{Q}\mathbf{w}\right]e^{-\frac{1}{2}\mathbf{w}^T\mathbf{Q}\mathbf{w}}\right]\mathrm{d}^n x\\
&\quad -2\frac{\partial_\tau\left[\det(2\pi\boldsymbol{\Sigma})\right]}{2\left(\det(2\pi\boldsymbol{\Sigma})\right)^{\frac{3}{2}}}\iint_{\mathbb{R}^n}\partial_\tau\left[e^{-\frac{1}{2}\mathbf{w}^T\mathbf{Q}\mathbf{w}}\right]\mathrm{d}^n x\\
&= \frac{1}{4}\left(\frac{\partial_\tau\left[\det(2\pi\boldsymbol{\Sigma})\right]}{\det(2\pi\boldsymbol{\Sigma})}\right)^2 + \frac{\partial^2_{\tau^2}\left[\sqrt{\det(2\pi\boldsymbol{\Sigma})}\right]}{\sqrt{\det(2\pi\boldsymbol{\Sigma})}} + \frac{1}{2\sqrt{\det(2\pi\boldsymbol{\Sigma})}}\iint_{\mathbb{R}^n}\partial^2_{\tau^2}\left[\mathbf{w}^T\mathbf{Q}\mathbf{w}\right]e^{-\frac{1}{2}\mathbf{w}^T\mathbf{Q}\mathbf{w}}\mathrm{d}^n x\\
&\quad -\frac{\partial_\tau\left[\det(2\pi\boldsymbol{\Sigma})\right]}{\left(\det(2\pi\boldsymbol{\Sigma})\right)^{\frac{3}{2}}}\partial_\tau\sqrt{\det(2\pi\boldsymbol{\Sigma})}.
\end{aligned}
\tag{III.27}
$$

Here,

$$
\partial^2_{\tau^2}\left[\mathbf{w}^T\mathbf{Q}\mathbf{w}\right] = \sum_{i,j=1}^n\left[\partial^2_{\tau^2}\left(q_{ij}w_iw_j\right)\right] = \sum_{i,j=1}^n\left[4q'_{ij}w'_iw_j + \underbrace{2q_{ij}w'_iw'_j}_{\text{independent of } x} + 2q_{ij}w''_iw_j + \underbrace{q''_{ij}w_iw_j}_{\mathbf{w}^T\mathbf{Q}''\mathbf{w}}\right].
\tag{III.28}
$$

We recall that ω'_i, q'_{ij} and ω''_i, q''_{ij} denote the first and second derivative over time of the elements ω_i and q_{ij}. By substituting (III.28) in (III.27) and making some arrangements, we obtain

$$
\begin{aligned}
\Gamma(\tau)^2 =& \frac{1}{4}\left(\frac{\partial_\tau\left[\det(2\pi\boldsymbol{\Sigma})\right]}{\det(2\pi\boldsymbol{\Sigma})}\right)^2 + \frac{\partial^2_{\tau^2}\left[\sqrt{\det(2\pi\boldsymbol{\Sigma})}\right]}{\sqrt{\det(2\pi\boldsymbol{\Sigma})}} + \frac{1}{2}\cancelto{0}{\left\langle 4\sum_{i,j=1}^n q'_{ij}w'_iw_j\right\rangle} + \frac{1}{2}\cancelto{0}{\left\langle\sum_{i,j=1}^n 2q_{ij}w''_iw_j\right\rangle}\\
&+\frac{1}{2}\left\langle\sum_{i,j=1}^n 2q_{ij}w'_iw'_j\right\rangle + \frac{1}{2}\left\langle\mathbf{w}^T\mathbf{Q}''\mathbf{w}\right\rangle - \frac{1}{2}\left(\frac{\partial_\tau\left[\det(2\pi\boldsymbol{\Sigma})\right]}{\det(2\pi\boldsymbol{\Sigma})}\right)^2.
\end{aligned}
\tag{III.29}
$$

Now using

- $\mathbf{w}^T\mathbf{Q}''\mathbf{w} = \mathrm{Tr}\left(\mathbf{Q}''\boldsymbol{\Sigma}\right)$ [71],
- $\partial_\tau\det(\boldsymbol{\Sigma}) = \det(\boldsymbol{\Sigma})\,\mathrm{Tr}(\mathbf{Q}\partial_\tau\boldsymbol{\Sigma})$ [72],
- $\partial^2_{\tau^2}\sqrt{\det(2\pi\boldsymbol{\Sigma})} = \frac{1}{4}\sqrt{\det(2\pi\boldsymbol{\Sigma})}\left(\mathrm{Tr}(\mathbf{Q}\partial_\tau\boldsymbol{\Sigma})\right)^2 + \frac{1}{2}\sqrt{\det(2\pi\boldsymbol{\Sigma})}\partial_\tau(\mathrm{Tr}(\mathbf{Q}\partial_\tau\boldsymbol{\Sigma}))$,

in Equation (III.29), we have

$$
\begin{aligned}
\Gamma(\tau)^2 =& -\frac{1}{4}\left(\mathrm{Tr}(\mathbf{Q}\partial_\tau\boldsymbol{\Sigma})\right)^2 + \frac{1}{2}\partial_\tau\left[\mathrm{Tr}(\mathbf{Q}\partial_\tau\boldsymbol{\Sigma})\right] + \frac{1}{4}\left(\mathrm{Tr}(\mathbf{Q}\partial_\tau\boldsymbol{\Sigma})\right)^2 + \langle\mathbf{x}'(\tau)\rangle^T\mathbf{Q}\langle\mathbf{x}'(\tau)\rangle + \frac{1}{2}\mathrm{Tr}\left(\mathbf{Q}''\boldsymbol{\Sigma}\right)\\
=& \frac{1}{2}\partial_\tau\left[\mathrm{Tr}(\mathbf{Q}\partial_\tau\boldsymbol{\Sigma})\right] + \langle\mathbf{x}'(\tau)\rangle^T\mathbf{Q}\langle\mathbf{x}'(\tau)\rangle + \frac{1}{2}\mathrm{Tr}\left(\mathbf{Q}''\boldsymbol{\Sigma}\right).
\end{aligned}
\tag{III.30}
$$

Simplifying a bit more

$$
\Gamma(\tau)^2 = \frac{1}{2}\left(\partial_\tau\left[\mathrm{Tr}(\boldsymbol{\Sigma}^{-1}\partial_\tau\boldsymbol{\Sigma})\right] + 2\left(\partial_\tau\langle\mathbf{x}(\tau)\rangle^T\right)\boldsymbol{\Sigma}^{-1}\left(\partial_\tau\langle\mathbf{x}(\tau)\rangle\right) + \mathrm{Tr}\left((\partial^2_{\tau^2}\boldsymbol{\Sigma}^{-1})\boldsymbol{\Sigma}\right)\right)
$$

$$
\begin{aligned}
&= \frac{1}{2}\left(2\left(\partial_\tau\langle\mathbf{x}(\tau)\rangle^T\right)\boldsymbol{\Sigma}^{-1}\left(\partial_\tau\langle\mathbf{x}(\tau)\rangle\right) + \mathrm{Tr}\left(\partial_\tau\left[\boldsymbol{\Sigma}^{-1}\partial_\tau\boldsymbol{\Sigma}\right] + (\partial^2_{\tau^2}\boldsymbol{\Sigma}^{-1})\boldsymbol{\Sigma}\right)\right) \\
&= \frac{1}{2}\left(2\left(\partial_\tau\langle\mathbf{x}(\tau)\rangle^T\right)\boldsymbol{\Sigma}^{-1}\left(\partial_\tau\langle\mathbf{x}(\tau)\rangle\right) + \mathrm{Tr}\left(\partial_\tau\boldsymbol{\Sigma}^{-1}\partial_\tau\boldsymbol{\Sigma} + \boldsymbol{\Sigma}^{-1}\partial^2_{\tau^2}\boldsymbol{\Sigma} + (\partial^2_{\tau^2}\boldsymbol{\Sigma}^{-1})\boldsymbol{\Sigma}\right)\right) \\
&= \frac{1}{2}\left(2\left(\partial_\tau\langle\mathbf{x}(\tau)\rangle^T\right)\boldsymbol{\Sigma}^{-1}\left(\partial_\tau\langle\mathbf{x}(\tau)\rangle\right) + \mathrm{Tr}\left(\partial_\tau\boldsymbol{\Sigma}^{-1}\partial_\tau\boldsymbol{\Sigma} + \boldsymbol{\Sigma}^{-1}\partial^2_{\tau^2}\boldsymbol{\Sigma} - \partial_\tau(\boldsymbol{\Sigma}^{-1}(\partial_\tau\boldsymbol{\Sigma})\boldsymbol{\Sigma}^{-1})\boldsymbol{\Sigma}\right)\right) \\
&= \frac{1}{2}\left(2\left(\partial_\tau\langle\mathbf{x}(\tau)\rangle^T\right)\boldsymbol{\Sigma}^{-1}\left(\partial_\tau\langle\mathbf{x}(\tau)\rangle\right) + \mathrm{Tr}\left((\boldsymbol{\Sigma}^{-1}\partial_\tau\boldsymbol{\Sigma})^2\right)\right) \\
&= \dot{\boldsymbol{\mu}}(\tau)^T\boldsymbol{\Sigma}^{-1}\dot{\boldsymbol{\mu}}(\tau) + \frac{1}{2}\mathrm{Tr}\left((\boldsymbol{\Sigma}^{-1}\dot{\boldsymbol{\Sigma}})^2\right) \qquad \text{(III.31)}
\end{aligned}
$$

■

A useful corollary from Theorem III.1 can be obtained when $\boldsymbol{\Sigma}$ is a diagonal matrix, i.e. all states in $\mathbf{x}$ are random variables independent of each other.

Corollary III.1: Information rate in an independent Gaussian process [7]

For a Gaussian process with n independent random variables $\mathbf{x} \in \mathbb{R}^n = [x_1, x_2, \ldots, x_n]^T$, the value of the information rate Γ is

$$\Gamma = \sum_{i=1}^{n} \Gamma_i, \qquad \text{(III.32)}$$

where

$$\Gamma_i = \frac{\dot{\mu}_i^2}{\Sigma_{ii}} + \frac{1}{2}\left(\frac{\dot{\Sigma}_{ii}}{\Sigma_{ii}}\right)^2. \qquad \text{(III.33)}$$

The value of Γ_i in Corollary III.1 is also the corresponding value of the information rate from the marginal PDF $p(x_i, t)$ of the random variable x_i defined as follows

Definition III.2: Marginal information rate

The value of the information rate produced by a random variable x_i in a multivariable Gaussian distribution noted as Γ_i is defined as follows

$$\Gamma_i := \sqrt{\int_{\mathbb{R}} p(x_i; t)\left[\partial_\tau \log p(x_i, t)\right]^2 \mathrm{d}x_i}. \qquad \text{(III.34)}$$

Corollary III.1 and Definition III.2 will be very useful in the subsequent chapters.

Remark III.3. *From the value of the marginal information rate Γ_i, we can also compute the marginal information length $\mathcal{L}_i$. Such a value gives the contribution of the random variable x_i to the total statistical changes in a multivariate Gaussian distribution (see Figure III.5). The marginal information length is straighforwardly defined as*

$$\mathcal{L}_i = \int_0^t \sqrt{\Gamma_i(\tau)}\,\mathrm{d}\tau. \qquad \text{(III.35)}$$

III.4 Case study: the Kramers equation

Theorem III.1 represents an easy way to compute the information rate Γ and information length $\mathcal{L}$ in high-order stochastic systems with Gaussian behaviour. As an example showing such practicality, let us consider

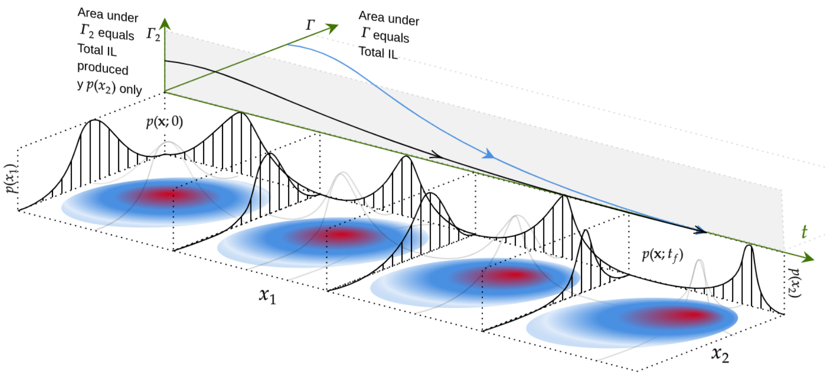

Figure III.5: Graphical description of the meaning of marginal information rate and length. In a bivariate distribution $p(x_1, x_2; t)$ changing over time, computing $\mathcal{L}_1$ or $\mathcal{L}_2$ allow us to describe the amount of statistical changes produced by x_1 and x_2, respectively.

the following case study presented in [6] of the classical Kramers equation given by

$$\begin{aligned}\frac{\mathrm{d}x}{\mathrm{d}t} &= v\\ \frac{\mathrm{d}v}{\mathrm{d}t} &= -\gamma v - \omega^2 x + \xi(t).\end{aligned} \tag{III.36}$$

Here, ω is a natural frequency and γ is the damping constant, both positive real numbers. ξ is a Gaussian white-noise acting on v with the zero mean value $\langle \xi(t) \rangle = 0$, with the statistical property

$$\langle \xi(t)\xi(t_1) \rangle = 2D\delta(t - t_1). \tag{III.37}$$

Comparing Equations (III.36) and (III.37) with Equations (II.68) and (II.69), we note that $x_1 = x$, $x_2 = v$, $\xi_1 = 0$, $\xi_2 = \xi$, $D_{11} = 0$, $D_{12} = 0$, and $D_{22} = D$ while the matrix $\mathbf{A}$ for (III.36) has the element $A_{11} = 0$, $A_{12} = 1$, $A_{21} = -\omega^2$, $A_{22} = -\gamma$ and the eigenvalues of $\mathbf{A}$ are $\lambda_{1,2} = -\frac{1}{2}\left(\gamma \pm \sqrt{\gamma^2 - 4\omega^2}\right)$.

To find the information length for the system (III.36), we use Proposition II.6 and Theorem III.1. First, Proposition II.6 requires the computation of the exponential matrix $e^{\mathbf{A}t}$ which, according to [38], can be obtained via the inverse Laplace transform $\mathscr{L}^{-1}$ of $(s\mathbf{I} - \mathbf{A})$. After some algebra, the result is

$$e^{\mathbf{A}t}=\mathscr{L}^{-1}\left[(s\mathbf{I}-\mathbf{A})^{-1}\right]=\mathscr{L}^{-1}\left[\begin{bmatrix}\frac{s+\gamma}{(s-\lambda_1)(s-\lambda_2)} & \frac{1}{(s-\lambda_1)(s-\lambda_2)}\\ -\frac{\omega^2}{(s-\lambda_1)(s-\lambda_2)} & \frac{s}{(s-\lambda_1)(s-\lambda_2)}\end{bmatrix}\right]=\begin{bmatrix}\frac{e^{\lambda_1 t}(\gamma+\lambda_1)-e^{\lambda_2 t}(\gamma+\lambda_2)}{\lambda_1-\lambda_2} & \frac{e^{\lambda_1 t}-e^{\lambda_2 t}}{\lambda_1-\lambda_2}\\ -\frac{\left(e^{\lambda_1 t}-e^{\lambda_2 t}\right)\omega^2}{\lambda_1-\lambda_2} & \frac{e^{\lambda_1 t}\lambda_1-e^{\lambda_2 t}\lambda_2}{\lambda_1-\lambda_2}\end{bmatrix}. \tag{III.38}$$

Here, $\mathbf{I} \in \mathbb{R}^{n\times n}$ is the identity matrix. Similarly, we can show

$$2\int_0^t e^{\mathbf{A}(t-t_1)}\mathbf{D}e^{\mathbf{A}^T(t-t_1)}\,\mathrm{d}t_1 = \begin{bmatrix}\frac{D\left(\frac{-1+e^{2\lambda_1 t}}{\lambda_1}+\frac{-\lambda_1-4e^{(\lambda_1+\lambda_2)t}\lambda_2+3\lambda_2+e^{2\lambda_2 t}(\lambda_1+\lambda_2)}{\lambda_2(\lambda_1+\lambda_2)}\right)}{(\lambda_1-\lambda_2)^2} & \frac{D\left(e^{\lambda_1 t}-e^{\lambda_2 t}\right)^2}{(\lambda_1-\lambda_2)^2}\\ \frac{D\left(e^{\lambda_1 t}-e^{\lambda_2 t}\right)^2}{(\lambda_1-\lambda_2)^2} & \frac{D\left(\left(-1+e^{2\lambda_2 t}\right)\lambda_2+\lambda_1\left(-\frac{4e^{(\lambda_1+\lambda_2)t}\lambda_2}{\lambda_1+\lambda_2}+\frac{4\lambda_2}{\lambda_1+\lambda_2}+e^{2\lambda_1 t}-1\right)\right)}{(\lambda_1-\lambda_2)^2}\end{bmatrix}. \tag{III.39}$$

Using Equations (III.38) and (III.39) in Equations (II.71) and (II.72), we have the time-dependent (joint) PDF (II.70) at any time t for our system (III.36) and (III.37). To calculate Equation (III.21) with the help of Equations (III.38) and (III.39), we perform numerical simulations (integrations) for various parameters in Equations (III.36) and (III.37) as well as initial conditions. Note that while we have simulated many different cases, for illustration, we show some representative cases by varying D, ω, γ and $\langle x(0)\rangle$, $\langle v(0)\rangle$ in Section III.4.1–III.4.3 and Section III.5, respectively, for the same initial covariance matrix $\Sigma(0)$ with elements $\Sigma_{11}(0) = \Sigma_{22}(0) = 0.01$ and $\Sigma_{12}(0) = \Sigma_{21}(0) = 0$. Note that the initial marginal distributions of $p(x(0))$ and $p(v(0))$ are Gaussian with the same variance 0.01. Results in the limit $\omega \to 0$ are presented in Section III.4.4.

III.4.1 Varying D

Figure III.6 shows the results when varying D as $D \in (0.0005, 0.04)$ for the fixed parameters $\gamma = 2$ and $\omega = 1$. The initial joint PDFs are Gaussian with the fixed mean values $\langle x(0)\rangle = -0.5$, $\langle v(0)\rangle = 0.7$; as noted above, the covariance matrix $\Sigma(0)$ with elements $\Sigma_{11}(0) = \Sigma_{22}(0) = 0.01$ and $\Sigma_{12}(0) = \Sigma_{21}(0) = 0$. Consequently, at $t = 0$, the marginal distributions of $p(x(0))$ and $p(v(0))$ are Gaussian PDFs with the same variance 0.01 and the mean values $\langle x(0)\rangle = -0.5$ and $\langle v(0)\rangle = 0.7$, respectively.

Figure III.6a,b show the snapshots[4] of time-dependent joint PDF $p(\mathbf{x}, t)$ for the two different values of $D = 0.0005$ and $D = 0.04$, respectively. The black solid represents the phase portrait of the mean value of $\langle x(t)\rangle$ and $\langle v(t)\rangle$ while the red arrows display the direction of time increase. Note that in Figure III.6b, as there is a great overlapping between the different PDFs when $t \to 0$ that would not permit us to appreciate the time evolution of the PDFs in the plots, for clarity, here we have erased some of the initial snapshots of the PDFs by increasing the simulation time-step when $t \to 0$. This procedure was implemented only for plotting purposes and did not affect the analytical or numerical analysis. Figure III.6c,d show the time-evolution of the information rate $\Gamma(t)$ and information length $\mathcal{L}(t)$, respectively, for different values of $D \in (0.0005, 0.04)$. It can be seen that the system approaches a stationary (equilibrium) state for $t \gtrsim 20$ for all values of D, $\mathcal{L}(t)$ approaching constant values (recall $\mathcal{L}(t)$ does not change in a stationary state). Therefore, we approximate the total information length as $\mathcal{L}_\infty = \mathcal{L}(t = 50)$, for instance. Finally, in Figure III.6e, we show a plot of $\mathcal{L}_\infty$ vs D and try to determine the dependence of $\mathcal{L}_\infty$ on D by fitting, as a candidate, an exponential function[5] $\mathcal{L}_\infty(D) = 7.84e^{-329.05D} + 11.21e^{-11.86D}$ (shown in red solid line). Given that the initial conditions of the covariance matrix are $\Sigma_{11}(0) = \Sigma_{22}(0) = 0.01$, $\Sigma_{12}(0) = \Sigma_{21}(0) = 0$ and that D represents the correlation strength of the noise term, note that a decay with D is expected because as D increases it generates a PDF whose snapshot is "similar" to the initial PDF (see Figures III.6a,b).

III.4.2 Varying ω or γ

We now explore how results depend on the two parameters ω and γ, associated with oscillation and damping, respectively. To this end, we use $D = 0.0005$ and the same initial conditions as in Figure III.6 but vary $\omega \in (0, 2)$ and $\gamma \in (0, 6)$ in Figures III.7[6] and III.8, respectively. Specifically, in different panels of these figures, we show the snapshots of the joint PDF $p(\mathbf{x}, t)$, the time-evolutions of $\Gamma(t)$ and $\mathcal{L}(t)$ for different

[4] We use the term snapshots when referring to contour plots of the PDF at different instants of time. In the snapshots, the isolines correspond to values of constant $p(\mathbf{x}, t)$. The isoline is blue when p is small and it goes to yellow colour when p has a large value.
[5] Throughout Section III.4, we do curve fittings using heuristically chosen functions. Specifically, we have used the MATLAB® function "*fit*" which offers polynomial and exponential models (see `https://uk.mathworks.com/help/curvefit/fit.html#bto2vuv-1-fitType`). Since these functions have no theoretical justification, they could be replaced with better candidates. We left for future work a rigorous selection of these curve-fitting functions.
[6] In the figures, the caption "Cont." means that the complete figure's caption is at the last figure with a similar figure's number.

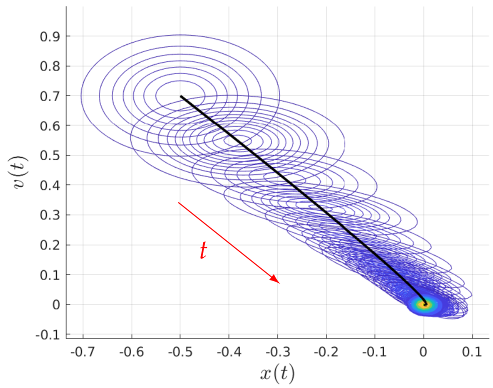

(a) Snapshots of $p(\mathbf{x}, t)$ for $D = 0.0005$.

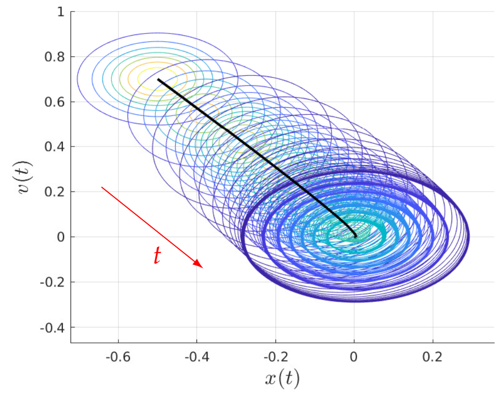

(b) Snapshots of $p(\mathbf{x}, t)$ for $D = 0.04$.

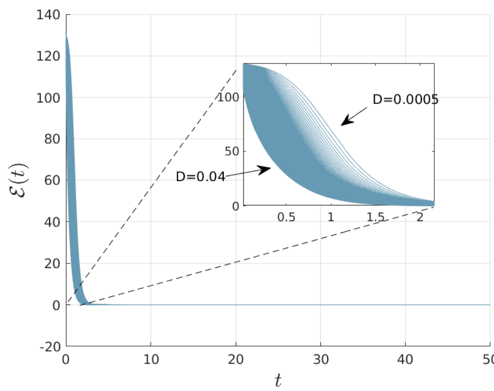

(c) Time-evolution of $\Gamma(t)$.

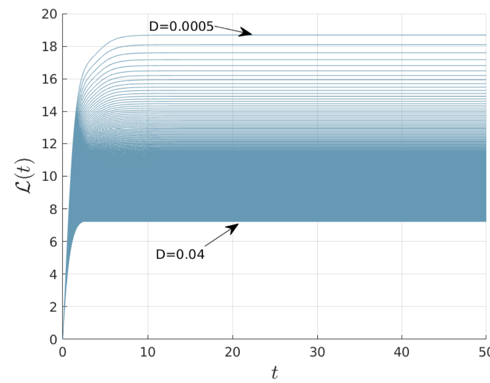

(d) Time-evolution of $\mathcal{L}(t)$.

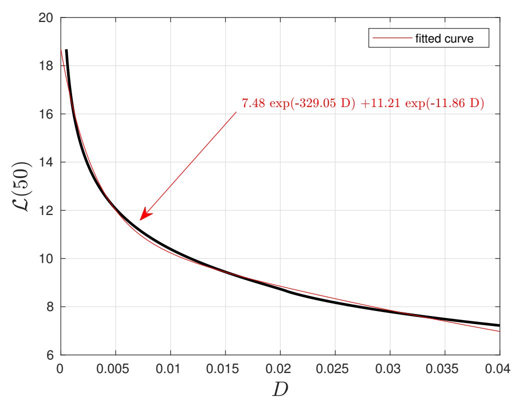

(e) $\mathcal{L}_\infty = \mathcal{L}(t = 50)$ against D. A fitted curve is shown in the red solid line.

Figure III.6: Results of Equations (III.36) and (III.37) for $\langle x(0) \rangle = -0.5$, $\langle v(0) \rangle = 0.7$, $\gamma = 2$, $\omega = 1$, $D \in (0.0005, 0.04)$ and the initial covariance matrix $\Sigma(0)$ with elements $\Sigma_{11}(0) = \Sigma_{22}(0) = 0.01$, $\Sigma_{12}(0) = \Sigma_{21}(0) = 0$.

values of $\omega \in (0,2)$ and $\gamma \in (0,6)$, and $\mathcal{L}_\infty$ against either ω or γ. From Figures III.7e and III.8e, we can see that the system is in a stationary state for sufficiently large $t = 10$ and $t = 100$, respectively. Thus, we use $\mathcal{L}_\infty = \mathcal{L}(t=10) = \mathcal{L}(10)$ in Figure III.7f,g and $\mathcal{L}_\infty = \mathcal{L}(t=100) = \mathcal{L}(10)$ in Figure III.8f,g.

Notably, Figure III.7f,g (shown on linear-linear and log-linear scales on $x-y$ axes, respectively) exhibit an interesting a non-monotonic dependence of $\mathcal{L}_\infty$ on ω for the fixed $\gamma = 2$, with the presence of a distinct minimum in $\mathcal{L}_\infty$ at certain ω. Similarly, Figure III.8f,g (shown in linear-linear and log-log scales on $x-y$ axes, respectively) also shows a non-monotonic dependence of $\mathcal{L}_\infty$ on γ for the fixed $\omega = 1$. These non-monotonic dependences are more clearly seen in Figures III.7f and III.8f. A close inspection of these figures then reveals that the minimum value of $\mathcal{L}_\infty$ occurs close to the critical damping (CD)[7] $\gamma \sim 2\omega$; specifically, this happens at $\omega \sim 1$ for $\gamma = 2$ in Figure III.7f while at $\gamma \sim 2$ for $\omega = 1$ in Figure III.8f. We thus fit $\mathcal{L}_\infty$ against ω or γ depending on whether ω or γ is smaller/larger than its critical value as follows:

$$\mathcal{L}_{10}(\omega) = -0.03e^{4.34\omega} + 19.63e^{0.06\omega} \quad \forall \quad \omega \in (0,1), \tag{III.40}$$

$$\mathcal{L}_{10}(\omega) = 19.52e^{-0.12\omega} + 0.11e^{2.48\omega} \quad \forall \quad \omega \in (1,2), \tag{III.41}$$

$$\mathcal{L}_{100}(\gamma) = 413.22e^{-12.4\gamma} + 95.39e^{-1.02\gamma} \quad \forall \quad \gamma \in (0,2), \tag{III.42}$$

$$\mathcal{L}_{100}(\gamma) = 3.23\gamma \quad \forall \quad \gamma \in (2,6). \tag{III.43}$$

The fitted curves in Equations (III.40)–(III.43) are superimposed in Figures III.7f and III.8f, respectively. It is important to notice from Equations (III.40)–(III.43) that $\mathcal{L}_\infty$ tends to increase as either $\omega \to \infty$ for a finite, fixed γ ($< \infty$) or $\gamma \to \infty$ for a finite, fixed ω ($< \infty$).

Finally, we note that for the critical damping $\gamma = 2\omega$, the eigenvalue becomes a real double root with the value $\lambda_{1,2} \to -\omega$. Thus, in this limit, we have that

$$\langle \mathbf{x}(t) \rangle = \begin{bmatrix} e^{-t\omega}(x(0) + t(v(0) + (\gamma - \omega)x(0))) \\ e^{-t\omega}\left(-tx(0)\omega^2 - tv(0)\omega + v(0)\right) \end{bmatrix} \tag{III.44}$$

and $\Sigma(t)$ is composed by the following elements

$$\begin{aligned}
\Sigma_{11}(t) &= \frac{e^{-2t\omega}\left(2\omega^3\left(\Sigma_{11}(\gamma t - t\omega + 1)^2 + t^2((\Sigma_{12}+\Sigma_{21})(\gamma-\omega)+\Sigma_{22}) + t(\Sigma_{12}+\Sigma_{21})\right) + D\left(-2t\omega(t\omega+1) + e^{2t\omega} - 1\right)\right)}{2\omega^3}, \\
\Sigma_{12}(t) &= e^{-2t\omega}\left(t\left(-\omega^2(\Sigma_{11}\gamma t + \Sigma_{11} + \Sigma_{21}t) + \Sigma_{11}t\omega^3 - \Sigma_{22}t\omega + \Sigma_{22} + Dt\right) - \Sigma_{12}(t\omega-1)(\gamma t - t\omega + 1)\right), \\
\Sigma_{21}(t) &= e^{-2t\omega}\left(t\left(-\omega^2(\Sigma_{11}\gamma t + \Sigma_{11} + \Sigma_{12}t) + \Sigma_{11}t\omega^3 - \Sigma_{22}t\omega + \Sigma_{22} + Dt\right) - \Sigma_{21}(t\omega-1)(\gamma t - t\omega + 1)\right), \\
\Sigma_{22}(t) &= \frac{e^{-2t\omega}\left(2t\omega^2\left(t\omega^2(\Sigma_{11}\omega + \Sigma_{12} + \Sigma_{21}) - \omega(\Sigma_{12}+\Sigma_{21}) + \Sigma_{22}(t\omega-2)\right) + 2\Sigma_{22}\omega + D\left(-2t\omega(t\omega-1) + e^{2t\omega} - 1\right)\right)}{2\omega}.
\end{aligned} \tag{III.45}$$

Equations (III.44) and (III.45) are used in Section III.4.1 (Figure III.6).

III.4.3 Varying $\langle x(0) \rangle$ or $\langle v(0) \rangle$

To elucidate the information geometry associated with the Kramer equation (Equations (III.36) and (III.37)), we now investigate how $\mathcal{L}_\infty$ behaves near the equilibrium point $\langle x(0) \rangle = \langle v(0) \rangle = 0$. To this end, we scan over $\langle x(0) \rangle$ for $\langle v(0) \rangle = 0$ in Figure III.9a–e while scanning over $\langle v(0) \rangle$ for $\langle x0) \rangle = 0$ in Figure III.9f–i. For our illustrations in Figure III.9, we use the same initial covariance matrix $\Sigma(0)$ as in Figures III.6–III.8, $D = 0.0005$ and $\omega = 1$ and a few different values of γ (above/below/at the critical value $\gamma = 2$). We note that the information geometry near a non-equilibrium point is studied in Appendix III.5.

[7] Critical damping corresponds to that value of damping that separates oscillation from non-oscillation of the free response (for further details, see [73]).

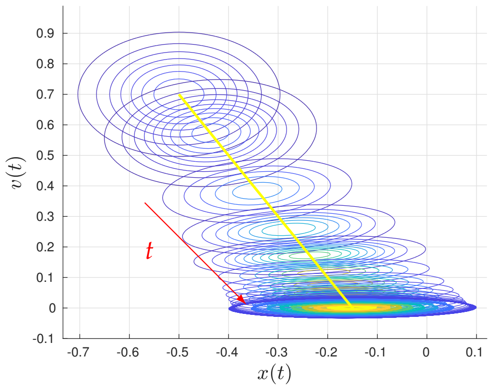

(a) Snapshots of $p(\mathbf{x}, t)$ for $\omega = 0$.

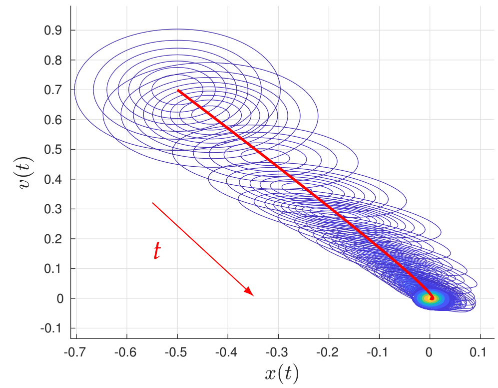

(b) Snapshots of $p(\mathbf{x}, t)$ for $\omega = 1$.

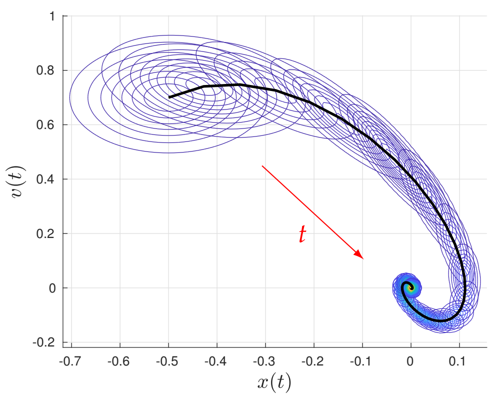

(c) Snapshots of $p(\mathbf{x}, t)$ for $\omega = 2$.

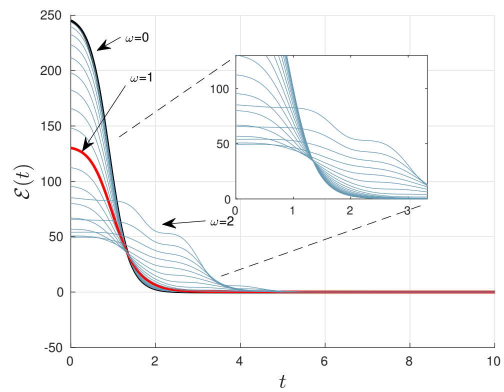

(d) Time-evolution of $\Gamma(t)$.

Figure III.7: Cont.

Specifically, snapshots of $p(\mathbf{x}, t)$ are shown in Figure III.9a–f for $\gamma = 2.5$ (above its critical value $\gamma = 2 = 2\omega$) while those in Figure III.9c–g are for $\gamma = 0.1$ below the critical value 2. By approximating $\mathcal{L}_\infty = \mathcal{L}(t = 100)$, we then show how $\mathcal{L}_\infty$ depends on $\langle x(0) \rangle$ and $\langle v(0) \rangle$ for different values of γ in Figure III.9d,e and Figure III.9h,i, respectively.

Figure III.9d,e show the presence of a minimum in $\mathcal{L}_\infty$ at the equilibrium $\langle x(0) \rangle = 0$ (recall $\langle v(0) \rangle = 0$); $\mathcal{L}_\infty$ is a linear function of $\langle x(0) \rangle$ for $\langle x(0) \rangle \gg 0.1$, which can be described as $\mathcal{L}_\infty(x(0), \gamma) = h(\gamma)|\langle x(0) \rangle| + f(\gamma)$[8]. Here, $h(\gamma)$ and $f(\gamma)$ are constant functions depending on γ for a fixed ω which represent the slope and the y-axis intercept, respectively. A non-zero value of $\mathcal{L}_\infty$ at $\langle x(0) \rangle = 0$ is caused by the adjustment (oscillation and damping) of the width of the PDFs in time due to the disparity between the width of the initial and equilibrium PDFs (see Figure III.9b). In other words, even though the mean values remain in equilibrium for all time $[\langle x(0) \rangle, \langle v(0) \rangle]^T = \lim_{t \to \infty} \langle \mathbf{x}(t) \rangle = [0, 0]^T$, the information length $\mathcal{L}$ depends on the covariance

[8] We can also suggest to describe $\mathcal{L}_\infty$ as an hyperbolic function of $\langle x(0) \rangle \in \mathbb{R}$. Take, for instance,

$$\mathcal{L}_\infty(x(0), \gamma) = h(\gamma) \sinh^2 (\langle x(0) \rangle) + f(\gamma) \text{ or } \mathcal{L}_\infty(x(0), \gamma) = h(\gamma) \cosh (\langle x(0) \rangle) + f(\gamma).$$

Again, $h(\gamma)$ and $f(\gamma)$ are constant functions depending on γ for a fixed ω which represent the slope and the y-axis intercept, respectively.

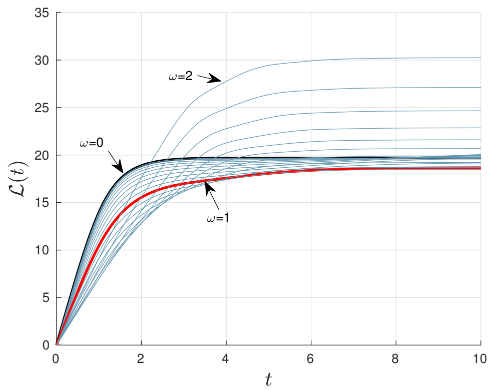

(e) Information Length $\mathcal{L}(t)$.

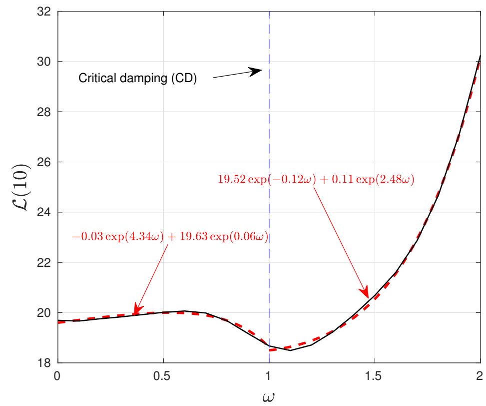

(f) $\mathcal{L}_\infty = \mathcal{L}(t=10)$ against ω; fitted curves are shown in the red dashed lines while a vertical line represents $\omega = 1$ at the critical damping.

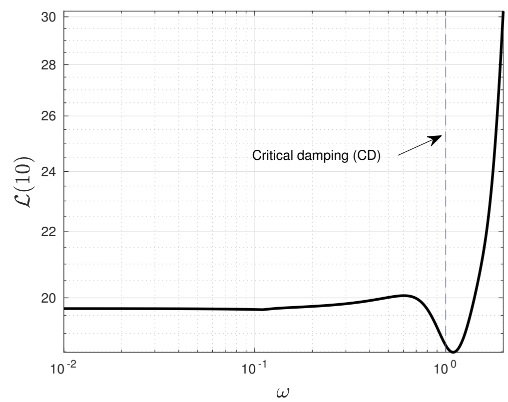

(g) The same as Figure III.7f but shown on log-linear scales on $x - y$ axes.

Figure III.7: Results of Equations (III.36) and (III.37) for $\langle x(0)\rangle = -0.5$, $\langle v(0)\rangle = 0.7$, $\gamma = 2$, $\omega \in (0, 2)$, $D = 0.0005$, and the initial covariance matrix $\Sigma(0)$ with elements $\Sigma_{11}(0) = \Sigma_{22}(0) = 0.01$, $\Sigma_{12}(0) = \Sigma_{21}(0) = 0$.

matrix Σ which changes from its initial value to the final equilibrium value as follows

$$\Sigma(0) = \begin{bmatrix} 0.01 & 0 \\ 0 & 0.01 \end{bmatrix} \Bigg(\text{to } \lim_{t\to\infty} \Sigma(t) = \begin{bmatrix} \frac{D}{\gamma\omega^2} & 0 \\ 0 & \frac{D}{\gamma} \end{bmatrix}.$$

On the other hand, $\mathcal{L}_\infty$ against $\langle x(0)\rangle$ shows parabolic behaviour for small $\langle x(0)\rangle < 0.1$ in Figure III.9e. This is caused by the finite width $0.1 = \sqrt{\Sigma_{11}(0)} = \sqrt{\Sigma_{22}(0)}$ of the initial $p(x, 0)$; we see that $\langle x(0)\rangle < 0.1$ is within the uncertainty of the initial $p(x, 0)$.

Similarly, Figure III.9h,i exhibit a minimum in $\mathcal{L}_\infty$ at the equilibrium $\langle v(0)\rangle = 0$ (recall $\langle x(0)\rangle = 0$ in this case); $\mathcal{L}_\infty$ is a linear function of $\langle v(0)\rangle$ for $\langle v(0)\rangle \gg 0.1$ described by $\mathcal{L}_\infty(v(0), \gamma) = H(\gamma)|\langle v(0)| + F(\gamma)$ (again parabolic for $\langle v(0)\rangle < 0.1$, see Figure III.9i). Here again, $H(\gamma)$ and $F(\gamma)$ are constant functions depending on γ for a fixed ω which represent the slope and the y-axis intercept, respectively.

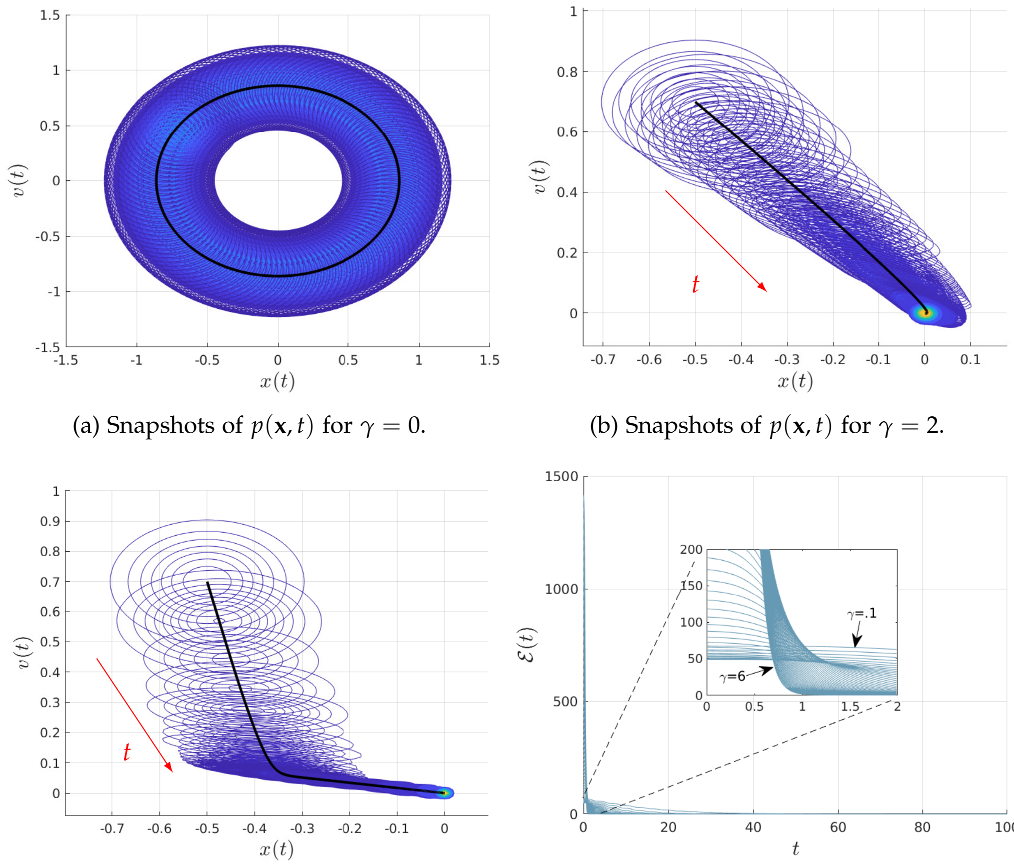

(a) Snapshots of $p(\mathbf{x}, t)$ for $\gamma = 0$.

(b) Snapshots of $p(\mathbf{x}, t)$ for $\gamma = 2$.

(c) Snapshots of $p(\mathbf{x}, t)$ for $\gamma = 6$.

(d) Time-evolution of $\Gamma(t)$.

Figure III.8: Cont.

Finally, Figure III.9j shows in logarithmic scale that the minimum value of $\mathcal{L}_\infty$ at $\langle x(0)\rangle = \langle v(0)\rangle$ monotonically increases with γ.

III.4.4 *The Limit Where $\omega \to 0$.*

When the natural frequency $\omega = 0$ (i.e. damped-driven system like the O-U process [74]) in Equation (III.36), the two eigenvalues of the matrix $\mathbf{A}$ become $\lambda_1 \to -\gamma$ and $\lambda_2 \to 0$. It then easily follows that

$$\langle \mathbf{x}(t)\rangle = \left[\begin{pmatrix} \frac{v(0)-e^{-\gamma t}v(0)}{\gamma} + x(0) \\ e^{-\gamma t}v(0) \end{pmatrix}\right] \tag{III.46}$$

and $\Sigma(t)$ is composed by the elements

$$\begin{aligned}
\Sigma_{11}(t) &= \frac{e^{-2\gamma t}\left(-D+\Sigma_{22}(0)\gamma+e^{\gamma t}(4D-\gamma(2\Sigma_{22}(0)+(\Sigma_{12}(0)+\Sigma_{21}(0))\gamma))+e^{2\gamma t}(\gamma(\Sigma_{22}(0)+\gamma(\Sigma_{12}(0)+\Sigma_{21}(0)+\Sigma_{11}(0)\gamma))+D(2\gamma t-3))\right)}{\gamma^3},\\
\Sigma_{12}(t) &= \frac{e^{-2\gamma t}\left(D(-1+e^{\gamma t})^2-\Sigma_{22}(0)\gamma+e^{\gamma t}\gamma(\Sigma_{22}(0)+\Sigma_{12}(0)\gamma)\right)}{\gamma^2}\\
\Sigma_{21}(t) &= \frac{e^{-2\gamma t}\left(D(-1+e^{\gamma t})^2-\Sigma_{22}(0)\gamma+e^{\gamma t}\gamma(\Sigma_{22}(0)+\Sigma_{21}(0)\gamma)\right)}{\gamma^2}
\end{aligned} \tag{III.47}$$

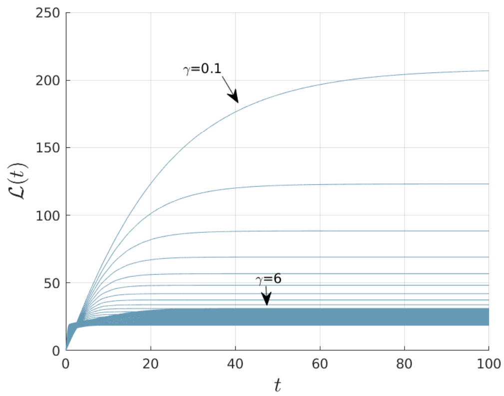

(e) Time-evolution of $\mathcal{L}(t)$.

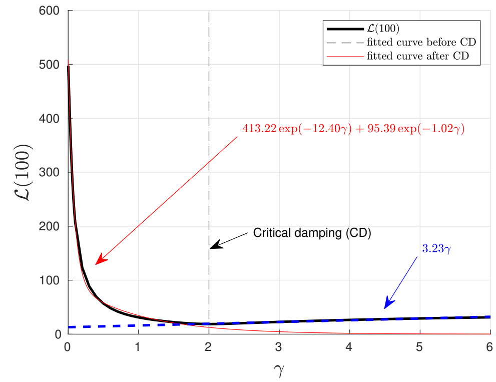

(f) $\mathcal{L}_\infty = \mathcal{L}(t = 100)$ against γ; fitted curves are shown in the red solid and blue dashed lines while a vertical line represents $\gamma = 2$ at the critical damping.

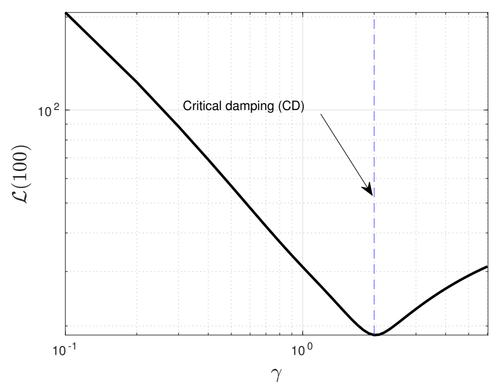

(g) The same as Figure III.8f but shown in log-log scales on x and y axes.

Figure III.8: Results of Equations (III.36) and (III.37) for $\langle x(0)\rangle = -0.5$, $\langle v(0)\rangle = 0.7$, $\gamma \in (0, 6)$, $\omega = 1$, $D = 0.0005$, and the initial covariance matrix $\Sigma(0)$ with elements $\Sigma_{11}(0) = \Sigma_{22}(0) = 0.01$, $\Sigma_{12}(0) = \Sigma_{21}(0) = 0$.

$$\Sigma_{22}(t) = \frac{e^{-2\gamma t}\left(D\left(-1+e^{2\gamma t}\right)+\Sigma_{22}(0)\gamma\right)}{\gamma}.$$

To investigate the case of $\omega \to 0$, we consider the scan over $D \in (0.0005, 0.04)$ for the same parameter value $\gamma = 2$, and the initial conditions as in Figure III.6, apart from using $\omega = 0$ instead of $\omega = 1$. Figure III.10 presents the results – snapshots of $p(\mathbf{x}, t)$, time evolutions of $\Gamma(t)$, $\mathcal{L}(t)$, and $\mathcal{L}_\infty = \mathcal{L}(t = 50)$ against D in Figure III.10a–e. In particular, in Figure III.10e, we identify the dependence of $\mathcal{L}_\infty$ on D by fitting the results to the curve $\mathcal{L}_= 8.99e^{-324.19D} + 10.83e^{-12.24D}$.

III.5 *Analysis for Non-Zero Fixed Initial Conditions*

In Section III.4.3 we analysed the behaviour of the information geometry associated with the Kramer equation (Equations (III.36) and (III.37)) for different $\gamma \in (0, 2.5)$ near the equilibrium point $\langle x(0)\rangle = \langle v(0)\rangle = 0$. To

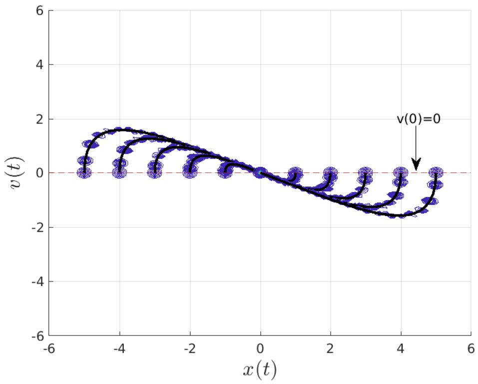

(a) Snapshots of $p(\mathbf{x}, t)$ for $\langle v(0) \rangle = 0$, $\gamma = 2.5$ and various $\langle x(0) \rangle \in (-5, 5)$.

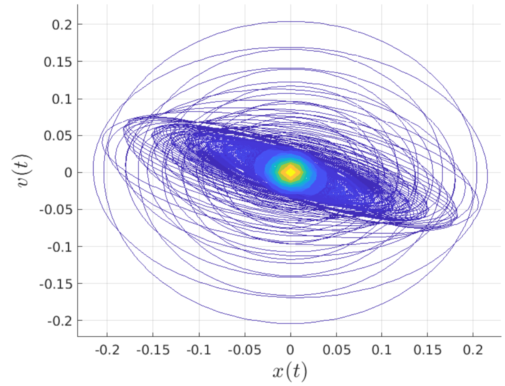

(b) Zoom-in of Figure III.9a showing $p(\mathbf{x}, t)$ for $\langle v(0) \rangle = 0$, $\gamma = 2.5$ and $\langle x(0) \rangle = 0$.

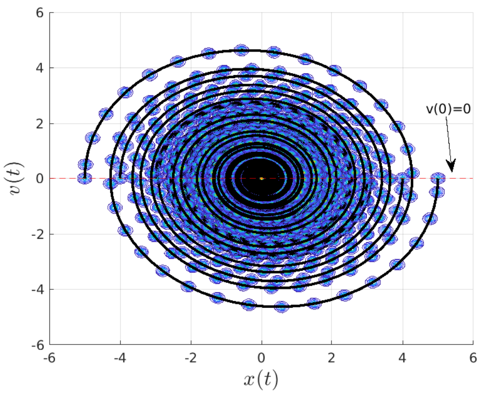

(c) Snapshots of $p(\mathbf{x}, t)$ for $\langle v(0) \rangle = 0$, $\gamma = 0.1$ and various $\langle x(0) \rangle \in (-5, 5)$.

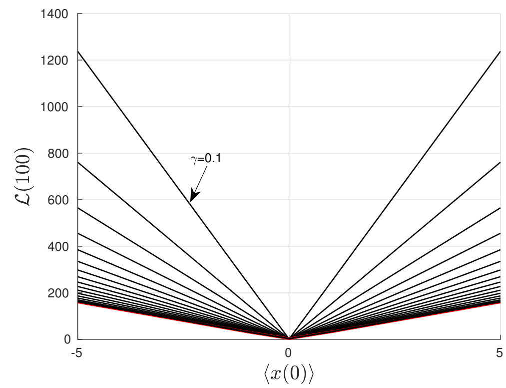

(d) $\mathcal{L}_\infty = \mathcal{L}(t = 100)$ against $\langle x(0) \rangle \in (-5, 5)$ for $\langle v(0) \rangle = 0$ and $\gamma \in (0, 2.5)$.

Figure III.9: Cont.

this end, we plotted $\mathcal{L}_\infty$ when varying $\langle x(0) \rangle$ and $\langle v(0) \rangle$ for a fixed $\langle v(0) \rangle = 0$ and $\langle x(0) \rangle = 0$, respectively. In this section, we want to show how such information geometry changes near a non-equilibrium point by scanning over $\langle x(0) \rangle$ and $\langle v(0) \rangle$ for a fixed non-zero $\langle v(0) \rangle = 0.7$ and $\langle x(0) \rangle = -0.5$, respectively. We show that the use of non-zero fixed initial conditions changes the location of the minimum $\mathcal{L}_\infty$ depending on γ. Here, we use the same parameter values $D = 0.0005$, $\omega = 1$, $\Sigma_{12}(0) = \Sigma_{21}(0) = 0$ and $\Sigma_{11}(0) = \Sigma_{22}(0) = 0.01$.

First, snapshots of $p(\mathbf{x}, t)$ are shown in Figure III.11a,f for $\gamma = 2.5$ (above its critical value $\gamma = 2 = 2\omega$) while those in Figure III.11b,g are for $\gamma = 0.1$ below the critical value 2. It is important to notice that there is a non-symmetric behaviour of the trajectories of the system for $\gamma \gg 0$. This is shown at Figure III.11a,f whose trajectories asymmetrically vary over the initial conditions in comparison with the results shown in Figure III.9a,f. By approximating $\mathcal{L}_\infty = \mathcal{L}(t = 100)$, we then show how $\mathcal{L}_\infty$ depends on $\langle x(0) \rangle$ and $\langle v(0) \rangle$ for different values of γ in Figure III.11c,d and Figure III.11h,i, respectively. Of prominence in Figure III.11c,d is the presence of a distinct minimum in $\mathcal{L}_\infty$ for a particular value of $\langle x(0) \rangle = x_c$, $\mathcal{L}_\infty$ linearly increasing with $|\langle x(0) \rangle - x_c|$ for a sufficiently large $|\langle x(0) \rangle - x_c|$; similarly, Figure III.11h,i shows a distinct minimum in $\mathcal{L}_\infty$ for a particular value of $\langle v(0) \rangle = v_c$, $\mathcal{L}_\infty$ linearly increasing with $|\langle v(0) \rangle - v_c|$ for a sufficiently large

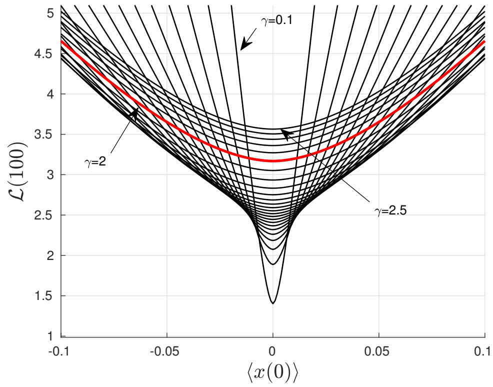

(e) Zoom-in of Figure III.9d.

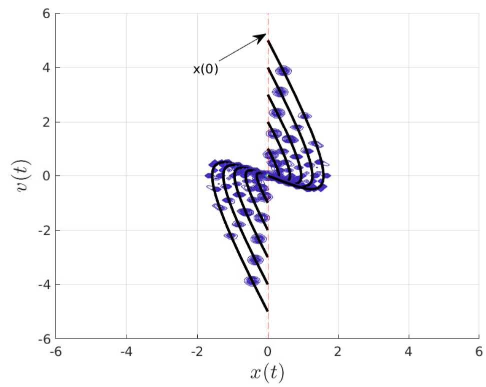

(f) Snapshots of $p(\mathbf{x},t)$ for $\langle x(0)\rangle = 0$, $\gamma = 2.5$ and various $\langle v(0)\rangle \in (-5,5)$.

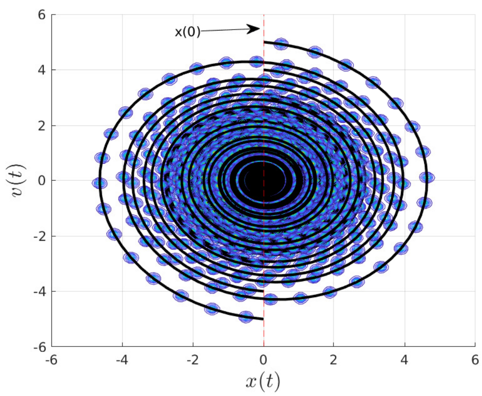

(g) Snapshots of $p(\mathbf{x},t)$ for $\langle x(0)\rangle = 0$, $\gamma = 0.1$ and various $\langle v(0)\rangle \in (-5,5)$.

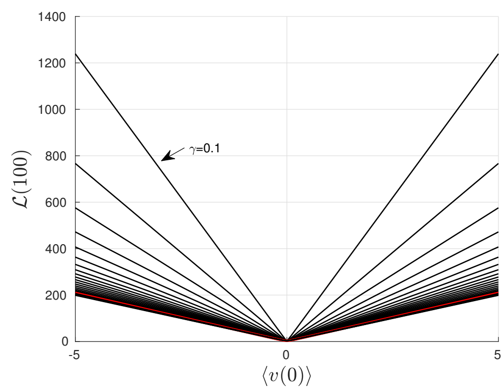

(h) $\mathcal{L}_\infty = \mathcal{L}(t = 100)$ against $\langle v(0)\rangle \in (-5,5)$ for $\langle x(0)\rangle = 0$ and $\gamma \in (0,2.5)$.

Figure III.9: Cont.

$|\langle v(0)\rangle - v_c|$.

Finally, we scan over $\langle x(0)\rangle$ and $\langle v(0)\rangle$ and identify the minimum value of $\mathcal{L}_\infty$ for a given γ and plot this minimum value of $\mathcal{L}_\infty$ (at x_c and v_c) against γ in Figure III.11e,j. In Figure III.11e,j, $\mathcal{L}_\infty$ against γ takes its minimum near the critical damping $\gamma = 2\omega = 2$ (shown in a vertical line), as observed previously in Sections III.4.1–III.4.2. This is clearly different from the behaviour of the minimum value of $\mathcal{L}_\infty$ against γ (for the equilibrium point $\langle x(0)\rangle = 0$ and $\langle v(0)\rangle = 0$) in Figure III.9j where $\mathcal{L}_\infty$ monotonically increases with γ. This is because for $\langle x(0)\rangle = 0$ and $\langle v(0)\rangle = 0$, mean values does not change over time, with less effect of oscillations (ω) and thus the critical damping $\gamma = 2\omega$.

III.6 IL in non-linear dynamics

The system PDF may no longer be Gaussian when studying non-linear dynamics, yet, it is still possible to apply Theorem III.1 to obtain the IL's value via the Laplace Assumption (recall Proposition II.7). For example,

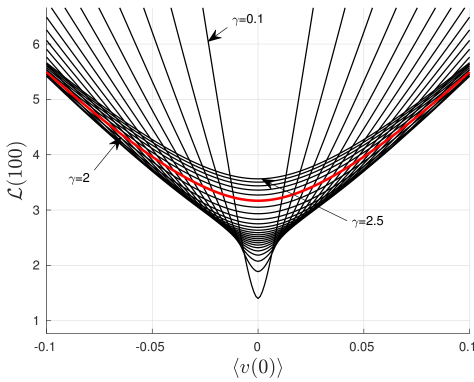

(i) Zoom-in of Figure III.9h.

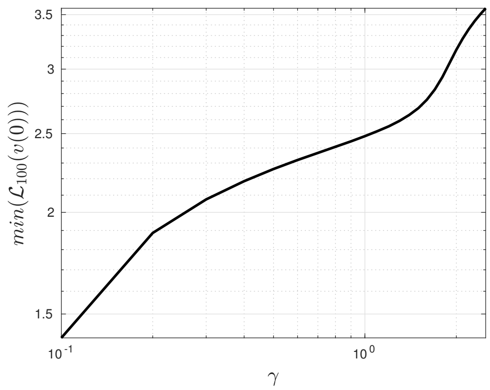

(j) The minimum value of $\mathcal{L}_\infty$ at $\langle x(0)\rangle = \langle v(0)\rangle = 0$ against γ on log-log scales; $\langle x(0)\rangle = 0$.

Figure III.9: Results of Equations (III.36) and (III.37) scanned over $\langle x(0)\rangle \in (-5,5)$ for $\langle v(0)\rangle = 0$ [Figure III.9a–e] and $\langle v(0)\rangle \in (-5,5)$ for $\langle x(0)\rangle = 0$ [Figure III.9f–i]. The parameter values $\omega = 1$, $D = 0.0005$, and $\gamma \in (0, 2.5)$ while the initial covariance matrix $\Sigma(0)$ has the elements $\Sigma_{11}(0) = \Sigma_{22}(0) = 0.01$, $\Sigma_{12}(0) = \Sigma_{21}(0) = 0$.

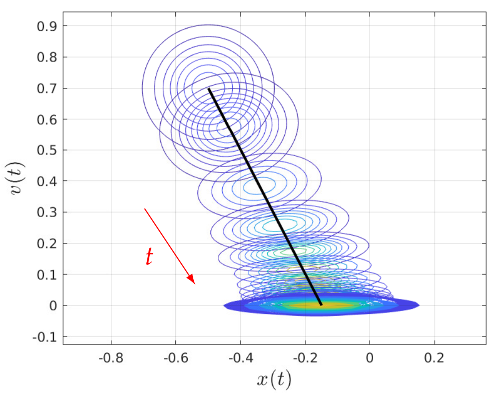

(a) Snapshots of $p(\mathbf{x}, t)$ for $D = 0.0005$.

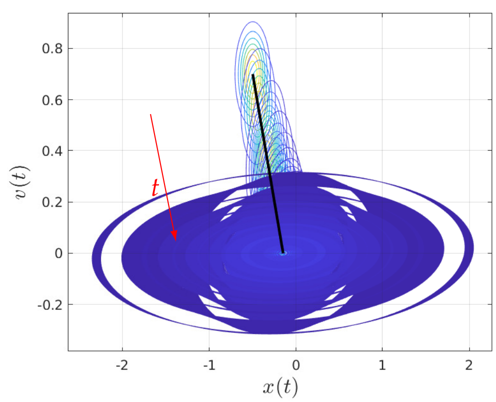

(b) Snapshots of $p(\mathbf{x}, t)$ for $D = 0.04$.

Figure III.10: Cont.

consider the following toy-model of a simple pendulum subject to a random force ξ

$$\ddot{\theta} + b\dot{\theta} + \frac{g}{\ell}\sin\theta = \xi(t), \tag{III.48}$$

where b is the constant friction, g is the gravity constant, ℓ is the length of the pendulum and ξ is again a random force with $\langle \xi \rangle = 0$ and $\langle \xi(t)\xi(t')\rangle = 2D\delta(t - t')$.

After transforming Equation (III.48) in a set of two first order differential equations and applying Proposition II.7, the mean value vector $\boldsymbol{\mu} = [\mu_1, \mu_2]^\top = [\langle\dot{\theta}\rangle, \langle\theta\rangle]^\top$ and the covariance matrix $\boldsymbol{\Sigma}$ dynamics are given

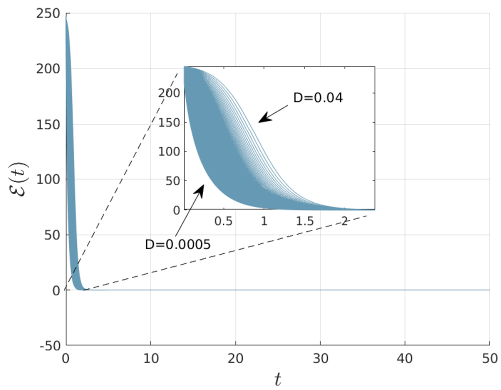

(c) Time-evolution of $\Gamma(t)$.

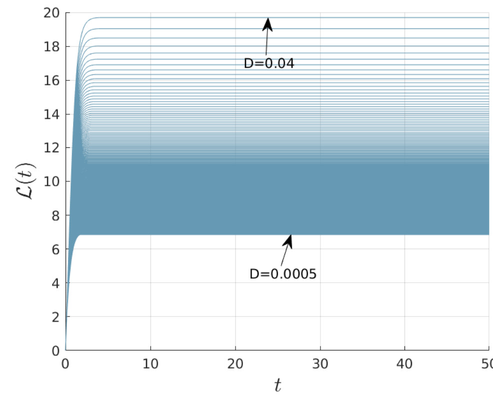

(d) Time-evolution of $\mathcal{L}(t)$.

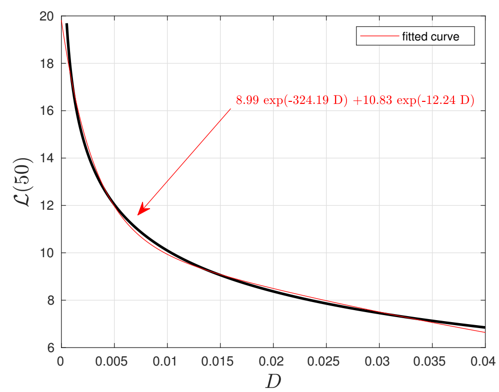

(e) $\mathcal{L}_\infty = \mathcal{L}(t = 50)$ against D; a fitted curve is shown in the red solid line.

Figure III.10: Results of Equations (III.36) and (III.37) for $\langle x(0)\rangle = -0.5$, $\langle v(0)\rangle = 0.7$, $\gamma = 2$, $\omega = 0$, $D \in (0.0005, 0.04)$ and the initial covariance matrix $\Sigma(0)$ with elements $\Sigma_{11}(0) = \Sigma_{22}(0) = 0.01$, $\Sigma_{12}(0) = \Sigma_{21}(0) = 0$.

by

$$\dot{\boldsymbol{\mu}} = \begin{pmatrix} \mu_2 \\ \frac{g(\Sigma_{11}-2)\sin(\mu_1)}{2L} - b\mu_2 \end{pmatrix} \tag{III.49}$$

$$\dot{\boldsymbol{\Sigma}} = \begin{pmatrix} 2\Sigma_{12} & -b\Sigma_{12} + \Sigma_{22} - \frac{g\Sigma_{11}\cos(\mu_1)}{L} \\ -b\Sigma_{12} + \Sigma_{22} - \frac{g\Sigma_{11}\cos(\mu_1)}{L} & 4\mathrm{d}22 - 2b\Sigma_{22} - \frac{2g\Sigma_{12}\cos(\mu_1)}{L} \end{pmatrix} \tag{III.50}$$

After solving Equations (III.49) and (III.50) numerically, we can get the simulation shown in Figure III.12[9]. Then, we can obtain the value of IL $\mathcal{L}$ and information rate Γ after substituting such solution in Equations (III.22)-(III.11) (results are shown in Figure III.13).

[9] Code `https://github.com/AdrianGuel/PhDThesis/blob/main/Chapter2/pendulumIL.m`

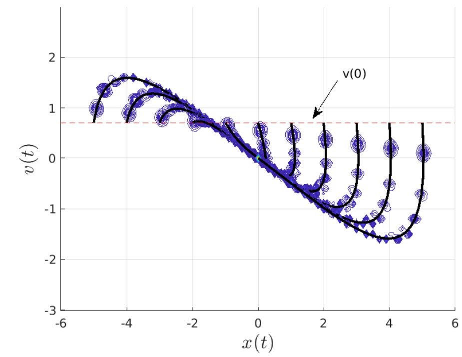

(a) Snapshots of $p(\mathbf{x},t)$ for $\langle v(0)\rangle = 0.7$, $\gamma = 2.5$ and various $\langle x(0)\rangle \in (-5,5)$.

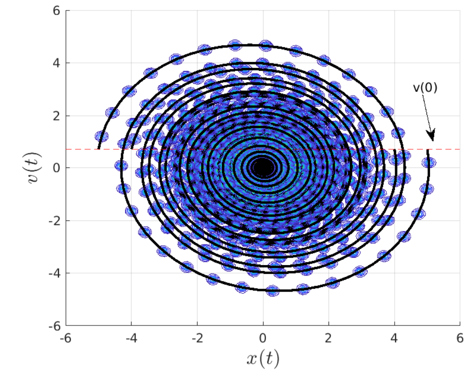

(b) Snapshots of $p(\mathbf{x},t)$ for $\langle v(0)\rangle = 0.7$, $\gamma = 0.1$ and various $\langle x(0)\rangle \in (-5,5)$.

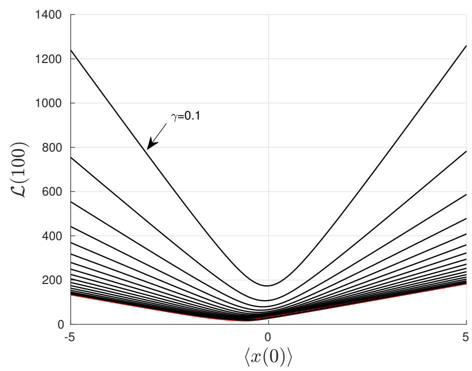

(c) $\mathcal{L}_\infty = \mathcal{L}(t=100)$ against $\langle x(0)\rangle \in (-5,5)$ for $\langle v(0)\rangle = 0.7$ and $\gamma \in (0, 2.5)$.

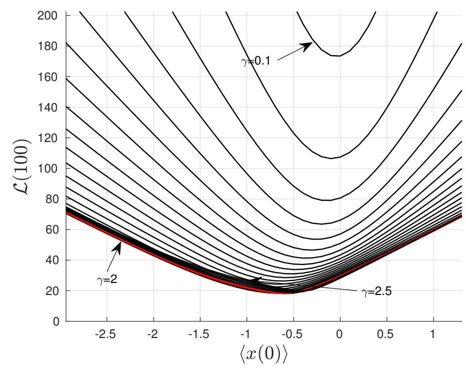

(d) Zoom-in of Figure III.11c.

Figure III.11: Cont.

III.7 *Relations between entropy rate and information rate*

To understand the value of IL and information rate Γ in any dynamical system, various articles have already proposed some relations between the Fisher information and physical observables (for instance, see [75]). Specifically, in [62], E. Kim deduces that if the PDF of Equation (III.12) is described by an univariate Gaussian PDF (i.e. the Ornstein–Uhlenbeck (OU) process) the information rate Γ is related to the entropy rate $\dot{S}$ and the entropy production Π via

$$\Gamma^2 = \frac{D}{\sigma}\Pi + \dot{S}^2. \tag{III.51}$$

Equation (III.51) can easily be confirmed after some algebra with the following expressions

$$\begin{aligned} \Pi &= \frac{\dot{\mu}^2}{D} + \frac{a^2\Sigma}{D} + \frac{D}{\Sigma} + 2a = \frac{\dot{\mu}^2}{D} + \frac{\dot{\Sigma}^2}{4\Sigma D}, \\ \dot{S} &= \frac{1}{2}\frac{\dot{\Sigma}}{\Sigma}, \quad \Gamma^2 = \frac{\dot{\mu}^2}{\Sigma} + \frac{1}{2}\left(\frac{\dot{\Sigma}}{\Sigma}\right)^2, \end{aligned} \tag{III.52}$$

where μ, Σ, D and a are the scalar version of $\boldsymbol{\mu}, \boldsymbol{\Sigma}, \mathbf{D}$ and $\mathbf{A}$, respectively. Pursuing a general connection between information rate Γ and thermodynamics, here, we extend (III.51) to the case of a n-variate Gaussian

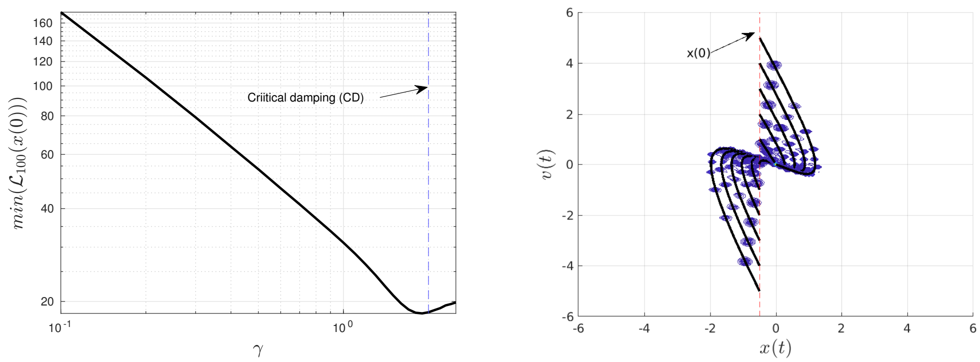

(e) The minimum value of $\mathcal{L}_\infty$ over $\langle x(0)\rangle \in (-5,5)$ against γ on log-log scales; $\langle v(0)\rangle = 0.7$.

(f) Snapshots of $p(\mathbf{x},t)$ for $\langle x(0)\rangle = -0.5$, $\gamma = 2.5$ and various $\langle v(0)\rangle \in (-5,5)$.

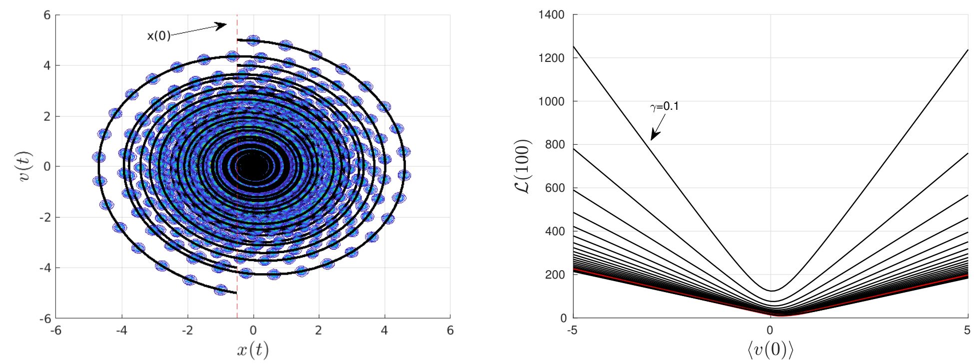

(g) Snapshots of $p(\mathbf{x},t)$ for $\langle x(0)\rangle = -0.5$, $\gamma = 0.1$ and various $\langle v(0)\rangle \in (-5,5)$.

(h) $\mathcal{L}_\infty = \mathcal{L}(t=100)$ against $\langle v(0)\rangle \in (-5,5)$ for $\langle x(0)\rangle = -0.5$ and $\gamma \in (0,2.5)$.

Figure III.11: Cont.

process. Such a result is given by the following relations.

Relation III.1

Given an n-variate Gaussian process whose mean and covariance are described by Equations (II.77)-(II.78), a relationship between entropy production Π, entropy rate $\dot{S}$, and information rate Γ is given by

$$0 \le \Gamma^2 \le \mathcal{E}_u := \mathrm{Tr}(\mathbf{\Sigma}^{-1})\Pi\,\mathrm{Tr}(\mathbf{D}) + \dot{S}^2 - 2g(\mathbf{s}), \tag{III.53}$$

where $\mathbf{s} = [\dot{S}_{J_1}, \dot{S}_{J_2}, \ldots, \dot{S}_{J_n}]^\top$, $g(\mathbf{s}) := \sum_{i<j}^{n} \dot{S}_{J_i}\dot{S}_{J_j}$ and $\dot{S}_{J_i}$ is the contribution to entropy rate by the current flow J_i (see Equation (II.67)), i.e.

$$\dot{S}_{J_i} = -\iint_{\mathbb{R}^n} \frac{\partial}{\partial x_i} J_i(\mathbf{x};t)\ln\left(p(\mathbf{x};t)\right)\mathrm{d}^n x = \Pi_i - \Phi_i. \tag{III.54}$$

Proof. For any real matrix $\mathbf{A}$ in system (II.77)-(II.78), we can rewrite the second term in the right hand side of (III.22) as follows

$$\mathrm{Tr}\left((\mathbf{\Sigma}^{-1}\dot{\mathbf{\Sigma}})^2\right) \;=\; \mathrm{Tr}\left(2\mathbf{A}^2 + 2\mathbf{\Sigma}^{-1}\mathbf{A}\mathbf{\Sigma}\mathbf{A}\right. \tag{III.55}$$

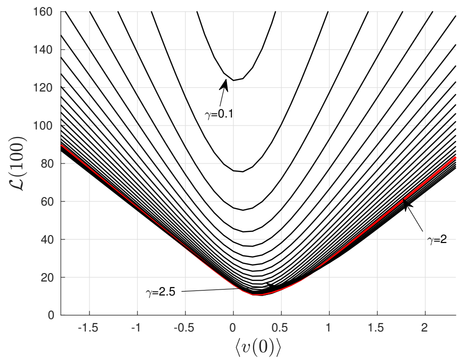

(i) Zoom-in of Figure III.11h.

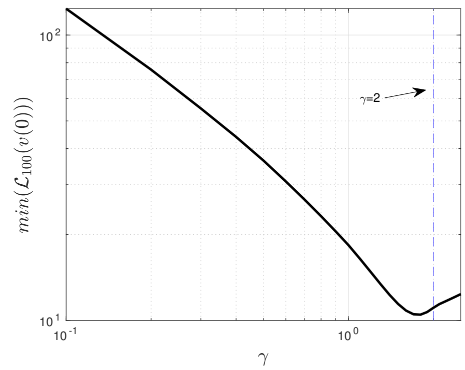

(j) The minimum value of $\mathcal{L}_\infty$ over $\langle v(0) \rangle \in (-5, 5)$ against γ on log-log scales; $\langle x(0) \rangle = -0.5$.

Figure III.11: Results of Equations (III.36) and (III.37) scanned over $\langle x(0) \rangle \in (-5, 5)$ for $\langle v(0) \rangle = 0.7$ [Figure III.11a–e] and $\langle v(0) \rangle \in (-5, 5)$ for $\langle x(0) \rangle = -0.5$ [Figure III.11f–j]. The parameter values $\omega = 1$, $D = 0.0005$, and $\gamma \in (0, 2.5)$ while the initial covariance matrix $\Sigma(0)$ has the elements $\Sigma_{11}(0) = \Sigma_{22}(0) = 0.01$, $\Sigma_{12}(0) = \Sigma_{21}(0) = 0$.

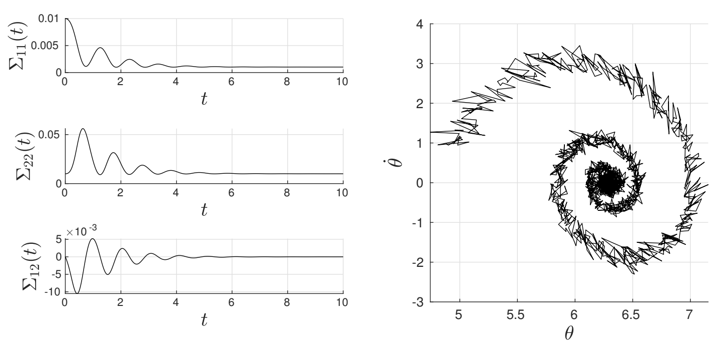

Figure III.12: Simulation under the Laplace assumption of the stochastic equation of a simple pendulum (III.48). The parameters are $\boldsymbol{\mu}(0) = [5, 1]^\top, \boldsymbol{\Sigma} = 1 \times 10^{-2}\mathbf{I}, D = 1 \times 10^{-2}, g = 9.81, L = 1, m = 1$, and $b = 1$.

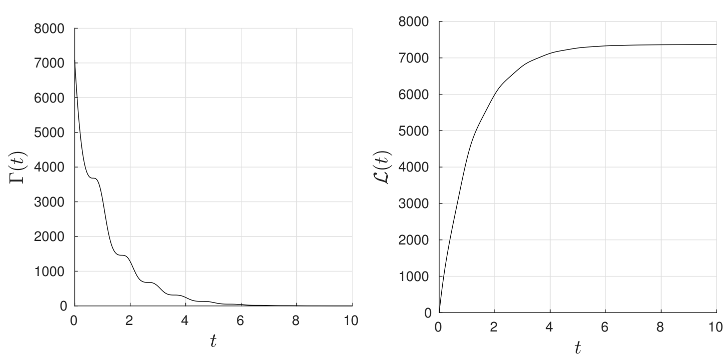

Figure III.13: Computation of the IL $\mathcal{L}$ under the Laplace assumption of the stochastic equation of a simple pendulum (III.48).

$$
\begin{aligned}
&+8\boldsymbol{\Sigma}^{-1}\mathbf{A}\mathbf{D} + 4\boldsymbol{\Sigma}^{-1}\mathbf{D}\boldsymbol{\Sigma}^{-1}\mathbf{D}\Big)\Big(\\
&= \mathrm{Tr}(2\mathbf{A}^2 + 4\boldsymbol{\Sigma}^{-1}\mathbf{A}\mathbf{D} + 2\boldsymbol{\Sigma}^{-1}\mathbf{D}\boldsymbol{\Sigma}^{-1}\mathbf{D}) \\
&+ \mathrm{Tr}(2\boldsymbol{\Sigma}^{-1}\mathbf{A}\boldsymbol{\Sigma}\mathbf{A} + 4\boldsymbol{\Sigma}^{-1}\mathbf{A}\mathbf{D} + 2\boldsymbol{\Sigma}^{-1}\mathbf{D}\boldsymbol{\Sigma}^{-1}\mathbf{D}) \\
&= 2\,\mathrm{Tr}\left((\boldsymbol{\Sigma}^{-1}\mathbf{D} + A)^2\right)\Big(\\
&+2\,\mathrm{Tr}(\boldsymbol{\Sigma}^{-1}(\mathbf{A}\boldsymbol{\Sigma}\mathbf{A}^\top\mathbf{D}^{-1}+2\mathbf{A}+\mathbf{D}\boldsymbol{\Sigma}^{-1})\mathbf{D}).
\end{aligned}
$$

Equation (III.55) can be written in terms of Entropy production Π and entropy rate $\dot{S}$ using the following results. First, from the fact that $\Pi \geq 0$ and $\Sigma^{-1}, \mathbf{D} \succeq 0$ we get

$$
\begin{aligned}
\mathrm{Tr}(\boldsymbol{\Sigma}^{-1})\Pi\,\mathrm{Tr}(\mathbf{D}) \quad &= \quad \mathrm{Tr}(\boldsymbol{\Sigma}^{-1})\,\mathrm{Tr}\left(\dot{\boldsymbol{\mu}}\dot{\boldsymbol{\mu}}^\top\mathbf{D}^{-1} + \mathbf{A}\boldsymbol{\Sigma}\mathbf{A}^\top\mathbf{D}^{-1} + 2\mathbf{A} + \mathbf{D}\boldsymbol{\Sigma}^{-1}\right)\Big(\mathrm{Tr}(\mathbf{D}) \\
&\geq \mathrm{Tr}(\boldsymbol{\Sigma}^{-1}\dot{\boldsymbol{\mu}}\dot{\boldsymbol{\mu}}^\top) + \mathrm{Tr}(\boldsymbol{\Sigma}^{-1}(\mathbf{A}\boldsymbol{\Sigma}\mathbf{A}^\top\mathbf{D}^{-1}+2\mathbf{A}+\mathbf{D}\boldsymbol{\Sigma}^{-1})\mathbf{D}).
\end{aligned}
\tag{III.56}
$$

Now, taking λ_i as the eigenvalues of the matrix $\mathbf{H} := \boldsymbol{\Sigma}^{-1}\mathbf{D} + \mathbf{A}$, we have

$$
\dot{S}^2 \;=\; \mathrm{Tr}(\mathbf{H})^2 \;=\; (\sum_{i=1}^{n}\lambda_i)^2 \;=\; \sum_{i=1}^{n}\lambda_i^2 + 2\sum_{j=1}^{n}\sum_{i=1}^{j-1}\lambda_i\lambda_j \;=\; \mathrm{Tr}(\mathbf{H}^2) + 2\sum_{i<j}^{n}\lambda_i\lambda_j \;=\; \mathrm{Tr}(\mathbf{H}^2) + 2g(\mathbf{H}). \tag{III.57}
$$

Finally, using (III.55)-(III.57) in (III.22) we get

$$
2g(\mathbf{H}) \leq \Gamma^2 + 2g(\mathbf{H}) \;\leq\; \mathrm{Tr}(\boldsymbol{\Sigma}^{-1})\Pi\,\mathrm{Tr}(\mathbf{D}) + \mathrm{Tr}(\mathbf{H}^2) + 2g(\mathbf{H}), \tag{III.58}
$$

$$
2g(\mathbf{H}) \leq \Gamma^2 + 2g(\mathbf{H}) \;\leq\; \mathrm{Tr}(\boldsymbol{\Sigma}^{-1})\Pi\,\mathrm{Tr}(\mathbf{D}) + \dot{S}^2, \tag{III.59}
$$

$$
0 \leq \Gamma^2 \;\leq\; \mathrm{Tr}(\boldsymbol{\Sigma}^{-1})\Pi\,\mathrm{Tr}(\mathbf{D}) + \dot{S}^2 - 2g(\mathbf{H}). \tag{III.60}
$$

Now, since $\dot{S} = \sum_i^n \dot{S}_{J_i}$ where $\dot{S}_{J_i}$ is the contribution of the current flow J_i to the total entropy rate $\dot{S}$, we know that each eigenvalue $\lambda_i = \dot{S}_{J_i}$. This ends our proof. ∎

Relation III.1 provides an inequality between information rate Γ (an information metric), entropy rate $\dot{S}$ and entropy production Π where the entropy rate $\dot{S}_i$ of each random variable x_i is explicitly taken into account. From Relation III.1 we have

$$
\mathcal{L}(t) \leq \mathcal{L}_u(t) := \int_0^t \sqrt{\mathcal{E}_u(\tau)}\,\mathrm{d}\tau. \tag{III.61}
$$

Since minimising $\mathcal{L}_u$ will minimise $\mathcal{L}$, we can obtain both a minimum entropy production and a minimum statistical variability behaviour through $\mathcal{L}_u$.

For unstable systems, we can avoid the computation of the term $g(\mathbf{s})$ involving the contribution to entropy rate by each current flow J_i via the following relation.

Relation III.2

Given the same conditions as in Relation III.1, but considering that the eigenvalues $\varphi_i \in \mathbb{C}$ of the matrix $\mathbf{A}$ satisfy the following inequality

$$\Re\{\varphi_i\} > 0 \quad \forall i = 1, 2, \dots, n. \tag{III.62}$$

Then, the following result holds

$$0 \leq \Gamma^2 \leq \mathcal{I}_u := \frac{1}{n}\operatorname{Tr}(\boldsymbol{\Sigma}^{-1})\Pi_u \operatorname{Tr}(\mathbf{D}) + \dot{S}^2, \tag{III.63}$$

where $\Pi_u \geq \Pi$ (an upper bound of entropy production) defined by

$$\Pi_u := \operatorname{Tr}(\dot{\boldsymbol{\mu}}\dot{\boldsymbol{\mu}}^\top)\operatorname{Tr}(\mathbf{D}^{-1}) + \frac{1}{4}\operatorname{Tr}(\boldsymbol{\Sigma}^{-1})\operatorname{Tr}(\dot{\boldsymbol{\Sigma}})^2\operatorname{Tr}(\mathbf{D}^{-1}). \tag{III.64}$$

Proof. To derive the result shown in Relation III.2, we first consider the following preliminary results [76; 77; 78]

$$\begin{aligned}
\operatorname{Tr}(\mathbf{XY}) &\leq \operatorname{Tr}(\mathbf{X})\operatorname{Tr}(\mathbf{Y}) \quad \forall \quad \mathbf{X}, \mathbf{Y} \succeq 0, && \text{(III.65)}\\
\operatorname{Tr}(\dot{\boldsymbol{\Sigma}}) &= \operatorname{Tr}(\mathbf{A}\boldsymbol{\Sigma}) + \operatorname{Tr}(\boldsymbol{\Sigma}\mathbf{A}^\top) + \operatorname{Tr}(2\mathbf{D})\\
&= 2\operatorname{Tr}(\boldsymbol{\Sigma}\mathbf{A} + \mathbf{D}), && \text{(III.66)}\\
\operatorname{Tr}(\dot{\boldsymbol{\Sigma}})^2 &= 4\operatorname{Tr}(\boldsymbol{\Sigma}\mathbf{A} + \mathbf{D})\operatorname{Tr}(\boldsymbol{\Sigma}\mathbf{A}^\top + \mathbf{D})\\
&\geq 4\operatorname{Tr}(\boldsymbol{\Sigma}\mathbf{A}\boldsymbol{\Sigma}\mathbf{A}^\top + 2\boldsymbol{\Sigma}\mathbf{A}\mathbf{D} + \mathbf{D}^2), && \text{(III.67)}\\
\operatorname{Tr}(\boldsymbol{\Sigma}^{-1})^2\operatorname{Tr}(\dot{\boldsymbol{\Sigma}})^2 &= \operatorname{Tr}(\boldsymbol{\Sigma}^{-1})\operatorname{Tr}(\dot{\boldsymbol{\Sigma}})\operatorname{Tr}(\boldsymbol{\Sigma}^{-1})\operatorname{Tr}(\dot{\boldsymbol{\Sigma}})\\
&\geq \operatorname{Tr}(\boldsymbol{\Sigma}^{-1}\dot{\boldsymbol{\Sigma}})^2 \geq \operatorname{Tr}((\boldsymbol{\Sigma}^{-1}\dot{\boldsymbol{\Sigma}})^2) && \text{(III.68)}
\end{aligned}$$

Then, by applying the previous results to the definition of Γ^2 in (III.22), we have

$$\begin{aligned}
0 \leq \Gamma^2 &= \operatorname{Tr}(\dot{\boldsymbol{\mu}}^\top\boldsymbol{\Sigma}^{-1}\dot{\boldsymbol{\mu}}) + \frac{1}{2}\operatorname{Tr}\left((\boldsymbol{\Sigma}^{-1}\dot{\boldsymbol{\Sigma}})^2\right)\\
&\leq \operatorname{Tr}(\dot{\boldsymbol{\mu}}\dot{\boldsymbol{\mu}}^\top)\operatorname{Tr}(\boldsymbol{\Sigma}^{-1}) + \frac{1}{2}\operatorname{Tr}(\boldsymbol{\Sigma}^{-1}\dot{\boldsymbol{\Sigma}})^2 && \text{(III.69)}\\
&\leq \operatorname{Tr}(\dot{\boldsymbol{\mu}}\dot{\boldsymbol{\mu}}^\top)\operatorname{Tr}(\boldsymbol{\Sigma}^{-1}) + \frac{1}{4}\operatorname{Tr}(\boldsymbol{\Sigma}^{-1})^2\operatorname{Tr}(\dot{\boldsymbol{\Sigma}})^2 + \dot{S}^2.
\end{aligned}$$

Now, multiplying both sides of inequality (III.69) by $\operatorname{Tr}(\mathbf{D}^{-1}\mathbf{D})$ and factorising $\operatorname{Tr}(\boldsymbol{\Sigma}^{-1})$ from its right hand side, we have

$$\begin{aligned}
0 \leq n\Gamma^2 &\leq \operatorname{Tr}(\boldsymbol{\Sigma}^{-1})\{\operatorname{Tr}(\dot{\boldsymbol{\mu}}\dot{\boldsymbol{\mu}}^\top)\operatorname{Tr}(\mathbf{D}^{-1}\mathbf{D})\\
&\quad + \frac{1}{4}\operatorname{Tr}(\boldsymbol{\Sigma}^{-1})\operatorname{Tr}(\dot{\boldsymbol{\Sigma}})^2\operatorname{Tr}(\mathbf{D}^{-1}\mathbf{D})\} + n\dot{S}^2\\
&\leq \operatorname{Tr}(\boldsymbol{\Sigma}^{-1})\{\operatorname{Tr}(\dot{\boldsymbol{\mu}}\dot{\boldsymbol{\mu}}^\top)\operatorname{Tr}(\mathbf{D}^{-1}) && \text{(III.70)}\\
&\quad + \frac{1}{4}\operatorname{Tr}(\boldsymbol{\Sigma}^{-1})\operatorname{Tr}(\dot{\boldsymbol{\Sigma}})^2\operatorname{Tr}(\mathbf{D}^{-1})\}\operatorname{Tr}(\mathbf{D}) + n\dot{S}^2.
\end{aligned}$$

From the right hand side of (III.70), we define the part inside the curly brackets as

$$\Pi_u := \operatorname{Tr}(\dot{\boldsymbol{\mu}}\dot{\boldsymbol{\mu}}^\top)\operatorname{Tr}(\mathbf{D}^{-1}) + \frac{1}{4}\operatorname{Tr}(\boldsymbol{\Sigma}^{-1})\operatorname{Tr}(\dot{\boldsymbol{\Sigma}})^2\operatorname{Tr}(\mathbf{D}^{-1}). \tag{III.71}$$

Which gives us the expression in our result (III.53). The value of Π_u can be proved to be an upper bound of Π from the following reasoning

$$\begin{aligned}
\Pi_u \quad &\geq \quad \mathrm{Tr}(\dot{\boldsymbol{\mu}}^\top \mathbf{D}^{-1} \dot{\boldsymbol{\mu}}) \\
&\quad + \mathrm{Tr}(\boldsymbol{\Sigma}^{-1})\,\mathrm{Tr}(\boldsymbol{\Sigma}\mathbf{A}\boldsymbol{\Sigma}\mathbf{A}^\top + 2\boldsymbol{\Sigma}\mathbf{A}\mathbf{D} + \mathbf{D}^2)\,\mathrm{Tr}(\mathbf{D}^{-1}) \\
&\geq \dot{\boldsymbol{\mu}}^\top \mathbf{D}^{-1}\dot{\boldsymbol{\mu}} + \mathbf{tr}\left(\boldsymbol{\Sigma}^{-1}\boldsymbol{\Sigma}(\mathbf{A}\boldsymbol{\Sigma}\mathbf{A}^\top\mathbf{D}^{-1} + 2\mathbf{A} + \boldsymbol{\Sigma}^{-1}\mathbf{D})\mathbf{D}\mathbf{D}^{-1}\right) \\
&= \dot{\boldsymbol{\mu}}^\top \mathbf{D}^{-1}\dot{\boldsymbol{\mu}} + \mathbf{tr}(\mathbf{A}\boldsymbol{\Sigma}\mathbf{A}^\top\mathbf{D}^{-1} + 2\mathbf{A} + \boldsymbol{\Sigma}^{-1}\mathbf{D}).
\end{aligned} \tag{III.72}$$

Note that for $\Pi_u \geq \Pi$ we need $\mathbf{A} \succeq 0$. A similar result can be found starting from the definition of Π_u in (III.71) as follows

$$\mathrm{Tr}(\boldsymbol{\Sigma}^{-1})\Pi_u\,\mathrm{Tr}(\mathbf{D}) \geq \mathrm{Tr}(\boldsymbol{\Sigma}^{-1})\{\mathrm{Tr}(\dot{\boldsymbol{\mu}}\dot{\boldsymbol{\mu}}^\top)\,\mathrm{Tr}(\mathbf{D}^{-1}\mathbf{D}) + \frac{1}{4}\mathrm{Tr}(\boldsymbol{\Sigma}^{-1})\,\mathrm{Tr}(\dot{\boldsymbol{\Sigma}})^2\,\mathrm{Tr}(\mathbf{D}^{-1}\mathbf{D})\}. \tag{III.73}$$

From (III.72), the main result follows straightforwardly using (III.70) leading to our main result in Relation III.2. ■

Now, we investigate the case when a relation between Γ, $\dot{S}$ and Π can be expressed in the form of equality. If and only if $\mathbf{A}$ in (II.77)-(II.78) is a diagonal matrix, i.e. we have a set of linearly independent stochastic differential equations (this can be after applying decoupling transformations [79]), the following result holds.

Relation III.3

Given a n-variate Gaussian process where all its random variables are independent, we have

$$\Gamma^2 := \sum_i \frac{D_{ii}}{\Sigma_{ii}}\Pi_i + \sum_i \dot{S}_i^2, \tag{III.74}$$

where Π_i and $\dot{S}_i$ are the entropy production and entropy rate from the marginal PDF $p(x_i, t)$ of x_i, respectively.

Proof. If $\mathbf{A}$ is an $n \times n$ diagonal matrix, then $\boldsymbol{\Sigma}$ and $\dot{\boldsymbol{\Sigma}}$ are also diagonal and the following expressions hold

$$\Gamma^2 \quad = \quad \sum_i \Gamma_i^2 \overset{\text{Def. III.2}}{=} \sum_i \left(\frac{\dot{\mu}_i^2}{\Sigma_{ii}} + \frac{1}{2}\left(\frac{\dot{\Sigma}_{ii}}{\Sigma_{ii}}\right)^2\right) \tag{III.75}$$

$$\begin{aligned}
\Pi \quad &= \quad \sum_i \Pi_i = \dot{\boldsymbol{\mu}}^\top \mathbf{D}^{-1}\dot{\boldsymbol{\mu}} + \frac{1}{4}\mathrm{Tr}\left(\boldsymbol{\Sigma}^{-1}\dot{\boldsymbol{\Sigma}}^2\mathbf{D}^{-1}\right) \\
&= \quad \sum_i \left(\frac{\dot{\mu}_i^2}{D_{ii}} + \frac{\dot{\Sigma}_{ii}^2}{4\Sigma_{ii}D_{ii}}\right)
\end{aligned} \tag{III.76}$$

$$\dot{S} \quad = \quad \sum_i \dot{S}_i = \frac{1}{2}\sum_i \frac{\dot{\Sigma}_{ii}}{\Sigma_{ii}}. \tag{III.77}$$

By rearranging Equations (III.76) and (III.77) to form Γ^2, we have

$$\Gamma_i^2 = \frac{D_{ii}}{\Sigma_{ii}}\Pi_i + \dot{S}_i^2. \tag{III.78}$$

which leads to our result. ■

From Equation (III.74), we can see that Equation (III.78) is just a special case of Relation III.3 where the system has only one random variable. In addition, Equation (III.74) tells us that the geodesic (length-minimising curve between the initial and final PDF) of $\mathcal{L}(t)$ can be computed utilising the entropy rate and entropy production values (for further details on the geodesic problem, see [64]). More importantly, since Relation III.3 permits us to equate the effects of IL geodesic dynamics on the system stochastic thermodynamics, **Equation (III.74) can be used as part of a cost function employed to design controls that lead to system closed-loop responses with high energetic efficiency and minimum information variability**. This statement will be explored with more detail in Chapter V.

Considering a fully decoupled nonlinear stochastic system and using the Laplace assumption (Proposition II.9), the value of the information rate Γ^2 is related to the entropy production Π and the entropy flow $\dot{S}$ as follows

$$\Gamma^2 = \sum_{i=1}^{n} \frac{D_{ii}}{\Sigma_{ii}} \Pi_i + \sum_{i=1}^{n} \dot{S}_i^2 + \frac{1}{2} \sum_{i=1}^{n} H_{f_i}(\dot{\mu}_i + f_i(\mu_i, u)), \tag{III.79}$$

where Π_i and $\dot{S}_i$ are the entropy production and entropy rate from the marginal PDF $p(x_i, t)$ of x_i. $H_{f_1} = \frac{\partial^2}{\partial x_i^2} f_i(\mu_i, t)$. Clearly, if f_i describes a harmonic potential (a linear system), then $H_{f_i} = 0$ and (III.79) leads to Relation III.3.

III.7.1 Case study: Harmonically bound particle

To study all the previously given relations in a practical setup, let us consider the motion of a Brownian particle immersed in a fluid (the Kramer process) modelled by the following second order stochastic differential equation

$$\begin{bmatrix} \dot{x}_1(t) \\ \dot{x}_2(t) \end{bmatrix} = \begin{bmatrix} 0 & 1 \\ -\omega^2 & -\gamma \end{bmatrix} \begin{bmatrix} x_1(t) \\ x_2(t) \end{bmatrix} + \begin{bmatrix} \xi_1(t) \\ \xi_2(t) \end{bmatrix}, \tag{III.80}$$

where the parameters ω and γ are related to the system's natural frequency and damping, respectively.

First, to explore Relation III.1, in Figure III.14 we plot the changes on entropy rate $\dot{S}$ computed by using equation (II.117) and compared them with the value of $\Pi - \Phi$ obtained from equations (II.104)-(II.105), confirming the expected relation $\dot{S} = \Pi - \Phi$. Second, to briefly verify that $\mathcal{E}_u \geq \Gamma^2$, we also show the difference between Γ^2 (using equation (III.22)) and $\mathcal{E}_u$ (from Relation III.1). Our simulations were done for fixed value of ω by varying the value of γ (Figure III.14(a)) and vice-versa (Figure III.14(b)).

As can be concluded from Figure III.14(a), for an undamped harmonic oscillator with $\gamma = 0$, the value of $\mathcal{E}_u - \Gamma^2$ tends to decrease with time, meaning that they become equal over time. Here, $\Gamma, \dot{S} > 0\ \forall t \geq 0$ because the system is permanently oscillating. Once we increase γ, the system goes to the equilibrium giving $\Gamma, \dot{S} \to 0$ and $\mathcal{E}_u \geq 0$ due to $\Pi = \Phi$. In general, for any $\mathbf{A}$ and $u(t) = 0$, entropy production Π and entropy flow Φ in the long-time limit take the following values

$$\begin{aligned} \lim_{t\to\infty} \Pi(t) &= \operatorname{Tr}\left(\mathbf{A}^\top \mathbf{D}^{-1} \mathbf{A} \boldsymbol{\Sigma}(\infty) + \boldsymbol{\Sigma}^{-1}(\infty)\mathbf{D} + 2\mathbf{A}\right), \\ \lim_{t\to\infty} \Phi(t) &= \operatorname{Tr}\left(\mathbf{A}^\top \mathbf{D}^{-1} \mathbf{A} \boldsymbol{\Sigma}(\infty) + \mathbf{A}\right), \end{aligned} \tag{III.81}$$

where $\boldsymbol{\Sigma}(\infty) = 2\lim_{t\to\infty}\{\int_0^t e^{\mathbf{A}(t-\tau)}\mathbf{D}e^{\mathbf{A}^\top(t-\tau)}\,\mathrm{d}\tau\}$. The time-evolution and longtime limit behaviour of entropy production and entropy flow are determined by the value of $e^{\mathbf{A}t}$, which in turn (obviously) depends on the eigenvalues of the matrix $\mathbf{A}$. As it will be discussed in Chapter V, such eigenvalues can be modified through a control algorithm (for example, using a full-state feedback control method [80]). In system (III.80),

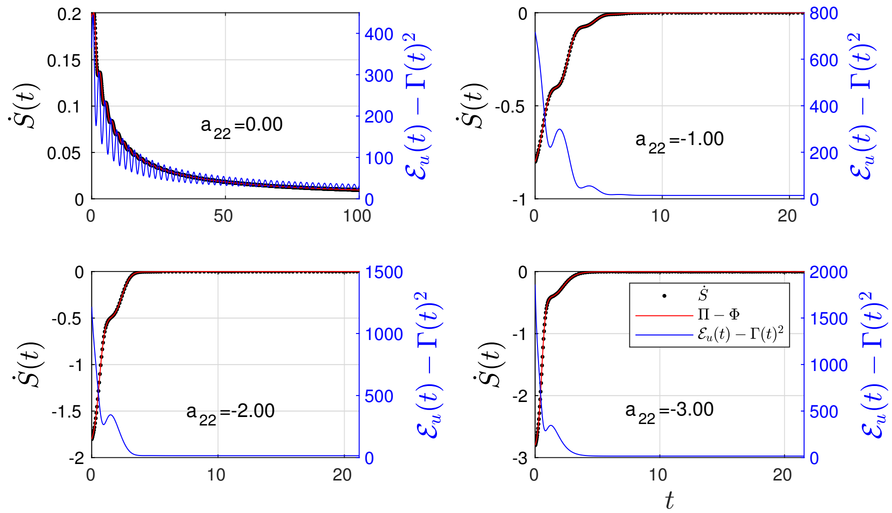

(a) $\omega^2 = 2, \gamma = \{0, 1, 2, 3\}$.

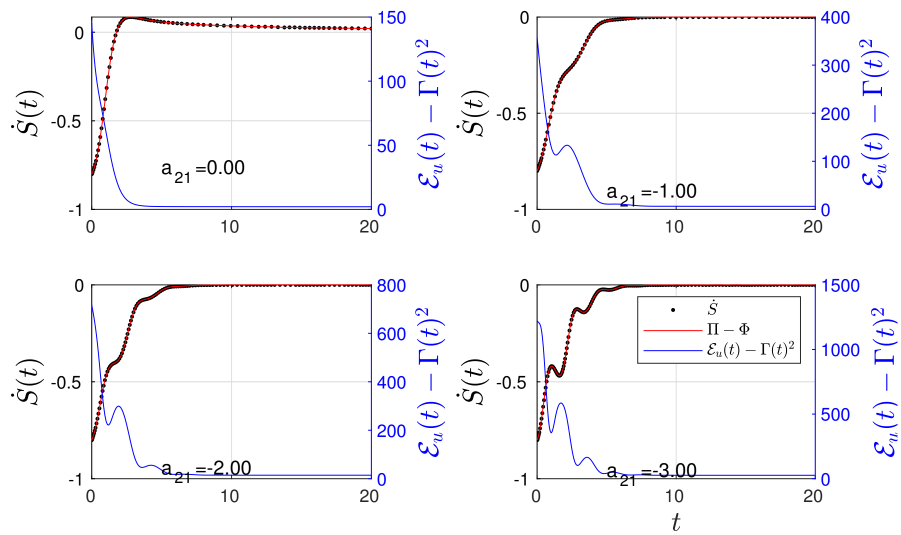

(b) $\omega^2 = \{0, 1, 2, 3\}, \gamma = 1$.

Figure III.14: Computational experiment of (III.80) using $D_{11} = D_{22} = 0.01$, $x(0) = 1$, $y(0) = 1$, $\Sigma_{11}^0 = \Sigma_{22}^0 = 0.1$ and $\Sigma_{12}^0 = \Sigma_{21}^0 = 0$. Figure III.14(a) contains simulations were ω is fixed and we vary γ. Figure III.14(b) contains simulations were γ is fixed and we vary ω. The plots show the comparison between changes on entropy rate $\dot{S}$ computed by using equation (II.117) and the value of $\Pi - \Phi$ obtained from equations (II.104)-(II.105). Additionally, they show the difference between Γ^2 (using equation (III.22)) and $\mathcal{E}_u$ (from Relation III.1).

the bigger the value of γ the quicker we arrive to equilibrium. On the other hand, increasing the value of ω with $\gamma > 0$ increments the oscillations on the transitory response (see Figures III.14(a) and III.14(b)) [7; 6].

III.7.2 Three-dimensional decoupled process

We now consider fully decoupled linear stochastic systems (i.e. where $\mathbf{A}$ is a diagonal matrix). A practical example of a three-dimensional linear decoupled process corresponds to the simplified version of the mathematical description of an optical trap shown in Figure III.15. The model consists of a set of three independent overdamped Langevin equations [81] given by equation (III.82). Here, x and y represent the position of the particle in the plane perpendicular to the beam propagation direction and z represents the position of the particle along the propagation direction. The stiffnesses of the trap in each of these directions are κ_x, κ_y and κ_z, respectively. γ is the particle friction coefficient. ξ_1, ξ_2 and ξ_3 are independent delta-correlated noises, i.e. $\langle \xi_i(t) \rangle = 0$, $\langle \xi_i(t)\xi_i(t') \rangle = 2D_{ii}\delta(t-t')$ and $\langle \xi_i(t)\xi_j(t') \rangle = 0 \quad \forall i \neq j$ with $i = 1, 2, 3$.

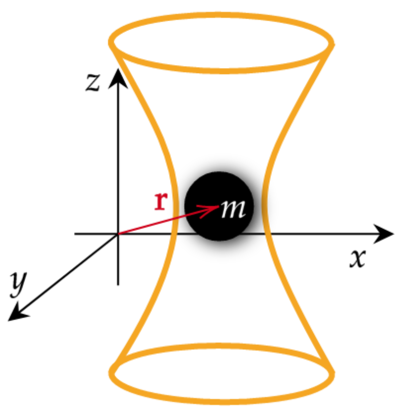

Figure III.15: Particle of mass m in a three dimensional optical trap.

$$\begin{bmatrix} \dot{x}(t) \\ \dot{y}(t) \\ \dot{z}(t) \end{bmatrix} = \begin{bmatrix} -\frac{\kappa_x}{\gamma} & 0 & 0 \\ 0 & -\frac{\kappa_y}{\gamma} & 0 \\ 0 & 0 & -\frac{\kappa_z}{\gamma} \end{bmatrix} \begin{bmatrix} x(t) \\ y(t) \\ z(t) \end{bmatrix} + \begin{bmatrix} \xi_1(t) \\ \xi_2(t) \\ \xi_3(t) \end{bmatrix}. \tag{III.82}$$

Since (III.82) is a fully decoupled linear stochastic model, it permits us to show the applicability of Relation III.3. To this end, in the left plot of Figure III.16, we show $\dot{S}$, $\Pi - \Phi$, and Γ computed from equations (II.117), (II.104) minus (II.105), and (III.22), respectively. In Figure III.16 we can see that both entropy rate $\dot{S} \to 0$ and information rate $\Gamma \to 0$ as the system goes to equilibrium. The right plot of Figure III.16, a plot depicting the value of the information rate upper bound $\mathcal{E}_u$ (Relation III.1) minus Γ^2 showing $\mathcal{E}_u \to 0$ at equilibrium. The exact value of $\mathcal{E}_u(t)$ in equilibrium is

$$\lim_{t\to\infty} \mathcal{E}_u = \mathrm{Tr}(\mathbf{\Sigma}^{-1}(\infty))\Pi(\infty)\,\mathrm{Tr}(\mathbf{D}) - 2g(\mathbf{H}(\infty)) = 0, \tag{III.83}$$

where

$$\mathbf{\Sigma}^{-1}(\infty) = -\mathbf{D}^{-1}\mathbf{A}, \quad \Pi(\infty) = 0. \quad \mathbf{H}(\infty) = 0. \tag{III.84}$$

Equation (III.84) applies only to systems with diagonal $\mathbf{A}$. Since $\Pi \to 0$, any decoupled linear system is reversible at equilibrium.

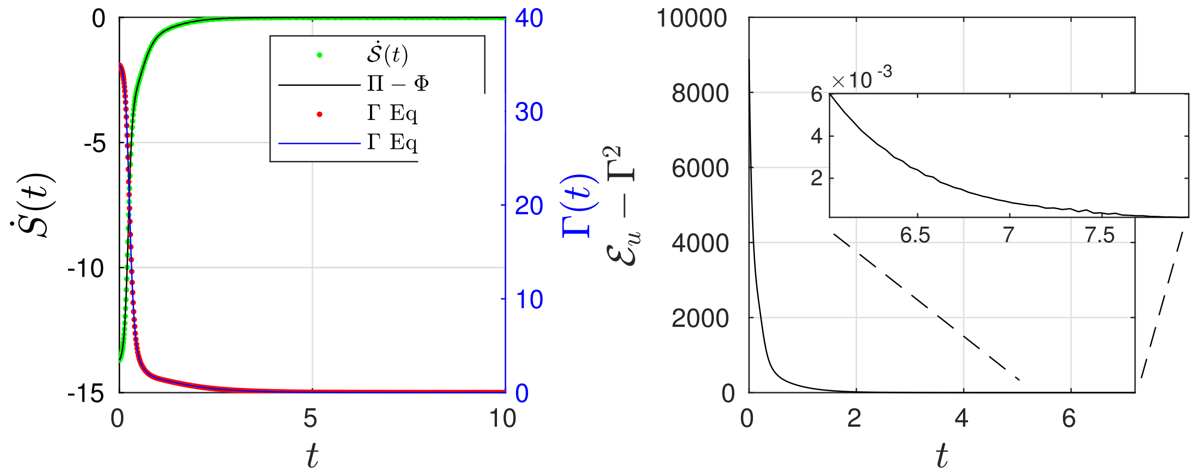

Figure III.16: Computational experiment of a three-dimensional optical trap using $\kappa_x = 10, \kappa_y = 3, \kappa_z = 1, \gamma = 1$, $D_{11} = D_{22} = D_{33} = 0.01$, $x(0) = 1$, $y(0) = 0.1$, $z(0) = 0.5$, $\Sigma^0_{11} = \Sigma^0_{22} = \Sigma^0_{33} = 0.1$ and $\Sigma^0_{ij} = 0 \forall i \neq j$.

III.7.3 *Higher order systems and the upper bounds of information rate* Γ

Relations III.1 to III.3 become highly relevant when the order of the stochastic models increase, for instance, when using toy models in control engineering scenarios [82]. In this section, we take the case when $\mathbf{A}$ is a randomly chosen Hurwitz matrix whose size varies from $2 - 50$, i.e. we choose linear stochastic systems that contain from 2 to 50 random variables.

Figure III.17 shows the phase portrait of $\Gamma(t_f)^2$ vs $\dot{S}(t_f)$, and the phase portrait of $\mathcal{E}_u(t_f) - \Gamma(t_f)^2$ vs $\Pi(t_f)$. Figure III.17 is also separated in sub-figures III.17(a) and III.17(b) showing the cases when matrix $\mathbf{A}$ is diagonal and non diagonal, respectively. Note, t_f refers to the time close enough the system's equilibrium; in our simulations $t_f = 300$. The phase portraits contain numbers to indicate the value at $t = t_f$; the number also indicates the order of the stochastic system.

Regarding the portraits of $\Gamma(t_f)^2$ vs $\dot{S}(t_f)$, for every Hurwitz $\mathbf{A}$ (i.e. diagonal and non diagonal matrix with negative real part eigenvalues) $\lim_{t\to\infty} \mathcal{E}(t) = \lim_{t\to\infty} \dot{S}(t) = 0$ as expected. Meanwhile, for the same processes $\Pi > 0$ at equilibrium (see equation (III.81)). When looking at the phase portraits of $\mathcal{E}_u(t_f) - \Gamma(t_f)^2$ vs $\Pi(t_f)$, we see that $\mathcal{E}_u(t_f) > 0$ when $\mathbf{A}$ is non diagonal due to $\Pi(t_f) > 0$ for some t (see Figure III.17(a)). On the other hand, as demonstrated in Equations (III.83) and (III.84) $\mathcal{E}_u(t_f) = \Pi(t_f) = 0$. Again, meaning that every fully decoupled linear system is reversible at equilibrium.

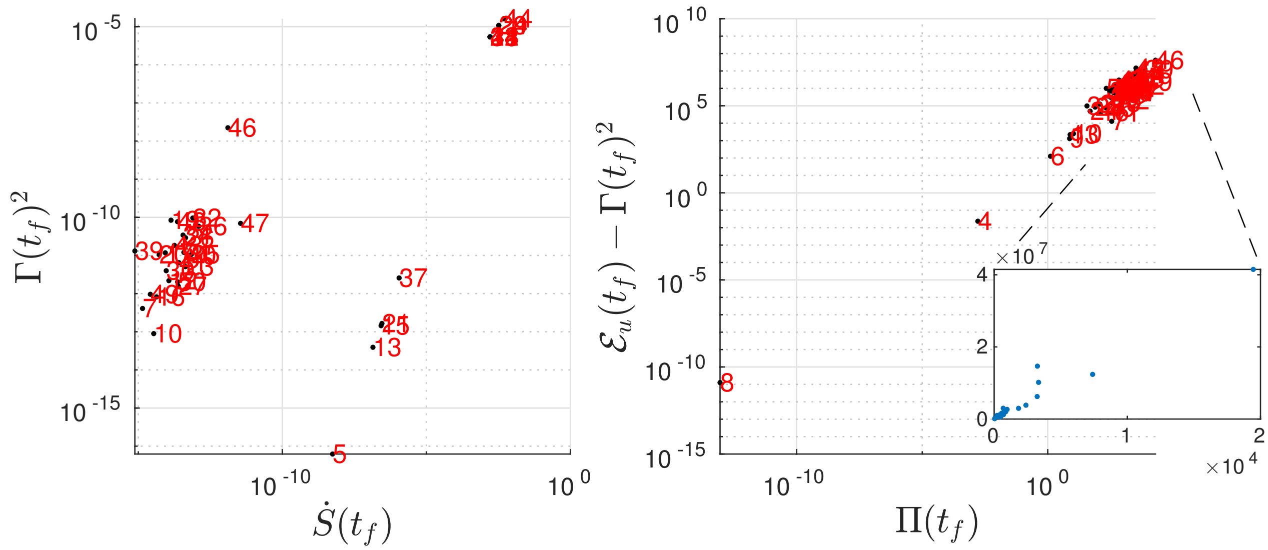

(a) **A** is non diagonal.

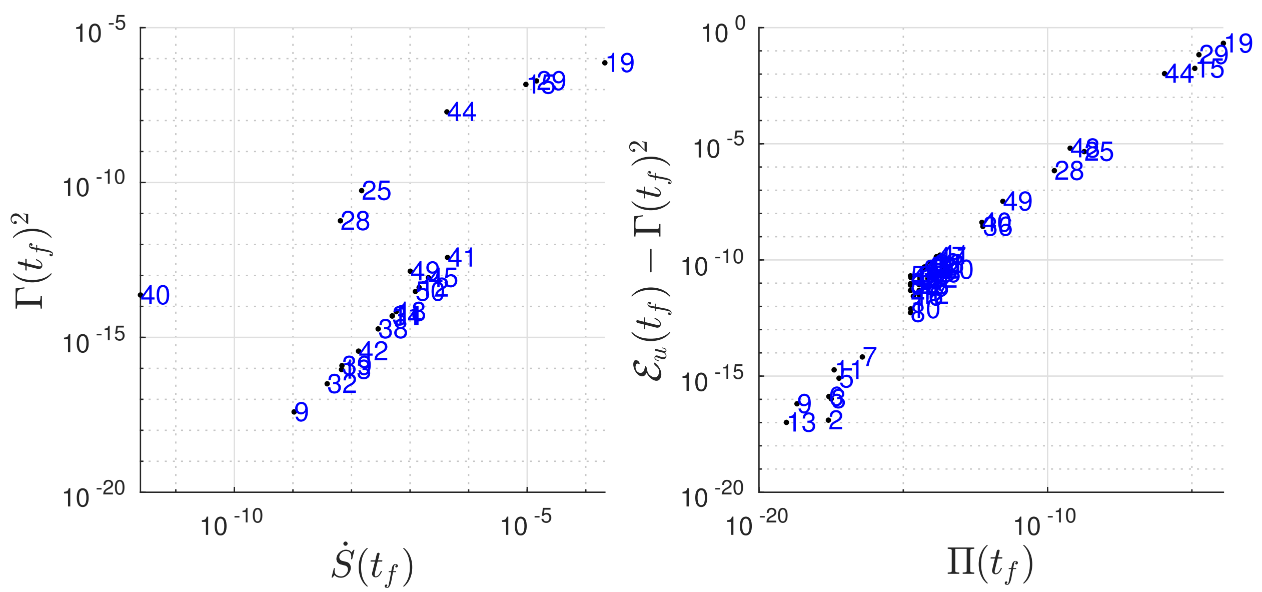

(b) **A** is diagonal.

Figure III.17: Entropy rate $\dot{S}(t_f)$ vs the square of information rate $\Gamma(t_f)^2$ and the values of $\mathcal{E}_u(t_f) - \Gamma(t_f)^2$ vs $\Pi(t_f)$. The simulations use randomly chosen stable linear systems from order $n = 2$ to $n = 50$. The red numbers indicate the order of the system and its position the value at $t_f = 300$.

Chapter concluding remarks

Throughout this chapter, we have presented theoretical results for the computation of the information length in n-th order Gaussian stochastic processes, which can be applied to a variety of practical problems. Specifically, the information length was found as a function of the mean and covariance dynamics. We showed a case study of a harmonically bound particle system with the natural oscillation frequency ω, subject to a damping γ and a Gaussian white-noise (Kramer equation). Such case study demonstrates the information length dependency on ω and γ, elucidating that the information length tends to take its minimum value near the critical damping $\gamma = 2\omega$. The latter can be viewed as the simplification of dynamics and thus the decrease in information change due to the reduction of the two characteristic time scales associated with ω and γ to the one value. The information length in the long time limit $\mathcal{L}(t \to \infty)$ was shown to preserve the linear geometry associated with the Gaussian statistics in a linear stochastic process, as in the case of the O-U process (III.13). Next, using the stochastic equation of a simple pendulum, we demonstrate that IL can be computed in non-linear Langevin equations through the Laplace assumption.

In addition, we have derived relations between information rate and thermodynamic quantities for stochastic Gaussian processes. The proposed results permit us to create cost functions that lead to energetically efficient (minimum entropy production) and organised (with minimum information variability) behaviours. In this context, in Chapter V, we explore connections between the area of control theory for applications in linear and non linear Langevin equations. We utilise modern control techniques such as the model-predictive-control [83] to find the solution to proposed optimisation problems in terms of the information rate. Future work would explore benefits in the research areas of population dynamics [84] or inference control [85; 86].

IV

Abrupt events detection

Chapter summary

Detecting and measuring abrupt changes in a process is a capability that can provide us with important information for decision-making, especially, in systems management. In this chapter, we investigate the prediction capability of information theory by focusing on how sensitive information-geometric theory (information length diagnostics) and entropy-based information theoretical method (information flow) are to abrupt changes. To this end, we use a non-autonomous Kramer equation by including a sudden perturbation to the system to imitate the onset of a sudden event. This case study enables us to calculate time-dependent probability density functions (PDFs) and various statistical quantities with the help of numerical simulations. The results show that information length diagnostics predict the onset of a proposed ongoing perturbation that models a sudden event better than the information flow. In addition, the case study explicitly shows that the information flow like any other entropy-based measure has limitations in measuring perturbations which do not affect entropy.

Then, as a method for detecting abrupt events, we propose the application of different correlation coefficients such as mutual information, Pearson coefficient and novel coefficients based on the information rate and entropy production of the stochastic process. The analysis of the correlation coefficients includes their application to different case studies which consider linear stochastic processes only. The results demonstrate that information rate and entropy production coefficients can detect abrupt events in the first and second moments of the stochastic dynamics. In a high-order scenario, we also include the application of the norm of the information/thermodynamic quantities, showing that such quantity permits us to approximately quantify the correlation between all the random variables in the system.

This chapter is based on the following author's publications: [7; 6; 11]

keywords: information geometry; information length; information flow; prediction; entropy

IV.1 Introduction

Even if occurring very infrequently, rare or extreme events can mediate large transport with significant impact. Examples would include the sudden outbreak of devastating infectious diseases, solar flares, extreme weather conditions, flood, forest fire, sudden stock market crash, flow sensor failure, bursty gene expression and protein productions. The resulting large transports can be either beneficial (e.g., promoting mixing and air circulations by atmospheric jets or removing toxins) or harmful. For instances, tornadoes cause a lot of damage; in magnetic fusion, plasma confinement is hampered by intermittent transport of particles and energy from hot plasma core to the colder plasma boundaries.

Given the damage that these events can cause, finding good statistical methods to predict their sudden onset, or abrupt changes in the system dynamics is a critical issue. For instance, there are different types of plasma disruptions in fusion plasmas [87] and the current guidance for the minimum required warning time for successful disruption mitigation on ITER is about 30 ms [88]. Increasing the warning time by the early detection of a sudden event will greatly help ensuring a sufficient time for a control strategy to minimise harmful effects.

Obviously, the whole mark of the onset of a sudden event is an abrupt dynamical change in the system or data over time—time-variability/large fluctuation, whose proper description requires non-stationary statistical measures such as time-dependent probability density functions (PDFs). By using time-dependent PDFs, we can quantify how the "information" unfolds in time through information geometry. As mentioned in the chapter's summary, here we examine the capability of the information-geometric theory proposed in a series of recent works [69; 89; 64; 66; 90; 70] in predicting the onset of a sudden event and compare it with one of the entropy-based information theoretical measures [91; 92; 93]. Let us recall that the information length [69; 89] measures the evolution of a system in terms of a dimensionless distance which represents the total number of different statistical states that are accessed by the system (see Chapter III). The larger time-variability, the more abrupt change in the information length; in a statistically stationary state, the information length does not change in time. For instance, the work [94] has demonstrated the capability of the information length in the early prediction of transitions in fusion plasmas.

Again, in this chapter, we mimic the onset of a sudden event by including a sudden perturbation to the system and calculate time-dependent PDFs and various statistical quantities including information length and one of the entropy-based information-theoretical measure (information flow) [95; 96]. The latter measures the directional information flow between two variables. This is more sensitive than mutual information which measures the correlation between the variables. The point we want to make is that this information flow like any other entropy-based measures depends solely on entropy, and thus it cannot pick up the onset of a sudden event which does not affect entropy, for instance, such as the mean value (recall, the entropy is independent of the local arrangement of the probability [97] as well as the mean value).

We should note that there are many other information theoretical measures [91; 92; 93; 98; 99; 96; 100; 101; 102; 103; 104; 105; 97; 45] that have been used to understand different aspects of complexity, emergent behaviours, etc in non-equilibrium systems. However, the main purpose of this chapter is not to provide an exhaustive exploration of these methods, but to point out the possible limitation of the entropy-based information measurements in predicting sudden events. Additionally, our intention is not on modelling the appearance of rare, extreme events (that are nonlinear, non-Gaussian) themselves, but on testing the predictability of information theoretical measures on the onset of such sudden events.

To gain a key insight about this chapter's discussion, consider an analytically solvable model such as —the non-autonomous Kramers equation (for the two variables, x_1 and x_2) [106]—which enables us to derive exact PDFs and analytical expressions for various statistical measures including entropy, information length and information flows. In this model the non-autonomy is introduced by an impulse which is included either in the strength of stochastic noise or by an external impulse input which models a sudden perturbation to the system. Examples of the abrupt event scenarios that we will explore in this Chapter are shown in Figure IV.1. The plots show blue dots representing a single trajectory $\boldsymbol{\mathcal{X}}$ of the Kramers equation sampled from $\mathcal{N}(\boldsymbol{\mu}, \boldsymbol{\Sigma})$ with a solid black line representing the phase portrait of the average value over time $\boldsymbol{\mu}(t) = \langle \mathbf{x}(t) \rangle$. Here. the values for $\boldsymbol{\mu}$ and $\boldsymbol{\Sigma}$ at evert instant of time t are computed by solving Equations (II.77)-(II.78). Panel (a) shows the phase portrait of x_1 and x_2 without any impulse. Panel (b) shows the case where an impulse causes the perturbation in the covariance matrix $\boldsymbol{\Sigma}$ while panel (c) is the case where the sudden perturbations affect both covariance matrix $\boldsymbol{\Sigma}$ and the mean value $\boldsymbol{\mu}$. The proposed impulse-like function used in these simulations is introduced in Section IV.3.

Now, we present the different case studies to abrupt event analysis including the corresponding applied tools. First, we consider the Non-autonomous Kramers equation. Then, the inclusion of correlation coefficients in the analysis of the same process. Finally, the study of abrupt events in a controllable canonical form via the norm of the entropy production, entropy rate and entropy production.

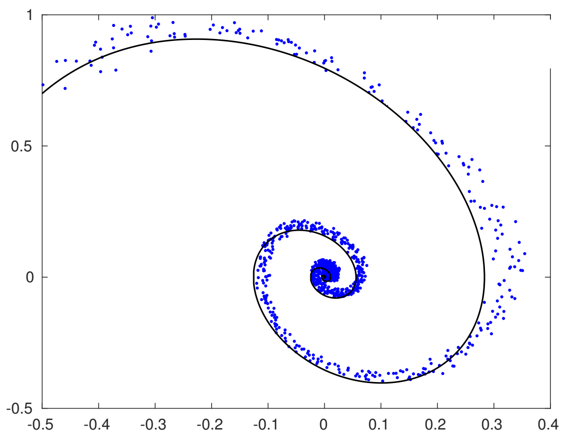

(a) Process without abrupt events.

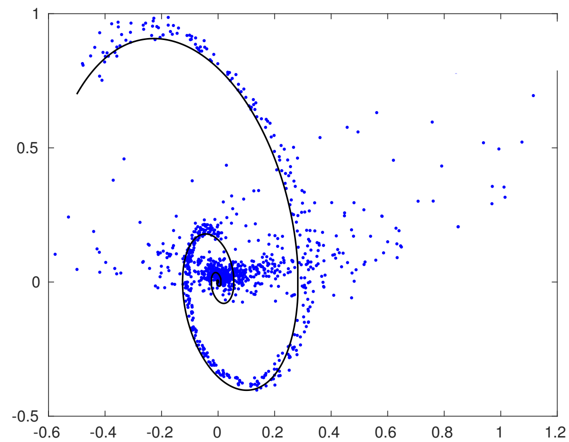

(b) Process with an abrupt change in $\mathbf{\Sigma}(t)$.

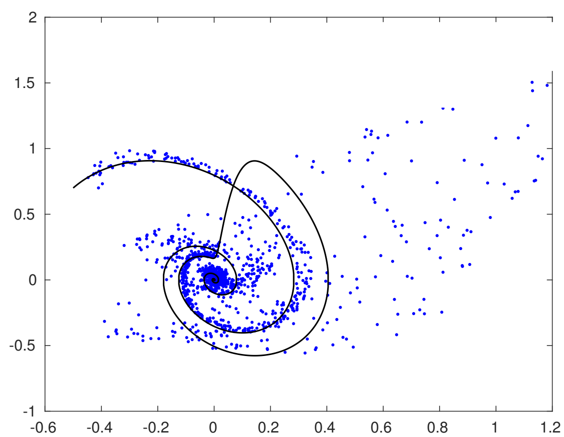

(c) Process with abrupt changes in $\boldsymbol{\mu}$ and $\mathbf{\Sigma}(t)$.

Figure IV.1: Stochastic simulation of a process with and without abrupt changes that are discussed in this work. The parameters of the simulation are $\gamma = 1, \omega = 1, D = 0.001$, $\boldsymbol{\mu}(0) = [-0.5, 0.7]^\top$ and $\mathbf{\Sigma} = 0.01\mathbf{I}_2$, where $\mathbf{I}$ is the identity matrix of order two. The blue dots represent a single trajectory $\boldsymbol{\mathcal{X}}$ of the Kramers equation sampled from $\mathcal{N}(\boldsymbol{\mu}, \mathbf{\Sigma})$ while the solid black line is the phase portrait of the average value over time $\boldsymbol{\mu}(t)$. The values for $\boldsymbol{\mu}$ and $\mathbf{\Sigma}$ at evert instant of time t are computed by solving Equations (II.77)-(II.78). The impulse-like function used in these simulations to represent a perturbation (abrupt event) is introduced in Section IV.3.

IV.2 *Preliminaries to the case study: Non-autonomous Kramers Equation*

As our goal is to compare the information length $\mathcal{L}$ metric (already defined in Chapter III) against the so-called information flow, let us first define the information flow of a two-random variable process.

IV.2.1 Information Flow (IF)

Information flow (IF), or also usually called information transfer, is one of the useful information-theory measure that has been studied for causality (causation), uncertainty propagation and predictability transfer [103; 102]. It also give us insight into the degree of interconnection among states of the system [95; 96]. [95] considered a system of two Brownian particles with coordinates $\mathbf{x} = (x_1, x_2)$ interacting with two independent thermal baths at temperatures T_1 and T_2, respectively, subject to a potential $H(\mathbf{x})$, which are described by the Langevin equations

$$\begin{aligned} 0 &= -\partial_{x_i} H(\mathbf{x}) - \Gamma_i \dot{x}_i(t) + u_i(t) + \eta_i(t), \\ \langle \eta_i(t)\eta_j(t_1)\rangle &= 2\Gamma_i T_i \delta_{ij}\delta(t - t_1), \quad i, j = 1, 2, \end{aligned} \tag{IV.1}$$

where Γ_i are the damping constants, which characterise the coupling of the particles to their baths/environments (with the temperature T_i), δ_{ij} is the Kronecker symbol and $u_i(t)$ is a bounded input. In this scenario, [95] defines the information flow as follows.

Definition IV.1: Information flow

The information flows T from $x_2 \to x_1$ and $x_1 \to x_2$ are then given by (see [95]):

$$T_{2\to 1} = \frac{1}{\Gamma_1}\int d\mathbf{x} P(\mathbf{x};t)\left[\partial_{x_1} H(\mathbf{x}) + T_1 \partial_{x_1} \ln P(\mathbf{x};t)\right] \partial_{x_1} \ln \frac{P_1(x_1;t)}{P(\mathbf{x};t)}, \tag{IV.2}$$

$$T_{1\to 2} = \frac{1}{\Gamma_2}\int d\mathbf{x} P(\mathbf{x};t)\left[\partial_{x_2} H(\mathbf{x}) + T_2 \partial_{x_2} \ln P(\mathbf{x};t)\right] \partial_{x_2} \ln \frac{P_2(x_2;t)}{P(\mathbf{x};t)}. \tag{IV.3}$$

To appreciate the physical meaning of IF, it is useful to recall that Equations (IV.2) and (IV.3)) can also be expressed in terms of entropy S or mutual information I (see Equations (17) and (23) in [95]), for instance, as follows:

$$T_{2\to 1} = \partial_t S[x_1(t)] - \partial_{t_1} S[x_1(t+t_1)|x_2(t)] \Big|_{t_1 \to 0}, \tag{IV.4}$$

where $S[x_1(t+t_1)|x_2(t)]$ denotes the entropy of $x_1(t+t_1)$ at time $t+t_1$ conditioned by $x_2(t)$ at the earlier time t. From (IV.4), we can see that IF represents the rate of change in the marginal entropy of x_1 minus that of the conditional entropy of x_1, x_2 being frozen between the time $(t, t+t_1)$. In other words, $T_{2\to 1}$ is that part of the entropy change of x_1 (between t and $t+t_1$), which exists due to fluctuations of x_2 [95].

Several important remarks are in order. First, IF $T_{2\to 1}$ and $T_{1\to 2}$ can be both negative and positive; a negative $T_{2\to 1}$ means that x_2 acts to reduce the marginal entropy of x_1 (S_1). This is different from the case of transfer entropy which is non-negative [107]. Second, the causality is inferred only from the absolute value of IF [103]. Third, the advantage of Equation (IV.2) over Equation (IV.4) would be that Equation (IV.2) can be calculated using the equal-time joint/marginal PDFs without needing two-point time PDFs, which will be especially useful in the analysis of actual (experimental or observational) data. Finally, although it is not immediately clear from either Equations. (IV.3) or (IV.4), we will show in §IV.3 that IF depends only on the (equal-time) covariance matrix. This is similar to other causality measures such as the classical Granger causality [108] and transfer entropy [107] which quantify the improvement of the predictability of one variable by the knowledge of the value of another variable in the past and at present. This means these entropy-based measures do not pick up the onset of a sudden event which does not affect the covariance matrix (variance), for instance, such as the mean value.

IV.2.2 *A tool to define the correlation in terms of the information rate*

In this case study, we will also apply a simple measure of correlation given by (see §IV.4.3)

$$\Gamma^2(t) - \Gamma_m^2(t), \tag{IV.5}$$

where $\Gamma(t)$ is the known information rate value (see Chapter III) and $\Gamma_m(t)$ is defined as follows

Definition IV.2: Γ_m^2 from marginal PDFs

For a n-variate linear process (II.68) with n random variables $\mathbf{x} \in \mathbb{R}^n = [x_1, x_2, \ldots, x_n]^T$, it is useful to introduce $\Gamma_m^2(t)$ as follows

$$\Gamma_m(t) = \sum_{i=1}^{n} \Gamma_i^2(t) = \sum_{i=1}^{n} \frac{(\partial_t \langle x_i \rangle)^2}{\Sigma_{x_i x_i}} + \sum_{i=1}^{n} \frac{(\partial_t \Sigma_{x_i x_i})^2}{2\Sigma_{x_i x_i}^2}, \tag{IV.6}$$

where, we recall that Γ_i^2 is calculated from a marginal PDF $p(x_i; t)$ of x_i. Note that Γ^2 in Equation (III.22) is identical to Γ_m^2 in Equation (IV.6) when the n random variables are independent (See Corollary III.1).

The interpretation of Equation (IV.5) is given in Section IV.4.3 through the numerical simulation of the Kramers equation.

IV.3 *Case study: Non-Autonomous Kramers Equation*

To demonstrate how IF and IL can be used in the prediction of abrupt changes in system dynamics, we focus on the non-autonomous Kramers equation, as noted in §IV.1. Recall that the original (autonomous) Kramers equation (see Equation (III.36)) describes the Brownian motion in a potential, for instance, as a model for reaction kinetics [30]. By including a time-dependent external input $u(t)$, we generalise this to the following non-autonomous model for the two stochastic variables $\mathbf{x} = [x_1, x_2]^T$

$$\dot{\mathbf{x}}(t) = \left[\begin{pmatrix} 0 & 1 \\ -\omega^2 & -\gamma \end{matrix}\right] \mathbf{x}(t) + \begin{bmatrix} 0 \\ 1 \end{bmatrix} u(t) + \begin{bmatrix} 0 \\ \xi(t) \end{bmatrix} \Bigg(\tag{IV.7}$$

Here, ξ is a short correlated Gaussian noise with a zero mean $\langle \xi \rangle = 0$ and the strength D with the following property

$$\langle \xi(t) \xi(t') \rangle = 2D(t)\delta(t - t'). \tag{IV.8}$$

In this case study, we consider a time-dependent $D(t)$ to incorporate a perturbation in D as follows

$$D(t) = D_0 + \frac{b}{|a|\sqrt{\pi}} e^{-\left(\frac{t - t_{1,0}}{a}\right)^2}. \tag{IV.9}$$

Here, the second term on RHS is an impulse function which takes a high value for a short time interval a around $t = t_{1,0}$ $b = \{0, 1\}$ is used to cover the two cases without and with the impulse. Hence, (IV.9) represents an ongoing perturbation with a peak around $t = t_{1,0}$[1].

[1] Note that there are other good candidates to represent "perturbations" such as a double step function. Yet, we have chosen (IV.9) due to its practicality when computing analytical results (see Appendix AIV). In addition, (IV.9) is often used as an approximation of the delta Dirac function δ (for instance, see [109]) which is also another good candidate to represent a sudden event.

Furthermore, we are interested in the case where $u(t)$ is as well an impulse like function given by

$$u(t) = \frac{d}{|c|\sqrt{\pi}} e^{-\left(\frac{t-t_{2,0}}{c}\right)^2}. \tag{IV.10}$$

Here, the impulse is localised around $t = t_{2,0}$ with the width c; again $d = \{0, 1\}$ is used to cover the two cases without and with the impulse. To find IL and IF for system (IV.7), we use Proposition II.6 and calculate the expressions for

$$\mathbf{\Sigma}(t) = \begin{bmatrix} \Sigma_{11} & \Sigma_{12} \\ \Sigma_{21} & \Sigma_{22} \end{bmatrix} \text{ and } \boldsymbol{\mu}(t) = [\langle x_1(t) \rangle, \langle x_2(t) \rangle]^T, \tag{IV.11}$$

using Equations (IV.9)–(IV.10), as shown in Appendix AIV.1.

Equation (IV.11) then determines the form of the joint PDF $p(\mathbf{x}; t)$ in Equation (II.70) for the two variables $i = 1, 2$. On the other hand, the marginal PDFs of x_1 and x_2 for Equation (IV.7) are given by

$$P_1(x_1; t) = \frac{1}{\sqrt{2\pi\Sigma_{11}}} e^{-\frac{(x-\langle x \rangle)^2}{2\Sigma_{11}}}, \quad P_2(x_2; t) = \frac{1}{\sqrt{2\pi\Sigma_{22}}} e^{-\frac{(x_2-\langle x_2 \rangle)^2}{2\Sigma_{22}}}. \tag{IV.12}$$

From these PDFs, we can easily obtain the entropy based on the joint and marginal PDFs, respectively, as follows

$$S(t) = -\int d\mathbf{x} p(\mathbf{x}; t) \ln p(\mathbf{x}; t) = \frac{1}{2}\left[1 + \ln\left((2\pi)^2 |\Sigma|\right)\right], \tag{IV.13}$$

$$S_1(t) = -\int dx_1 p(x_1; t) \ln p(x_1; t) = \frac{1}{2}\left[1 + \ln(2\pi\Sigma_{11})\right], \tag{IV.14}$$

$$S_2(t) = -\int dx_2 p(x_2; t) \ln p(x_2; t) = \frac{1}{2}\left[1 + \ln(2\pi\Sigma_{22})\right]. \tag{IV.15}$$

IV.3.1 Information Length for Equation (IV.7)

We now use Proposition II.6 (Equation (II.70) for (IV.7)) and Theorem III.1. Since the covariance matrix Σ as well as the mean values $\boldsymbol{\mu}(t)$ (see Appendix AIV.1) for the joint PDF involve many terms including special (error) functions, it requires a long algebra and numerical simulations (integrations) to calculate Equations (III.21) and (III.22), respectively. The following thus summarise the main steps only. First, we can show that $\Gamma^2(t)$ for the linear non-autonomous stochastic process (II.68) can be rewritten as

$$\Gamma^2(t) = \boldsymbol{\mu}^T \mathbf{A}^T \mathbf{\Sigma}^{-1} \mathbf{A} \boldsymbol{\mu} + u \mathbf{B}^T \mathbf{\Sigma}^{-1} \mathbf{B} u + \boldsymbol{\mu}^T \mathbf{A}^T \mathbf{\Sigma}^{-1} \mathbf{B} u + u \mathbf{B}^T \mathbf{\Sigma}^{-1} \mathbf{A} \boldsymbol{\mu} + \frac{1}{2} \operatorname{Tr}\left(\left(\mathbf{\Sigma}^{-1} \partial_{t_1} \mathbf{\Sigma}\right)^2\right) \tag{IV.16}$$

We can then show that for Equation (IV.7), Equation (IV.16) becomes

$$\begin{aligned} \Gamma^2(t) = & \frac{1}{|\mathbf{\Sigma}|}\left(\langle x_2 \rangle^2 \Sigma_{22} + \left(\gamma \langle x_2 \rangle + \omega^2 \langle x_1 \rangle + u\right)\left(2 \langle x_2 \rangle \Sigma_{12} + \Sigma_{11}\left(\gamma \langle x_2 \rangle + \omega^2 \langle x_1 \rangle + u\right)\right)\right) \\ & + \frac{1}{|\mathbf{\Sigma}|^2}\left(2\Sigma_{12}^2\left((\partial_t \Sigma_{22})(\partial_t \Sigma_{11}) + (\partial_t \Sigma_{12})^2\right) + 2\Sigma_{11}(\partial_t \Sigma_{12})\left(\Sigma_{22}(\partial_t \Sigma_{12})\right.\right. \\ & \left.\left. -2\Sigma_{12}(\partial_t \Sigma_{22})\right) + \Sigma_{11}^2(\partial_t \Sigma_{22})^2 + 4\Sigma_{22}\Sigma_{12}(\partial_t \Sigma_{12})(\partial_t \Sigma_{11}) + \Sigma_{22}^2(\partial_t \Sigma_{11})^2\right) \end{aligned} \tag{IV.17}$$

By using $\langle x_1 \rangle, \langle x_2 \rangle, \Sigma_{11}, \Sigma_{12}$ and Σ_{22} given in Appendix AIV.1, we calculate (IV.17). Finally, to calculate IL in Equation (III.22), we perform the numerical integration of Γ over time for the chosen parameters and initial conditions. Results are presented in § IV.4.

IV.3.2 Information Flow for Equation (IV.7)

To find the information flow for Equation (IV.7), we compare it with Equation (IV.1)

$$\frac{\partial_{x_1} H(\mathbf{x})}{\Gamma_1} = -x_2(t), \quad \frac{\partial_{x_2} H(\mathbf{x})}{\Gamma_2} = \gamma x_2(t) + \omega^2 x_1(t) - u(t), \quad T_1 = 0, \frac{T_2}{\Gamma_2} = D(t). \tag{IV.18}$$

After some algebra using Equation (IV.18) in Equations (IV.2) and (IV.3), we can show (see Appendix AIV.2 for derivation)

$$T_{1\to 2} = -\omega^2 \frac{\Sigma_{12}}{\Sigma_{22}} - D\frac{\Sigma_{12}^2}{|\Sigma|\Sigma_{22}}, \tag{IV.19}$$

$$T_{2\to 1} = \frac{1}{2}\frac{d}{dt}\ln \Sigma_{11}. \tag{IV.20}$$

It is important to note that unlike (IV.17), Equations (IV.19) and (IV.20) depend only on the covariance matrix Σ, being independent of the mean values, as noted in §IV.1.

IV.4 Simulations of the case study

In this section, we present simulation results that show how IF and IL capture abrupt changes in the system dynamics of the Kramers equation. To this end, we designed four simulation experimental scenarios, which are summarised in Table IV.1. The different scenarios were chosen depending on whether $D(t)$ and $u(t)$ (defined in Equations (IV.9) and/or (IV.10), respectively) include(s) an impulse function (that is, whether $b = 0$ or 1 and $d = 0$ or 1), which caused the abrupt changes in the values of $\mathbf{\Sigma}(t)$ and $\boldsymbol{\mu}$, respectively. Specifically, Case 1 was without any impulse ($b = d = 0$); Cases 2 and 3 were when the impulse was included in D and $u(t)$ ($b = 1, d = 0$ and $b = 0, d = 1$), respectively; Case 4 was with both impulses ($b = d = 1$). As noted at the end of §IV.4, IL and IF in Equation (IV.17) and Equations (IV.19)-(IV.20) clearly reveal that IF was not affected by the change in the mean values. This means, IF took the same value in both Cases 1 and 3; it also took the same value in both Cases 2 and 4. This is highlighted in Table IV.1 by the purple colour.

For Cases 1–4 in Table IV.1, we fixed the value of ω to be $\omega = 1$ and varied γ to explore different scenarios of no damping $\gamma = 0$, underdamping $\gamma < 2\omega$, critically damping $\gamma = 2\omega$ and over damping $\gamma > 2\omega$. Furthermore, we fixed the values of the initial covariance matrix as follows

$$\mathbf{\Sigma}(0) = \begin{bmatrix} 0.01 & 0 \\ 0 & 0.01 \end{bmatrix} \Bigg(\tag{IV.21}$$

The initial mean values were fixed as $\boldsymbol{\mu}(0) = [-0.5, 0.7]^T$ for all Cases.

In addition, we performed the stochastic simulations for Cases 1–4 according to the Gaussian statistics $\mathbf{x} \sim \mathcal{N}(\mu, \Sigma)$, specified by the values of $\mathbf{\Sigma}$ and $\langle x_i \rangle$ $(i = 1, 2)$ given in Appendix AIV.1. Simulated random trajectories are shown in blue dots in the phase portrait of x_1 and x_2 in Figures IV.2-IV.7 of the following subsections.

IV.4.1 Information Flow Simulation Results

As noted in Section IV.2.1, we recall that IF is used to measure a directional information flow in terms of its entropy and that IF is either positive or negative unlike transfer entropy. In our experimental simulations, we were interested in how sensitive IF was to abrupt changes. The time-evolutions of IF $T_{1\to 2}$, $T_{2\to 1}$, joint $S(t)$

Table IV.1: A summary of the simulated scenarios of abrupt changes in $\mathbf{\Sigma}(t)$ and $\boldsymbol{\mu}(t)$ in the Kramers equation. Case 1 is without any impulse; Cases 2 and 3 are when the impulse is used for $D(t)$ and $u(t)$, respectively; Case 4 is with both impulses. We emphasise that IF is affected only by changes in $D(t)$ while IL is affected both by $D(t)$ and $u(t)$. For each case, we fix the value of ω as $\omega = 1$ and vary γ to explore different scenarios of no damping $\gamma = 0$, underdamping $\gamma < 2\omega$, critically damping $\gamma = 2\omega$ and over damping $\gamma > 2\omega$.

	Cases (IF, IL)			
Parameters	1	2	3	4
$D(t)$ $u(t)$	$D(t) = 0.001$ $u(t) = 0$	$D(t) = 0.001 + \frac{1}{\pi\lvert 0.1\rvert}\exp\left(-\frac{(t-4)^2}{(0.1)^2}\right)$ $u(t) = 0$	$D(t) = 0.001$ $u(t) = \frac{1}{\pi\lvert 0.1\rvert}\exp\left(-\frac{(t-4)^2}{(0.1)^2}\right)$	$D(t) = 0.001 + \frac{1}{\pi\lvert 0.1\rvert}\exp\left(-\frac{(t-4)^2}{(0.1)^2}\right)$ $u(t) = \frac{1}{\pi\lvert 0.1\rvert}\exp\left(-\frac{(t-4)^2}{(0.1)^2}\right)$
Changing γ while fixing ω	$\gamma = 0$ Undamped	$\gamma < 2\omega$ Underdamped	$\gamma = 2\omega$ Critically damped	$\gamma > 2\omega$ Overdamped

and marginal $S_1(t)$, $S_2(t)$ entropies in Equations (IV.13)-(IV.15), and the phase portrait of x_1 vs x_2 are shown in Figures IV.2 and IV.3. We used the same initial condition $\Sigma(0)$ given by Equation (IV.21) and $\omega = 1$ while varying the value of γ. As noted above, random trajectories from stochastic simulations were overplotted in blue dots in the phase portraits. Specifically, Figures IV.2 and IV.3 are for Case 1 and Case 2, respectively (with $b = 0$ and $b = 1$ in (IV.9), respectively). The exact value of $D(t)$ is shown in Table IV.1 and as a blue dotted line in all panels of Figures IV.2 and IV.3 (using the y-axis on the right of each panel).

Case 1—Constant $D(t)$ and $u(t) = 0$

We started with Case 1 which had no perturbation (constant $D(t) = D_0 = 0.001$ and $u(t) = 0$) and examined the effects of the system parameters γ on IF. First, with no damping $\gamma = 0$ (Figure IV.2a), S_1, S_2 and S all increased monotonically in time from a negative value (a less disordered state) to a positive value (more disordered state) due to the stochastic noise. On the other hand, $T_{1\to2}$ and $T_{2\to1}$ showed similar behaviours but with opposite sign, making $T_{2\to1} + T_{1\to2} \approx 0$. The opposite sign of $T_{1\to2}$ and $T_{2\to1}$ suggests that x_2 acted to increase the marginal entropy of x_1 (by transferring the stochasticity fed into x_2 by ξ) while x_1 decreased the marginal entropy of x_2 (by providing a restoring/inertial force causing the harmonic oscillations). The fact that $T_{2\to1} + T_{1\to2} \approx 0$ can be corroborated by the similarity between the marginal entropies S_1 and S_2.

Second, in the underdamped case with $0 < \gamma < 2\omega$ shown in Figure IV.2b, the phase portrait exhibited the behaviour of an underdamped harmonic oscillator. The role of the damping $\gamma \neq 0$ was to bring the system to an equilibrium in the long time limit where PDFs were stationary and S_1, S_2 and S took constant values

$$\lim_{t\to\infty} S_1(t) = \frac{1}{2}\ln\left(\frac{2D\pi}{\gamma\omega^2}\right), \quad \lim_{t\to\infty} S_2(t) = \frac{1}{2}\ln\left(\frac{2D\pi}{\gamma}\right), \quad \lim_{t\to\infty} S(t) = \ln\left(\frac{2D\pi}{\gamma\omega}\right),$$

as can be shown by using (AIV.40) in (IV.13)-(IV.15). Specifically, in Equation (II.72), the first term in RHS (which depended on $\mathbf{\Sigma}(0)$) vanisheed as $t \to \infty$ while the second term in RHS (which depended on $D(t)$)

determined the value of $\lim_{t\to\infty} \mathbf{\Sigma}(t)$ which for $\gamma = 1$ was as follows (see Equation AIV.40)

$$\mathbf{\Sigma}(t \to \infty) = \begin{bmatrix} 0.001 & 0 \\ 0 & 0.001 \end{bmatrix} \Bigg(\tag{IV.22}$$

The reason why S_1, S_2 and S overall decreased in time is because the equilibrium had a narrower PDF ($\Sigma_{12}(t \to \infty) = 0.001, \Sigma_{22}(t \to \infty) = 0.001$) (see Equation (IV.22)) than the initial PDF ($\Sigma_{11}(0) = \Sigma_{22}(0) = 0.01$). Consequently,

$$\lim_{t\to\infty} T_{1\to 2}(t) = \lim_{t\to\infty} T_{2\to 1}(t) = 0.$$

Third, in the critical/overdamped case $\gamma \geq 2\omega$ in Figures IV.2c-IV.2d, we observed a much faster decrease in S_2 than S_1 as γ damps x_2 quickly (recall that $\frac{dx_1}{dt} = x_2$ and see (IV.7)). Consequently, there was a faster and higher transient in $T_{1\to 2}$ compared with $T_{2\to 1}$ for larger γ, fluctuations in x_1 having a greater effect on the rate of change in the marginal entropy S_2. It is worth emphasising that our results for $\gamma \neq 0$ above (e.g., the decrease in entropies) involved the narrowing of a PDF over time. In particular, $T_{1\to 2}$ and $T_{2\to 1}$ for a constant $D(t) = 0.001$ were caused by the change in $\mathbf{\Sigma}(t)$ from its initial value $\mathbf{\Sigma}(0)$ to the equilibrium value in Equation (IV.22) due to $D(t) = 0.001$. For a much larger $D(t)$, Equation (IV.22) took a larger value than $\Sigma_{11}(0) = \Sigma_{22}(0)$, and PDFs became broaden over time, entropies increasing in time, for instance. As a result, $T_{2\to 1} \leq 0$ while $T_{1\to 2} > 0$. Appendix IV.4.4 explores how different values of the constant $D(t)$ affect IF. Finally, we note that in the phase portrait plots, the stochastic trajectories shown in blue dots generated by $\mathbf{x} \sim \mathcal{N}(\mu, \Sigma)$ remained near the trajectories of the mean values.

Case 2—Perturbation in $D(t)$ and $u(t) = 0$

To study how sensitive IF was to a sudden perturbation in $D(t)$ (therefore in $\mathbf{\Sigma}(t)$), we included an impulse function localised around $t = 4$ (see Table IV.1) in $D(t)$, which is shown in blue dotted line using the right y axis on Figure IV.3. As before, Figure IV.3 shows results for the undamped, underdamped, critically damped and over damped cases, respectively.

First, in Figure IV.3a for $\gamma = 0$, we observed that in a sharp contrast to Figure IV.2a, the impulse rendered large fluctuations in the simulated trajectory $\mathbf{x} \sim \mathcal{N}(\mu, \Sigma)$, with significant deviation from the mean trajectory $\boldsymbol{\mu}$. On the other hand, such an abrupt change in $\mathbf{\Sigma}(t)$ led to a rapid increase in S_1, S_2, S, $T_{1\to 2}$ and $T_{2\to 1}$ followed by oscillations. The amplitude of these oscillations slowly decreased in time, the oscillation frequency set by ω (as expected for no-damping).

Second, in the underdamped case $0 < \gamma < 2\omega$ shown in IV.3b, $T_{1\to 2}$ and $T_{2\to 1}$ exhibited some oscillations before reaching the equilibrium, as can also be seen from the phase portrait behaviour. Since the damping was still small, there was rather a long transient. It is interesting to notice that $T_{1\to 2}$ and $T_{2\to 1}$ flipped their signs (e.g., $T_{2\to 1} < 0$ to $T_{2\to 1} > 0$ around $t = 4$ as t increased) due to a sudden increase in D (Σ). This can be understood since the perturbation applied to x_2 increased marginal entropy S_1 while x_1 decreased the marginal entropy S_2. As a result, around the time $t = 4$ where D was maximum, the sign of IF became opposite to that without the perturbation shown in Figure IV.2b. Third, for the case $\gamma \geq 2\omega$ shown in Figures IV.3c and IV.3d, the sign of $T_{1\to 2}$ and $T_{2\to 1}$ behaved similarly to the underdamped case IV.3b). Overall, Figure IV.3 shows that $|T_{1\to 2|}$ and $|T_{2\to 1}|$ exhibited their peaks around $t = 4$. However, a close examination of the cases with $\gamma \neq 0$ revealed that the peak of $|T_{1\to 2}|$ and $|T_{2\to 1}|$ appeared after the peak of the impulse (in blue dotted line). That is, the peaks of $|T_{1\to 2}|$ and $|T_{2\to 1}|$ trailed (not preceded) the actual impulse peak. This will be compared with the case of IL in the next section where the peak of the information length diagnostics Γ^2 tended to precede the impulse peak, predicting the abrupt changes earlier than IF. Furthermore, IF was independent of external perturbations in $\boldsymbol{\mu}$.

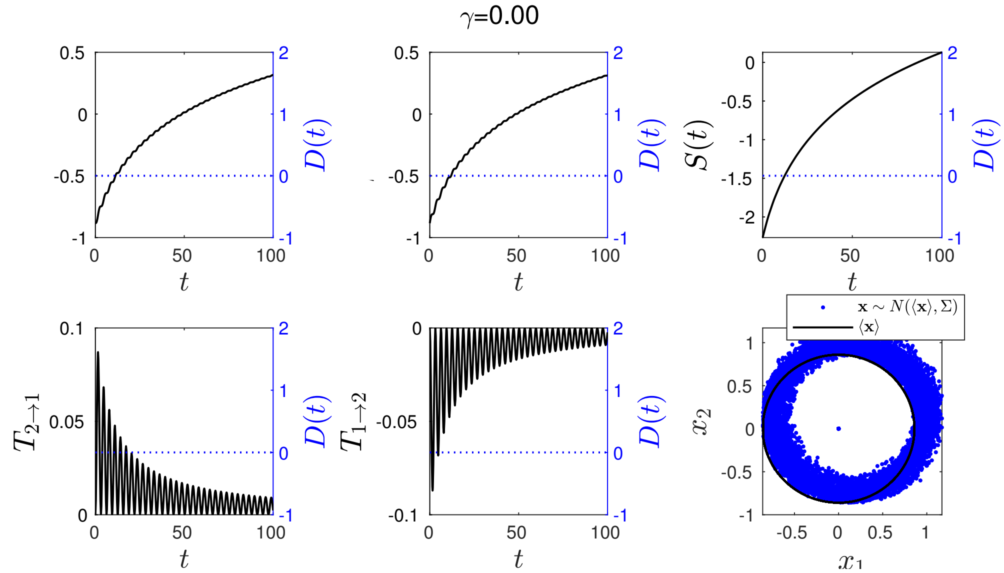

(a) Undamped.

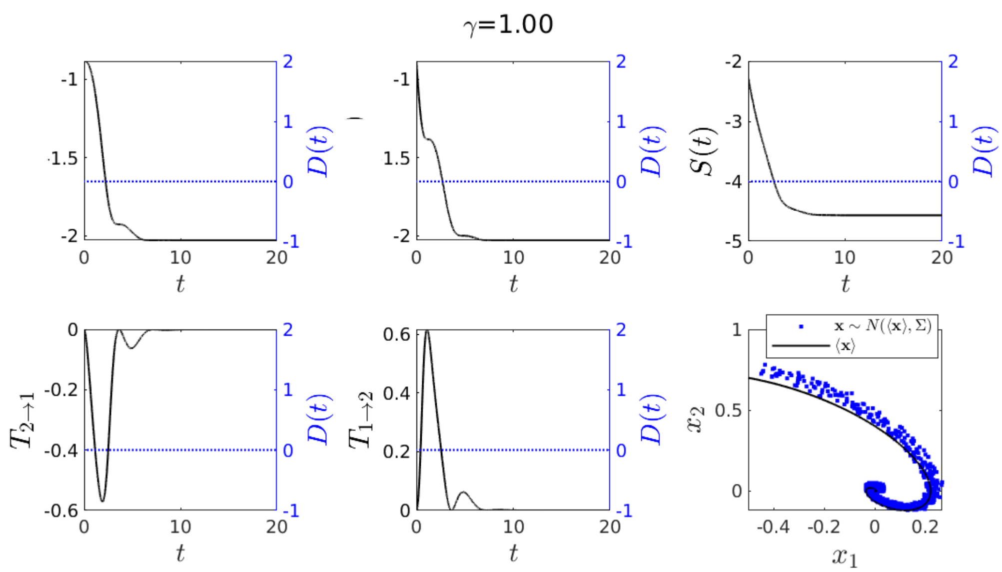

(b) Underdamped.

Figure IV.2: Cont.

IV.4.2 *Information Length Diagnostics Simulation Results*

In this subsection, we investigated how sensitive information length diagnostics ($\mathcal{L}$, Γ^2) were to the abrupt changes in the system dynamics. In contrast to IF, IL was capable of detecting changes in both mean values ($u(t)$) and $\boldsymbol{\Sigma}$ ($D(t)$), as can be inferred from Equation (III.22). We considered the four Cases 1–4 in Table IV.1 in Figures IV.4 to IV.7, respectively. In each case, we present the results of $\mathcal{L}$, Γ^2, Γ_1^2, Γ_2^2, $\Gamma^2 - \Gamma_m^2$ and the phase portrait of x_1 vs x_2 (where the stochastic simulations are shown in blue dots). As before, we used the

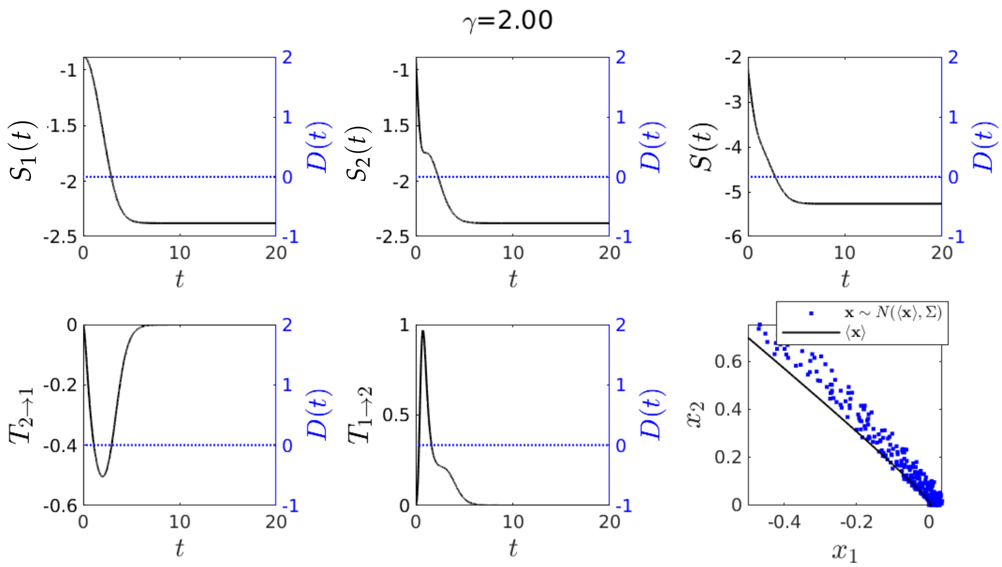

(c) Critically damped.

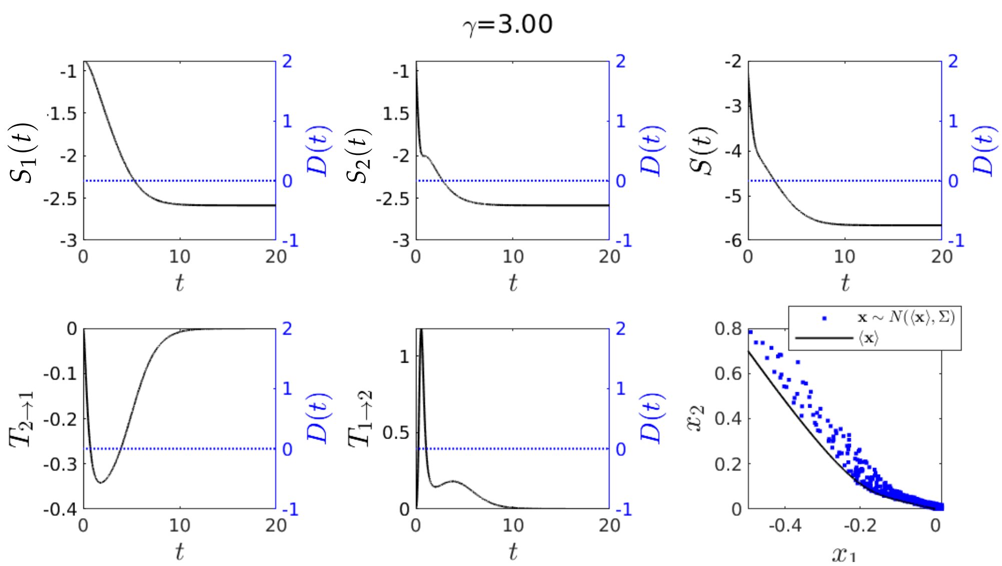

(d) Overdamped.

Figure IV.2: Graphs for $T_{1\to2}(t), T_{2\to1}(t), S_1(t), S_2(t)$ and $S(t)$ using $\omega = 1$, $\boldsymbol{\mu}(0) = [-0.5, 0.7]^T$, $\Sigma_{11}(0) = \Sigma_{22}(0) = 0.01$, and $\Sigma_{12}(0) = \Sigma_{21}(0) = 0$. (a) undamped case ($\gamma = 0$), (b) underdamped case ($\gamma = 1$), (c) critically damped case ($\gamma = 2$), and (d) overdamped case ($\gamma = 3$). Each panel also includes the phase portrait of x_1 vs x_2. In these plots there is no perturbations in the Kramers equation (IV.7), i.e., $D(t) = 0.001$ and $u(t) = 0$.

same initial conditions $\boldsymbol{\Sigma}(0)$ in Equation (IV.21) and the same parameter values ($\omega = 1$) while varying γ for undamped, underdamped, critically damped and overdamped cases. The initial mean values are fixed as $\boldsymbol{\mu}(0) = [-0.5, 0.7]^T$ for all Cases.

It is worth noting that (the unperturbed) Case 1 in Table IV.1 corresponded to the usual Kramers equation, previously studied in [6]. We nevertheless show results for Case 1 below to be able to compare with Cases

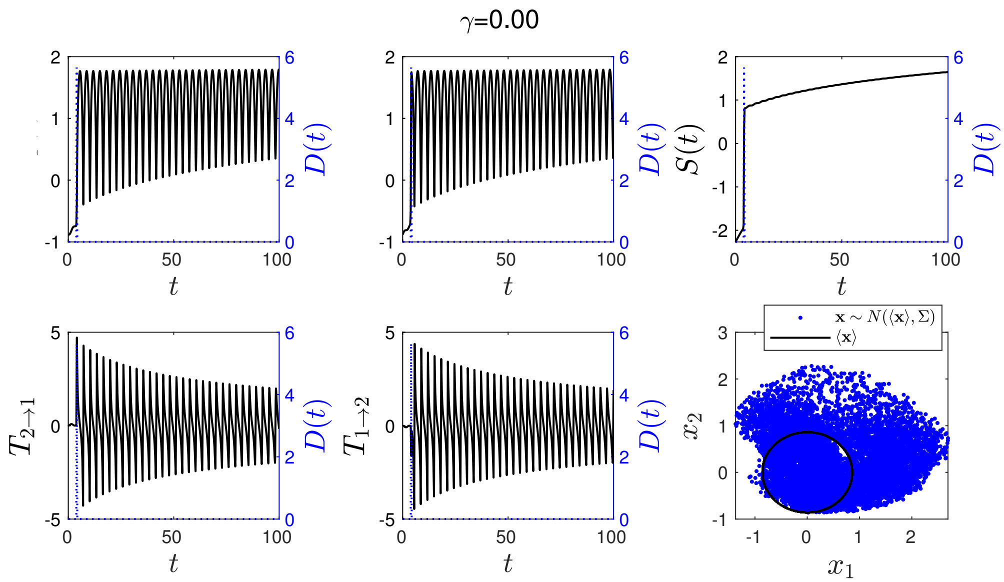

(a) Undamped.

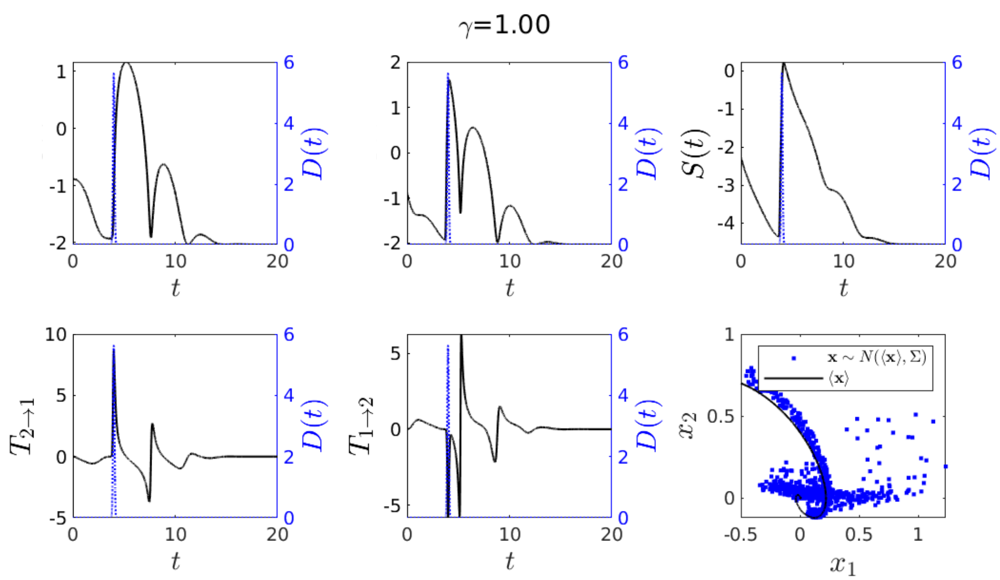

(b) Underdamped.

Figure IV.3: Cont.

2–4 as well as show new results such as Γ_1^2, Γ_2^2, and $\Gamma^2 - \Gamma_m^2$ that might be useful for understanding the correlation between variables. Note that in the following, $\Gamma^2 - \Gamma_m^2$ plots are not discussed in each Case, but instead discussed separately in Section IV.4.3.

Case 1—Constant $D(t)$ and $u(t) = 0$

In this unperturbed case, our main focus here was on the effects of γ on $\mathcal{L}$, Γ^2 and the marginal information velocities Γ_1^2 and Γ_2^2.

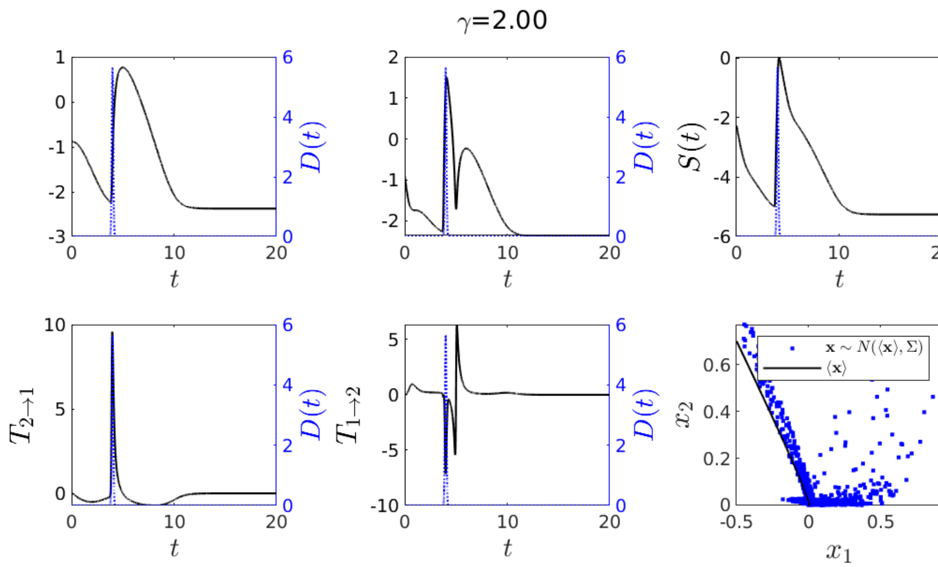

(c) Critically damped.

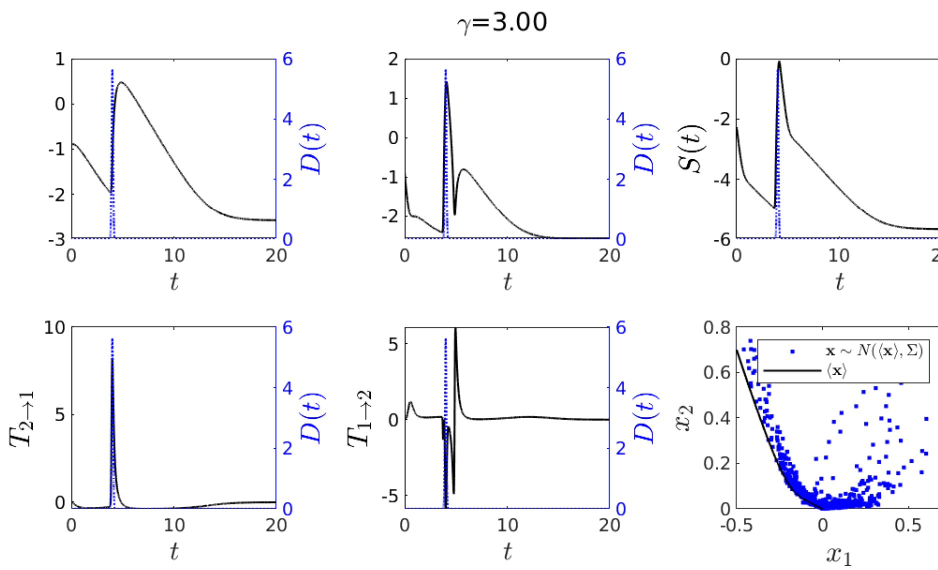

(d) Overdamped.

Figure IV.3: Graphs for $T_{1\to2}(t), T_{2\to1}(t), S_1(t), S_2(t)$ using $\omega = 1$, $\boldsymbol{\mu}(0) = [-0.5, 0.7]^T$, $\Sigma_{11}(0) = \Sigma_{22}(0) = 0.01$, and $\Sigma_{12}(0) = \Sigma_{21}(0) = 0$. (a) undamped case ($\gamma = 0$), (b) underdamped case ($\gamma = 1$), (c) critically damped case ($\gamma = 2$), and (d) overdamped case ($\gamma = 3$). Each panel also includes the phase portrait of x_1 vs x_2. In these plots, we have a perturbation over $\boldsymbol{\Sigma}$ in the Kramers equation (IV.7), i.e., $D(t) = 0.001 + \frac{1}{\sqrt{\pi}|0.1|}\exp(-(t-4)^2/(0.1)^2)$ and $u(t) = 0$.

First, for the undamped case $\gamma = 0$ shown in Figure IV.4a, harmonic oscillations (e.g., seen in the phase portrait) appeared in Γ_1^2 and Γ_2^2, their oscillation frequency determined by ω. We recall that Γ_1^2 and Γ_2^2 are calculated from the marginal PDF of x_1 and x_2, respectively. Because of the absence of damping, $\Gamma^2(t)$ decreased but never reached 0. The finite value of $\Gamma^2(t)$ is due to $\partial_t\boldsymbol{\Sigma}(t) \neq 0$ and $\partial_t\boldsymbol{\mu} \neq 0$ as the PDF $p(\mathbf{x}; t)$

evolved according to (II.70).

When $0 < \gamma < 2\omega$ in Figure IV.4b, a non-zero damping led to $\lim_{t\to\infty} \Gamma^2(t) = 0$, as the PDF reached its equilibrium value while $\mathcal{L}$ converged to a finite value. It is worth highlighting that non-zero Γ, Γ_1 and Γ_2^2 signified transient behaviour far from equilibrium. Finally, in Figures IV.4c and IV.4d for $\gamma \geq 2\omega$, we observed that a higher value of γ led to the shorter duration of transients and larger fluctuations in Γ^2.

Case 2—Perturbation in $D(t)$ and $u(t) = 0$

Figure IV.5 shows the effect of an impulse like function in $D(t)$ (see (IV.9)), which then led to an abrupt change in the covariance of the system PDF $p(\mathbf{x}; t)$ given by (II.70). Since IL depended on the value of $\frac{1}{2}\operatorname{Tr}\left((\mathbf{\Sigma}^{-1}\partial_{t_1}\mathbf{\Sigma})^2\right)$ (see Equation (III.22)), this abrupt change in $\mathbf{\Sigma}$ had a considerable impact on $\Gamma^2(t)$.

For the case $\gamma = 0$ shown in Figure IV.5a, the amplitude of Γ^2 and $\mathcal{L}$ was seen to be increased around the time of the impulse peak. The phase portrait clearly shows the increase in the uncertainty (more scattered data). The values of Γ_1^2 and Γ_2^2 were also seen to increase due to the perturbation.

For $0 < \gamma < 2\omega$, the oscillations in Γ_1^2 and Γ_2^2 were much less pronounced due to damping (see Figure IV.5b). This behaviour prevailed also for $\gamma \geq 2\omega$ shown in Figures IV.5c and IV.5d. Interestingly, a close examination revealed that the maxima in Γ^2 and Γ_2^2 followed the peaks of the impulse (in blue dotted line), as alluded at the end of Section IV.4.1. This was seen more clearly for larger γ in Figures IV.5c to IV.5d where the maxima in Γ^2, Γ_1^2 and Γ_2^2 all preceded the impulse peaks. These results demonstrate that the information diagnostics predicted the onset of an ongoing perturbation earlier than the information flow.

Case 3—Constant $D(t)$ and Perturbation in $u(t)$

Figure IV.6 shows results for a constant $D(t)$ and an impulse-like external input $u(t)$ (see (IV.10)) which caused an abrupt change in $\boldsymbol{\mu}$. $u(t)$ is shown in a red dotted line using the right y axis.

When $\gamma = 0$, Figure IV.6a shows how the perturbation changed the dynamics of $\boldsymbol{\mu}$ while $\mathbf{\Sigma}(t)$ remained unchanged in the phase portrait plot. When a non-zero damping was included in Figures IV.6b to IV.6d, Γ^2, Γ_1^2 and Γ_2^2 approached zero as $t \to \infty$. The phase portrait in Figures IV.6b to IV.6d shows how the perturbation changed the trajectory temporarily.

Overall, we observed a very large increase in Γ^2, Γ_1^2 and Γ_2^2 (larger increase in Γ_2^2 than in Γ_1^2), their peaks forming a little before or around the impulse peak (shown in red dotted line). Besides, the value of $\mathcal{L}$ was higher when we had a perturbation on $u(t)$ and a constant $D(t)$ than when $D(t)$ was perturbed and $u(t) = 0$ for $\gamma > 0$ (see it by comparing Figure IV.5 to Figure IV.6). Furthermore, Γ_2^2 was the most affected by the changes in $u(t)$ since x_2 directly depends on $u(t)$.

Finally, it is important to highlight that our result of a high sensitivity of IL to abrupt changes in $u(t)$ was not shared with IF which was insensitive to $u(t)$.

Case 4—Perturbations in Both $D(t)$ and $u(t)$

Case 4 in Table IV.1 is when we added impulse like functions to both $D(t)$ and $u(t)$ ($b = 1$ and $d = 1$ in Equations (IV.9) and (IV.10), respectively.). Again, note that $u(t)$ is shown in a red dotted line using the right y axis. Overall, the phase portraits in Fig. IV.7 for the undamped, underdamped, critically damped and overdamped scenarios show that the perturbations momentarily broadened the width of PDF (II.70) while causing a large deviation of the trajectory of $\boldsymbol{\mu}$.

Figure IV.7a for the undamped case $\gamma = 0$ shows that the perturbations increased the value of $\mathcal{L}$ in comparison to Case 3 with $\gamma = 0$ (See Figure IV.6a). This is due to the increase in $\mathbf{\Sigma}$ in Case 4 by the impulse in $D(t)$, which increased the uncertainty against which the information was measured.

For non-zero damping in Figures IV.7b to IV.7d, we saw a substantial increment in the amplitude of Γ_2^2 (similar to Case 2 but smaller than in Case 3). In fact, in all cases of the underdamped, critically damped and overdamped scenarios, the overall behaviour was close to that observed in Case 2 (see Figure IV.5) than that in Case 4. It is because the increase in mean values due to the impulse $u(t)$ was somewhat compensated by the uncertainty increase due to the impulse in $D(t)$. This is a consequence of both impulses having the same form, e.g., taking their maximum values at the same time $t = 4$ (see Table IV.1). For instance, if Case 4 were considered with the two impulses that were timed differently, much larger values of $\Gamma, \Gamma_1, \Gamma_2$ were expected for Case 4 compared with Case 2. There were obviously differences between Case 2 and Case 4, for instance, in the long time limit $t \to \infty$, $\mathcal{L}$ in Case 4 was always bigger than that in Case 3. Finally, similar comments as before could be made in regards to the prediction capabilities of the information length diagnostics Γ^2.

IV.4.3 Interpretation of the $\Gamma^2 - \Gamma_m^2$ Plots

We now discuss the plot of $\Gamma^2 - \Gamma_m^2$ for all Cases 1-4 collectively to point out its usefulness.

First, according to (III.22), it is clear that Γ^2 considered the contribution from the non-independent random variables $\langle x_1 \rangle$, $\langle x_2 \rangle$, and its covariance matrix $\mathbf{\Sigma}(t)$ to the information changes in time, while Γ_m was based on the sum of Γ_i from a marginal PDF of x_i (see Definition III.1). Thus plotting $\Gamma^2 - \Gamma_m^2$ gave an approximation of the contribution from the cross-correlation $\Sigma_{ij} \forall i \neq j$ to Γ^2.

As an example, Figure IV.8 shows the simulation of a non-perturbed scenario ($u(t) = 0$ and $D(t) = 0.001$) using $\boldsymbol{\mu}(0) = [-0.5, 0.7]^T$, $\Sigma_{11}(0) = \Sigma_{22}(0) = 0.01$, $\Sigma_{12}(0) = \Sigma_{21}(0) = 0$, $\gamma = 1$ and $\omega = 2$ (underdamped). This example permitted us to compare the evolution/deformation of the width of $p(\mathbf{x}; t)$ (given by Equation (II.70)) in the x_1-x_2 plane with the value of $\Gamma^2 - \Gamma_m^2$ over time shown in the right panel of Figure IV.8.

Figure IV.8 when $\Gamma^2 - \Gamma_m^2 = 0$ (at $t = 0$, for instance), shows that the shape of $p(\mathbf{x}; t)$ was a perfect circle (this because $\Sigma_{12}(t \to 0) = 0$). For $\Gamma^2 - \Gamma_m^2 \neq 0$, the shape of $p(\mathbf{x}; t)$ was deformed according to the value of $\Gamma^2 - \Gamma_m^2$. The simulations suggest that the bigger the value of $|\Gamma^2 - \Gamma_m^2|$ the higher the correlation between the random variables x_1 and x_2 ($p(\mathbf{x}; t)$ was highly deformed).

In summary, in regard to Cases 1–4, we can remark two characteristics on the behaviour of $\Gamma^2 - \Gamma_m^2$ in Figures IV.4 to IV.7. First, the value presented more variations when we had a perturbation on $D(t)$, for instance when $\gamma = 0$ there were high oscillations not presented when there was a perturbation on $u(t)$ but not on $D(t)$. Second, the higher the value of γ the less the deformations through time of $p(\mathbf{x}; t)$'s width since $\Gamma^2 - \Gamma_m^2$ showed less changes through time.

IV.4.4 Effects of Different Constant $D(t)$ on IF

As noted in Section IV.4.1, the sign of $T_{1\to2}$ and $T_{2\to1}$ is determined by whether a PDF becomes narrower or broader in time since in Equation (II.72), the first term in RHS (which depends on $\Sigma(0)$ in Equation (IV.21)) vanishes as $t \to \infty$ while the second term in RHS (which depends on $D(t)$) determines the value of $\lim_{t\to\infty} \mathbf{\Sigma}(t)$. Specifically, $\Sigma_{11}(0) = \Sigma_{22}(0) = 0.01$ and $\Sigma_{12}(t \to \infty) = \frac{D_0}{\gamma\omega^2}, \Sigma_{22}(t \to \infty) = \frac{D_0}{\gamma}$. In this subsection, we look at this in detail by focusing on Case 1 (see Table IV.1).

We start by recalling that in Section IV.4.1, we have discussed the effects of certain fixed value D_0 for $D(t)$ on IF including the case of no perturbation (Case 1), showing the effects of the parameters γ. In the following, we present the effect of different values of constant $D(t) = D_0 \in [0, 0.5]$ on $T_{2\to1}$ and $T_{1\to2}$ in Figure IV.9. Note that results for $D_0 \gg 0.5$ have quite similar behaviours to the case of $D_0 = 0.5$. As before, the different

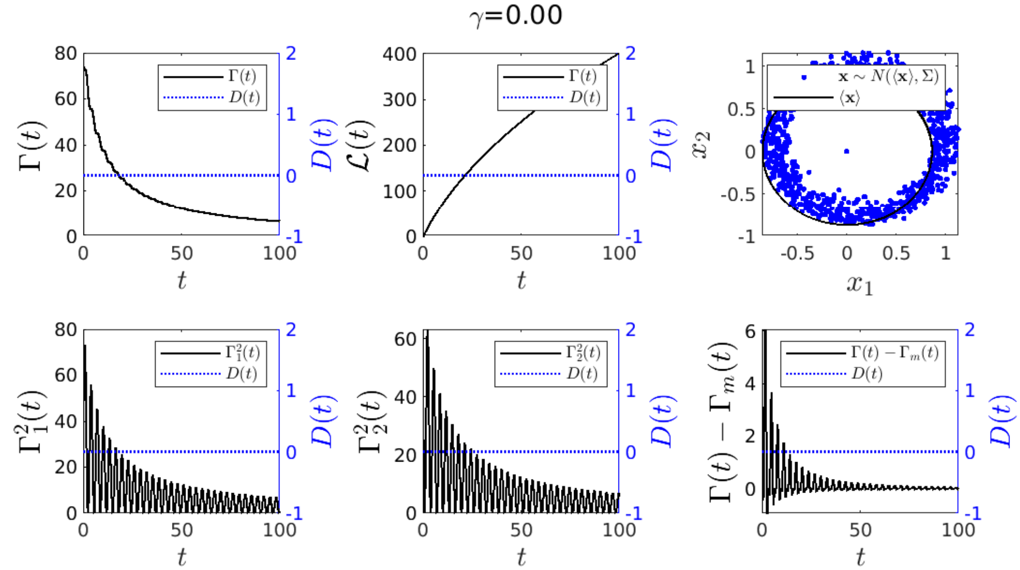

(a) Undamped.

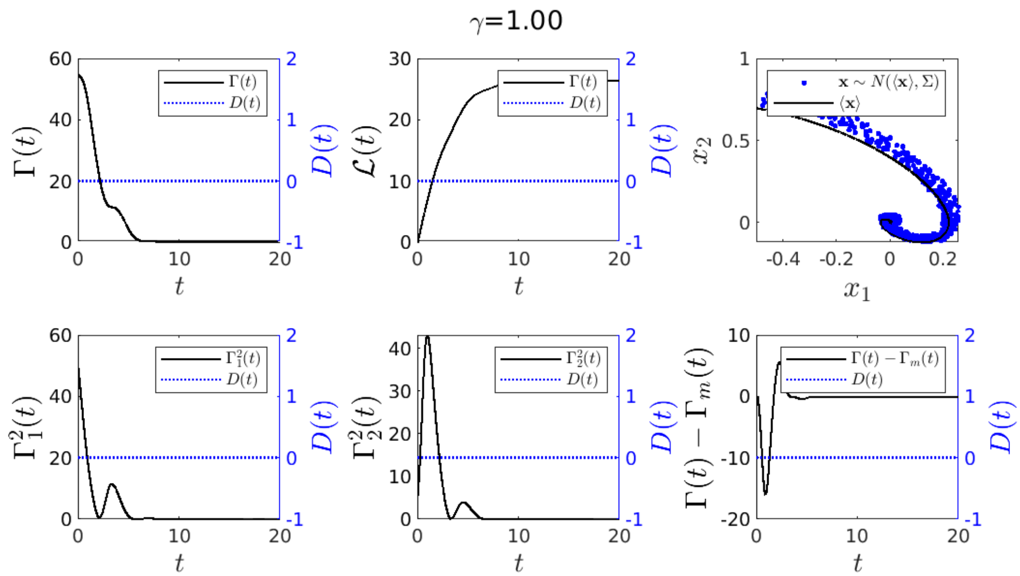

(b) Underdamped.

Figure IV.4: Cont.

values of γ are considered to examine undamped, underdamped, critically damped or overdamped scenarios. All other parameter values and initial conditions are the same as those used in Figure IV.2.

Figure IV.9a shows the evolution of $T_{2\to1}$ and $T_{1\to2}$ for different D_0 without damping $\gamma = 0$. As D_0 decreases, $T_{1\to2}$ and $T_{2\to1}$ also decrease their amplitude. There is a higher peak in the transient in both $T_{1\to2}$ and $T_{2\to1}$ for $D_0 = 0.5$. An interesting behaviour is observed when $D_0 = 0$ (the deterministic case without noise $\xi = 0$), where $T_{1\to2} \approx T_{2\to1} \approx 0$; the zooming of Figure IV.9a shows very small-amplitude ($O(10^{-7})$) oscillations with the angular frequency ω. In the underdamped case $0 < \gamma < 2\omega$ shown in Fig. IV.9b, the value of D_0 determines the sign of $T_{1\to2}$ and $T_{2\to1}$, changing their sign around $D_0 = D_c$ where $0.001 < D_c < 0.1$. Specifically, this change in the sign of $T_{1\to2}$ and $T_{2\to1}$ tells us that when x_2 minimises S_1

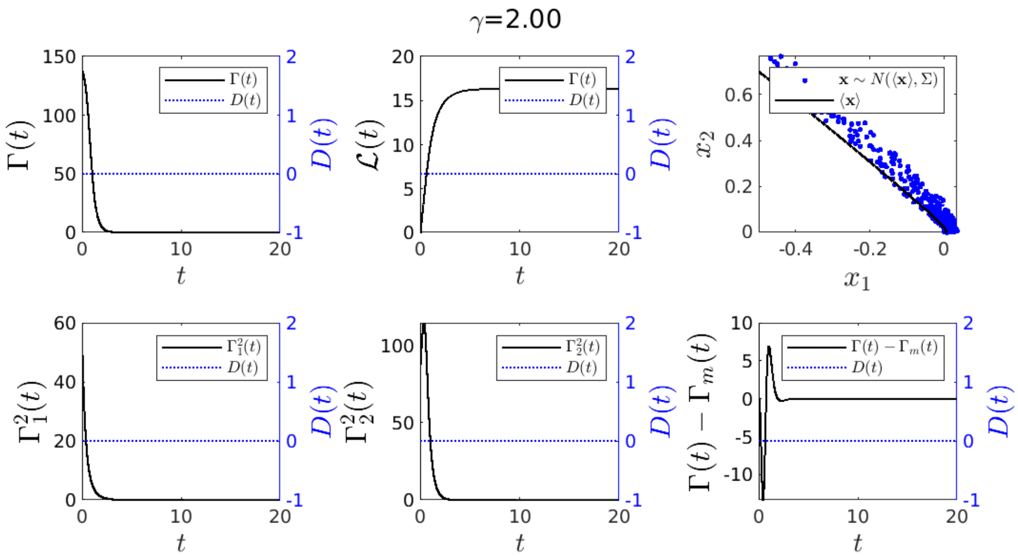

(c) Critically damped.

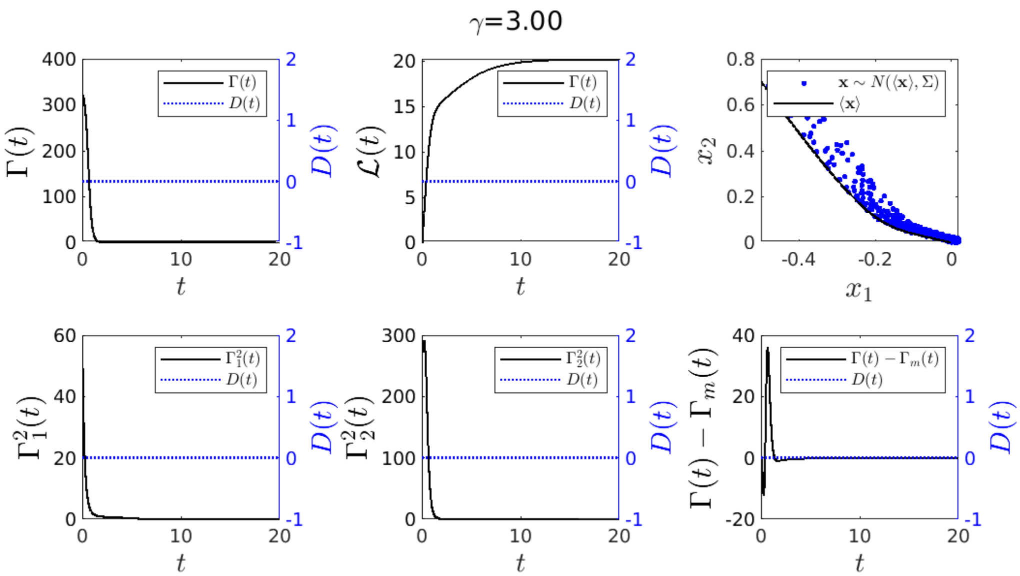

(d) Overdamped.

Figure IV.4: Graph for $\Gamma^2(t)$ and $\mathcal{L}(t)$ using $\omega = 1$, $\boldsymbol{\mu}(0) = [-0.5, 0.7]^T$, $\Sigma_{11}(0) = \Sigma_{22}(0) = 0.01$ and $\Sigma_{12}(0) = \Sigma_{21}(0) = 0$ for various values of γ. (a) undamped case ($\gamma = 0$), (b) underdamped case ($\gamma = 1$), (c) critically damped case ($\gamma = 2$), and (d) overdamped case ($\gamma = 3$). Each panel also includes the phase portrait of x_1 vs x_2. In these plots, we have no perturbations over the Kramers equation (IV.7), i.e., $D(t) = 0.001$ and $u(t) = 0$.

when $D_0 < D_c$ while maximising it when $D_0 > D_c$. The opposite holds for the effect of x_1 on S_2. Note that $D_0 = 0$, IF oscillates forever due to the absence of damping while it asymptotically converges for a non-zero D_0. Even when $\gamma \geq 2\omega$ (see Figures IV.9c and IV.9d), we observe similar behaviours of $T_{1\to 2}$ and $T_{2\to 1}$. In particular, x_2 minimises S_1 when $D < D_c$ while maximising it when $D_0 > D_c$, with the opposite effect of x_1 on S_2.

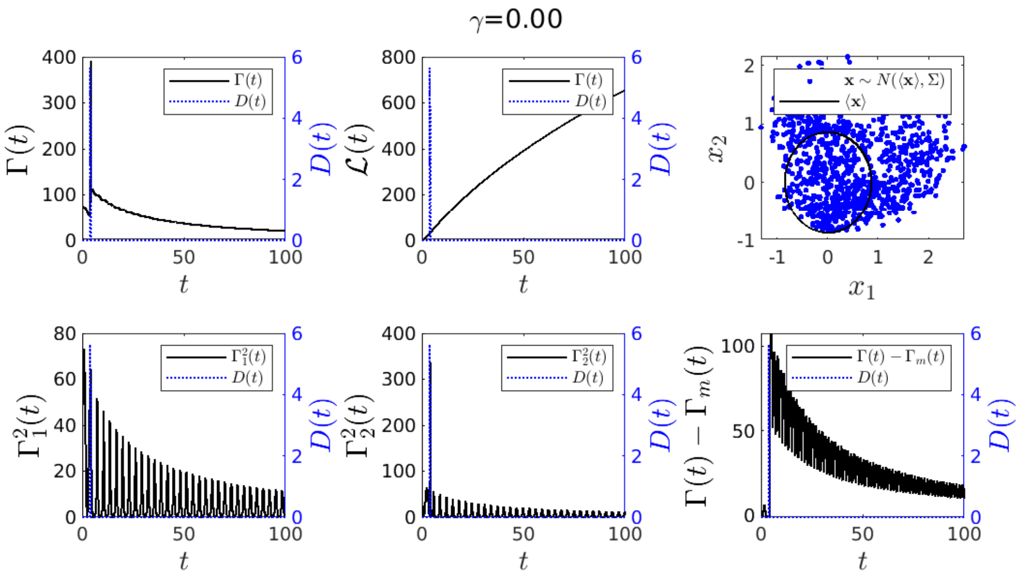

(a) Undamped.

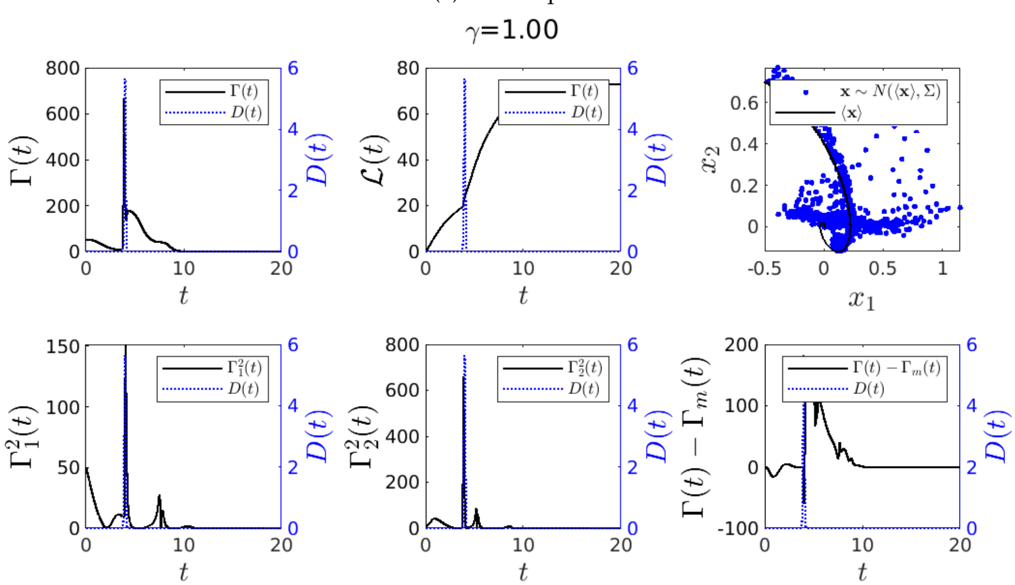

(b) Underdamped.

Figure IV.5: Cont.

IV.5 Abrupt event analysis via correlation coefficients

In this section, we define different correlations coefficients in terms of entropy production and information rate as a possible tool for abrupt event detection and causality analysis. The information and entropy-based coefficients are compared through case studies against the mutual information and Pearson correlation coefficients.

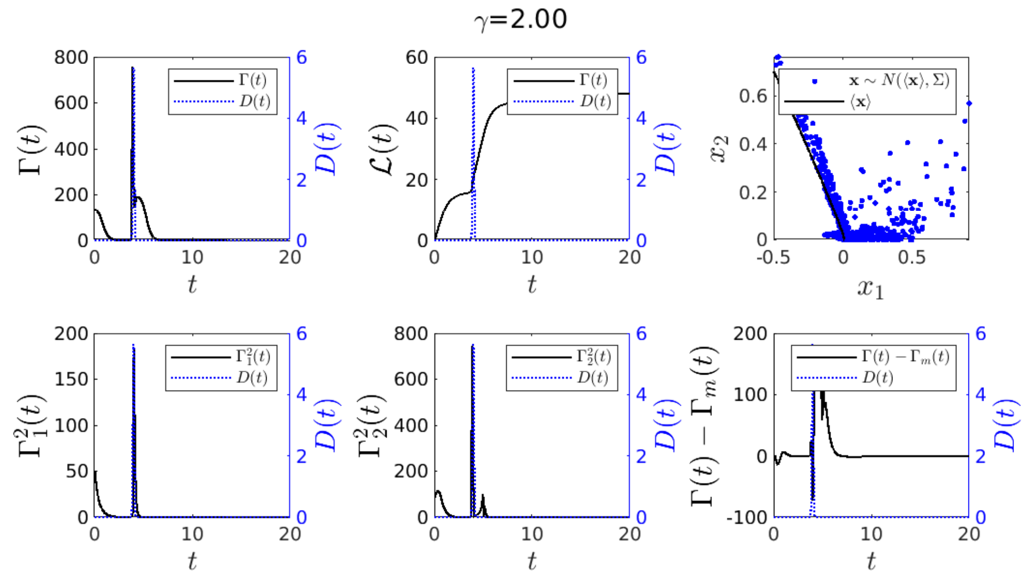

(c) Critically damped.

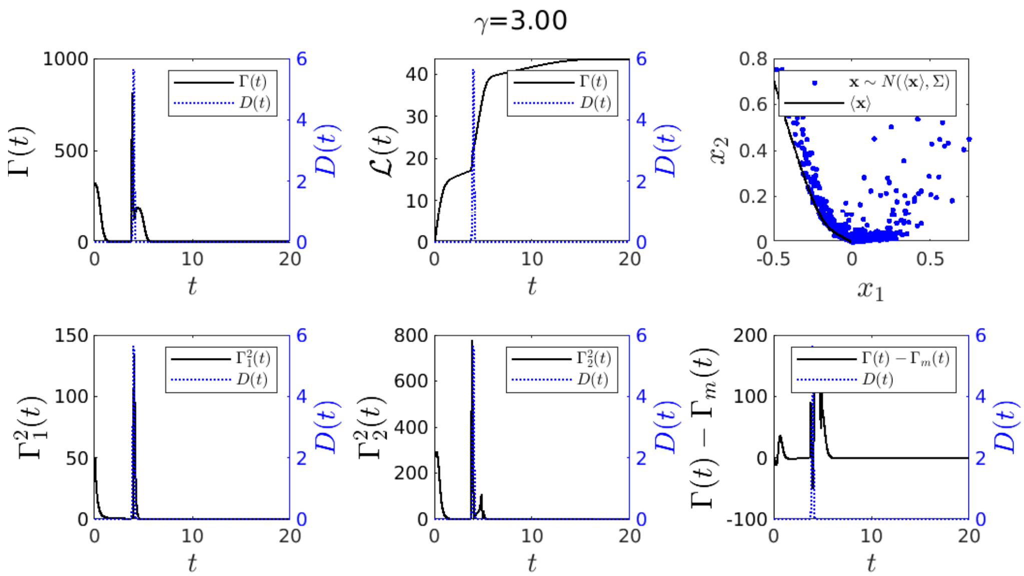

(d) Overdamped.

Figure IV.5: Graph for $\Gamma^2(t)$ and $\mathcal{L}(t)$ using $\omega = 1$, $\boldsymbol{\mu}(0) = [-0.5, 0.7]^T$, $\Sigma_{11}(0) = \Sigma_{22}(0) = 0.01$ and $\Sigma_{12}(0) = \Sigma_{21}(0) = 0$ for various values of γ. (a) undamped case ($\gamma = 0$), (b) underdamped case ($\gamma = 1$), (c) critically damped case ($\gamma = 2$), and (d) overdamped case ($\gamma = 3$). Each panel also includes the phase portrait of x_1 vs x_2. In these plots, we have a perturbation over the covariance matrix $\boldsymbol{\Sigma}$ of the Kramers equation (IV.7), i.e., $D(t) = 0.001 + \frac{1}{\sqrt{\pi}|0.1|} \exp(-(t-4)^2/(0.1)^2)$ and $u(t) = 0$.

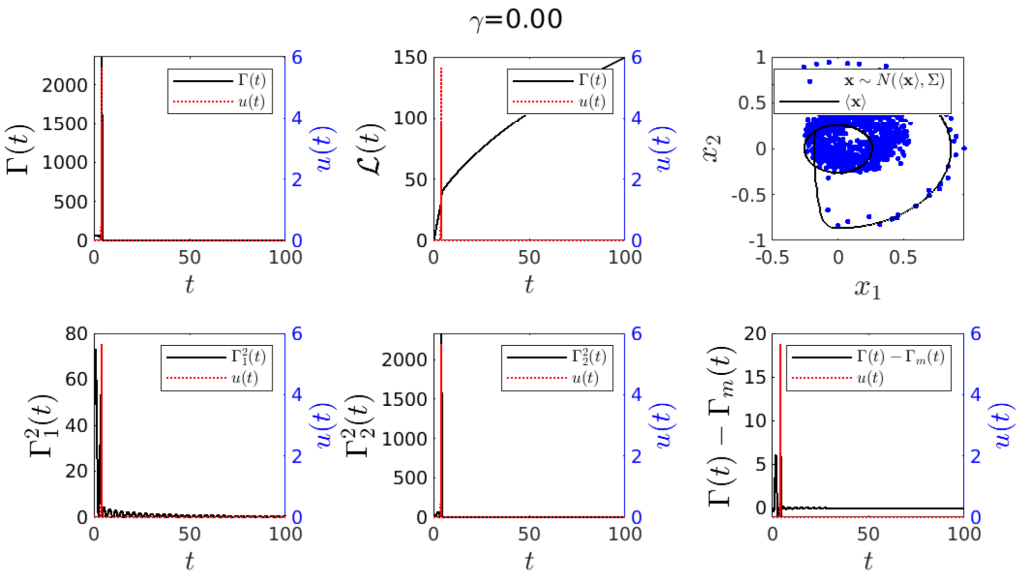

(a) Undamped.

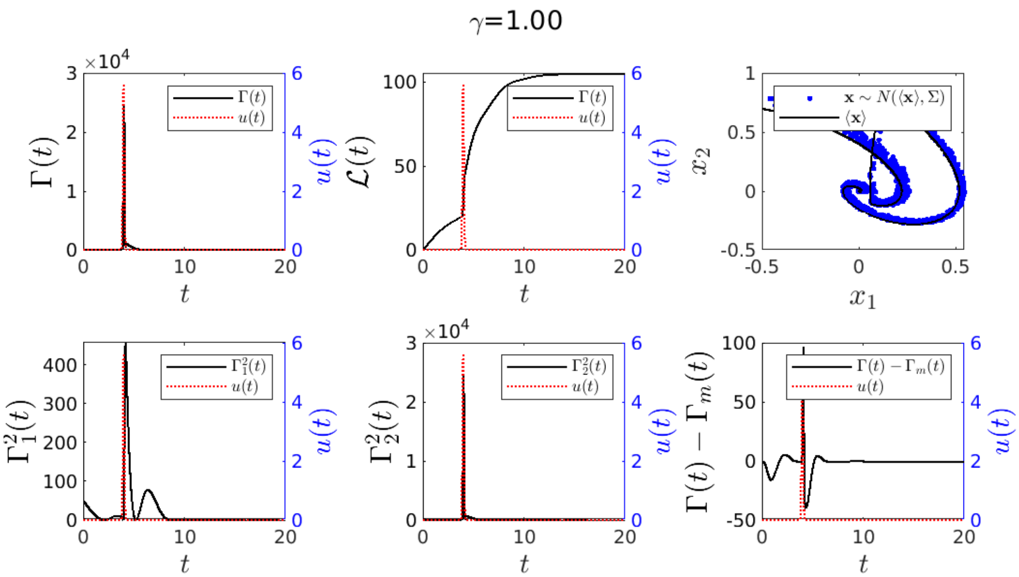

(b) Underdamped.

Figure IV.6: Cont.

IV.5.1 Mutual information

The mutual information between two continuous random variables x_i and x_j with a joint Gaussian PDF $p(\mathbf{x};t)$ at time t is defined as

$$I_{ij}(t) := \iint_{\mathbb{R}^2} p(\mathbf{x};t) \ln\left(\frac{p(\mathbf{x};t)}{p(x_i,t)p(x_j,t)}\right) \mathrm{d}\mathbf{x} = S_i(t) + S_j(t) - S(t). \tag{IV.23}$$

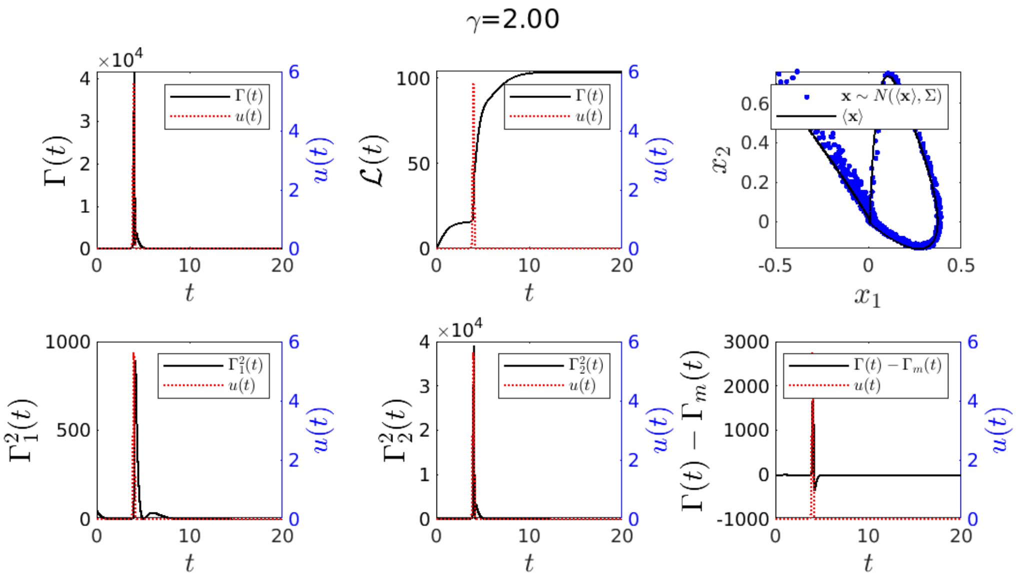

(c) Critically damped.

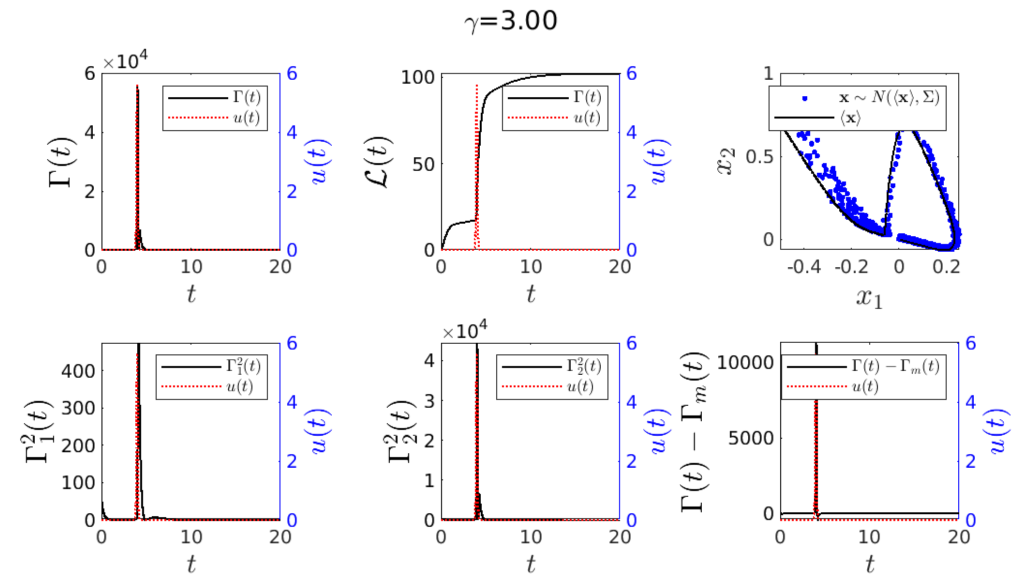

(d) Overdamped.

Figure IV.6: Graph for $\Gamma^2(t)$ and $\mathcal{L}(t)$ using $\omega = 1$, $\boldsymbol{\mu}(0) = [-0.5, 0.7]^T$, $\Sigma_{11}(0) = \Sigma_{22}(0) = 0.01$ and $\Sigma_{12}(0) = \Sigma_{21}(0) = 0$ for various values of γ. (a) undamped case ($\gamma = 0$), (b) underdamped case ($\gamma = 1$), (c) critically damped case ($\gamma = 2$), and (d) overdamped case ($\gamma = 3$). Each panel also includes the phase portrait of x_1 vs x_2. Here, we have a perturbation over the mean value $\boldsymbol{\mu}$ of the Kramers equation (IV.7), i.e., $D(t) = 0.001$ and $u(t) = \frac{1}{\sqrt{\pi}|0.1|}\exp(-(t-4)^2/(0.1)^2)$.

Here, $p(x_i, t)$ and $p(x_j, t)$ are the marginal PDFs of the random variables x_i and x_j, respectively. Recall, the sub-index i in the entropy S refers to the entropy from the marginal PDF of x_i and its value is simply

$$S_i(t) = \frac{1}{2} + \ln\left(\sqrt{2\pi\Sigma_{ii}(t)}\right). \tag{IV.24}$$

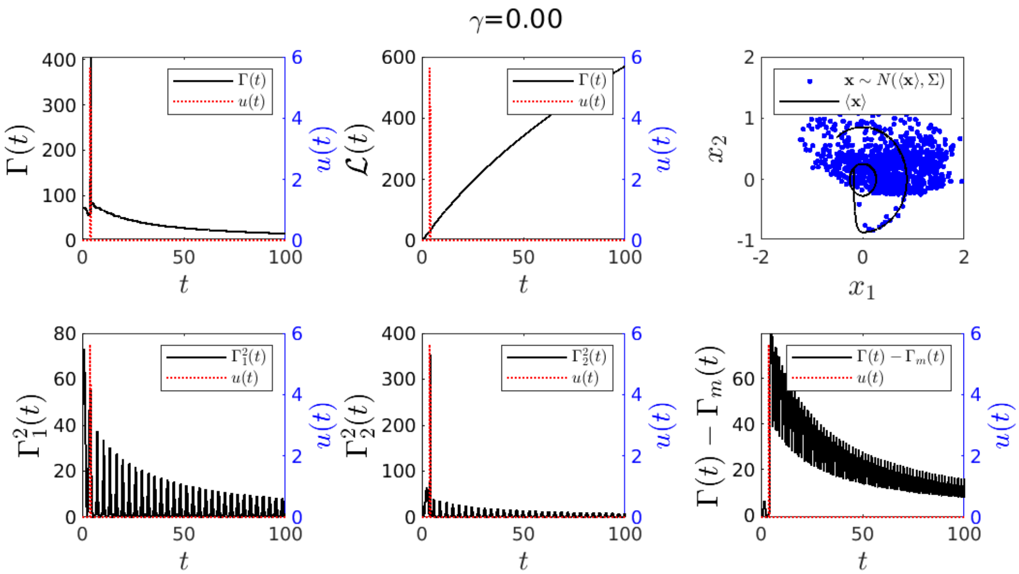

(a) Undamped.

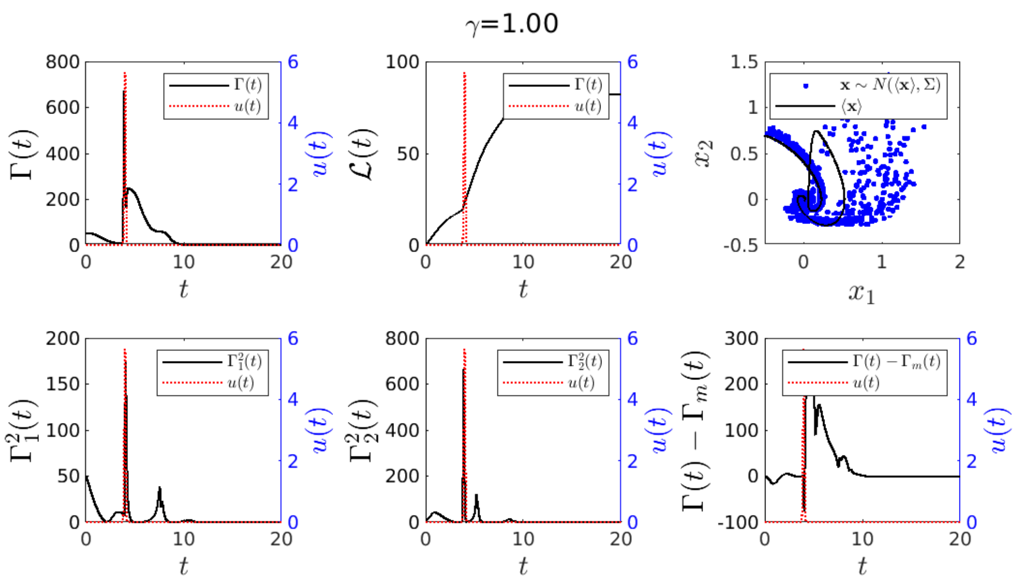

(b) Underdamped.

Figure IV.7: Cont.

Mutual information represents the amount of information of a random variable that can be obtained by observing another random variable. Hence, it is a measure of the mutual dependence between the two variables [110]. To measure correlations between two random variables in a process, we can utilise common normalised variants of the mutual information, for instance, the total correlation formula [111; 112]

$$\rho_I(t) := 2\frac{I_{ij}(t)}{S_i(t) + S_j(t)}, \tag{IV.25}$$

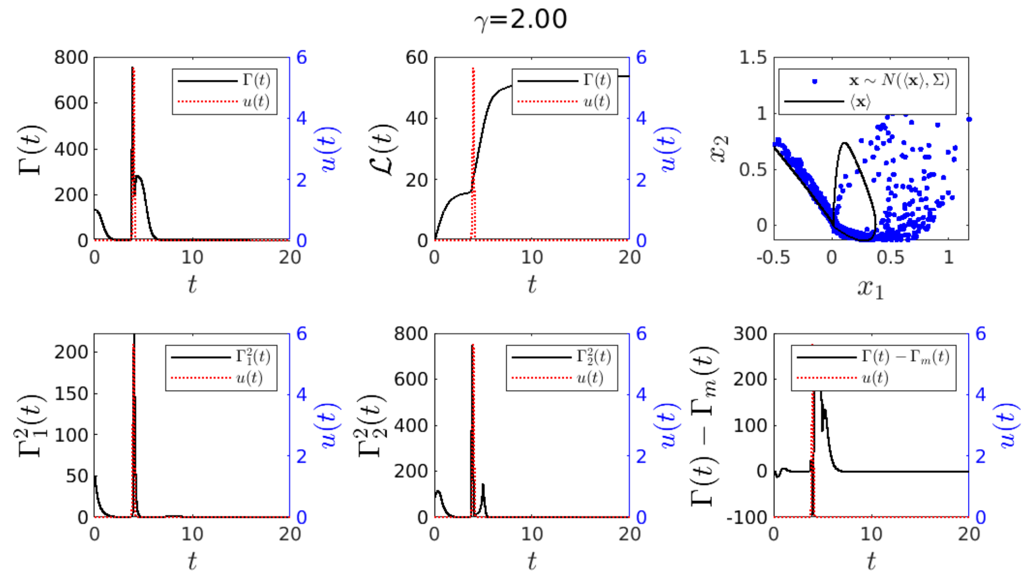

(c) Critically damped.

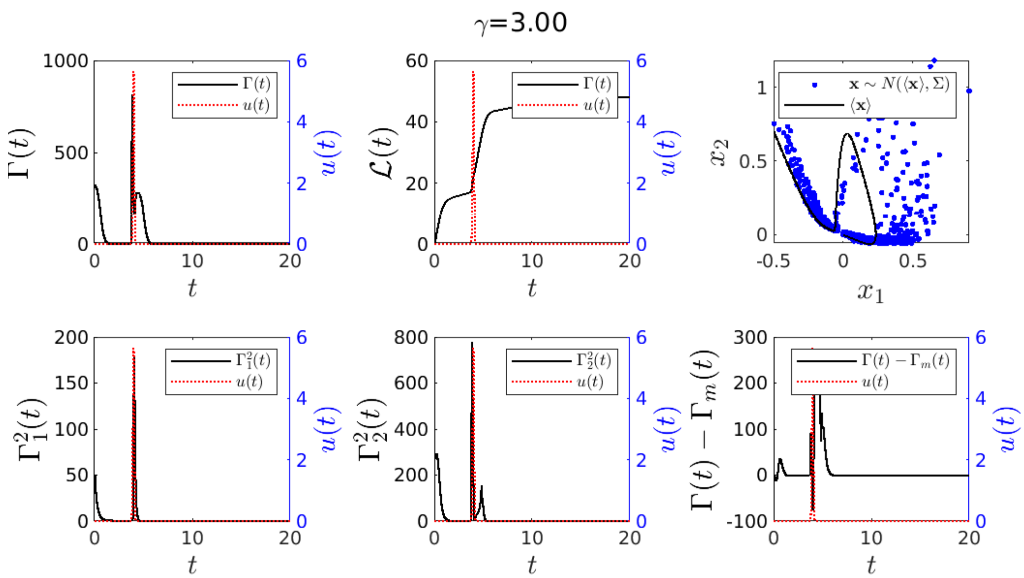

(d) Overdamped.

Figure IV.7: Graph for $\Gamma^2(t)$ and $\mathcal{L}(t)$ using $\omega = 1$, $\boldsymbol{\mu}(0) = [-0.5, 0.7]^T$, $\Sigma_{11}(0) = \Sigma_{22}(0) = 0.01$ and $\Sigma_{12}(0) = \Sigma_{21}(0) = 0$ for various values of γ. (a) undamped case ($\gamma = 0$), (b) underdamped case ($\gamma = 1$), (c) critically damped case ($\gamma = 2$), and (d) overdamped case ($\gamma = 3$). Each panel also includes the phase portrait of x_1 vs x_2. Here, we add a perturbation over the mean $\boldsymbol{\mu}$ and covariance $\boldsymbol{\Sigma}$ of the Kramers equation (IV.7), i.e., $D(t) = 0.001 + \frac{1}{\sqrt{\pi}|0.1|} \exp(-(t-4)^2/(0.1)^2)$ and $u(t) = \frac{1}{\sqrt{\pi}|0.1|} \exp(-(t-4)^2/(0.1)^2)$.

where x_i and x_j are treated symmetrically. Equation (IV.25) is the inverse of the mean of the inverted uncertainty coefficients $\mathcal{C}_{ij}(t)$ and $\mathcal{C}_{ji}(t)$, defined as

$$\mathcal{C}_{ij}(t) := \frac{I_{ij}(t)}{S_i(t)}, \quad \mathcal{C}_{ji}(t) := \frac{I_{ij}(t)}{S_j(t)}, \tag{IV.26}$$

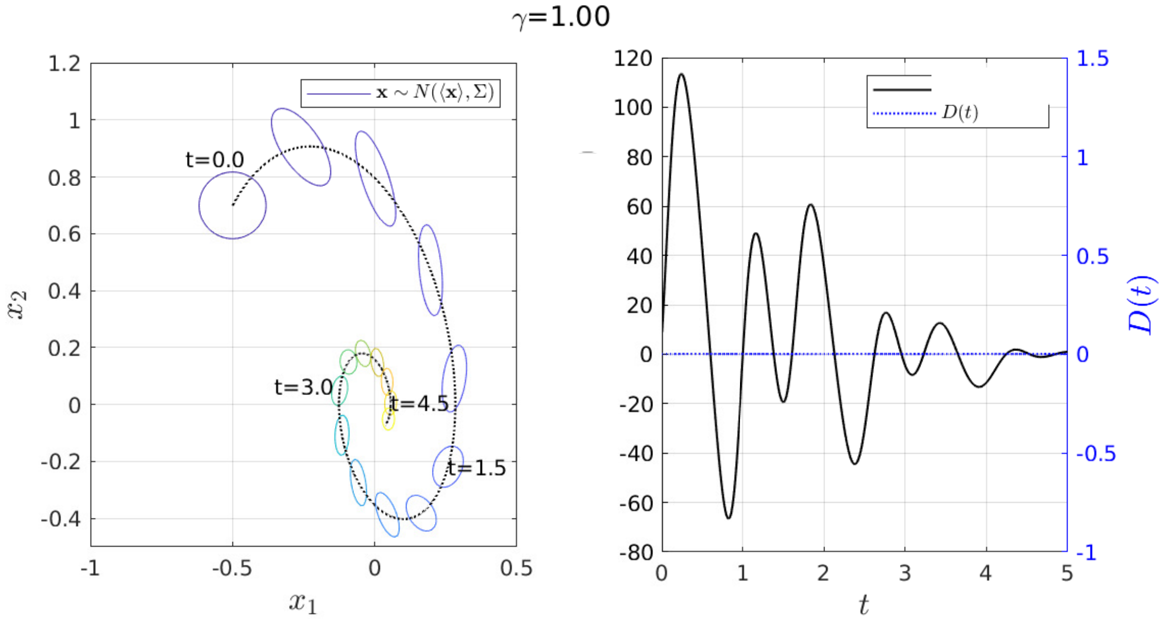

Figure IV.8: The value of $\Gamma^2 - \Gamma_m^2$ give us information about the deformation of $p(\mathbf{x};t)$, affected by the cross-correlation Σ_{12}. The values used here are $\omega = 2$, $\boldsymbol{\mu}(0) = [-0.5, 0.7]^T$, $\Sigma_{11}(0) = \Sigma_{22}(0) = 0.01$, $\Sigma_{12}(0) = \Sigma_{21}(0) = 0$, $D(t) = 0.001$ and $u(t) = 0$.

weighted by the entropy of each variable separately [113]. The uncertainty coefficient (IV.26) gives a value between 0 and 1, indicating no association or complete predictability of x_i from x_j (given x_j, what fraction of x_i we can predict), respectively. Thus, (IV.25) gives an average of the predictability between x_i and x_j. The total correlation formula (IV.25) is as an alternative to the well-known Pearson correlation coefficient

$$\rho := \frac{\Sigma_{ij}}{\sqrt{\Sigma_{ii}\Sigma_{jj}}}, \tag{IV.27}$$

when dealing with non-linear relationships between the random variables [114; 115; 116].

IV.5.2 Information rate and entropy production correlation coefficients

In analogy to (IV.25) and (IV.27), we define new normalised correlation coefficients between two variables x_i and x_j in terms of information rate and entropy production as follows

$$\rho_\Gamma(t) := \frac{\Gamma_i(t) + \Gamma_j(t) - \Gamma(t)}{\Gamma(t)}, \tag{IV.28}$$

$$\rho_\Pi(t) := \frac{\Pi_i(t) + \Pi_j - \Pi(t)}{\Pi(t)}. \tag{IV.29}$$

Here, Π_i and Π_j are the contributions from the variable x_i and x_j to the entropy production Π (see Equation (III.76)). The values of Γ_i and Γ_j are the information rates from the marginal PDFs of x_i and x_j, respectively. For instance, given the marginal PDF $p(x_i, t)$ of the random variable x_i the value of Γ_i is defined as in Definition III.2. Equations (IV.28)-(IV.29) are not defined exactly as the Pearson correlation coefficient (IV.27)

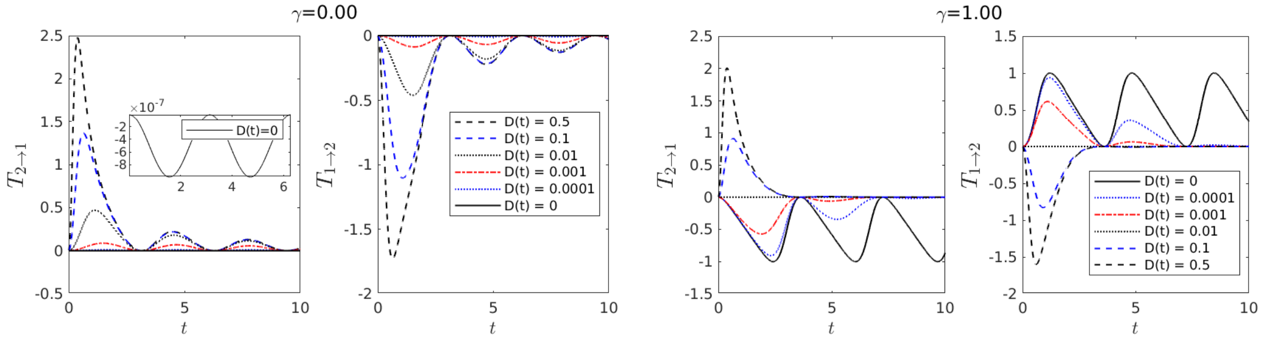

(a) Undamped. (b) Underdamped.

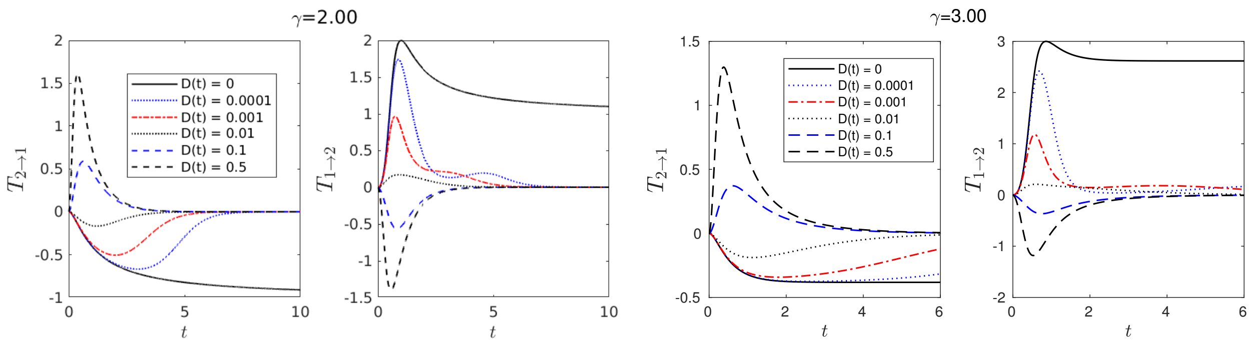

(c) Critically damped. (d) Overdamped.

Figure IV.9: Graphs for $T_{1\to2}(t)$ and $T_{2\to1}(t)$ using $\omega = 1$, $\boldsymbol{\mu}(0) = [-0.5, 0.7]^T$, $\Sigma_{11}(0) = \Sigma_{22}(0) = 0.01$ and $\Sigma_{12}(0) = \Sigma_{21}(0) = 0$ for various values of γ. Specifically, (a) undamped case ($\gamma = 0$ varying $D = \{0, 0.0001, 0.001, 0.01, 0.1, 0.5\}$), (b) underdamped case ($\gamma = 1$ varying $D = \{0, 0.0001, 0.001, 0.01, 0.1, 0.5\}$), (c) critically damped case ($\gamma = 2$ varying $D = \{0, 0.0001, 0.001, 0.01, 0.1, 0.5\}$), and (d) overdamped case ($\gamma = 3$ varying $D = \{0, 0.0001, 0.001, 0.01, 0.1, 0.5\}$). Since the entropic measures $T_{1\to2}(t)$ and $T_{2\to1}(t)$ fully depend on the value of $\boldsymbol{\Sigma}$, the value of $u(t)$ does not affect the results.

or the normalised correlation coefficient of the mutual information (IV.25). Instead, they are expressed analogously to the information quality ratio, a quantity of the amount of information of a variable based on another variable against total uncertainty [117]. Hence, ρ_Γ/ρ_Π is said to quantify the predictability of information rate/entropy production of a variable based on another variable. A graphical description of Equation (IV.28) in the form of Venn diagram is shown in Figure IV.10.

When the temperature changes abruptly in a system like (III.80), the value of D (noise amplitude) is affected. In the case of Brownian motion, such abrupt event will contribute to the uncertainty in the control of the position of the Brownian particle. To bring light to the analysis and study of abrupt events, we use our toy models and simulate an abrupt change in the system's temperature by using the following impulse like function for the ii-element of the noise amplitude matrix $\mathbf{D}$ and on the input function $u(t)$

$$D_{ii}(t) = D_0 + \frac{1}{|a|\sqrt{\pi}} e^{-\left(\frac{t-t_p}{a}\right)^2}, \tag{IV.30}$$

$$u(t) = \frac{1}{|a|\sqrt{\pi}} e^{-\left(\frac{t-t_p}{a}\right)^2}. \tag{IV.31}$$

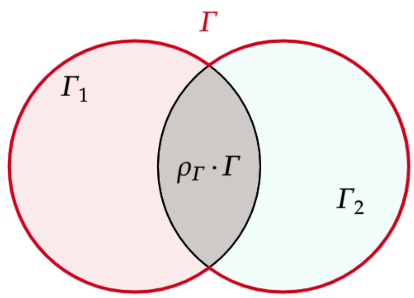

Figure IV.10: Venn diagram describing the meaning of (IV.28). A similar diagram can be made for (IV.29).

Here, the second term on RHS of (IV.30) and (IV.31) takes a high value for a short time interval around t_p and a changes the amplitude of the impulses.

IV.5.3 Case study: Harmonically bound particle

We start analysing the proposed correlation coefficients by considering its application to abrupt event analysis of system (III.80). Figures IV.11 and IV.12 show the computer simulation results and time evolution of abrupt events in $\mathbf{D}$ and u, respectively. The noise amplitude is perturbed via the element D_{22} of the matrix $\mathbf{D}$ and the input force u only affects the state x_2. Figures IV.11 and IV.12 are divided in three panels, IV.11a/IV.12a which includes the phase portrait of x_1 vs x_2 and the time evolution of the correlation coefficients ρ and ρ_I; IV.11b/IV.12b shows the time evolution of $\rho_\Gamma, \Gamma, \Gamma_1$ and Γ_2; IV.11c/IV.12c the time evolution of ρ_Π, Π, Π_1 and Π_2.

From Figure IV.11, the coefficient ρ_I is the most sensitive to noise amplitude perturbations, as it shows an asymptote around the peak of the perturbation at $t = 4$ (see Figure IV.11a). On the other hand, the value of Γ predicts[2] the ongoing perturbation (corroborating the previous results shown in [7]) since it precedes the aforementioned perturbation (see Figure IV.11b). Regarding the perturbation in $u(t)$ shown in Figure IV.12, the coefficients ρ and ρ_I are no longer useful because they are not sensitive to changes in the mean value of the PDF (see Figure IV.12a). In contrast, an abrupt event in the mean value is well captured by ρ_Γ and ρ_Π.

Figures IV.12b and IV.12c show that the values of ρ_Γ and ρ_Π change abruptly at the time $t = 4$ when perturbation occurs. Figure IV.12b presents negative ρ_Γ at $t \approx 4$ due to the large difference between Γ_2 and Γ_1. For the similar reasons, ρ_Π also presents a high decrement at $t \approx 4$. Here, the coefficients are able to detect the perturbation over the mean value but they are no longer able to predict it.

Remark IV.1. *In Figures IV.11 and IV.12, the perturbation is exerted close to the system equilibrium point as Γ is small by $t = 4$ when the impulse occurs. Hence, we expect similar results when the perturbation is applied at the equilibrium state $\partial_t p(\mathbf{x}, t) = 0$. Yet, future work will expand in this direction to give more conclusive and rigorous results.*

IV.5.4 Case study: Controllable canonical form

To analyse abrupt events in high order systems, we propose, as an offline method, the application of the Euclidean norm to each marginal or joint information rate/entropy production of the random variables in the system. Recall that the Euclidean norm of any time dependant function $\vartheta(t)$ is defined as follows

$$\|\vartheta(t)\| := \left(\int_0^{t_f} \vartheta(\tau)^2 d\tau\right)^{\frac{1}{2}}. \tag{IV.32}$$

[2] More precisely, it seems to forecast the perturbation with an small forecasting horizon.

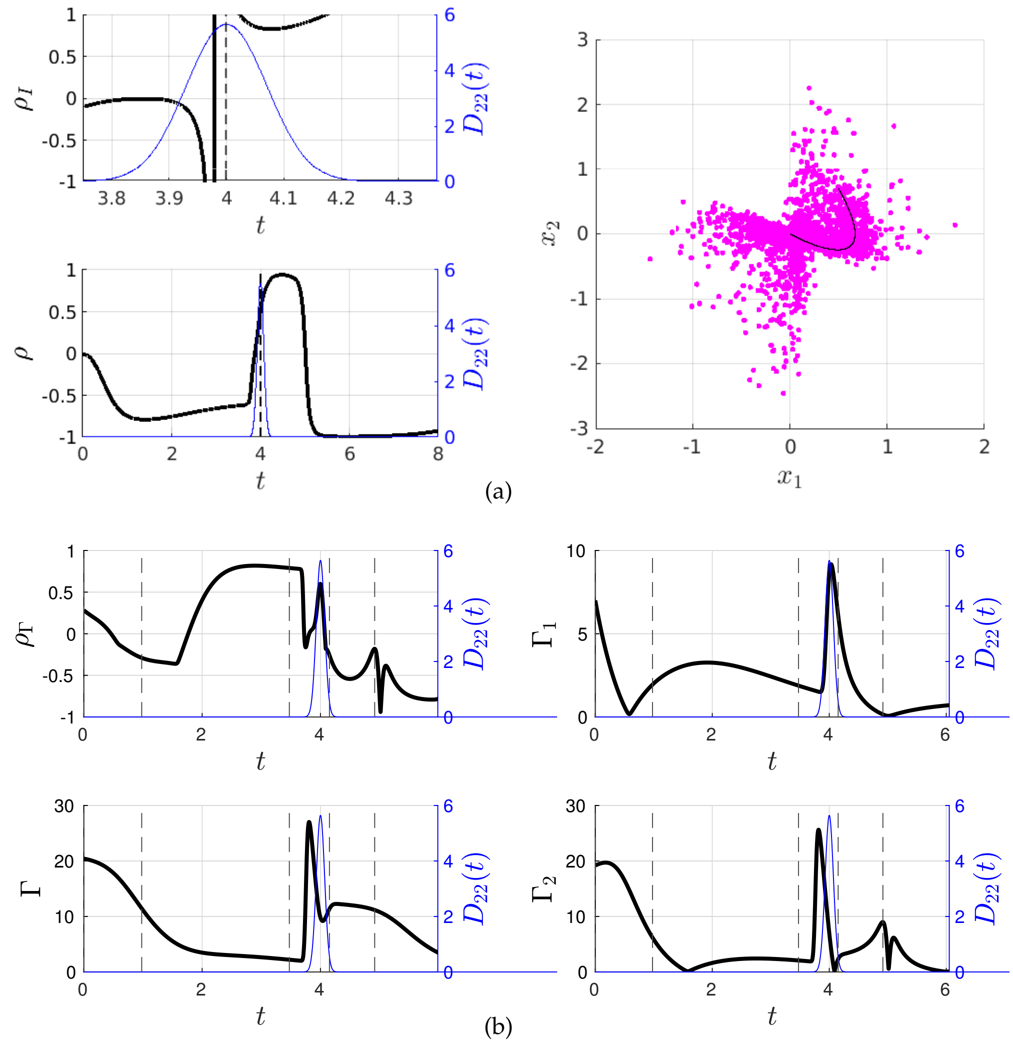

Figure IV.11: Cont.

As a demonstration of this technique, here we study the effects of abrupt events in the noise amplitude matrix $\mathbf{D}(t)$ and the force input $u(t)$ of the popular controllable canonical form of the state-space realization of a linear system given by

$$\dot{\mathbf{x}}(t) = \begin{bmatrix} 0 & 1 & 0 & \cdots & 0 \\ 0 & 0 & 1 & \cdots & 0 \\ \vdots & \vdots & \vdots & \ddots & \vdots \\ 0 & 0 & 0 & \cdots & 1 \\ -d_n & -d_{n-1} & -d_{n-2} & \cdots & -d_1 \end{bmatrix} \mathbf{x}(t) + \begin{bmatrix} 0 \\ \vdots \\ 1 \end{bmatrix} u(t) + \boldsymbol{\xi}(t). \tag{IV.33}$$

Here, $\mathbf{x} := [x_1, x_2, \ldots, x_n]^\top \in \mathbb{R}^n$, $u \in \mathbb{R}$ (see Equation (IV.31)) and $\boldsymbol{\xi} := [\xi_1, \xi_2, \ldots, \xi_n]^\top \in \mathbb{R}^n$ is a vector of random variables with $\langle \xi_i(t) \rangle = 0$, $\langle \xi_i(t)\xi_j(t') \rangle = 2D_{ij}\delta(t-t')$, and D_{ij} defined as in (IV.30). Model (IV.33) provides us with a structure where the input enters a chain of integrators making it to move every state in the Langevin equation (i.e. they are fully controllable). We consider the case when (IV.33) is of 4th order. The

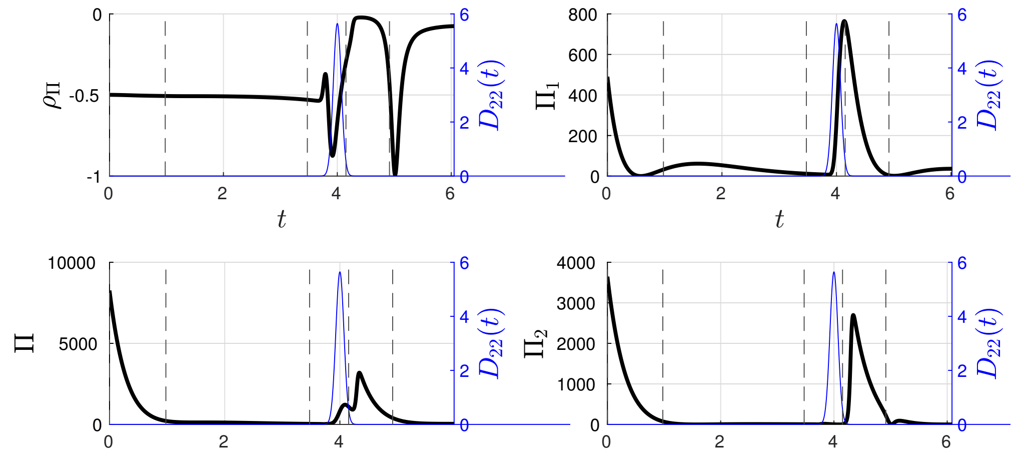

(c)

Figure IV.11: Numerical experiment of an abrupt event analysis in the model (III.80) via correlation coefficients. (a) plots of the total correlation ρ_I, Pearson correlation ρ and a phase portrait of x_1 vs x_2. In the phase portrait, the pink dots and the solid line represent a single trajectory $\mathcal{X}$ and the mean value $\boldsymbol{\mu}$ of (III.80), respectively. (b) plots of the information rate correlation coefficient ρ_Γ, information rate Γ, and the contributions from x_1 and x_2 to the information rate given by Γ_1 and Γ_2, respectively. (c) plots of the entropy production correlation coefficient ρ_Π, entropy production Π, and the contributions from x_1 and x_2 to the entropy production given by Π_1 and Π_2, respectively. Here, the perturbation acts over the covariance $\boldsymbol{\Sigma}$ of (III.80), i.e., $u(t) = D_{11}(t) = 0$ and $D_{22}(t) = 0.001 + \frac{1}{|0.1|\sqrt{\pi}} e^{-\left(\frac{t-4}{0.1}\right)^2}$.

values of the parameters are $\mathbf{d}_4 = [d_1, \ldots, d_n]^\top = [-1.5165, -5.2614, -6.7985, -4.2206]^\top$. In Figures IV.13 to IV.15, we use the notation x_i $\forall i = 1,2,3,4$ and $\mathbf{x}$ to refer to the values of $\Pi, \dot{S}$ and Γ computed from marginal PDF $p(x_i, t)$ and from the joint PDF $p(\mathbf{x}; t)$, respectively.

Figure IV.13a depicts the time evolution of Γ_i, Π_i and $\dot{S}_i$ $\forall i = 1,2,3,4$. It also includes the time evolution of the three dimensional space $(\Gamma, \Pi, \dot{S})$. Figure IV.13b shows the norms of $\Gamma_i, \Pi_i, \dot{S}_i$ $\forall i = 1,2,3,4$ and $\Gamma, \Pi, \dot{S}$ in the form of a spider plot. For instance, the value of the norm of the information rate Γ computed from the joint PDF $p(\mathbf{x}; t)$ and from the marginal PDF $p(x_2, t)$ is $||\Gamma|| \approx 10000$ and $||\Gamma_2|| \approx 31.6$, respectively. As we can see, the effects on Γ_i, Π_i and $\dot{S}_i$ $\forall i = 1,2,3,4$ by the random variables is hierarchical with regards to their amplitude (for example $|\dot{S}_4| > |\dot{S}_3| > |\dot{S}_2| > |\dot{S}_1|$ at almost all the time) and the equilibrium of $(\Gamma, \Pi, \dot{S})$ is $(0,0,0)$.

When we add a perturbation in u which affects directly x_4 (see Equation (IV.33)), we obtain the results shown in Figure IV.14. Such an abrupt event causes a notable increment in the norms of the states (See Figure IV.14b) which still maintains the same hierarchical order in the states (x_4 is the most affected in comparison with x_1) due to the system's structure as expected. The direct effect of the abrupt event on each variable's time evolution is shown in Figure IV.14a. Recall that u is applied directly to x_4. Again, $\dot{S}$ is unperturbed since the event affects only the mean value of the PDF. On the other hand, if we separately include a perturbation in each element D_{ii} of the noise matrix $\mathbf{D}$, similar results occur. Figure IV.15 illustrates the norms of $\Gamma, \Pi, \dot{S}$ in the form of bar plots (after applying perturbations to each D_{ii}). The plots indicate a domino effect in the marginal PDFs as follow. When only D_{11} is perturbed no clear effects can be seen in the rest of the variables but when D_{33} is perturbed x_3, x_2 and x_1 increase their values. Same happens after perturbing D_{44}, again

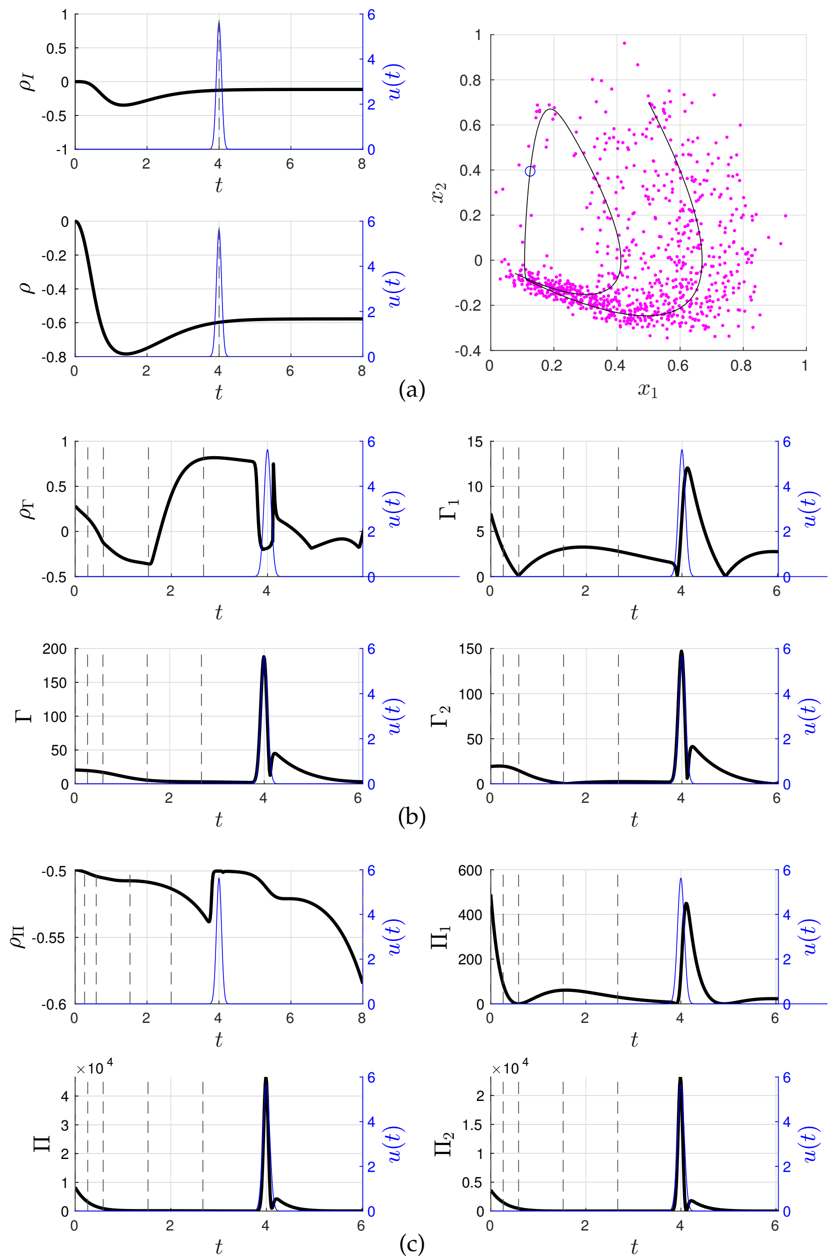

Figure IV.12: Numerical experiment of an abrupt event analysis in the model (III.80) via correlation coefficients. (a) plots of the total correlation ρ_I, Pearson correlation ρ and a phase portrait of x_1 vs x_2. In the phase portrait, the pink dots and the solid line represent a single trajectory $\mathcal{X}$ and the mean value $\boldsymbol{\mu}$ of (III.80), respectively. (b) plots of the information rate correlation coefficient ρ_Γ, information rate Γ, and the contributions from x_1 and x_2 to the information rate given by Γ_1 and Γ_2, respectively. (c) plots of the entropy production correlation coefficient ρ_Π, entropy production Π, and the contributions from x_1 and x_2 to the entropy production given by Π_1 and Π_2, respectively. Here, the perturbation acts over the mean value $\boldsymbol{\mu}$ of (III.80), i.e., $D_{22}(t) = D_{11}(t) = 0$ and $u(t) = \frac{1}{|0.1|\sqrt{\pi}} e^{-\left(\frac{t-4}{0.1}\right)^2}$.

this is due to the structure interaction of the system we are studying. This implies that norms provide an approximate value of the dependence between the variables of the random process.

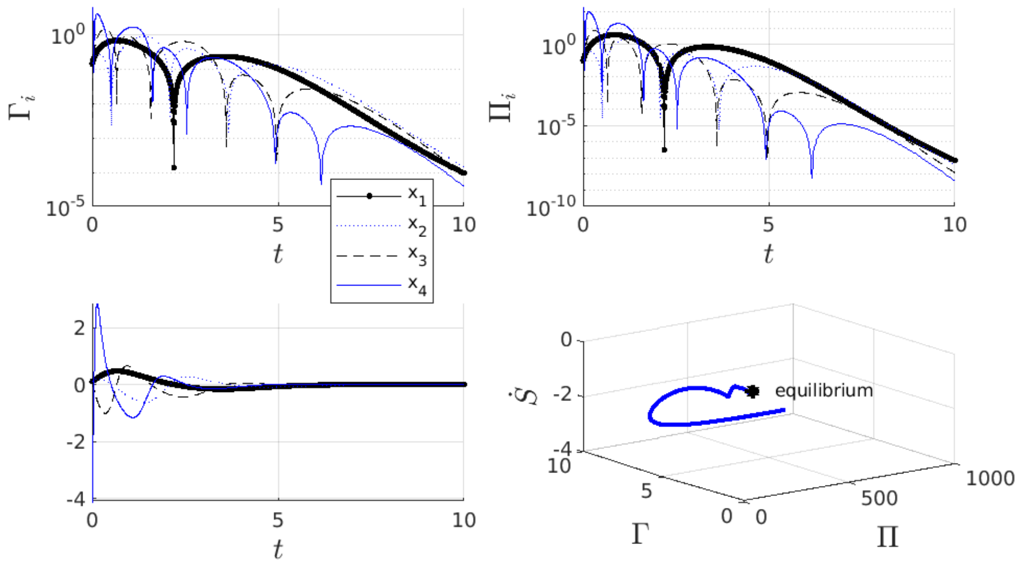

(a)

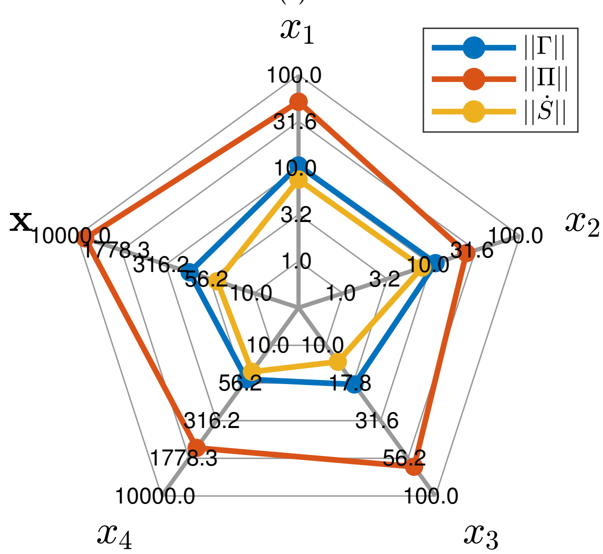

(b)

Figure IV.13: Numerical experiment of an abrupt event analysis in system (IV.33). (a) time evolution of the contribution by the i-th random variable $x_i \forall i = 1, 2, 3, 4$ on the information rate Γ_i (y-axis in log scale), the entropy production Π_i (y-axis in log scale) and entropy rate $\dot{S}_i$. The plot also contains the time evolution of the three dimensional space $(\Gamma, \Pi, \dot{S})$. (b) Euclidean norms of $\Gamma_i, \Pi_i, \dot{S}_i \forall i = 1, 2, 3, 4$ and $\Gamma, \Pi, \dot{S}$ in the form of a spider plot. In the simulations, the system has no perturbation, i.e., $D_{ii}(t) = u(t) = 0$.

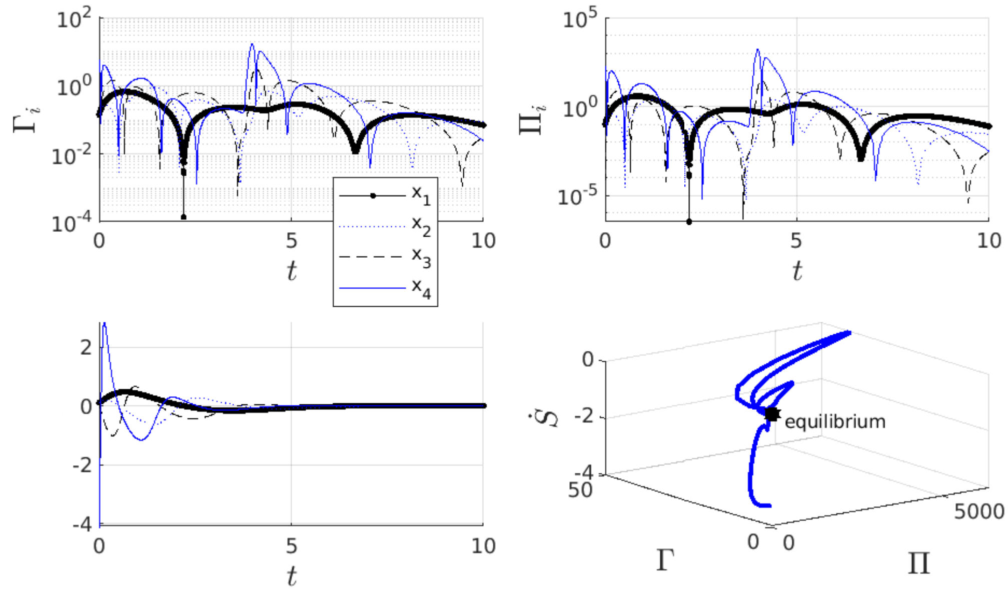

(a)

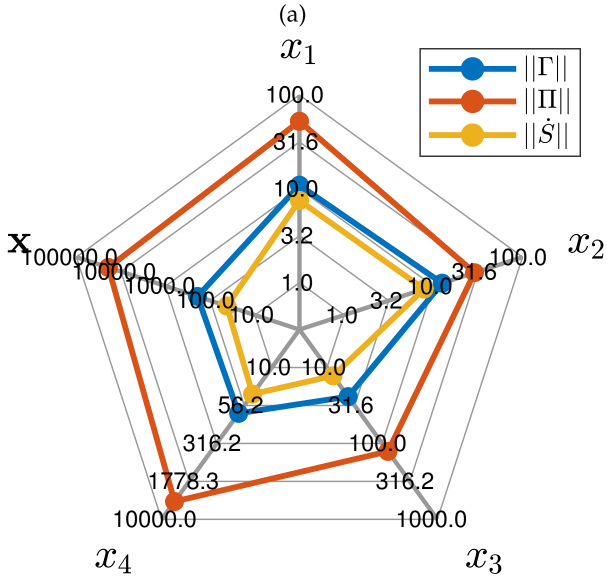

(b)

Figure IV.14: Numerical experiment of an abrupt event analysis in system (IV.33). (a) time evolution of the contribution by the i-th random variable $x_i \forall i = 1, 2, 3, 4$ on the information rate Γ_i (y-axis in log scale), the entropy production Π_i (y-axis in log scale) and entropy rate $\dot{S}_i$. The plot also contains the time evolution of the three dimensional space $(\Gamma, \Pi, \dot{S})$. (b) Euclidean norms of $\Gamma_i, \Pi_i, \dot{S}_i \forall i = 1, 2, 3, 4$ and $\Gamma, \Pi, \dot{S}$ in the form of a spider plot. In the simulations, the system has a perturbation in the mean value of the system $\boldsymbol{\mu}$, i.e., $D_{ii}(t) = 0, u(t) \neq 0$ at $t_p = 4$.

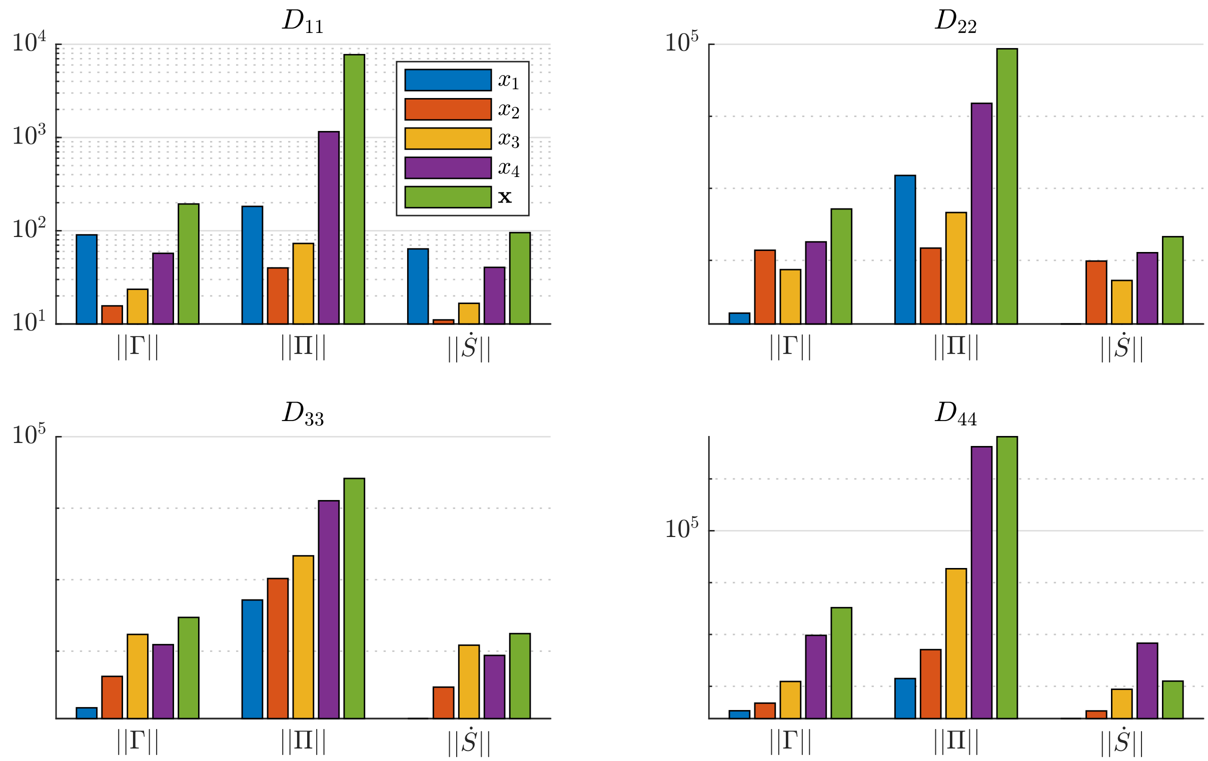

Figure IV.15: Abrupt event analysis in system (IV.33) using the norms of Π, $\dot{S}$, Γ at the marginal PDF $p(x_i, t)$ and the joint PDF $p(\mathbf{x}; t)$. Each plot depicts a perturbation on a given D_{ii} at $t_p = 6$ in system (IV.33).

Chapter concluding remarks

We have investigated the prediction capability of information theory by focusing on how sensitive information-geometric theory (information length diagnostics) [69; 89; 64; 66; 90; 70] and one of the entropy-based information theoretical methods (information flow) [95; 96] are to abrupt changes. Specifically, we proposed a non-autonomous Kramers equation by including sudden perturbations to the system as impulses to mimic the onset of a sudden event and calculate time-dependent probability density functions (PDFs) and various statistical quantities with the help of numerical simulations. It was explicitly shown that the information flow like any other entropy-based measures is insensitive to to perturbations which do not affect entropy (such as the mean values). Specifically, the information length diagnostics are very sensitive to both perturbations in the covariance $\mathbf{\Sigma}(t)$ and mean $\boldsymbol{\mu}$ of the process while the information flow only detects perturbations in its covariance. Furthermore, we demonstrated that information length diagnostics predict the onset of an ongoing perturbation earlier than the information flow; the peaks of $T_{1\to 2}$ (or $T_{2\to 1}$) tend to proceed the impulse peak while the peak of information length diagnostics Γ^2 tends to precede the impulse peak.

In addition, we demonstrate that the information rate and entropy production correlation coefficients ρ_Γ and ρ_Π, respectively, detect the proposed perturbation function (IV.9) modelling of an abrupt event in the first and second moments of the stochastic dynamics, respectively. For higher-order systems, the norm of the information/thermodynamic quantities represents a fair approximation of the correlation between all the system random variables.

We expect that some of the results presented in this work would be useful in different engineering applications [3; 118] since linear approximations are often useful [119] for control engineering applications. For instance, one can develop an information-geometric cost function for control design to achieve a guided self-organisation [120; 121], instead of using entropy as a cost function [122]. Given high variabilities involved in complexity and emergent behaviour [91; 92; 93], it will be interesting to further extend this work to investigate interconnection of the components in a complex system, or causality and also to non-linear, non-Gaussian models or real data.

AIV Appendix Chapter IV

AIV.1 Derivations of $\boldsymbol{\mu}$ and $\Sigma(t)$

After a long algebra, we can show that $\langle x_1(t)\rangle$ and $\langle x_2(t)\rangle$ in

$$\boldsymbol{\mu} = \begin{bmatrix} \langle x_1(t)\rangle \\ \langle x_2(t)\rangle \end{bmatrix} \tag{AIV.34}$$

is given by the following:

$$\begin{aligned}
\langle x_1(t)\rangle=&\tfrac{1}{2(\lambda_1-\lambda_2)}\left(d\,\mathrm{sgn}(c)\left(e^{\frac{1}{4}\lambda_1 p_1(t)}\left(\mathrm{erf}\left(q_1(t)\right)-\mathrm{erf}\left(r_1(t)\right)\right)+e^{\frac{1}{4}\lambda_2 p_2(t)}\left(\mathrm{erf}\left(r_2(t)\right)-\mathrm{erf}\left(q_2(t)\right)\right)\right)\right.\\
&\left.+2e^{\lambda_1 t}(x_1(0)(\gamma+\lambda_1)+x_2(0))-2e^{\lambda_2 t}(x_1(0)(\gamma+\lambda_2)+x_2(0))\right) \qquad \text{(AIV.35)}\\
\langle x_2(t)\rangle=&\tfrac{1}{2(\lambda_1-\lambda_2)}\left(d\,\mathrm{sgn}(c)\left(\lambda_1 e^{\frac{1}{4}\lambda_1 p_1(t)}\left(\mathrm{erf}\left(q_1(t)\right)-\mathrm{erf}\left(r_1(t)\right)\right)+\lambda_2 e^{\frac{1}{4}\lambda_2 p_2(t)}\left(\mathrm{erf}\left(r_2(t)\right)-\mathrm{erf}\left(q_2(t)\right)\right)\right)\right.\\
&\left.+2e^{\lambda_1 t}\left(\lambda_1 x_2(0)-\omega^2 x_1(0)\right)+e^{\lambda_2 t}\left(2\omega^2 x_1(0)-2\lambda_2 x_2(0)\right)\right) \qquad \text{(AIV.36)}
\end{aligned}$$

where $p_1(t)=c^2\lambda_1+4t-4t_{2,0}$, $p_2(t)=c^2\lambda_2+4t-4t_{2,0}$, $q_1(t)=\frac{c^2\lambda_1+2t-2t_{2,0}}{2c}$, $q_2(t)=\frac{c^2\lambda_2+2t-2t_{2,0}}{2c}$, $r_1(t)=\frac{c\lambda_1}{2}-\frac{t_{2,0}}{c}$ and $r_2(t)=\frac{c\lambda_2}{2}-\frac{t_{2,0}}{c}$.

On the other hand, the covariance matrix Σ can be shown to have the following elements:

$$\begin{aligned}
\Sigma_{11}(t)=&\tfrac{1}{(\lambda_1-\lambda_2)^2}\left(\left(-\tfrac{abe^{-2t_{1,0}(\lambda_1+\lambda_2)}}{|a|}\left(-2\mathrm{erf}\left(\tfrac{1}{2}a(\lambda_1+\lambda_2)-\tfrac{t_{1,0}}{a}\right)\exp\left(\tfrac{1}{4}(\lambda_1+\lambda_2)\left(a^2(\lambda_1+\lambda_2)+4(t+t_{1,0})\right)\right)\right.\right.\right.\\
&+\mathrm{erf}\left(a\lambda_1-\tfrac{t_{1,0}}{a}\right)e^{a^2\lambda_1^2+2\lambda_1 t+2\lambda_2 t_{1,0}}+\mathrm{erf}\left(a\lambda_2-\tfrac{t_{1,0}}{a}\right)e^{a^2\lambda_2^2+2\lambda_1 t_{1,0}+2\lambda_2 t}\Big)\\
&+\tfrac{abe^{-2(\lambda_1+\lambda_2)(t+t_{1,0})}}{|a|}\left(-2\mathrm{erf}\left(\tfrac{a^2(\lambda_1+\lambda_2)+2t-2t_{1,0}}{2a}\right)\exp\left(\tfrac{1}{4}(\lambda_1+\lambda_2)\left(a^2(\lambda_1+\lambda_2)+4(3t+t_{1,0})\right)\right)\right.\\
&\left.+\mathrm{erf}\left(\tfrac{a^2\lambda_1+t-t_{1,0}}{a}\right)e^{a^2\lambda_1^2+4\lambda_1 t+2\lambda_2(t+t_{1,0})}+\mathrm{erf}\left(\tfrac{a^2\lambda_2+t-t_{1,0}}{a}\right)e^{a^2\lambda_2^2+2\lambda_1(t+t_{1,0})+4\lambda_2 t}\right)\\
&+D_0\left(-\tfrac{4e^{t(\lambda_1+\lambda_2)}}{\lambda_1+\lambda_2}+\tfrac{e^{2\lambda_1 t}}{\lambda_1}+\tfrac{e^{2\lambda_2 t}}{\lambda_2}\right)-\tfrac{D_0(\lambda_1-\lambda_2)^2}{\lambda_1\lambda_2(\lambda_1+\lambda_2)}\\
&+\left(\left(\gamma+\lambda_1\right)e^{\lambda_1 t}-(\gamma+\lambda_2)e^{\lambda_2 t}\right)\left(\Sigma_{11}^0(\gamma+\lambda_1)e^{\lambda_1 t}-\Sigma_{11}^0(\gamma+\lambda_2)e^{\lambda_2 t}+\Sigma_{12}^0\left(e^{\lambda_1 t}-e^{\lambda_2 t}\right)\right)\\
&\left.+\left(e^{\lambda_1 t}-e^{\lambda_2 t}\right)\left(\Sigma_{12}^0(\gamma+\lambda_1)e^{\lambda_1 t}-\Sigma_{12}^0(\gamma+\lambda_2)e^{\lambda_2 t}+\Sigma_{22}^0\left(e^{\lambda_1 t}-e^{\lambda_2 t}\right)\right)\right) \qquad \text{(AIV.37)}\\
\Sigma_{22}(t)=&\tfrac{1}{(\lambda_1-\lambda_2)^2}\left(\left(-\tfrac{abe^{-2(\lambda_1+\lambda_2)(t+2t_{1,0})}}{|a|}\left(-2\lambda_1\lambda_2\mathrm{erf}\left(\tfrac{1}{2}a(\lambda_1+\lambda_2)-\tfrac{t_{1,0}}{a}\right)\exp\left(\tfrac{1}{4}(\lambda_1+\lambda_2)\left(a^2(\lambda_1+\lambda_2)\right.\right.\right.\right.\right.\\
&\left.\left.+12(t+t_{1,0})\right)\right)+2\lambda_1\lambda_2\mathrm{erf}\left(\tfrac{a^2(\lambda_1+\lambda_2)+2t-2t_{1,0}}{2a}\right)\exp\left(\tfrac{1}{4}(\lambda_1+\lambda_2)\left(a^2(\lambda_1+\lambda_2)+12(t+t_{1,0})\right)\right)\\
&+\lambda_1^2\mathrm{erf}\left(a\lambda_1-\tfrac{t_{1,0}}{a}\right)e^{a^2\lambda_1^2+4\lambda_1 t+2\lambda_1 t_{1,0}+2\lambda_2 t+4\lambda_2 t_{1,0}}-\lambda_1^2\mathrm{erf}\left(\tfrac{a^2\lambda_1+t-t_{1,0}}{a}\right)e^{a^2\lambda_1^2+4\lambda_1 t+2\lambda_1 t_{1,0}+2\lambda_2 t+4\lambda_2 t_{1,0}}\\
&\left.+\lambda_2^2\mathrm{erf}\left(a\lambda_2-\tfrac{t_{1,0}}{a}\right)e^{a^2\lambda_2^2+2\lambda_1 t+4\lambda_1 t_{1,0}+4\lambda_2 t+2\lambda_2 t_{1,0}}-\lambda_2^2\mathrm{erf}\left(\tfrac{a^2\lambda_2+t-t_{1,0}}{a}\right)e^{a^2\lambda_2^2+2\lambda_1 t+4\lambda_1 t_{1,0}+4\lambda_2 t+2\lambda_2 t_{1,0}}\right)\\
&+\tfrac{D_0\left(\lambda_1^2\left(e^{2\lambda_1 t}-1\right)+\lambda_1\lambda_2\left(-4e^{t(\lambda_1+\lambda_2)}+e^{2\lambda_1 t}+e^{2\lambda_2 t}+2\right)+\lambda_2^2\left(e^{2\lambda_2 t}-1\right)\right)}{\lambda_1+\lambda_2}\\
&\left.+\omega^2\left(e^{\lambda_1 t}-e^{\lambda_2 t}\right)\left(\Sigma_{11}^0\omega^2\left(e^{\lambda_1 t}-e^{\lambda_2 t}\right)+\Sigma_{12}^0\left(2\lambda_2 e^{\lambda_2 t}-2\lambda_1 e^{\lambda_1 t}\right)\right)+\Sigma_{22}^0\left(\lambda_1 e^{\lambda_1 t}-\lambda_2 e^{\lambda_2 t}\right)^2\right), \qquad \text{(AIV.38)}
\end{aligned}$$

$$
\begin{aligned}
\Sigma_{12}(t)=&\tfrac{1}{(\lambda_1-\lambda_2)^2}\Big(\Big(-\tfrac{abe^{-2t_{1,0}(\lambda_1+\lambda_2)}}{|a|}\Big(-(\lambda_1+\lambda_2)\mathrm{erf}\left(\tfrac{1}{2}a(\lambda_1+\lambda_2)-\tfrac{t_{1,0}}{a}\right)\exp\left(\tfrac{1}{4}(\lambda_1+\lambda_2)\left(a^2(\lambda_1+\lambda_2)\right.\right.\\
&\left.\left.+4(t+t_{1,0})\right)\right)+\lambda_1\mathrm{erf}\left(a\lambda_1-\tfrac{t_{1,0}}{a}\right)e^{a^2\lambda_1^2+2\lambda_1 t+2\lambda_2 t_{1,0}}+\lambda_2\mathrm{erf}\left(a\lambda_2-\tfrac{t_{1,0}}{a}\right)e^{a^2\lambda_2^2+2\lambda_1 t_{1,0}+2\lambda_2 t}\Big)\\
&+\tfrac{abe^{-2(\lambda_1+\lambda_2)(t+t_{1,0})}}{|a|}\Big(-(\lambda_1+\lambda_2)\mathrm{erf}\left(\tfrac{a^2(\lambda_1+\lambda_2)+2t-2t_{1,0}}{2a}\right)\exp\left(\tfrac{1}{4}(\lambda_1+\lambda_2)\left(a^2(\lambda_1+\lambda_2)+4(3t+t_{1,0})\right)\right)\\
&+\lambda_1\mathrm{erf}\left(\tfrac{a^2\lambda_1+t-t_{1,0}}{a}\right)e^{a^2\lambda_1^2+4\lambda_1 t+2\lambda_2(t+t_{1,0})}+\lambda_2\mathrm{erf}\left(\tfrac{a^2\lambda_2+t-t_{1,0}}{a}\right)e^{a^2\lambda_2^2+2\lambda_1(t+t_{1,0})+4\lambda_2 t}\Big)\\
&+D_0\left(e^{\lambda_1 t}-e^{\lambda_2 t}\right)^2-\omega^2\left(e^{\lambda_1 t}-e^{\lambda_2 t}\right)\left(\Sigma_{11}^0(\gamma+\lambda_1)e^{\lambda_1 t}-\Sigma_{11}^0(\gamma+\lambda_2)e^{\lambda_2 t}+\Sigma_{12}^0\left(e^{\lambda_1 t}-e^{\lambda_2 t}\right)\right)\\
&+\left(\lambda_1 e^{\lambda_1 t}-\lambda_2 e^{\lambda_2 t}\right)\left(\Sigma_{12}^0(\gamma+\lambda_1)e^{\lambda_1 t}-\Sigma_{12}^0(\gamma+\lambda_2)e^{\lambda_2 t}+\Sigma_{22}^0\left(e^{\lambda_1 t}-e^{\lambda_2 t}\right)\right)\Big)
\end{aligned}
\tag{AIV.39}
$$

Here, the superscript ^{0} denotes the initial time $t=0$ and $\lambda_{1,2}=-\frac{1}{2}\left(\gamma\pm\sqrt{\gamma^2-4\omega^2}\right)$. Besides, it can be proved that

$$
\lim_{t\to\infty}\Sigma_{11}(t)=\frac{D}{\gamma\omega^2},\quad \lim_{t\to\infty}\Sigma_{22}(t)=\frac{D}{\gamma},\quad \lim_{t\to\infty}\Sigma_{12}(t)=\lim_{t\to\infty}\Sigma_{21}(t)=0. \tag{AIV.40}
$$

AIV.2 Derivation of the Information Flow from the Kramers equation

We provide the main steps used in the derivation of $T_{2\to1}$ and $T_{1\to2}$ after substituting Equations (IV.18) in Equations (IV.2)–(IV.3). For $T_{2\to1}$ we have

$$
\begin{aligned}
T_{2\to1} &= -\int d\mathbf{x}P(\mathbf{x};t)x_2\partial_{x_1}\left[\ln P_{x_1}(x_1;t)-\ln P(\mathbf{x};t)\right]\\
&= -\int d\mathbf{x}P(\mathbf{x};t)\partial_{x_1}\left[x_2\ln P_{x_1}(x_1;t)\right]+\int d\mathbf{x}P(\mathbf{x};t)\partial_{x_1}\left[x_2\ln P(\mathbf{x};t)\right]\\
&= -\int d\mathbf{x}P(\mathbf{x};t)\partial_{x_1}\left[x_2\ln P_{x_1}(x_1;t)\right]+\int d\mathbf{x}\partial_{x_1}\left[x_2P(\mathbf{x};t)\right]\\
&= -\int d\mathbf{x}P(x_2|x;t)\partial_{x_1}\left[x_2P_{x_1}(x_1;t)\right]+0\\
&= \left\langle\frac{x_2(x_1-\langle x_1\rangle)}{\Sigma_{11}}\right\rangle=\frac{1}{\Sigma_{11}}\left(\langle x_1\rangle\langle x_2\rangle+\Sigma_{12}-\langle x_1\rangle\langle x_2\rangle\right)\\
&= \frac{\Sigma_{12}}{\Sigma_{11}}=\frac{1}{2}\frac{d}{dt}\ln\Sigma_{11}.
\end{aligned}
\tag{AIV.41}
$$

On the other hand, for $T_{1\to2}$ we have

$$
\begin{aligned}
T_{1\to2}=&\int d\mathbf{x}P(\mathbf{x};t)\left[\gamma x_2+\omega^2x_1-u\right]\partial_{x_2}\ln\frac{P_{x_2}(x_2;t)}{P(\mathbf{x};t)}+D\int d\mathbf{x}P(\mathbf{x};t)\partial_{x_2}\left(\ln P(\mathbf{x};t)\right)\partial_{x_2}\left(\ln\frac{P_{x_2}(x_2;t)}{P(\mathbf{x};t)}\right)\\
=&\int d\mathbf{x}P(\mathbf{x};t)\left[\gamma x_2+\omega^2x_1-u\right]\left\{\frac{\partial_{x_2}P_{x_2}(x_2;t)}{P_{x_2}(x_2;t)}-\frac{\partial_{x_2}P(\mathbf{x};t)}{P(\mathbf{x};t)}\right\}\\
&+D\int d\mathbf{x}P(\mathbf{x};t)\frac{\partial_{x_2}P(\mathbf{x};t)}{P(\mathbf{x};t)}\left\{\frac{\partial_{x_2}P_{x_2}(x_2;t)}{P_{x_2}(x_2;t)}-\frac{\partial_{x_2}P(\mathbf{x};t)}{P(\mathbf{x};t)}\right\}\\
=&\int d\mathbf{x}P(\mathbf{x};t)\left[\gamma x_2+\omega^2x_1-u\right]\left\{\partial_{x_2}\left[-\tfrac{(x_2-\langle x_2\rangle)^2}{2\Sigma_{22}}\right]-\partial_{x_2}\left[Q(\mathbf{x})\right]\right\}\\
&+D\int d\mathbf{x}P(\mathbf{x};t)\left\{\partial_{x_2}\left[-\tfrac{(x_2-\langle x_2\rangle)^2}{2\Sigma_{22}}\right]\partial_{x_2}\left[Q(\mathbf{x})\right]-\left(\partial_{x_2}\left[Q(\mathbf{x})\right]\right)^2\right\}\\
=&\left\langle\left(\gamma x_2+\omega^2x_1-u\right)\left[-\tfrac{(x_2-\langle x_2\rangle)}{\Sigma_{22}}\right]\right\rangle-\left\langle\left(\gamma x_2+\omega^2x_1-u\right)\partial_{x_2}\left[Q(\mathbf{x})\right]\right\rangle\\
&+\left\langle D\left[-\tfrac{(x_2-\langle x_2\rangle)}{\Sigma_{22}}\right]\partial_{x_2}\left[Q(\mathbf{x})\right]\right\rangle-\left\langle D\left(\partial_{x_2}\left[Q(\mathbf{x})\right]\right)^2\right\rangle
\end{aligned}
$$

$$
\begin{aligned}
&= \left\langle \left(\gamma x_2 + \omega^2 x_1 - u\right) \left[-\tfrac{(x_2 - \langle x_2 \rangle)}{\Sigma_{22}}\right] \right\rangle \\
&\quad + \frac{1}{|\Sigma|} \left\langle \left(\gamma x_2 + \omega^2 x_1 - u\right) \left(-\langle x_2 \rangle \Sigma_{11} + \langle x_1 \rangle \Sigma_{12} - \Sigma_{12} x_1 + \Sigma_{11} x_2\right) \right\rangle \\
&\quad + \frac{D}{|\Sigma|} \left\langle \left[\tfrac{(x_2 - \langle x_2 \rangle)}{\Sigma_{22}}\right] \left(-\langle x_2 \rangle \Sigma_{11} + \langle x_1 \rangle \Sigma_{12} - \Sigma_{12} x_1 + \Sigma_{11} x_2\right) \right\rangle \\
&\quad - \frac{D}{|\Sigma|^2} \left\langle (-\langle x_2 \rangle \Sigma_{11} + \langle x_1 \rangle \Sigma_{12} - \Sigma_{12} x_1 + \Sigma_{11} x_2)^2 \right\rangle \\
&= -\gamma - \omega^2 \frac{\Sigma_{12}}{\Sigma_{22}} + \gamma + \frac{D}{\Sigma_{22}} - \frac{D\Sigma_{11}}{|\Sigma|} = -\omega^2 \frac{\Sigma_{12}}{\Sigma_{22}} - D \frac{\Sigma_{12}^2}{|\Sigma| \Sigma_{22}}. \qquad \text{(AIV.42)}
\end{aligned}
$$

Here, we have used the properties $\langle x_1^2 \rangle = \Sigma_{11} + \langle x_1 \rangle^2$, $\langle x_1 x_2 \rangle = \Sigma_{12} + \langle x_1 \rangle \langle x_2 \rangle$, $\Sigma_{12} = \Sigma_{21}$, and $Q(\mathbf{x}) = -\frac{1}{2}(\mathbf{x} - \boldsymbol{\mu})^T \Sigma^{-1} (\mathbf{x} - \boldsymbol{\mu})$.

V

Information geometry based control

Chapter summary

Controlling the time evolution of a probability distribution that describes the dynamics of a given complex system is a challenging problem. If successful, this will benefit a wide range of practical scenarios, e.g., controlling mesoscopic systems. In such a context, this chapter proposes a method of control based on the so-called model-predictive-control technique and the information geometric theory for controlling the time evolution of probability distributions of linear and non-linear Langevin systems. Specifically, the method combines an online optimisation algorithm and the concept of information length to minimise the deviations from the information length's geodesic of the system's probability distribution through time. Additionally, we simulate the effects on the closed-loop system's entropy production and entropy rate. The control algorithm is tested numerically in the Ornstein–Uhlenbeck process, the Kramers equation and a simple cubic system illustrating its feasibility. Furthermore, we explore the application of a non-dynamic control algorithm called the full-state feedback control to solve different cost functions in terms of the system's information rate and entropy production demonstrating the effects of IL's geodesic in the stochastic thermodynamics.

This chapter is based on the following author's publications [10; 11; 9]:

keywords: Model-predictive-control; Stochastic control; Optimisation

V.1 Introduction

From Chapter II, we know that time-varying probability density functions (PDFs) are a preferred approach when describing the dynamics governing different complex systems through statistical methods. In addition, we noted that PDFs also appear commonly in fields including inference control or stochastic thermodynamics where their value is obtained through data analysis or by solving the Fokker-Planck (FP) equation of an Itô or Stratonovich stochastic differential equation, respectively.

Inspired by control theory [82], if the dynamics of the system of our interest are proved to be governed by an FP equation, we can consider the regulation (set to a constant value) or tracking (follow a time-varying reference) control problems of the time-varying PDFs [64]. In other words, we can design control strategies to guide the PDFs time evolution through the information that the FP equation provides. Although controlling PDFs seems unfeasible through control engineering methods, it has become viable in applications like colloidal systems thanks to technology such as optical tweezers [81; 123; 124]. In this regard, the seminal work [125; 126] presents a methodology to control the system PDF governed by a Fokker-Planck equation [30]. Further developments of this work include [127] which discusses a bilinear optimal control problem where the control function depends on time and space. In [128], authors prove the existence of optimal controls while considering first-order necessary conditions in the optimisation problem.

Since, FP equations are often mathematical descriptions of mesoscopic systems (for further details, see [30]), i.e. systems of nano/micro scale such as molecular motors, the system's PDF evolution through time may also need to satisfy multiple of the so-called "thermodynamic constraints" to be called "efficient". For instance, the system may need to minimise entropy production [122; 129], information variability [130], or self-organisation [51]. The addition of these "thermodynamic constraints" in the optimisation process implies an extension of the current literature FP control results.

From what we learned at Chapter III, we can perceive that a theory which may provide us with insights to solve the previously mentioned optimisation problems comes from information geometry. Recall that information geometry results out of the combination of information theory and differential geometry [42]. Additionally, as an emerging field, information geometry proposes new solutions to tasks such as maximum likelihood estimation [131], state prediction [132; 7], quantification of causality [16; 108; 103] or maximum work extraction [64; 96]. In stochastic thermodynamics [23; 95], information geometry is used to obtain time-varying descriptions of the aforementioned constraints. For instance, based on the well known Cauchy-Schwartz inequality [133], [134] presents an inequality between the *Fisher divergence* [135] and the *information length* (IL) [6; 7] to quantify the amount of the disorder in an irreversible decay processes. In [64], the geodesic of IL is used to describe the path with the least amount of statistical variations connecting the initial and final probability distributions of the system dynamics (for further details, see [130]). Hence, information geometry can be used in a control protocol to impose geodesic dynamics on the system's PDF time evolution such that the system behaves with the minimum "geometric information variability" [51]. The design and application of a technique that allows us to achieve such minimum geometric information variability constitutes the main problem to be solved in this Chapter.

Before we create an optimal protocol for the PDF's time evolution, it is important to briefly review some of the existing control algorithms. In this vein, the literature presents significant amount of control procedures from the classical PID control [136] to more sophisticated algorithms like data-driven, model-free or fractional-order controls (for instance, see [118; 137; 138]). Nonetheless, for our scenario, we require an algorithm to handle complicated optimisation problems while being a feasible option to be implemented in an experimental setup for future work.

To solve our problem, we can consider one of the most popular optimisation-based control techniques called the model-predictive-control (MPC) scheme [139]. Generally, MPC is an online optimisation algorithm for constrained control problems whose benefits have been noticed in applications to robotics [140], solar energy [141] or bioengineering [142]. Furthermore, MPC can be easily implemented thanks to packages such as CasADi [143] or the Hybrid Toolbox [144].

Based on the presented discussion, the chapter presents the solution of an optimisation problem which consist of a cost function combining the concepts of information length and the quadratic-regulator (QR) [145] to guide the system's PDF time evolution through the path with the minimum geometric information variability (the geodesic of the information length) via MPC. In our applications, the system's PDF will remain Gaussian at all instants of time given that the system's initial conditions follow a Gaussian distribution or that we use the Laplace assumption. The restriction to Gaussian dynamics enables us to use a set of deterministic differential equations to describe the dynamics of the mean and covariance of the Gaussian distribution (See Proposition II.7) as part of the prediction algorithm in the MPC method.

As mentioned in the Chapter's summary, the algorithm is applied to the Ornstein–Uhlenbeck process [67], the Kramers equation [7] and a cubic stochastic differential equation [11]. As noted in Chapter II, such systems are used to describe a particle over a heat reservoir (*mesoscopic stochastic dynamics*) and, in practice, the dynamics of both the noise amplitude and mean value in such systems can be manipulated via changes in temperature and optical tweezers, respectively [23; 146; 124]. Through the application of previous results from [62], the effects of the MPC method in the Ornstein–Uhlenbeck and cubic processes' stochastic thermodynamics are analysed by simulating the values of entropy production and entropy rate in the closed-loop system. In the chapter, we also present a brief description of the BIBO stability conditions which are considered to constrain the control actions proposed by the MPC. Furthermore, we explore the application of a non-dynamic control algorithm called the full-state feedback control to solve different cost functions in terms of the system's information rate and entropy production demonstrating the effects of IL's geodesic in the stochastic thermodynamics. Finally, we give a set of concluding remarks and a discussion of the future work.

V.2 *Minimum information variability problem*

Before we proceed, let us explain in more detail how IL can be used to minimise deviations from the geodesic of the system's PDF time evolution. In [134], the authors use the inequality $\mathcal{J}(t_f) \geq \mathcal{L}(t_f)^2$ where $\mathcal{J}(t_f) = \tau \int_{t_0}^{t_f} \Gamma^2(t)\,\mathrm{d}t = \int_{t_0}^{t_f} \mathrm{d}t \int \mathrm{d}x \frac{1}{p(x;t)} \left[\frac{\partial p(x;t)}{\partial t}\right]^2$ (Fisher divergence) with $\tau = t_f - t_0$ and $\mathcal{L}$ given by (III.21). Such inequality follows from the Cauchy-Schwartz inequality $\int \Gamma^2\,\mathrm{d}t \int u^2\,\mathrm{d}t \geq \left(\int \Gamma u\,\mathrm{d}t\right)^2$ with $u = 1$. But, most importantly, the equality holds for the minimum path where Γ is constant (see, e.g. [147; 134]), and the deviation from this equality is said to quantify the amount of the disorder in an irreversible process [134].

From [130], such statement can be clarified by the following procedure. Let us define the time-average for a function $f(t)$ as $\mathbb{E}[f(t)] = \frac{1}{\tau}\int_{t_0}^{t_f} f(t)\,\mathrm{d}t$. Then, we can define the time-averaged variance

$$\sigma^2 = \frac{\mathcal{J} - \mathcal{L}^2}{\tau^2} = \mathbb{E}[\Gamma^2] - \mathbb{E}[\Gamma]^2 \geq 0. \tag{V.1}$$

Equation (V.1) describes an accumulative deviation from the geodesic connecting the initial and final distributions of the system dynamics. Thus, we can conclude that by setting Γ as a constant, we obtain a geodesic that defines a path where the process has the minimum *geometric information variability*.

V.3 *Minimum variability control in Gaussian dynamics*

In a stochastic Gaussian process, to drive the system's PDF time evolution through the geodesic of IL while also having a desired set-point at time $t = t_f$, we propose the following cost function

$$J = \int_0^{t_f} \left(I_L(\Gamma^2(\tau) - \Gamma^2(0))^2 + (\mathbf{Y}(\tau) - \mathbf{Y}_d(\tau))^\top \mathbf{Q}\,(\mathbf{Y}(\tau) - \mathbf{Y}_d(\tau)) + \mathbf{c}^\top(\tau)\mathbf{R}\mathbf{c}(\tau) \right) \mathrm{d}\tau, \tag{V.2}$$

where $I_L \in \mathbb{R}, \mathbf{Q} \in \mathbb{R}^{(n+n^2)\times(n+n^2)}$, $\mathbf{Y} := [\boldsymbol{\mu}, \mathbf{vec}(\boldsymbol{\Sigma})]^\top \in \mathbb{R}^{n+n^2}$ is the vector of states $\boldsymbol{\mu}$ and $\mathbf{vec}(\boldsymbol{\Sigma})$[1] that define the time evolution of $p(\mathbf{x};t)$ as described by Proposition II.6 and II.7 when considering linear and non-linear SDE, respectively. $\mathbf{Y}_d = [\boldsymbol{\mu}_d, \mathbf{vec}(\boldsymbol{\Sigma}_d)]^\top$ is the desired position of the $n + n^2$ states defined by $\boldsymbol{\mu}_d$ and $\boldsymbol{\Sigma}_d$ at time t, and $\mathbf{c} \in \mathbb{R}^m$ (such that $m \leq 1 + n^2$) is the vector of controls defined by $\mathbf{c} = [c_1, c_2, \ldots, c_m]^\top := [u(t), \mathbf{w} := \{(D_{ij} | D_{ij} \neq 0 \in \mathbf{D} \forall i, j = 1, 2, \ldots, n\}]^\top$, therefore $\mathbf{R} \in \mathbb{R}^{m\times m}$. In this work, we call Equation (V.2) *The Information Length Quadratic Regulator* (IL-QR). As it will be discussed in §V.3.2, the solution of (V.2) will be obtained via a numerical scheme which allows us to avoid analytic complications while being useful for practical scenarios. To find the geodesic dynamics analytically, we can use the solution of the Euler-Lagrange equations of IL. The steps of such approach are discussed and successfully applied in [64] for a first order

[1] $\mathbf{vec}(\mathbf{A})$ of a matrix $\mathbf{A} \in \mathbb{R}^{m\times n}$ stands for the vectorisation of the matrix $\mathbf{A}$, i.e., a linear transformation which converts the matrix $\mathbf{A}$ into a column vector. Specifically,

$$\mathbf{vec}(\mathbf{A}) = [a_{11}, \ldots, a_{m,1}, a_{1,2}, \ldots, a_{m,2}, \ldots, a_{1,n}, \ldots, a_{m,n}]^\top.$$

stochastic differential equation. In § (V.7), we give the details of the procedure when considering a more generalised scenario.

From (V.2), we see that the first term in the right-hand side imposes a constant Γ^2 (needed to minimise the deviations from the geodesic [64]). The term involving $\mathbf{Q}$ imposes the system to reach a given PDF defined by $\mathbf{Y}_d$. The third term in the right-hand side of (V.2) regularises the control action $\mathbf{c}$ to avoid abrupt changes in the inputs. Finally, $\mathbf{Q}$ and $\mathbf{R}$ are matrices that penalise the error $\epsilon = \mathbf{Y} - \mathbf{Y}_d$ and the control input u, respectively.

In our method, the control of the dynamics for $\boldsymbol{\mu}$ is given by $u(t)$, while the dynamics of $\boldsymbol{\Sigma}(t)$ is modified by controlling the noise-width via a time-dependant vector $\mathbf{w}(t)$ whose elements substitute the nonzero constant values of the matrix $\mathbf{D}$ (numerically, we can also apply control to all elements in such a matrix regardless of having a mathematical model where they are imposed to be zero). As it is discussed through the numerical examples, the noise width can be modified by changing a macroscopic observable like temperature (for further details, see the Brownian motion models presented in [30]).

V.3.1 BIBO Stability in linear stochastic process

Since we are dealing with a control problem, it is important to describe the stability conditions for the dynamics we try to control. Specifically, for the linear SDE (II.68), the system's bounded-input bounded-output (BIBO) stability is described by the following Theorem.

Theorem V.1: BIBO stability in linear SDE

The mean (II.77) and covariance (II.78) dynamics of (II.68) are BIBO stable if and only if the eigenvalues λ_i of the matrix $\mathbf{A}$ satisfy the following inequality

$$\Re[\lambda_i] < 0, \tag{V.3}$$

where $\Re[s]$ stands for the real part of the complex value $s \in \mathbb{C}$.

Proof. For a detailed proof of this result, please refer to [38] and [148]. ∎

Remark V.1. *Theorem V.1 is considered to be satisfied throughout our examples. i.e. the control method is applied to stable systems only. Furthermore, the control actions are constrained to finite values. For non-linear SDE, the explicit BIBO stability conditions are left for future work.*

V.3.2 A solution via model-predictive-control

As discussed in §V.1, the solution of our optimisation problem will be computed through the MPC method. Hence, the following discrete optimal control problem encoding the MPC formulation is required

$$\begin{aligned}
\mathbf{c} \quad = \quad & \arg\min_{\tilde{\mathbf{c}}} \quad J_N = \sum_{k=0}^{N} \Bigg(I_L\Big(\widehat{\Gamma}^2[k] - \Gamma^2[0]\Big)^2 \\
& \qquad + (\widehat{\mathbf{Y}}[k] - \mathbf{Y}_d)^\top \mathbf{Q} (\widehat{\mathbf{Y}}[k] - \mathbf{Y}_d) + \tilde{\mathbf{c}}^\top[k] \mathbf{R} \tilde{\mathbf{c}}[k] \Bigg) \Bigg) \Bigg(\\
\text{s.t.} \qquad & \widehat{\Gamma}^2[k] = f(\widehat{\mathbf{Y}}[k], \tilde{\mathbf{c}}[k])
\end{aligned}$$

$$
\begin{aligned}
&\widehat{\mathbf{Y}}[k] = [\boldsymbol{\mu}[\tilde{\mathbf{c}}, k], \mathbf{vec}(\boldsymbol{\Sigma}[\tilde{\mathbf{c}}, k])]^\top \\
&\boldsymbol{\mu}[\tilde{\mathbf{c}}, k] = \mathbf{A}_d \boldsymbol{\mu}[k-1] + \mathbf{B}_d u[\tilde{\mathbf{c}}, k-1] \\
&\boldsymbol{\Sigma}[\tilde{\mathbf{c}}, k] = \mathbf{A}_d \boldsymbol{\Sigma}[k-1] + \boldsymbol{\Sigma}[k-1]\mathbf{A}_d^\top + 2\mathbf{D}[\tilde{\mathbf{c}}, k-1] \\
&\boldsymbol{\mu}[0] = \mathbf{m}, \boldsymbol{\Sigma}[0] = \mathbf{S} \quad \forall \mathbf{m} \in \mathbb{R}^n, \mathbf{S} \in \mathbb{R}^{n\times n} \\
&\tilde{\mathbf{c}}[k] = [u[k], \mathbf{w}[k]]^\top \\
&c_{l,i} \le c_i \le c_{u,i} \quad c_{l,i}, c_{u,i} \in \mathbb{R} \forall i = 1, 2, \ldots, m.
\end{aligned} \tag{V.4}
$$

In Equation (V.4), the $\widehat{\ }$-symbol over $\mathbf{Y}$ and Γ refer to their predicted values over the influence of the control $\tilde{\mathbf{c}}$ throughout the optimisation process in the finite horizon of length N. Note that the value of $\widehat{\mathbf{Y}}$ is constrained by the discretised version of the set of equations (II.77)-(II.78) given by

$$
\begin{aligned}
\boldsymbol{\mu}[k] &= \mathbf{A}_d \boldsymbol{\mu}[k-1] + \mathbf{B}_d u[k-1], && \text{(V.5)} \\
\boldsymbol{\Sigma}[k] &= \mathbf{A}_d \boldsymbol{\Sigma}[k-1] + \boldsymbol{\Sigma}[k-1]\mathbf{A}_d^\top + 2\mathbf{D}[k-1], && \text{(V.6)}
\end{aligned}
$$

where $\mathbf{A}_d = \mathbf{I} + T_s\mathbf{A}, \mathbf{B}_d = T_s\mathbf{B}$ if a first-order approximation of the time derivative considering the sample-period T_s is applied (we apply a 4th order Runge Kutta instead of a first-order approximation to compute $\widehat{\mathbf{Y}}$ in our simulations). Note that we have added the argument $\tilde{\mathbf{c}}$ in Equation (V.4) when describing Equations (V.5)-(V.6) to emphasise the application of the control during the optimisation procedure. The initial conditions $\mu[0], \boldsymbol{\Sigma}[0]$ of (V.5)-(V.6) change every time an optimal control $\mathbf{c}$ solution has been computed and they are subject to the measurements $\mathbf{m}, \mathbf{S}$ of the real/simulated process. Every element c_i of the control vector $\tilde{\mathbf{c}}$ is constrained by a lower and an upper limit denoted $c_{l,i}$ and $c_{u,i}$, respectively. Finally, f is the function describing the predicted value $\widehat{\Gamma}^2$ defined as follows

$$
\begin{aligned}
f(\widehat{\mathbf{Y}}[k], \tilde{\mathbf{c}}[k]) = {} & (\mathbf{A}\boldsymbol{\mu}[k] + \mathbf{B}u[\tilde{\mathbf{c}}, k])^\top \boldsymbol{\Sigma}[k]^{-1} (\mathbf{A}\boldsymbol{\mu}[k] + \mathbf{B}u[\tilde{\mathbf{c}}, k]) \\
& + \frac{1}{2}\operatorname{Tr}\left((\boldsymbol{\Sigma}[k]^{-1} \left(\mathbf{A}\boldsymbol{\Sigma}[k-1] + \boldsymbol{\Sigma}[k-1]\mathbf{A}^\top + 2\mathbf{D}[\tilde{\mathbf{c}}, k-1]\right))^2 \right)
\end{aligned} \tag{V.7}
$$

To have a better understanding of the MPC method when applied to solve the IL-QR problem in a real scenario, Figure V.1 shows the MPC method control diagram and the functioning of the MPC's optimiser when considering a second order stochastic system in the sub-figures V.1a and V.1b, respectively. Figure (V.1a) shows that in real-time (i.e. while the process is evolving), the MPC algorithm takes a given setpoint $\Gamma^2[0], \mathbf{Y}_d$, the prediction value $\tilde{\mathbf{Y}}$ of $\boldsymbol{\mu}$ and $\boldsymbol{\Sigma}$ from a prediction model, a set of constrains, the cost function J_N and the current system dynamics $\mathbf{Y}$ to solve the optimisation problem given in (V.4). Afterwards, the optimal control $\mathbf{c}$ solution of Equation (V.4) is applied to the system. The MPC method finds the optimal control $\mathbf{c}$ by considering the differential equations of $\dot{\boldsymbol{\mu}}$ and $\boldsymbol{\Sigma}$ as a prediction model in a finite horizon of length N.

Figure V.1b briefly details the working principle of the MPC's optimiser block when considering a stochastic process described by a bivariate time-varying PDF p with random variables x_1 and x_2. Here, the MPC's optimiser method considers the measured systems PDF output (given in black colour) to initialise the optimisation process. The optimisation is perform by extrapolating the values of the PDF p in a finite horizon of length N comparing it with the reference trajectory described by the PDF p_d. The optimisation problem is solved via the interior point method using CasADi [143]. In this work, thanks to the type of Langevin equations being considered, the control, prediction and simulation of the PDF has been eased through the use of deterministic descriptions of the first two statistical moments through time (for further, details see Chapter II). When considering pure data or more complicated stochastic differential equations, the time-varying PDFs need to be estimated through inference methods [149] or stochastic simulations [150].

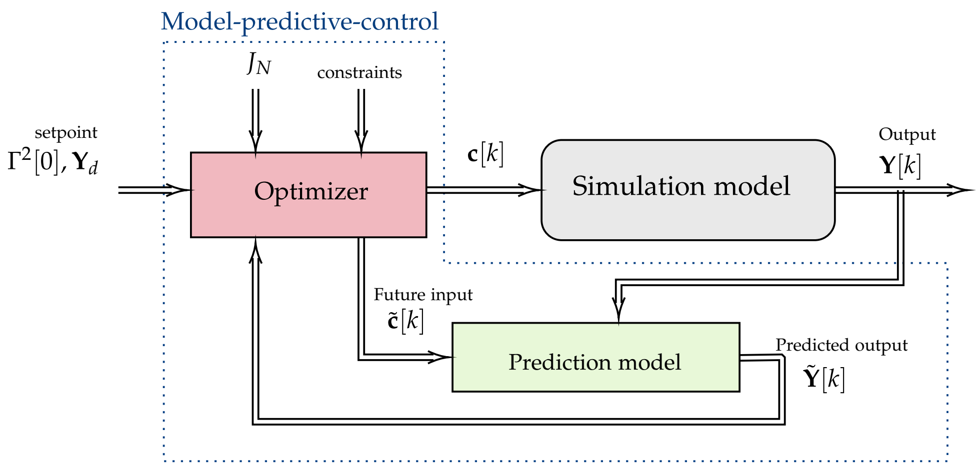

(a)

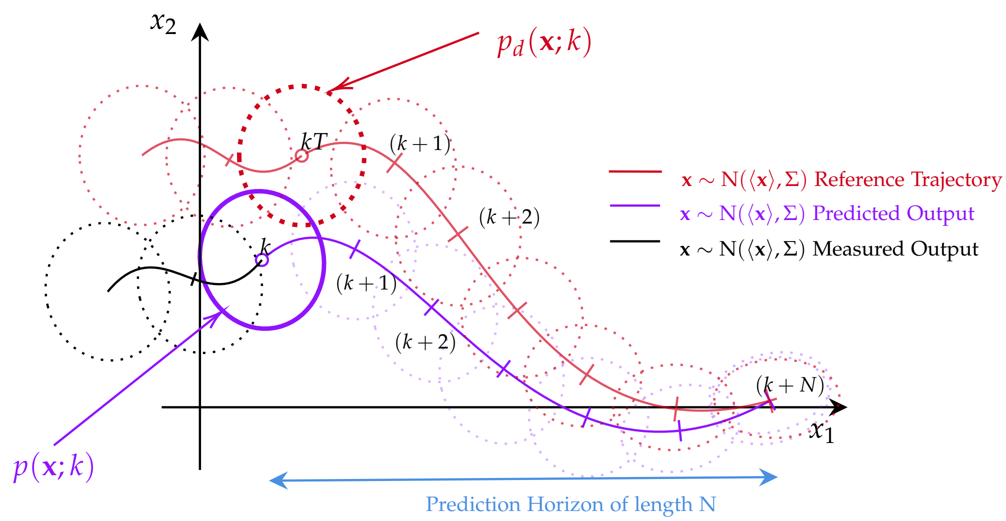

(b)

Figure V.1: a) Control diagram describing the main parts of the implemented MPC methodology. b) Diagram of a discrete MPC scheme applied to a second order stochastic process.

V.4 Case study: The O-U process

To present the numeric implementation of the MPC for the solution of the IL-QR cost function, we first consider its application to the Ornstein–Uhlenbeck (O-U) process (see Figure V.2) defined by the following Langevin equation

$$\dot{\zeta} = -\gamma(\zeta(t) - u(t)) + \xi(t), \tag{V.8}$$

where $\zeta(t)$ is a random variable, $u(t)$ is a deterministic force, $\xi(t)$ is a short correlated random forcing such that $\langle\xi(t)\xi(t_1)\rangle = 2D\delta(t - t_1)$ with $D \geq 0$ and $\langle\xi(t)\rangle = 0$.

The results of the MPC implementation are shown in Figures V.3 to V.6. Figure V.3 depicts the case when the desired state $\mathbf{Y}_d$ of the O-U process is $\mathbf{Y}_d = [1/30, 1/(2 \times 0.3)]^\top$. Figure V.3 also shows the time evolution of the states $\mathbf{Y}(t) = [\mu, \beta(t)]$ and controls $\mathbf{c}(t) = [u(t), D(t)]^\top$ (the rest of the parameter simulation details are

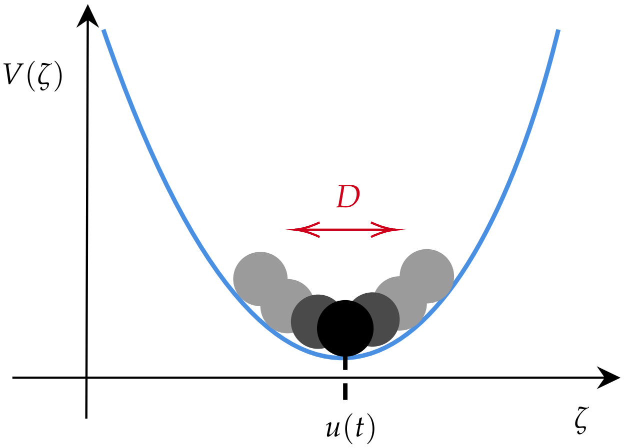

Figure V.2: The O-U process equation is commonly used to describe a prototype of a noisy relaxation process. For instance, the movement of a particle confined to a harmonic potential $V(\zeta) = \frac{1}{2}\gamma(\zeta - u(t))^2$ and thermal fluctuations with temperature T ($D = k_B T\gamma$ and k_B is the Boltzmann constant) such that $\zeta(t)$ fluctuates stochastically.

given in Figure V.3 caption). From the results, we see that the method finds a geodesic motion (solution to the IL-QR) from the initial to the final state in less than 0.4 seconds. The geodesic motion is corroborated by the constant value of $\Gamma^2(t) \approx \Gamma^2(0) = 2.4$ and the plot of the information length $\mathcal{L}$ whose shape is a line with slope of 1.5526. $\Gamma^2(0)$ is computed by considering that $u(t=0) = D(t=0) = 0$. Here, we highlight that the value of Σ is found to temporally vary very slightly compared with the hyperbolic analytical solution in [64] given for a non-constant Σ (see Appendix V.7).

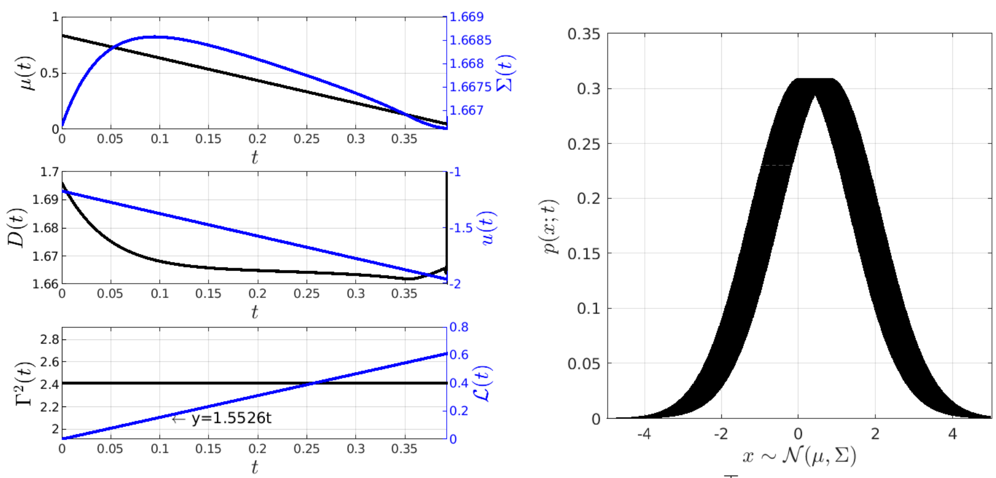

Figure V.3: IL-QR for the O-U process using $\mathbf{Y}(0) = [5/6, 1/(2\times 0.3)]^\top$ and $\mathbf{Y}_d(t) = [1/30, 1/(2\times 0.3)]^\top$. The control is applied in $u(t)$ and $D(t)$. Besides, $\gamma = 1$, $T_s = 1\times 10^{-3}$, $N = 50$, $I_L = 1\times 10^3$, $\mathbf{R} = 1\times 10^{-2}\mathbf{I}_2$, $Q_{12} = Q_{21} = 0, Q_{11} = 1\times 10^2$ and $Q_{22} = 5\times 10^2$.

When analysing the stochastic thermodynamics of the closed-loop system. Figure V.4 shows the plot of the entropy rate $\dot{S}$ in comparison with the entropy production Π, and a plot of the value of Γ^2 with the value of expression (III.51). Recall that the analytical expressions for $\dot{S}$ and Π with their derivation are given in Chapter II. In the closed-loop system, we can see that the MPC method slightly changes the value of both the entropy production Π and the entropy rate $\dot{S}$ in the process. Since the value of Σ and μ in the desired state $\mathbf{Y}_d$ are close and far from its initial condition at state $\mathbf{Y}(0)$, respectively, the balance between $\dot{S}, \Pi$ and Γ^2

given by (III.51) is kept by maintining an almost constant $D(t)$ and a $u(t)$ with almost constant velocity.

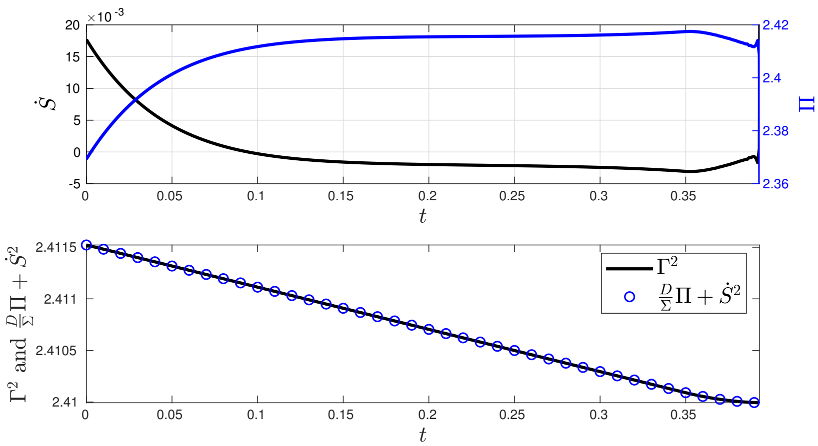

Figure V.4: Stochastic thermodynamics of IL-QR for the O-U process using parameters described in Figure V.3.

Under conditions almost similar to the case of Figure V.3, Figure V.5 shows the behaviour of the closed-loop system PDF, the states μ, Σ, the controls D and u as well as the behaviour of Γ^2 for $\mathbf{Y}_d(t) = [1/30, 1/(2 \times 3)]^\top$. Here, $\Gamma^2(0)$ is computed by considering that $u(t=0) = 0$ and $D(t=0) = 1/(2 \times 0.3)$. The final state $\mathbf{Y}_d$ is reached at a time around $t = 2.8$. Again, the geodesic behaviour is corroborated by the constant value of $\Gamma^2(t) \approx \Gamma^2(0) = 0.41$ and the graph of the information length $\mathcal{L}$ showing a line with slope of 0.64759.

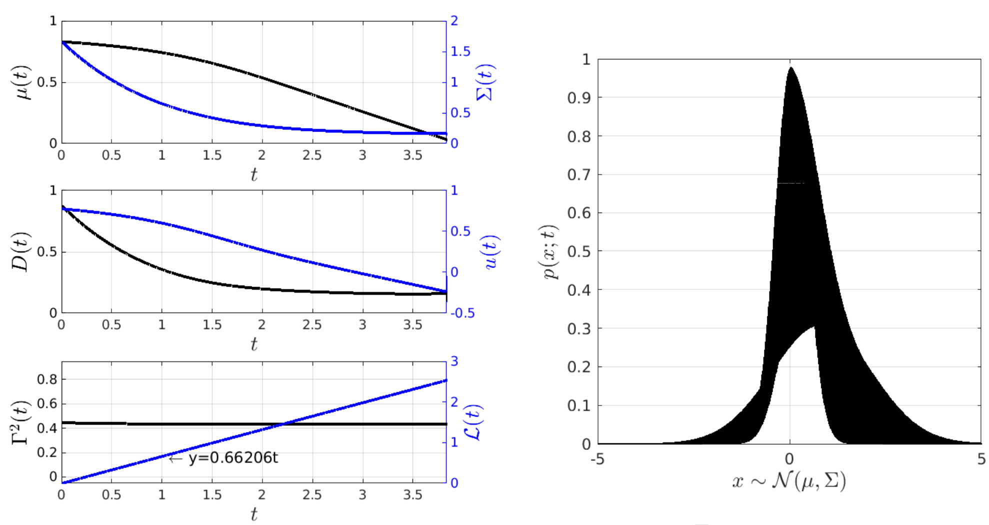

Figure V.5: IL-QR for the O-U process using $\mathbf{Y}(0) = [5/6, 1/(2 \times 0.3)]^\top$ and $\mathbf{Y}_d(t) = [1/30, 1/(2 \times 3)]^\top$. The control is applied in $u(t)$ and $D(t)$. Besides, $\gamma = 1$, $T_s = 1 \times 10^{-3}$, $N = 50$, $I_L = 1 \times 10^4$, $\mathbf{R} = 1 \times 10^{-2}\mathbf{I}_2$, $Q_{12} = Q_{21} = 0, Q_{11} = 1 \times 10^2$ and $Q_{22} = 5 \times 10^2$.

In comparison to the stochastic thermodynamics shown in Figure V.4, Figure V.6 shows small changes in the entropy production Π and considerable variations in the entropy rate $\dot{S}$ of the closed-loop system as the value of Σ and μ in the desired state $\mathbf{Y}_d$ are both different from its initial condition $\mathbf{Y}(0)$. This difference also causes slight variations in both $D(t)$ and $u(t)$. Figure V.6 also shows that the balance equation (III.51) holds.

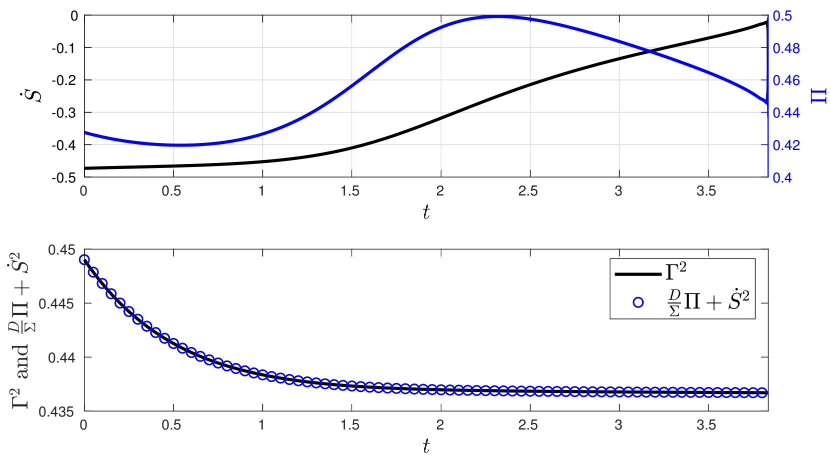

Figure V.6: Stochastic thermodynamics of IL-QR for the O-U process using parameters described in Figure V.5.

V.5 Case study: The Kramers equation

To study the solution of the IL-QR problem in a higher order system via the MPC method, let us now consider the non-autonomous version of the Kramers equation (IV.7). Recall that the Kramers equation is an equation of motion in position and velocity space describing the Brownian motion of particles in an external field [30] and, in practice, as shown in Figure III.15, the Kramers equation (IV.7) is also a good first approximation to describe the dynamics in one-dimension of a particle in an optical trap [81]. The Kramers equation control **c** and state **Y** vectors are defined by

$$\mathbf{c} = [u, D]^\top, \tag{V.9}$$
$$\mathbf{Y} = [\mu_1, \mu_2, \Sigma_{11}, \Sigma_{12}, \Sigma_{22}]^\top. \tag{V.10}$$

Here, μ_1 and μ_1 are the mean values of the random variables ζ_1 and ζ_2, respectively. $\Sigma_{11}, \Sigma_{12}, \Sigma_{22}$ are the values describing the covariance matrix $\boldsymbol{\Sigma}$.

Figures V.7 and V.8 show the simulation results of the Kramers equation closed-loop when considering the desired states $\mathbf{Y}_d(t) = [0, 0, 1/(2\times 3), 0, 1/(2\times 3)]^\top$ and $\mathbf{Y}_d(t) = [-5/6, 0, 1/(2\times 3), 0, 1/(2\times 3)]^\top$, respectively. Figures V.7 and V.8 include the time evolution plots of the mean values μ_1, μ_2 and the covariance matrix values $\Sigma_{11}, \Sigma_{12}, \Sigma_{22}$ of the Kramers equation random variables ζ_1 and ζ_2. In addition, they include the time evolution of the bivariate PDF $p(\mathbf{x}; t)$ with the spatial vector $\mathbf{x} = [x_1, x_2]^\top$ with x_1 and x_2 representing the position and velocity of the system dynamics, respectively. The rest of the parameters used throughout the simulations are mentioned in the Figure captions.

For the first numerical experiment, Figure V.7 demonstrates that the MPC method is capable of maintaining Γ^2 constant through time while reaching the desired state $\mathbf{Y}_d$. Here, the value of $\Gamma(0)$ in (V.4) is obtained as follows

$$\Gamma^2(0) = (\mathbf{A}\boldsymbol{\mu}(0) + \mathbf{B}u(0))^\top \boldsymbol{\Sigma}^{-1}(0)\,(\mathbf{A}\boldsymbol{\mu}(0) + \mathbf{B}u(0)) + \frac{1}{2}\,\mathrm{Tr}\left(\left(\boldsymbol{\Sigma}^{-1}(0)(\mathbf{A}\boldsymbol{\Sigma}(0) + \boldsymbol{\Sigma}(0)\mathbf{A}^\top + 2\mathbf{D}(0))\right)^2\right)$$

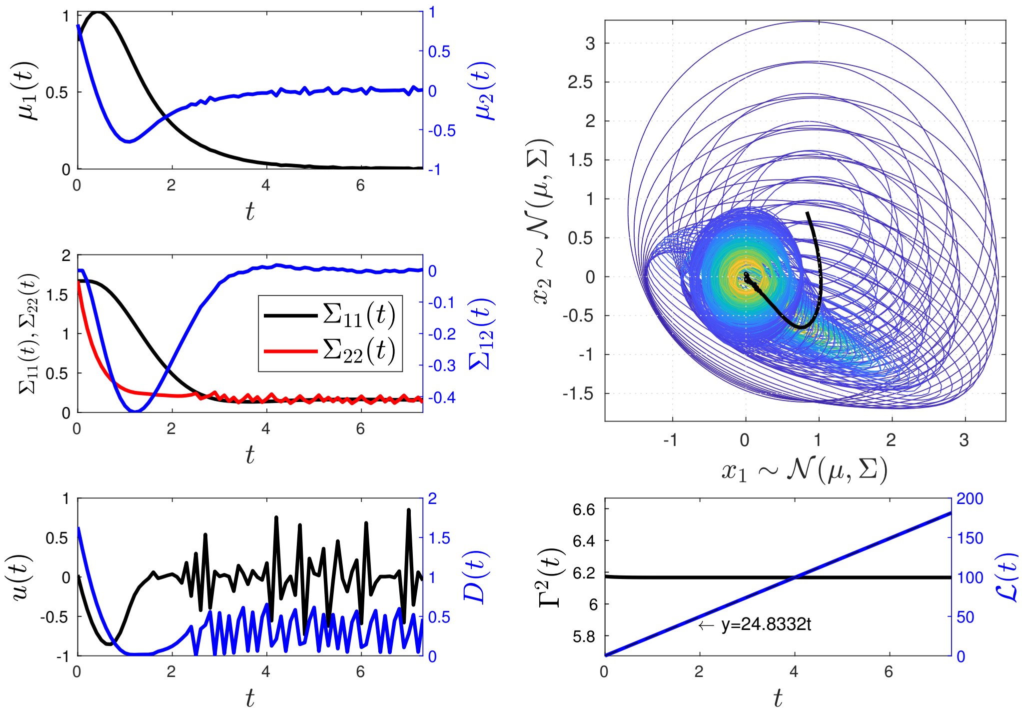

Figure V.7: IL-QR for the Kramers equation using $\mathbf{Y}(0) = [5/6, 5/6, 1/(2 \times 0.3), 0, 1/(2 \times 0.3)]^\top$ and $\mathbf{Y}_d(t) = [0, 0, 1/(2 \times 3), 0, 1/(2 \times 3)]^\top$. The control is applied in $u(t)$ and $D(t)$. Besides, $\omega = 1$, $\gamma = 2$, $T_s = 1 \times 10^{-1}$, $N = 50$, $I_L = 5 \times 10^3$, $\mathbf{R} = 1 \times 10^{-5}\mathbf{I}_3$, $\mathbf{Q} = 1 \times 10^2\mathbf{I}_5$.

$$= 6.16667, \quad \text{(V.11)}$$

where $u(0) = 0$ and $\mathbf{vec}(\mathbf{D}(0)) = [0, 0, 0, 1/(2 \times 0.3)]^\top$ while $\mathbf{A}, \boldsymbol{\mu}(0)$ and $\boldsymbol{\Sigma}(0)$ are taken from the corresponding $\mathbf{Y}(0)$ and the mathematical model (IV.7), respectively. The geodesic dynamics gives a behaviour with slow oscillations in the state $\mathbf{Y}$. The controls u and D present high oscillations as the system reaches the desired state $\mathbf{Y}_d$. The system gets to $\mathbf{Y}_d$ at $t \approx 7$ with an error of 1×10^{-3}. The geodesic behaviour is corroborated by the linear behaviour of the information length $\mathcal{L}$ compared to the fitted equation $y = 24.8332t$.

Figure V.7 shows a second numerical experiment where $\mathbf{Y}_d$ is even farther from the system's equilibrium. Yet, the MPC method can maintain Γ^2 constant trough time while reaching $\mathbf{Y}_d$. Like the example of Figure V.7, in this case $\Gamma^2(0) = 6.16667$. Small oscillations remain in the time evolution of $\mu_1, \mu_2, \Sigma_{11}, \Sigma_{12}$ and Σ_{22}. The system reaches the desired state $\mathbf{Y}_d$ at $t \approx 8.5$. Hence, the farther the desired state $\mathbf{Y}_d$ is from the initial state $\mathbf{Y}$ the longer the time it takes to reach it while following the geodesic path. The geodesic behaviour is shown by the plot of the information length $\mathcal{L}$ whose behaviour is compared to the fitted equation $y = 24.8336t$. As in the example of Figure V.7, the controls present high oscillatory behaviour as the system gets to $\mathbf{Y}_d$.

V.6 *Case study: Cubic system*

We now present an example of the application of the MPC method to obtain the minimum variability behaviour of a non-linear stochastic system. Figure V.10 shows the IL-QR applied to the cubic stochastic

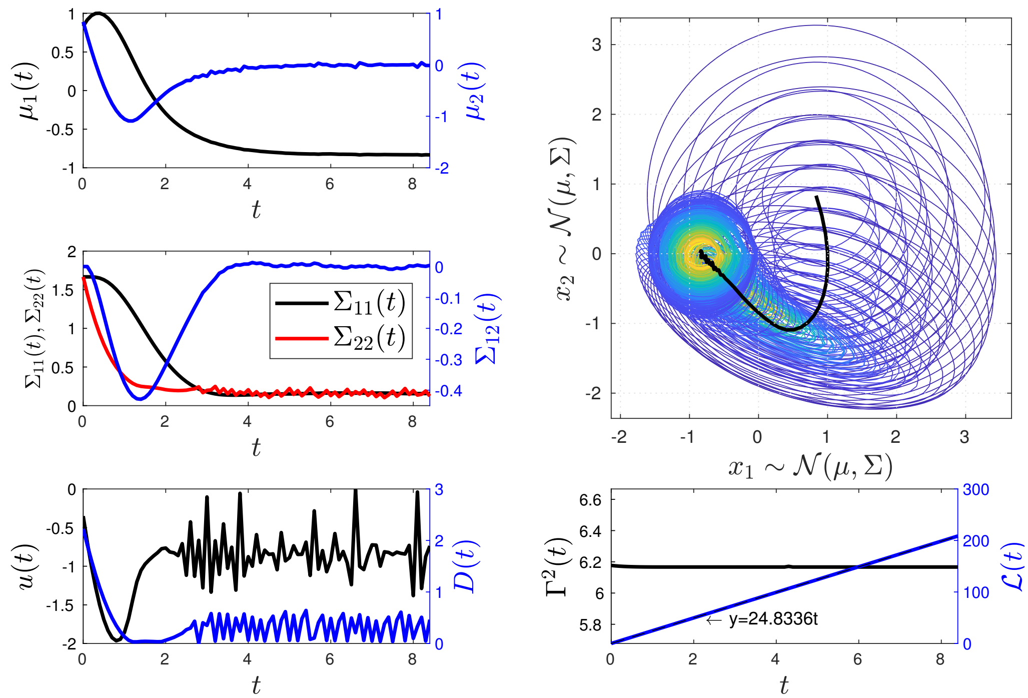

Figure V.8: IL-QR for the Kramers equation using $\mathbf{Y}(0) = [5/6, 5/6, 1/(2\times 0.3), 0, 1/(2\times 0.3)]^\top$ and $\mathbf{Y}_d(t) = [-5/6, 0, 1/(2\times 3), 0, 1/(2\times 3)]^\top$. The control is applied in $u(t)$ and $D(t)$. Besides, $\omega = 1$, $\gamma = 2$, $T_s = 1\times 10^{-1}$, $N = 50$, $I_L = 5\times 10^3$, $\mathbf{R} = 1\times 10^{-5}\mathbf{I}_3$, $\mathbf{Q} = 1\times 10^2\mathbf{I}_5$.

process given by

$$\dot{x}(t) = -\gamma x(t)^3 + u(t) + \xi(t). \tag{V.12}$$

where $\langle \xi \rangle = 0$, $\langle \xi(t)\xi(t')\rangle = 2D\delta(t-t')$ and $\gamma \in \mathbb{R}^+$. Via the Laplace assumption (see Proposition II.7), we can define the control vector and the state vector as $\mathbf{c} = [u, D]^\top$ and $\mathbf{Y} = [\mu, \Sigma]^\top$, respectively. In the simulation the initial state $\mathbf{Y}(0) = [2+5/6, 1/(2\times 30)]^\top$ while the desired state is $\mathbf{Y}_d(t) = [2+1/30, 1/(2\times 3)]^\top$. Additionally, we consider the parameters $\gamma = 0.1$, $T_s = 1\times 10^{-3}$, $N = 5$, $I_L = 1\times 10^3$, $\mathbf{R} = 1\times 10^{-5}\mathbf{I}_2$, $Q_{12} = Q_{21} = 0, Q_{12} = 1\times 10^2$ and $Q_{22} = 8\times 10^2$. Here, T_s is the integration time step and N is the number of future time steps considered in the prediction model. The value of $\Gamma(0)$ is imposed via the initial conditions and equation (III.22).

V.6.1 Limits of the Laplace Assumption

Since the Laplace assumption imposes Gaussian dynamics, it is important to check on its limitations. For such a purpose, consider a comparison between the PDF that is based on the Laplace Assumption (Proposition II.7) $q(x,t)$ defined as

$$q(x,t) = \frac{1}{\sqrt{2\pi\Sigma}} e^{\frac{1}{2}\frac{(x-\mu)^2}{\Sigma}}, \tag{V.13}$$

where μ and Σ are determined by the solution of

$$\dot{\mu} \quad = \quad -\gamma\mu^3 + u - 3\gamma\mu\Sigma, \tag{V.14}$$

$$\dot{\Sigma} = -6\gamma\Sigma\mu^2 + 2D, \tag{V.15}$$

and the "real" system PDF $\tilde{p}(x,t)$ of system (V.12) obtained via stochastic simulations and kernel density estimators (for further details see [151]). Now, to highlight the limits of the Gaussian approximation $q(x,t)$, we apply the Kullback-divergence (KL) D_{KL} or relative entropy between the estimated $\tilde{p}$ and the Gaussian approximation q of the time-varying system (V.12) PDFs defined as

$$D_{KL}(\tilde{p}||q) = \int_{\mathbb{R}} p(x;t) \log\left(\frac{p(x;t)}{q(x;t)}\right) dx. \tag{V.16}$$

Figure V.9 shows the KL divergence trough time between $\tilde{p}$ and q when changing the parameters γ and D in equation (V.12) [2]. The result shows that a valid LA requires a small damping (slow behaviour) and a wider noise amplitude in comparison with the initial value of Σ.

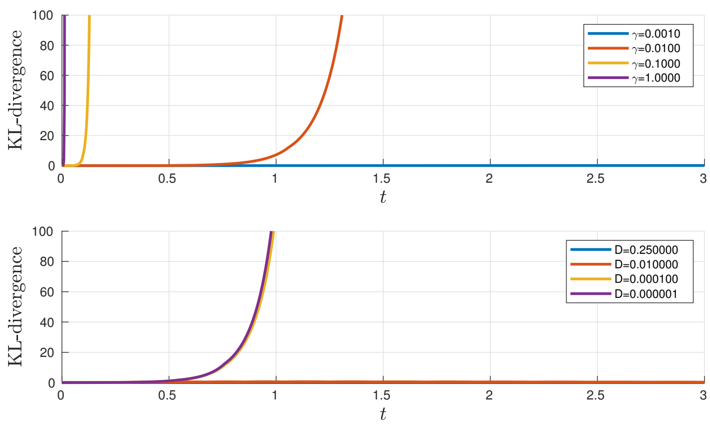

Figure V.9: KL divergence between the value $\tilde{p}(x;t)$ and the value $q(x,y)$ varying the values γ and D of Equation (V.12). When γ changes $D = 0.01$, when D changes $\gamma = 0.01$. The initial condition is a Gaussian distribution defined by $\mu(0) = 5$ and $\Sigma(0) = 0.01$.

V.6.2 Simulation results

In Figure V.10(a), we show the time evolution of the mean μ, the inverse temperature $\beta = \frac{1}{2\Sigma}$, the input force u, the noise amplitude D, the information rate Γ^2 and the information length $\mathcal{L}$. We also show the PDF time evolution of the simulation model computed via the Laplace approximation (q) or via stochastic simulations ($\tilde{p}$) and the corresponding KL-divergence (V.16) between them. In the subplot of μ and β, the legend LA and SS stand for Laplace assumption and stochastic simulations, respectively. Interestingly, we can see from this that the Laplace approximation works fine when used as a prediction model in the MPC method. The controls have a chattering effect (oscillations having a finite frequency and amplitude), similar to the one encountered when implementing other control methods like the sliding mode control [152], when trying to keep the system in the desired state $\mathbf{Y}_d$.

Figure V.10(b) demonstrates the effects of controls (V.28) on the closed-loop system stochastic thermodynamics. The results show that at the desired state $\mathbf{Y}_d$ the value of $\dot{S}$ oscillates around zero with a small amplitude. This means, $\Phi = -\Pi$ holds at some instants of time when $\mathbf{Y}$ reaches $\mathbf{Y}_d$. In other words, all the energy is exchanged with the system's environment when the control keeps $\mathbf{Y}$ on the non-equilibrium state $\mathbf{Y}_d$.

[2] Code `https://github.com/AdrianGuel/StochasticProcesses/blob/main/CubicvsLA.ipynb`

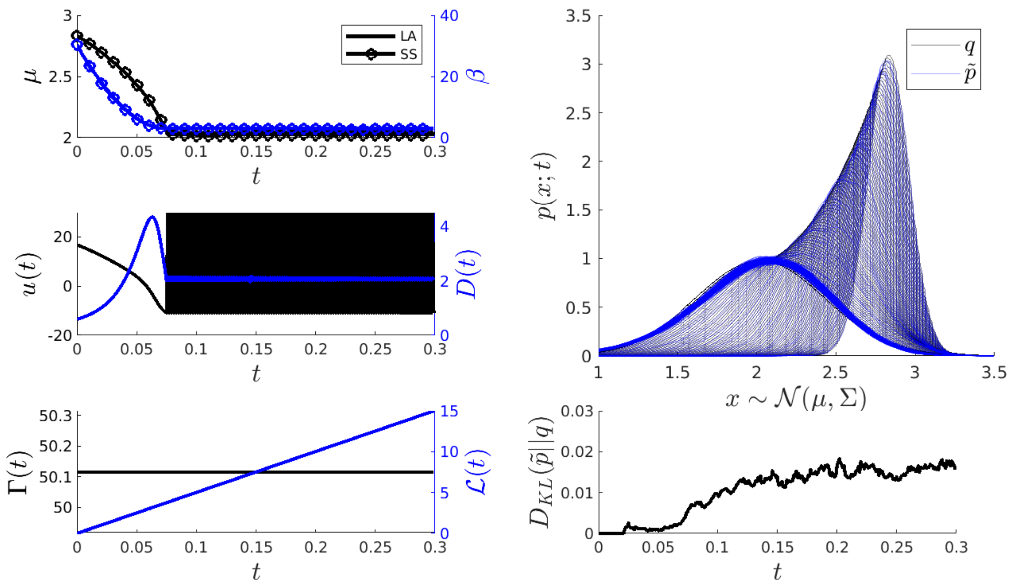

(a) PDF, $D, u, \mu, \beta = \frac{1}{2\Sigma}, \Gamma$ and $\mathcal{L}$ time evolution.

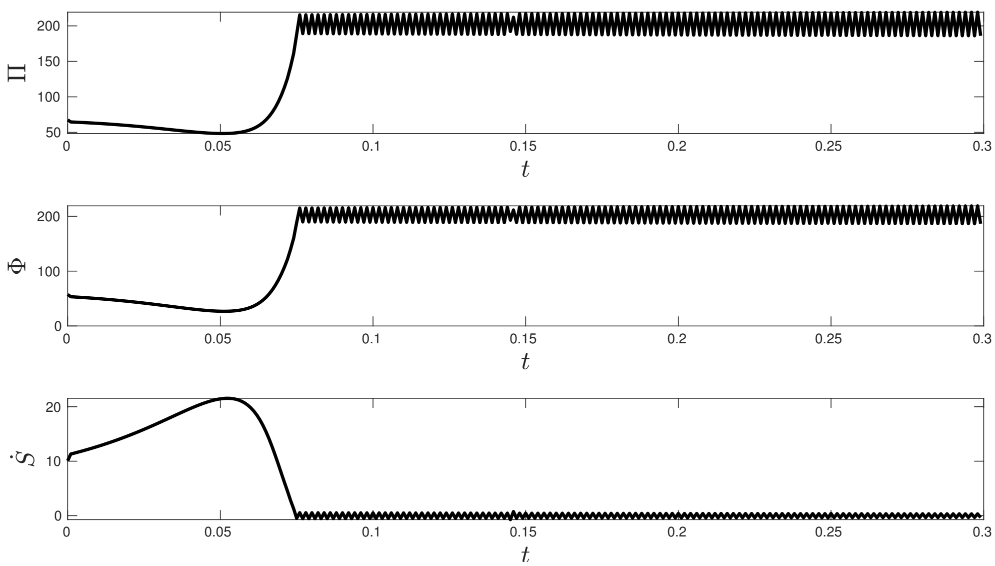

(b) Stochastic thermodynamics time evolution.

Figure V.10: IL-QR under LA applied to system (V.12) with $\mathbf{Y}(0) = [2 + 5/6, 1/(2 \times 30)]^\top$ and $\mathbf{Y}_d(t) = [2 + 1/30, 1/(2 \times 3)]^\top$. The control is applied in $u(t)$ and $D(t)$. Besides, $\gamma = 0.1$, $T_s = 1 \times 10^{-3}$, $N = 5$, $I_L = 1 \times 10^3$, $\mathbf{R} = 1 \times 10^{-5}\mathbf{I}_2$, $Q_{12} = Q_{21} = 0, Q_{12} = 1 \times 10^2$ and $Q_{22} = 8 \times 10^2$.

V.7 A solution by the Euler-Lagrange equation

In the work [64], E. Kim et al. present an analytical solution describing the geodesic motion connecting a given initial $p(\mathbf{x}; 0)$ and a final $p(\mathbf{x}; t_F)$ probability distribution by solving the Euler-Lagrange equations in terms of the covariance Σ and mean μ value of a first order stochastic process. Here, we take the O-U process to compare such analytical solution of the geodesic dynamics with the solution obtained by the MPC method. Additionally, we give the set of differential equations describing the geodesic motion for an n-variate Gaussian process utilising [64]'s approach.

The Euler Lagrange equations for the Lagrangian Γ^2 in terms of the vector $\boldsymbol{\mu}$ (mean value) and the matrix $\boldsymbol{\Sigma}$ (covariance) are

$$\frac{d}{dt}\left(\frac{\partial\Gamma^2(t)}{\partial\dot{\boldsymbol{\mu}}}\right) = \frac{\partial\Gamma^2(t)}{\partial\boldsymbol{\mu}}, \tag{V.17}$$

$$\frac{d}{dt}\left(\frac{\partial\Gamma^2(t)}{\partial\dot{\boldsymbol{\Sigma}}}\right) = \frac{\partial\Gamma^2(t)}{\partial\boldsymbol{\Sigma}}. \tag{V.18}$$

Using (III.22) in (V.17) and (V.18), we obtain (see Appendix AV.1)

$$\ddot{\boldsymbol{\mu}} + \dot{\boldsymbol{\Sigma}}\boldsymbol{\Sigma}^{-1}\dot{\boldsymbol{\mu}} = 0, \tag{V.19}$$

$$\ddot{\boldsymbol{\Sigma}} + \dot{\boldsymbol{\mu}}\dot{\boldsymbol{\mu}}^\top - \dot{\boldsymbol{\Sigma}}\boldsymbol{\Sigma}^{-1}\dot{\boldsymbol{\Sigma}} = 0. \tag{V.20}$$

As mentioned above, [64] presents a closed-form analytical solution to the boundary value problem of equations (V.19) and (V.20) when the dimension of both $\boldsymbol{\mu}$ and $\boldsymbol{\Sigma}$ are one. Specifically, equations (V.19)-(V.20) have a trivial solution where Σ is constant. For non-constant Σ, the following hyperbolic solutions are found in [64]:

$$\beta(t) = \beta_* \cosh\left[\frac{1}{2}\sqrt{\alpha}(t-A)\right], \tag{V.21}$$

$$\mu(t) = -\frac{1}{\sqrt{\beta_*}}\tanh\left[\frac{1}{2}\sqrt{\alpha}(t-A)\right] + \mu_M. \tag{V.22}$$

Here, $\beta = \frac{1}{2\Sigma}$ and $\mu(t=A) = (\mu(0)+\mu(t_F))/2 = \mu_M$. The values of β_*, α and A are computed using a given set of boundary conditions (for the complete discussion, see [64]). For instance, the parameter

$$A = \frac{1}{\gamma\sqrt{\beta(0)}\mu(0)}\frac{Q}{\cosh(Q)}, \tag{V.23}$$

where $Q = \sinh^{-1}(\frac{\phi}{2})$ using $\phi = \sqrt{\beta(0)}(\mu(0) - \mu(t_F))$. Clearly, through equations (V.21)-(V.22) and the dynamical model of the O-U process (V.8), we can construct the optimal control $f(t)$ of the input $u(t)$ and the optimal noise amplitude $D_I(t)$ of $D(t)$. From [64], given that $u(0) = 0$ such optimal controls are given by

$$f(t) = \mu(t) - \frac{\beta(0)\mu(0)}{\beta(t)}, \tag{V.24}$$

$$D_I(t) = \frac{1}{2\beta(t)}\left[\gamma - \frac{\sqrt{\alpha}}{2}\tanh(\frac{1}{2}\sqrt{\alpha}(t-A))\right]. \tag{V.25}$$

To compare the analytical and the MPC solution of the geodesic of the IL, Figure V.11 shows the behaviour of the O-U process when controlled through the analytical solution (V.24)-(V.25) or the IL-MPC method. The Figure contains different subplots that show the time evolution of $\mu, \beta^{1/2}, \Gamma^2, \mathcal{L}$ and the optimal controls D_I and f. In the simulation, the desired state and the damping are $\mathbf{Y}_d(t) = [1/30, 1/(2\times 0.3)]^\top$ and $\gamma = 1$, respectively. Additionally, we set a fixed final time $t_F = 2A = 0.9304$ (one cycle of the hyperbolic geodesic motion (V.21)-(V.22)) by considering the initial state $\mathbf{Y}(0) = [5/6, 1/(2\times 0.3)]^\top$. Figure V.11 uses dashed and non-dashed lines for the MPC and the analytical response, respectively. From the comparison, a major

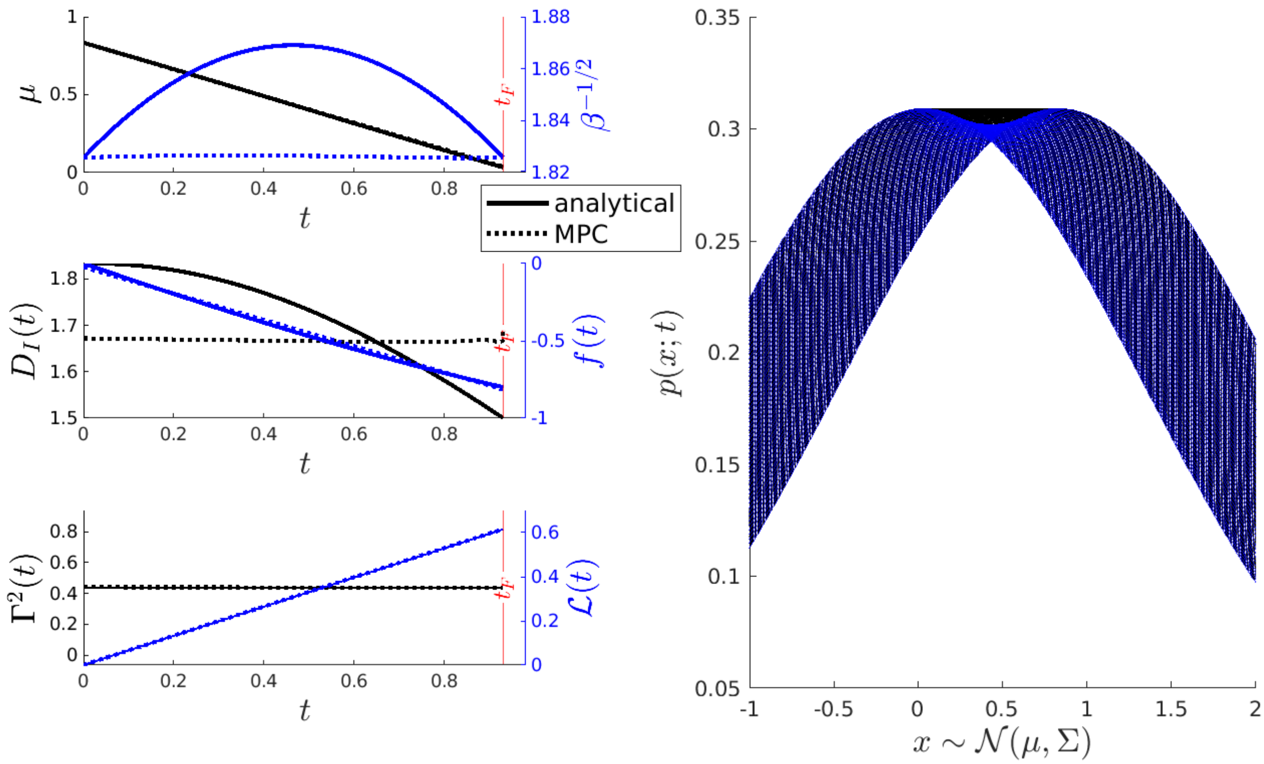

Figure V.11: Comparison between the analytical solution of Eqs (V.19)-(V.20) vs the IL-QR solution for the O-U process (V.8). The IL-QR parameters are $\mathbf{Y}(0) = [5/6, 1/(2 \times 0.3)]^\top$, $\mathbf{Y}_d(t) = [1/30, 1/(2 \times 0.3)]^\top$, $\gamma = 1$, $T_s = 1 \times 10^{-3}$, $N = 50$, $I_L = 1 \times 10^3$, $\mathbf{R} = 1 \times 10^{-4}\mathbf{I}_2$, $\mathbf{Q} = 1 \times 10^2\mathbf{I}_2$.

conclusion is that the time evolution of β is no longer hyperbolic when using the MPC method. This means that the MPC method finds an almost constant Σ solution but not the hyperbolic solution shown in [64]. The MPC allow us to reach the final state $\mathbf{Y}_d$ at t_F with an error of 6.6×10^{-4}.

As a second example, Figure V.12 shows the dynamics of the controlled O-U process when the initial state is $\mathbf{Y}(0) = [5/6, 1/(2 \times 3)]^\top$ (fixing $t_F = 2A = 0.7367$), the desired state $\mathbf{Y}_d(t) = [1/30, 1/(2 \times 3)]^\top$ and the damping $\gamma = 1$. Again, the MPC method recovers a geodesic solution where β time evolution is constant. In this scenario, the MPC method reaches to the desired state $\mathbf{Y}_d$ with an error of 9.8×10^{-4} in a time $t > t_F$ demonstrating that the numerical optimisation scheme may not recover an optimal time.

As a final remark, note that if the n-variate case is considered, Equations (V.19)-(V.20) form a set of non-linear differential equations whose solution may be obtained by a numerical procedure. But, even for the case of a second-order stochastic process, this becomes a challenging problem (we have a boundary value problem of 12 non-linear differential equations). Hence, the MPC method provides an alternative solution to this problem while being an experimentally feasible approach as demonstrated by the application to the Kramers equation in Section V.5.

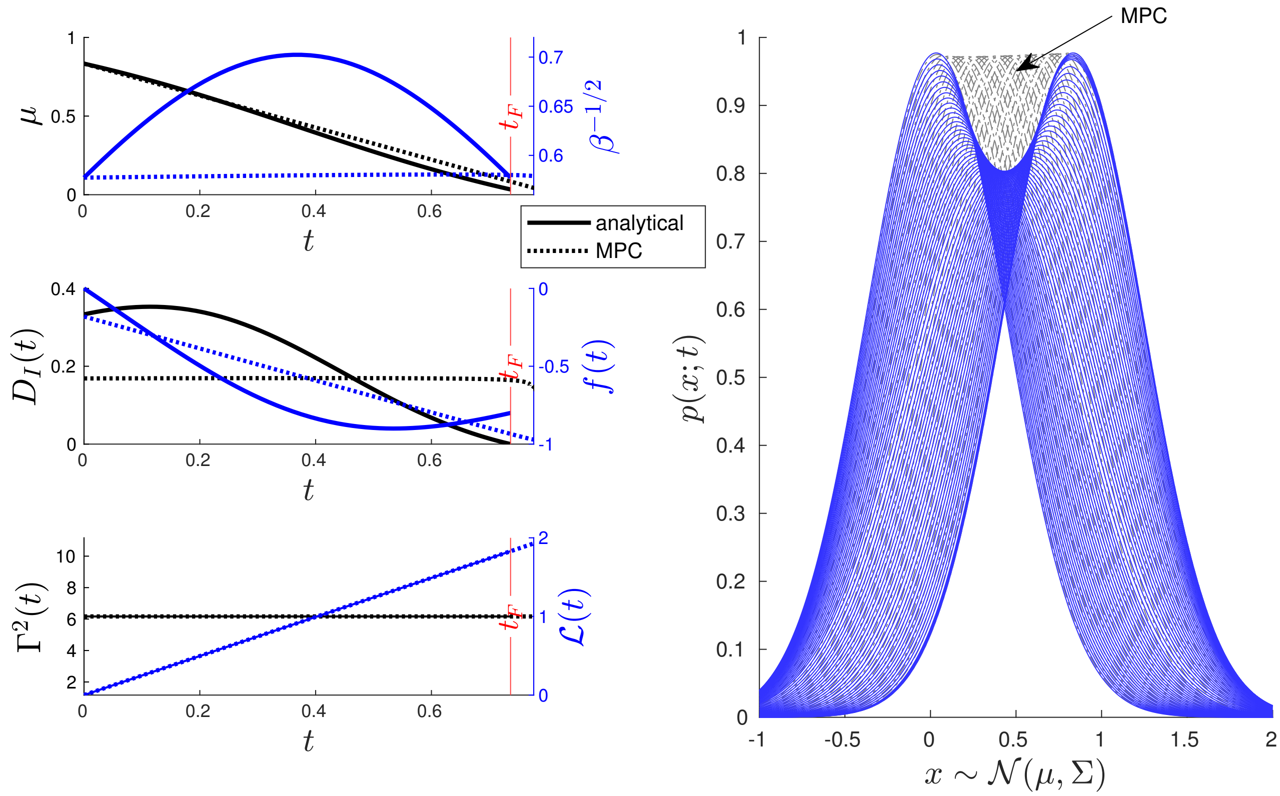

Figure V.12: Comparison between the analytical solution of Eqs (V.19)-(V.20) vs the IL-QR solution for the O-U process (V.8). The IL-QR parameters are $\mathbf{Y}(0) = [5/6, 1/(2\times 3)]^\top$, $\mathbf{Y}_d(t) = [1/30, 1/(2\times 3)]^\top$, $\gamma = 1$, $T_s = 1\times 10^{-3}$, $N = 10$, $I_L = 1\times 10^3$, $\mathbf{R} = 1\times 10^{-4}\mathbf{I}_2$, $\mathbf{Q} = 1\times 10^2\mathbf{I}_2$.

V.8 Full-state feedback control

So far, we have successfully employed a control algorithm that allows minimum information variability. Yet, it would be interesting to explore other classical control techniques subject to thermodynamic constraints for the generation of efficient processes.

As a final application, here we explore the use of IL for control design in a given linear stochastic process but through what control engineers call the full-state feedback controller given by

$$u(t) = -\mathbf{k}\mathbf{x}(t), \tag{V.26}$$

where $\mathbf{k} \in \mathbb{R}^{1\times n}$. Through this control, we obtain the following closed-loop system

$$\dot{\mathbf{x}}(t) = \mathbf{A}_{cl}\mathbf{x}(t) + \boldsymbol{\xi}(t), \tag{V.27}$$

where $\mathbf{A}_{cl} = \mathbf{A} - \mathbf{B}\mathbf{k}$. The full-state feedback control permits us to manipulate the system's mean value via changing the eigenvalues of $\mathbf{A}$. As discussed previously, such eigenvalues also modify the time evolution of $\boldsymbol{\Sigma}$. In systems like (III.80), the value of $\boldsymbol{\Sigma}$ can as well be manipulated by the temperature of the fluid whose value is related to the elements D_{11} and D_{22} of the noise amplitude matrix $\mathbf{D}$.

Taking the aforementioned details into consideration, the following optimisation problems for the design of minimum variability control can be solved

$$\begin{aligned}
\min_{\mathbf{k},\mathbf{D}} \quad & J_1 = \int_0^{t_f} \Gamma(\tau)\, \mathrm{d}\tau, \\
\text{s.t.} \quad & \dot{\boldsymbol{\mu}} = \mathbf{A}_{cl}\boldsymbol{\mu} \\
& \dot{\boldsymbol{\Sigma}} = \mathbf{A}_{cl}\boldsymbol{\Sigma} + \boldsymbol{\Sigma}\mathbf{A}_{cl}^{\top} + 2\mathbf{D} \\
& \boldsymbol{\mu}(0) = \mathbf{m}, \boldsymbol{\Sigma}(0) = \mathbf{S} \\
& k_{l,i} \leq k_i \leq k_{u,i}, \quad 0 \leq D_{ii} \leq D_{\max} \\
& \forall i = 1, 2, \ldots, n,
\end{aligned} \tag{V.28}$$

and

$$\begin{aligned}
\min_{\mathbf{k},\mathbf{D}} \quad & J_2 = ||\Gamma(t)^2 - \Gamma(0)^2||, \\
\text{s.t.} \quad & \dot{\boldsymbol{\mu}} = \mathbf{A}_{cl}\boldsymbol{\mu} \\
& \dot{\boldsymbol{\Sigma}} = \mathbf{A}_{cl}\boldsymbol{\Sigma} + \boldsymbol{\Sigma}\mathbf{A}_{cl}^{\top} + 2\mathbf{D} \\
& \boldsymbol{\mu}(0) = \mathbf{m}, \boldsymbol{\Sigma}(0) = \mathbf{S} \\
& k_{l,i} \leq k_i \leq k_{u,i}, \quad 0 < D_{ii} \leq D_{\max} \\
& \forall i = 1, 2, \ldots, n.
\end{aligned} \tag{V.29}$$

In Equation (V.28), J_1 is a cost function that considers the minimisation of IL from $t = 0$ to $t = t_f$ to obtain the "minimum" statistical changes in the given period of time. On the other hand, Equation (V.29) considers a cost function J_2 equal to the norm of $\Gamma(t)^2 - \Gamma(0)^2$. The objective of J_2 is to keep Γ^2 constant through time (with the least amount of fluctuations) to approximately follow the "geodesic", a problem well described in [64]. Both optimisation problems are subject to the dynamics of the mean and covariance of the PDF given certain initial conditions for them. The problems also consider upper and lower limits to k_i and D_{ii} $\forall i = 1, 2, \ldots, n$ given by $k_{l,i}, k_{u,i}$ and $0, D_{\max}$, respectively. Note $D_{ii} \geq 0$ because the temperature cannot be negative. The values of $k_{l,i}$ and $k_{u,i}$ are determined such that the following stability condition is satisfied

$$|s\mathbf{I} - \mathbf{A}_{cl}| \neq 0 \quad \forall s \in \mathbb{C} \quad \text{s.t.} \quad \Re s > 0. \tag{V.30}$$

Using $\omega = 1, \gamma = 2, \mu_1(0) = 0.5, \mu_2(0) = 0.7, \Sigma_{11} = \Sigma_{22} = 0.01, \Sigma_{12} = \Sigma_{21} = 0$, $D_{\max} = \infty$, $k_{l,1} = -1, k_{l,2} = -2, k_{u,1} = k_{u,2} = \infty$ and $u(t) = -\begin{bmatrix} k_1 & k_2 \end{bmatrix} \begin{bmatrix} x_1 \\ x_2 \end{bmatrix}$ in system (III.80), we have explored the solution of Equations (V.28) and (V.29) via the MATLAB Toolbox FMINCON [153]. The solutions give us the set values of $\mathbf{k}$ and $\mathbf{D}$ that give at least a local minimum. Note that our goal here is to see the implications of a solution to such problems instead of rigorously finding the global optimal solution.

Figure V.13 depicts the time evolution of $\Gamma, \mathcal{L}, \Pi, x_1, x_2$ and the spaces $(p(\mathbf{x}, t), x_1, x_2)$ and (x_1, x_2) after applying the values of $\mathbf{k}$ and $\mathbf{D}$ that give a solution to the optimisation problem (V.28). As a result, the value of $\mathbf{k}$ contains $k_1 = 2.1229$ and $k_2 = 4.4453$ and $\mathbf{D}$, contains $D_{11} = 0.2684$ and $D_{22} = 2.1181$. This values produce an abrupt change in Γ, a quasi-logarithmic change in $\mathcal{L}$ with a maximum value slightly over 5 and a slow almost critically damped change in the system dynamics towards the equilibrium. In addition, the control quickly drives Π and $\dot{S}$ to zero. Even though the control action imposes a slow evolution of the mean value, the information rate quickly decreases. Such behaviour is desirable for systems where minimum information variability is more important than the speed under which we reach the equilibrium.

The solution of the optimisation problem (V.29) depicted in Figure V.14 shows that a geodesic solution is obtained when entropy production Π and entropy rate $\dot{S}$ are zero. This is imposed by the resultant control parameters $k_1 = -0.8431$, $k_2 = -2$, $D_{11} = 0$ and $D_{22} = 0$ which generate a harmonic oscillatory behaviour of the mean value $\boldsymbol{\mu} = [\mu_1, \mu_2]^\top$ and small changes in the time evolution of the covariance matrix elements Σ_{11}, Σ_{12} and Σ_{22} to keep Γ constant at all t.

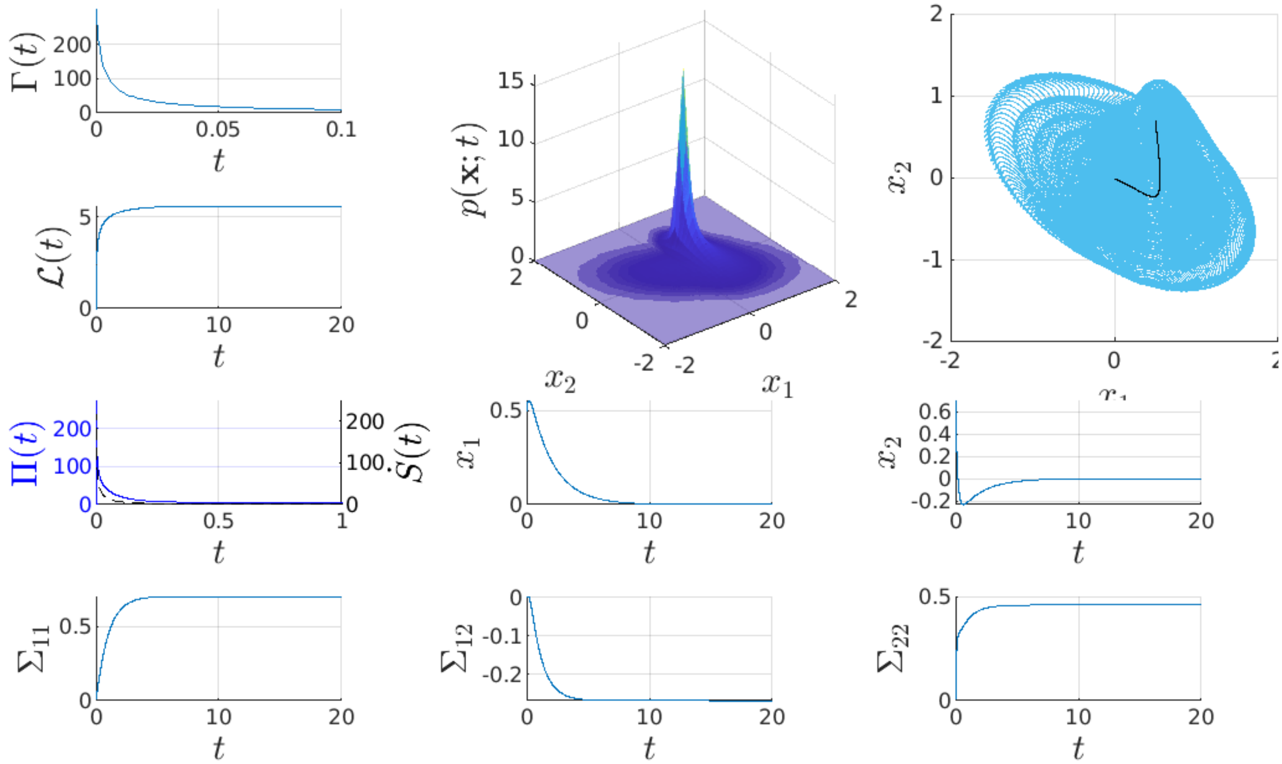

Figure V.13: Full-state feedback control and temperature setting minimising J_1. A local minima is at $\mathbf{k} = [2.1229, 4.4453]^\top$ and $\mathbf{D} = [0.2684, 0; 0, 2.1181]$.

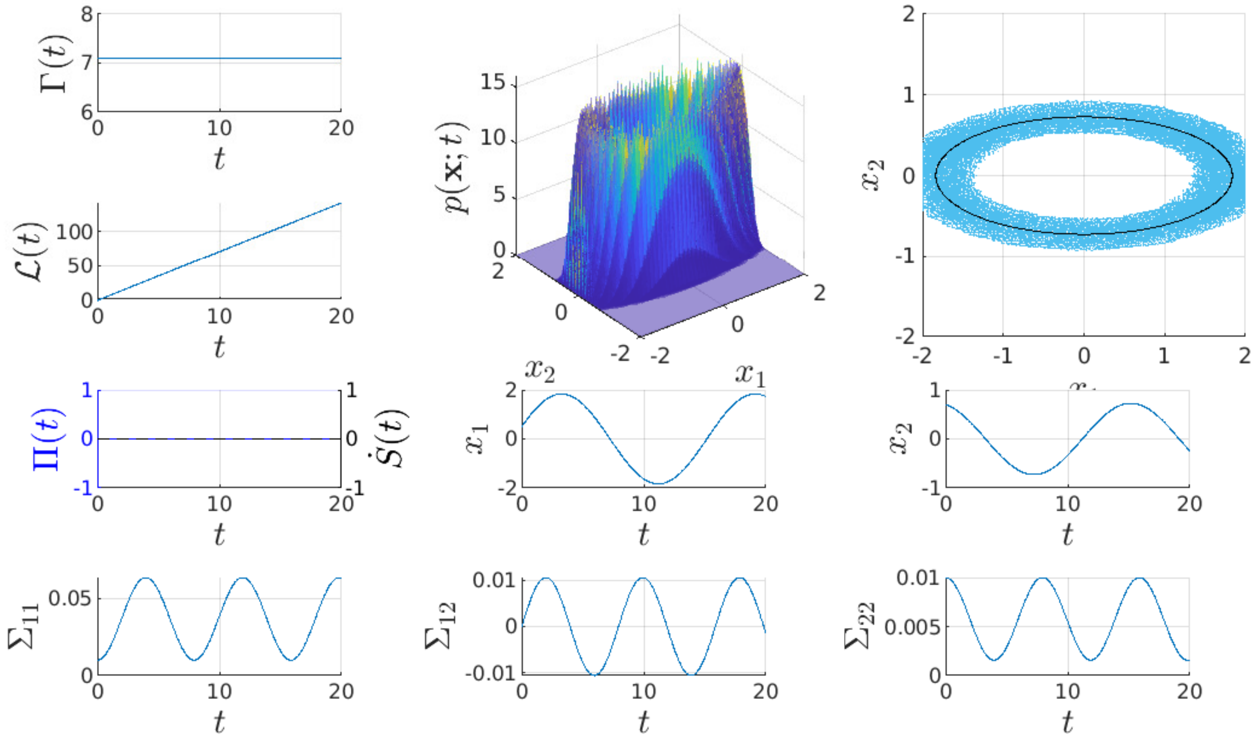

Figure V.14: Full-state feedback control and temperature setting minimising J_2. A local minima is at $\mathbf{k} = [-0.8431, -2]^\top$ and $\mathbf{D} = [0, 0; 0, 0]$.

Chapter concluding remarks

In this chapter, we demonstrated the application of the MPC method to obtain the minimum information variability in systems governed by linear and non-linear stochastic differential equations. The system's linearity produces time-varying Gaussian PDFs with statistical moments governed by a set of deterministic differential equations via the Laplace assumption. The simulations demonstrate that the MPC method is a practical approach to solving the geodesic of the information length between the initial and the desired probabilistic state via the solution of the proposed IL-QR loss function. From the Thermodynamics perspective, the simulations of the MPC in the O-U process show that the MPC directly affects the amount of entropy production generated by the system to fulfil all the optimisation requirements.

In addition, we identified the limitations of the Laplace assumption and proved it to reduce the computational cost of calculating the time-varying PDFs and to develop a prediction model in the MPC algorithm. Furthermore, we show that it is possible to obtain the geodesic of the information length via a simple full-state feedback control algorithm.

Future work will include the maximisation of the free-energy [51] by minimising the value of the entropy production, the application to non-linear stochastic dynamics (for instance, toy models [154], systems with uncertain physical parameters [155], Brownian motion [156] or diffusion [157; 158]) and the analysis of the closed-loop stochastic thermodynamics for higher-order systems.

AV Appendix Chapter V

AV.1 Geodesic dynamics derivation

Based on matrix calculus identities from [55], we can derive the the Euler-Lagrange equations for $\Gamma^2(t)$. First, for $\boldsymbol{\mu}$ we have

$$\frac{d}{dt}\left(\frac{\partial\Gamma^2(t)}{\partial\dot{\boldsymbol{\mu}}}\right) = 0, \tag{AV.31}$$

where $\frac{\partial\Gamma^2(t)}{\partial\dot{\boldsymbol{\mu}}} = 2\boldsymbol{\Sigma}^{-1}\dot{\boldsymbol{\mu}}$. Therefore

$$\frac{d}{dt}\left(\boldsymbol{\Sigma}^{-1}\right)\dot{\boldsymbol{\mu}} + \boldsymbol{\Sigma}^{-1}\ddot{\boldsymbol{\mu}} = -\boldsymbol{\Sigma}^{-1}\dot{\boldsymbol{\Sigma}}\boldsymbol{\Sigma}^{-1}\dot{\boldsymbol{\mu}} + \boldsymbol{\Sigma}^{-1}\ddot{\boldsymbol{\mu}} = 0, \tag{AV.32}$$

which leads to equation (V.19). For $\boldsymbol{\Sigma}$ we have

$$\begin{aligned}
\frac{\partial\Gamma^2(t)}{\partial\dot{\boldsymbol{\Sigma}}} &= \frac{1}{2}\operatorname{Tr}\left(\boldsymbol{\Sigma}^{-1}(\partial\dot{\boldsymbol{\Sigma}})\boldsymbol{\Sigma}^{-1}\dot{\boldsymbol{\Sigma}} + \boldsymbol{\Sigma}^{-1}\dot{\boldsymbol{\Sigma}}\boldsymbol{\Sigma}^{-1}(\partial\dot{\boldsymbol{\Sigma}})\right) \\
&= \frac{1}{2}\left(2(\boldsymbol{\Sigma}^{-1}\dot{\boldsymbol{\Sigma}}\boldsymbol{\Sigma}^{-1})^{\top}\right),
\end{aligned} \tag{AV.33}$$

$$\begin{aligned}
\frac{d}{dt}\left(\frac{\partial\Gamma^2(t)}{\partial\dot{\boldsymbol{\Sigma}}}\right) &= \frac{d}{dt}\left(\boldsymbol{\Sigma}^{-1}\dot{\boldsymbol{\Sigma}}\boldsymbol{\Sigma}^{-1}\right) \\
&= -\boldsymbol{\Sigma}^{-1}\dot{\boldsymbol{\Sigma}}\boldsymbol{\Sigma}^{-1}\dot{\boldsymbol{\Sigma}}\boldsymbol{\Sigma}^{-1} + \boldsymbol{\Sigma}^{-1}\ddot{\boldsymbol{\Sigma}}\boldsymbol{\Sigma}^{-1} \\
&\quad -\boldsymbol{\Sigma}^{-1}\dot{\boldsymbol{\Sigma}}\boldsymbol{\Sigma}^{-1}\dot{\boldsymbol{\Sigma}}\boldsymbol{\Sigma}^{-1},
\end{aligned} \tag{AV.34}$$

$$\begin{aligned}
\frac{\partial\Gamma^2(t)}{\partial\boldsymbol{\Sigma}} &= -\boldsymbol{\Sigma}^{-1}\dot{\boldsymbol{\mu}}\dot{\boldsymbol{\mu}}^{\top}\boldsymbol{\Sigma}^{-1} + \frac{1}{2}\frac{\partial}{\partial\boldsymbol{\Sigma}}\operatorname{Tr}\left(\boldsymbol{\Sigma}^{-1}\dot{\boldsymbol{\Sigma}}\boldsymbol{\Sigma}^{-1}\dot{\boldsymbol{\Sigma}}\right) \\
&= -\boldsymbol{\Sigma}^{-1}\dot{\boldsymbol{\mu}}\dot{\boldsymbol{\mu}}^{\top}\boldsymbol{\Sigma}^{-1} + \frac{1}{2}\operatorname{Tr}\left((\partial\boldsymbol{\Sigma}^{-1})\dot{\boldsymbol{\Sigma}}\boldsymbol{\Sigma}^{-1}\dot{\boldsymbol{\Sigma}}\right. \\
&\quad \left.+\boldsymbol{\Sigma}^{-1}\dot{\boldsymbol{\Sigma}}(\partial\boldsymbol{\Sigma}^{-1})\dot{\boldsymbol{\Sigma}}\right) \\
&= -\boldsymbol{\Sigma}^{-1}\dot{\boldsymbol{\mu}}\dot{\boldsymbol{\mu}}^{\top}\boldsymbol{\Sigma}^{-1} + \frac{1}{2}\left(-2(\boldsymbol{\Sigma}^{-1}\dot{\boldsymbol{\Sigma}}\boldsymbol{\Sigma}^{-1}\dot{\boldsymbol{\Sigma}}\boldsymbol{\Sigma}^{-1})^{\top}\right)
\end{aligned} \tag{AV.35}$$

VI

Information geometry application to engineering. An electrical power system case study

Chapter summary

In this chapter, we explore the application of the information length to data-driven systems, specially, systems where data are given in the form of time-series. For such a purpose, we first describe a simple algorithm to compute the value of the information rate Γ and information length $\mathcal{L}$ from the given time-series. In addition, we apply a basic recursive neural network (RNN) structure in combination with the previously mentioned algorithm to forecast the IL. Then, we apply these algorithms to a case study consisting on the analysis of Kinetic Energy (KE) of the Nordic Power System during three consecutive years as a way to provide useful insights into the power system KE variability and to demonstrate its utility as a starting point in decision making for power systems management. Our results reveal that the proposed method provides an effective description of the seasonal statistical variability enabling the identification of the particular month and day that have the least and the most KE variability.

This chapter is based on the following author's publications: [8; 7]

keywords: Model-predictive-control; Stochastic control; Optimisation

VI.1 A data-driven world

As society progresses, science and engineering deal with increasingly complex problems characterised by larger sets of variables and information usually presented as data. From such data, the engineer/scientist is supposed to provide hypotheses and correct conclusions. In this scenario, model-based approaches do not become obsolete but rather a limited tool to fully describe aspects of dynamical systems such as anomalies, rare events or observations in real-time that significantly deviate from an expected behaviour. This, for instance, in applications to finance, cyber security, and health care [159].

In the previous chapters, we have shown how Information Length can be used to analyse and control complex systems described via linear and non-linear Langevin equations. Specifically, we demonstrated the capabilities of information geometry to detect and predict abrupt events, its connection to stochastic thermodynamics, unveiling a possible metric to create energetically efficient processes, and its application in a control algorithm that generates minimum variability or optimal PDF time evolution.

Even though our discussion has focused on information geometry applied to SDEs, we highlight that IL is a model-free tool that can impact a wider range of problems as it only requires the system's

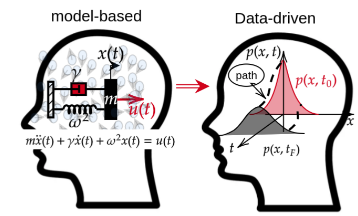

Figure VI.1: Modern engineering applications may require a paradigm shift from model-based to data-driven thinking. Model-based techniques commonly impose a solid mathematical description of the world while a data-driven approach would directly infer from direct measurements, for instance, via statistical methods. IL provides a data-driven tool as it only requires the system's time-varying PDF to extract features that can be used for control or anomaly detection.

time-varying PDF (see Figure VI.1). From the latter, in this chapter, we aim to extend our work by exploiting IL's model-free properties. Specifically, we introduce IL as a tool to analyse data presented as time series. Recall that time series are ubiquitously used to describe raw measurements of complex systems' time-evolving quantities [160].

VI.2 IL from Time-series

As shown in Figure VI.2, a time series is a set of data points indexed in time order. Here, we will define $x[kT_s]$ as a data point in a time series X such that k is the time index and T_s is the sampling period, i.e. [161; 162]

$$\mathrm{X} = (x[T_s], x[2T_s], x[3T_s], \dots). \tag{VI.1}$$

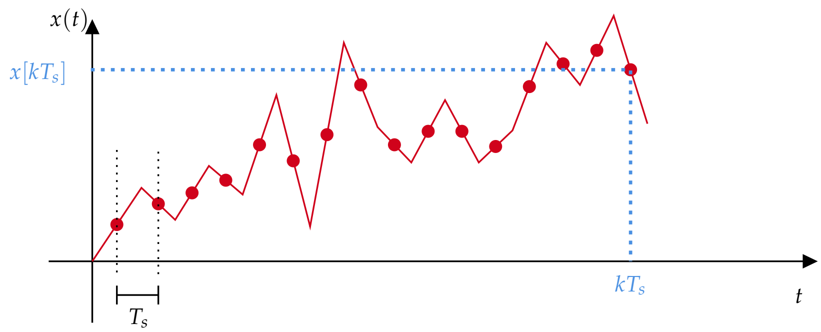

Figure VI.2: Time series plot. A time series is a series of data points indexed in time order. The data in the time series commonly come from information sampled with a sampled period T_s from an evolving measurement $x(t)$ such that $x[kT_s]$ represents the data in the time series sampled at time kT_s where $k \in \mathbb{Z}^+$.

As data sets in the form of X exist everywhere in practical applications, for example in financial systems, electrical and mechanical signals, to exploit information geometry capabilities on X, it is important to define a methodology to estimate the value of IL from discrete time measurements.

VI.2.1 The discrete information length

Specifically, to compute the value of IL for a time series of a random variable x, a discrete version of Equation (III.11) is applied. Such expression can be defined as follows [163]

$$\begin{aligned} \mathcal{L}[n] &= T_s \sum_{k=0}^{n} \frac{1}{\mathcal{T}[kT_s]}, \\ \frac{1}{\mathcal{T}[kT_s]^2} &= \Gamma^2[kT_s] = \frac{s}{h^2} \sum_j P[j;kT_s] \left(\ln \frac{P[j;(k+1)T_s]}{P[j;kT_s]} \right)^2 . \end{aligned} \tag{VI.2}$$

where k denotes discrete time with sampling period T_s and j denotes a spatial point in the discretization of the space variable x. The probability mass function[1] (PMF) is denoted by $P[j, kT_s]$; and the sampling time and spatial step are denoted as $T_s = (t_f/n)$ (t_f is the total time) and s respectively. Since, logarithm is used in

[1] The discrete version of the time-dependent PDF $p(x;t)$.

(VI.2), when $P[j;kT_s]$ takes the smallest value 0, the $\ln(0)$ gives an undefined value. To overcome this issue, we apply the following change of variable

$$q^2 = p, \tag{VI.3}$$

we have

$$p\left(\frac{d}{dt}\ln(p)\right)^2 = \frac{\left[\frac{dp}{dt}\right]^2}{p} = 4\left[\frac{dq}{dt}\right]^2. \tag{VI.4}$$

Therefore, we can rewrite the information rate Γ of the random variable x in terms of the variable q (defined in (VI.3)) by substituting (VI.4) in (III.11) as follows

$$\Gamma(t)^2 = 4\int_{\mathbb{R}}\left(\frac{d}{dt}q(x,t)\right)^2 \mathrm{d}x. \tag{VI.5}$$

Now retrieving p in (VI.5) and discretising the time-derivative of q using the limit

$$\frac{d}{dt}q(x,t) = \lim_{T_s\to 0}\frac{\sqrt{P[j;(k+1)T_s]} - \sqrt{P[j;kT_s]}}{T_s}, \tag{VI.6}$$

we have the following version of the discrete time information rate

$$\begin{aligned} \Gamma^2[kT_s] &= \frac{s}{T_s^2}\sum_j 4\left(\sqrt{P[j;(k+1)T_s]} - \sqrt{P[j;kT_s]}\right)^2, \\ \mathcal{L}[n] &= T_s\sum_{k=0}^{n}\Gamma[kT_s]. \end{aligned} \tag{VI.7}$$

Equation (VI.7) defines the IL in discrete time.

VI.2.2 IL computation from a time series

In this work, we use equation (VI.7) to compute IL time series. In the procedure, we estimate each $p[j;kT_s]$ via an sliding-window algorithm [164], i.e. we select a set of data points over the time series and move it over time. As we will discuss, the sliding window can move over the set of real data (see Algorithm 2) or the set of estimated values (see Algorithm 3). The corresponding PMF of the k-th time is found by using the kernel smoothing function method[2], described in [165] (named **ksdensity** in MATLAB®), over the sliding-window.

The pseudo-code description for computing IL from time series is shown in Algorithm 2. The algorithm considers an initial data set $\mathcal{D}_i$ of size N, i.e. at least N measurements are necessary to estimate the first value of Γ. The result of the algorithm corresponds to the value of $\mathcal{L}$ in (VI.7). Inside the procedure, the function **InformationLength** in Algorithm 2 corresponds to the programming of the discrete functions in Eq. (VI.7).

[2] This method returns a probability density estimate based on a normal kernel function (for further details, see `https://uk.mathworks.com/help/stats/ksdensity.html`).

Algorithm 2: Algorithm for the estimation of the Information Length from a time series.

Data: Consider the initial data set: $\mathcal{D}_i := \{D[kT_s] | D[kT_s] \in \mathbb{R} \quad \forall k = i-N, i-N+1, \ldots, i\}$ such that N is the number of samples (window size) in the data set (KE data in our case) sampled with sampling period T_s and $i \in \mathbb{N}$ is the current time. Besides, $n \in \mathbb{N}$ is the final discrete time of the experiment.

Result: The value of $\mathcal{L}[n]$ and $\Gamma^2[nT_s]$ (see Eq. (VI.7)).

P_0 = **ksdensity**($\mathcal{D}_0$) `// Estimate the initial PMF using the function ksdensity from MATLAB® on the initial data` $\mathcal{D}_0$.

$i = 1$

while $i \leq n$ **do**

  P_i = **ksdensity**($\mathcal{D}_i$)`// Estimate next PMF.`

  `/* Compute IL using Eq. (VI.7). */`

  $[\mathcal{L}[i], \Gamma^2[iT_s]]$=**InformationLength**($P_i, P_{i-1}$)

  $i = i + 1$

end

return $\mathcal{L}[n], \Gamma^2[nT_s]$

VI.3 IL forecasting through deep learning

Now, since IL has been proved to detect ongoing perturbations that simulate abrupt events in the statistical space [7], predicting its future value on real-time can be of great importance in any decision-making process such as power-systems management. To this end, as a proof of concept, we introduce a forecasting algorithm that implements a basic recursive neural network over a sliding window to estimate the value of the PMF $P[j, kT_s]$ at the discrete time kT_s.

Remark VI.1. *Here, our goal is to provide the basics for applying IL with a forecasting algorithm. We do not intend to provide a full study of the forecasting algorithm methodologies that could be implemented. Instead, we explore a popular method and combine it with the IL metric to analyse the possible implications.*

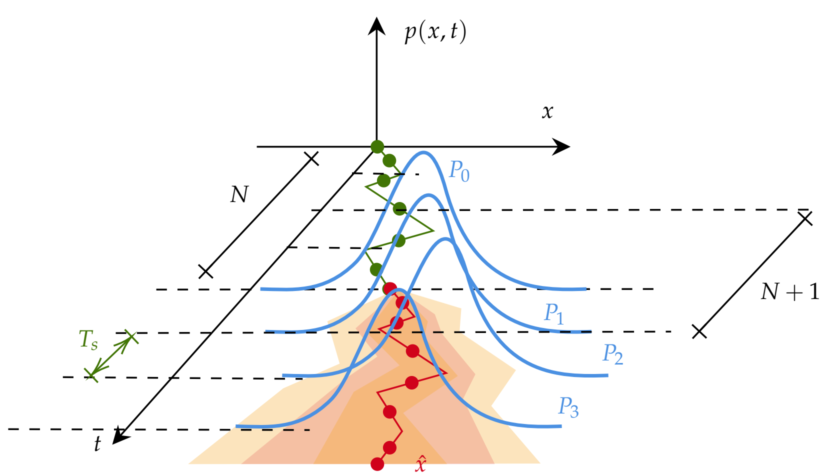

Figure VI.3: Schematic describing the data-driven methodology to compute IL through a forecasting algorithm. The method uses the predicted value $\hat{x}$ from the time series x (the present and predicted values presented in green and red colour, respectively) with sampling period T_s and includes it in the sliding window of size N to estimate the next value of the PMF (thus, the next value of Γ^2).

First, we recall that NNs are a series of architectures and algorithms based on brain behaviour [3]. The goal

[3] For a complete discussion about NN and its applications see `https://machine-learning-for-physicists.org/`

behind these models is to learn from examples and, in a similar way as human cerebral cells do and to change the interactions between basic units known as neurons [166]. Here, the NN is used as a regressor which incorporates non-linearity and the potential to learn from data. Specifically, the methodology uses a long short-term memory (LSTM) model.

A LSTM is an Recurrent Neural Network (RNN)-based architecture, where the ability to retain part of the information that belongs to the hidden layer can be used for forecasting at particular times [167]. The advantage of LSTM, in relation to common RNN models, is the improvement of the performance over the gradient vanishing problem, which represents a difficulty in the traditional back-propagation algorithm employed for training. However, the comparison of other neural models or the usage of different forecasting methods is out of the scope of this paper.

For our analysis, we have used the implemented LSTM network in MATLAB®[4], a deep leaning method using 200 hidden units [168]. In Algorithm 3, we provide the pseudocode that computes IL using (VI.7) and the time series forecasted value $\hat{x}$. Figure VI.3 illustrates the proposed methodology. In brief, as suggested by Fig. VI.3, in the first prediction Algorithm 3 uses N data (data set $\mathcal{D}_0$) with sampling period T_s to train the RNN via the function **TrainingFunc** and estimate the initial PMF P_0 using the function **ksdensity**. Next, it forecasts the next value in the time series $\hat{x}$ using the **PredictandUpdate** function, and adds it to the next sliding window $N+1$ (data set $\mathcal{D}_1$) via the function **UpdateDataSet** to estimate the next PMF P_1. Finally, the value of IL is computed from the initial PMF P_0 and the forecasted P_1. Note that, after the value $\hat{x}$ is predicted by the RNN, we update the network with the real value of the previous prediction using the function **PredictandUpdate** in the next prediction. This process is repeated till we reach the final discrete time n and return the values of $\mathcal{L}[n], \Gamma^2[nT_s]$.

Algorithm 3: Information length forecasting algorithm.

Data: Consider the normalised initial data set: $\mathcal{D}_i := \{D[kT_s] | D[kT_s] \in \mathbb{R} \quad \forall k = i-N, i-N+1, \ldots, i\}$ such that N is the number of samples (window size) in the data set sampled with sampling period T_s and $i \in \mathbb{N}$ is the current time. Besides, $n \in \mathbb{N}$ is the final discrete time.
Result: The value of $\mathcal{L}[n]$ and $\Gamma^2[nT_s]$ (see Eq. (VI.7)).

`/* Train the LSTM arquitecture` $\mathcal{N}$. `*/`
$\mathcal{N} =$ **TrainingFunc**$(\mathcal{D}_0)$
$P_0 =$ **ksdensity**$(\mathcal{D}_0)$ `// Estimate the initial PMF using the function ksdensity from MATLAB® on the initial data` $\mathcal{D}_0$.
$i = 1$
while $i \leq n$ **do**
  `/* Insert a new measurement, predict the new value` $\hat{x}$ `and update the network` $\mathcal{N}$. `*/`
  $[\mathcal{N}, \hat{x}] =$ **PredictandUpdateNet**$(\mathcal{N}, D[iT_s])$
  $\mathcal{D}_i$=**UpdateDataSet**$(\mathcal{D}_{i-1}, \hat{x})$ `// Move the sliding window adding prediction` $\hat{x}$.
  $P_i =$ **ksdensity**$(\mathcal{D}_i)$ `// Estimate next PMF.`
  `/* Compute IL using Eq. (VI.7). */`
  $[\mathcal{L}[i], \Gamma^2[iT_s]]$=**InformationLength**$(P_i, P_{i-1})$
  $i = i + 1$
end
return $\mathcal{L}[n], \Gamma^2[nT_s]$

[4] For further details, see https://uk.mathworks.com/help/deeplearning/ug/long-short-term-memory-networks.html

VI.4 Case study: An electrical power systems

In this section, we now explore the application of the previously given algorithms as a way to provide useful insights into a power system KE variability and to demonstrate its utility as a starting point in decision making for power systems management. Specifically, the proposed IL metric is applied to monthly collected data from the Nordic Power System (NPS) during three consecutive years in order to investigate its KE evolution.

Figure VI.4: Map of countries that belong to the Nordic Power System (NPS).

The NPS is the interconnected and single market area of the Nordic countries that belongs to the region in Northern Europe and the North Atlantic, specifically Sweden, Norway, Finland, and eastern Denmark (See Figure VI.4). For the past ten years, the reduction of rotational inertia[5] has been a concern for the NPS Transmission System Operators (TSOs)[6] as its value indicates the capacity of a generator to cope with active power imbalances (for further details, see [171]). One of the short-term measures to ensure the system frequency stability has consisted in installing a measurement and monitoring system to capture the rotational inertia available in the NPS. This monitoring system produces situational awareness alarms to indicate when the levels of the inertia fall below a predefined limit. Using this approach, the TSOs attempt to avoid operational scenarios where the reduced inertia and an $N-1$ contingency criterion[7] can negatively affect the frequency stability.

The NPS used the so-called 'unit commitment method' to calculate the total system rotational inertia, and it is based on adding the rotational inertia of each synchronous machine connected to the system. The TSOs of the NPS have calculated the KE of the NPS in real-time since 2015. This chapter takes advantage of the recorded data of the KE to develop a metric to quantify its variability and unveil hidden information.

We utilise the historical data of the KE in the NPS (in GWs) recorded during the entire years of 2018, 2019, and 2020. The time series of the KE consists of 44640 samples; it comprises the total data of these years with a resolution of one sample per minute. Figure VI.5a shows a plot of the KE data where seasonal variation of

[5] Here, we refer to the rotational inertial of the synchronous generators in the system. In a few words, in power systems, the term inertia refers to the energy stored in large rotating generators and some industrial motors, which gives them the tendency to remain rotating [169].
[6] TSOs are the agents responsible for the reliable transmission of power from generation plants to regional or local electricity distribution operators by way of a high voltage electrical grid [170].
[7] (N-1)-Criterion means the rule according to which elements remaining in operation after a fault of one element within TSO's control area must be capable of accommodating the new operational situation without exceeding operational security limits [172].

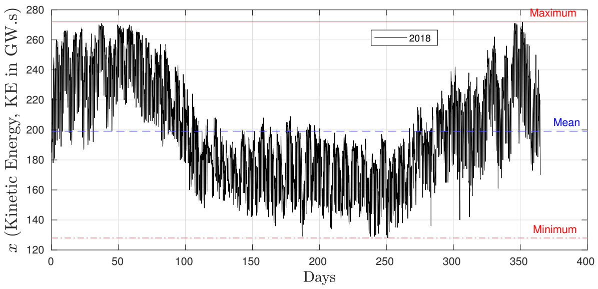

(a) KE time series Data Used in 2018

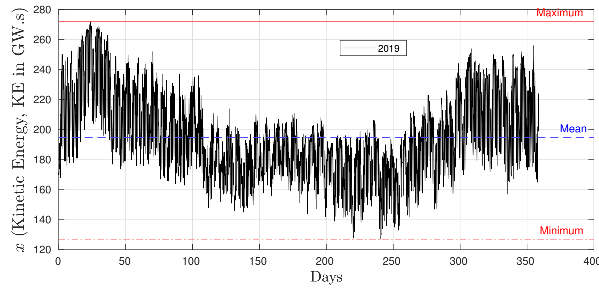

(b) KE time series Data Used in 2019

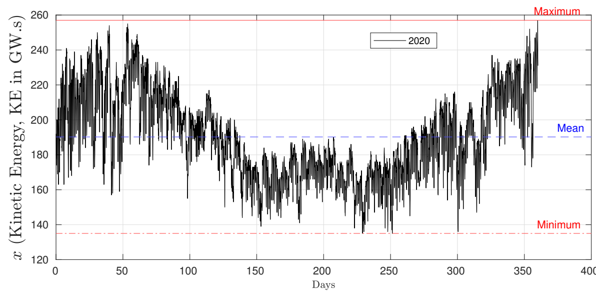

(c) KE time series Data Used in 2020

Figure VI.5: KE time series of 2018, 2019, and 2020.

the KE is evident. For 2018, low values are located during the summer months where the dominant-heating and lighting load is reduced (min: 127 GWs) and as a consequence, the number of generators to cope with the load is minor. As expected, the maximum KE is located during the winter months (max 272 GW.s). Figure VI.5 reflects the raise of concern about the reduction of KE by comparing the annual averages of KE. Average KE during 2018 had a value of 200 GWs, whereas during 2019, and 2020 is 195 and 190 respectively, representing 5% reduction.

A further descriptive using classical statistics of the KE raw data in the form of a monthly box plot is performed in Figure VI.6 (including distribution of the data as a histogram, the left side of the boxplot). Figure VI.6 allows identifying the mean and variance per month of the KE during the years studied. From Figure VI.6a, November 2018 shows the highest variance of the KE with extreme values outside the upper and lower quartiles that almost reach the minimal global inertia reached during summer months. On the other hand, May 2018 exhibits minimum changes in the KE, and it coincides with mild temperature and moderate load in the Nordic countries. For years 2019 and 2020, the histograms show the highest variance during January and November, respectively. In addition, the lowest variance occurs during June, and July respectively. Although these statistical measurements can provide us with information from the KE of the entire month, a day-by-day or hour-per-hour description of the statistical fluctuations is still missing. Here, the IL metric can provide us with such information since, as we have discussed previously, it tracks time series evolution through time-variant PMFs [61; 7].

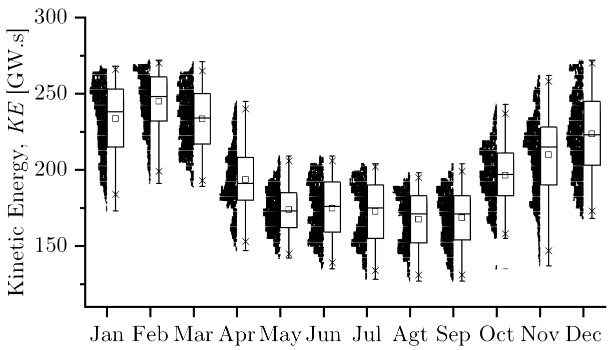

(a) 2018

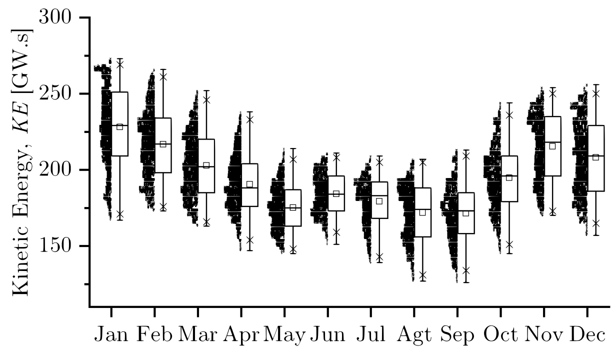

(b) 2019

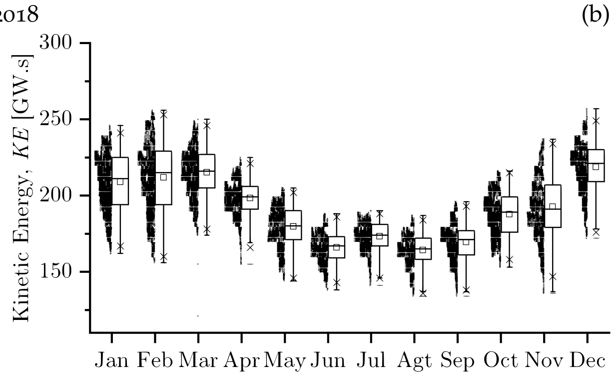

(c) 2020

Figure VI.6: Classic statistical Analysis of the KE Analysed per Month. The charts show a combination of histograms and boxplots per month in the years 2018, 2019 and 2020.

VI.4.1 Information Length Metric Results

In the following, to visualise and analyse the given data, we have assigned the measurements to seasonal groups per year. Typically, in the Nordic countries, spring runs from March/April to May, summer from June to August, fall from September to October/November and winter from November/December to March/February. However, the seasons might have longer winter and summer periods, and the seasons in between, spring and fall, can be shorter. Thus, the demand and power reserves vary accordingly.

From Figure VI.5, the dramatic effect of seasonality on the KE is perceived, the summer and winter trends are well defined whereas the spring and fall periods can be considered as the decreasing/increasing ramps as the consumption during the months on those seasons decrease/ increase respectively. Additionally, less consumption typically occurs during summer nights. Note that, the load and generation conditions of the KE data are unknown and out of the scope of this work.

Information Length $\mathcal{L}(t)$ per Month during 2018

Figure VI.7 shows the value of IL $\mathcal{L}(t)$ per month in the years 2018, 2019 and 2020. Here, we start the analysis of the IL metric in the KE from the year 2018. Although, the months with higher load demand (in the Nordic countries are during the winter season due to the lighting and heating households necessity) could be intuitively assigned as the ones with the higher amount of fluctuations. By analysing the value of the IL metric per month during 2018, the highest and the lowest $\mathcal{L}(t)$ are during August, and December, respectively.

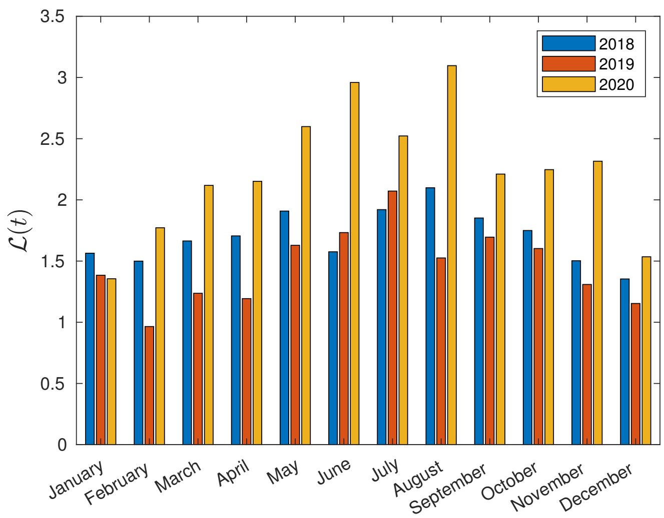

Figure VI.7: Monthly IL $\mathcal{L}(t)$ of the KE during 2018, 2019 and 2020.

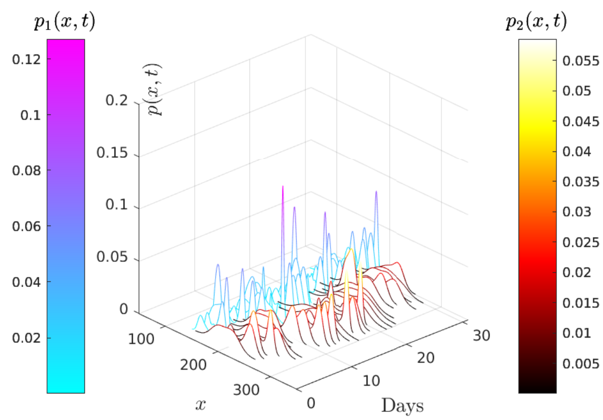

(a) PMF Evolution per day. August ($p_1(x,t)$) vs December ($p_1(x,t)$) 2018.

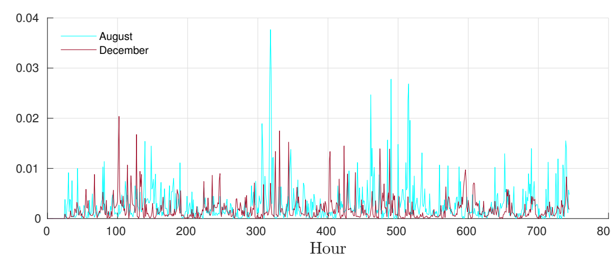

(b) Information Rate Γ per hour. August vs December 2018.

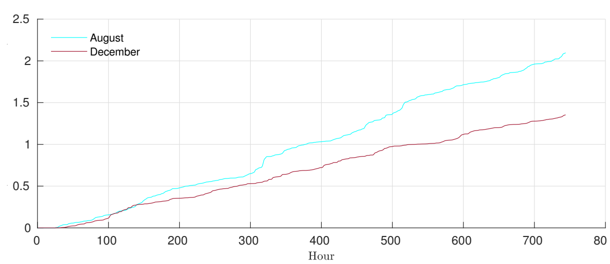

(c) Information Length $\mathcal{L}$ per hour. August vs December 2018.

Figure VI.8: IL Metric Comparison during August and December Months in 2018

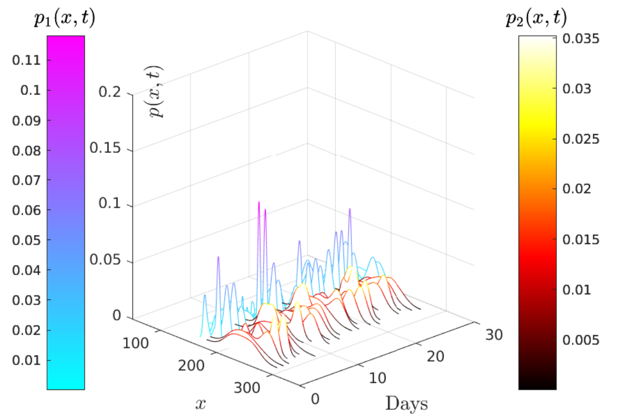

(a) PMF Evolution per day. July ($p_1(x,t)$) vs February ($p_2(x,t)$) 2019.

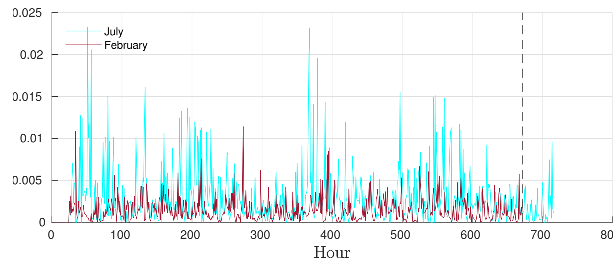

(b) Information Rate Γ per hour. July vs February 2019.

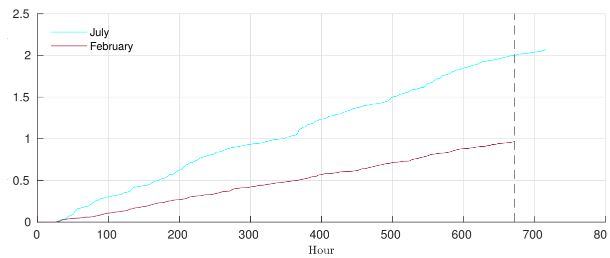

(c) Information Length $\mathcal{L}$ per hour. July vs February 2019.

Figure VI.9: IL Metric Comparison between the month with the minimum and maximum $\mathcal{L}$ in 2019 and 2020

Thus, indicating that during those months the KE vary the most or remain stiff, respectively. In this regard, from Figure VI.6a, we can also distinguish an anticorrelation between the variance and IL per month, which persists in the analysis of the two consecutive years. In other words, in comparison to IL, when IL tends to be high the covariance is small. In addition, although in summer the power consumption is reduced (the heating is not needed), the typical load fluctuations during the day show a high $\mathcal{L}(t)$ value. This is because compared to the less variability in winter, where fewer variations in the consumption indicate less variation in the PMF, in summer load fluctuations are more repetitive. This analysis implies that the capacity and reserves need to be adjusted while the day-ahead planning should be carefully optimised. This optimisation process is not analysed in this paper.

To perform a more detailed analysis of the $\mathcal{L}(t)$ metric, we have selected the months with the highest and lowest IL in the year to create Figure VI.8, where the evolution over the month of $\mathcal{L}$ and Γ are depicted. When talking about 2018, these are August and December, as we have mentioned before. Figure VI.8a presents a collection of time-dependent PMFs that describe the KE evolution through the month. Note that, even though all the computations are per hour, the PMFs in Figure VI.8a are sampled per day to permit a better visualisation of their fluctuations. Besides, Figure VI.8b shows the value of the Information Rate Γ which describes the gradients of the variation of both months PMFs through time. High values and more concurrent peaks during August can be seen, which means that August presents faster and rapid PMF variations. These are depicted by high peaks in Γ on the KE. Lower values of Γ represent slower changes. Let us recall that all

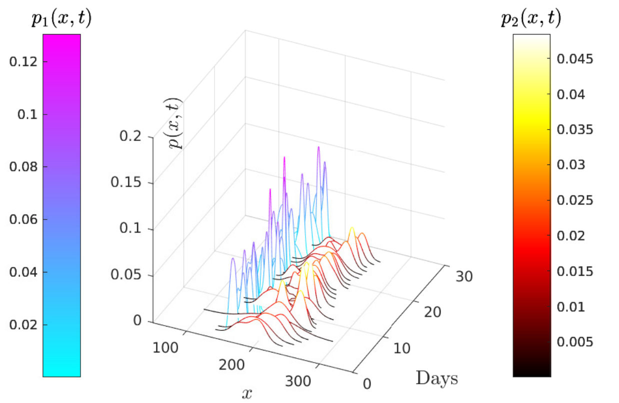

(d) PMF Evolution per day. August ($p_1(x,t)$) vs January ($p_2(x,t)$) 2020.

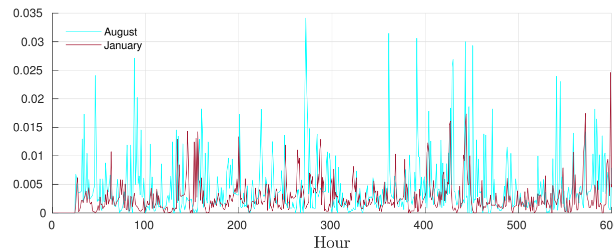

(e) Information Rate Γ per hour. August vs January 2020.

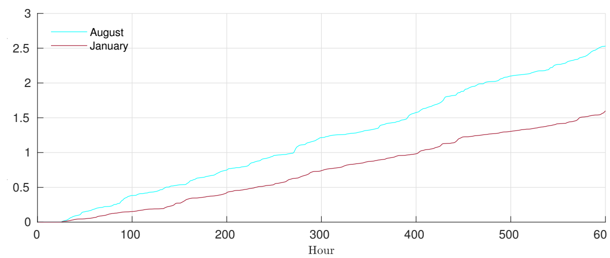

(f) Information Length $\mathcal{L}$ per hour. August vs January 2020.

Figure VI.9: IL Metric Comparison between the month with the minimum and maximum $\mathcal{L}$ in 2019 and 2020

quantities are dimensionless.

Furthermore, in Figure VI.8b, the Information Rate allows to identify the specific days or hours with extreme transitions (abrupt events), as it is seen on the day 11 and, 12 during August, and three subsequent peaks on days 18, 19, and 20. The highest peak in December happens on the third day, and subsequent peaks on the days 12, and 13. Both months tend to have fewer fluctuations at the end of the month.

Figure VI.8c shows the information length $\mathcal{L}(t)$ associated with the results presented in Figure VI.8b. We see that $\mathcal{L}(t)$ during August increases faster overtime rate than in December, specifically in the days 12 and 20 whose rates are considerably ramping up, whereas in December there are fewer fluctuations around the smaller slope. This corroborates how $\mathcal{L}(t)$ can be interpreted as a measure of information changes in PMFs.

Information Length $\mathcal{L}(t)$ per Month during 2019 and 2020

To expand the analysis of the IL metric, we explore the KE time series of the next consecutive years 2019 and 2020. Based on Figure VI.7, for 2019, the months with the highest and lowest variability are July and February, respectively. Besides, for 2020, the months with the highest and lowest variability are August and January, respectively. These months present similar characteristics in comparison to the winter and summer seasons of 2018 mentioned in the previous subsection. Note that February has fewer days than July, for such a reason, we have included a dashed line in Figures VI.9b and VI.9c setting the end of February.

For July of 2019, in Figure VI.9b, the days with the highest variability peaks are the 1st and 14th, which interestingly are at the beginning and middle of the month followed by the increasing consumption. The summer in the Nordic countries is characterised by population movement to summer households which are continuously being modernised, for instance, by including new electricity services. The abrupt and joint activation of these households produce significant changes (strong variations) in power consumption. Two main variability peaks are observed on February 1st and 10th of 2019, while the remainder of the month remains with few strong variations.

Along August of 2020, several KE fluctuations are more visible as seen in Figure VI.9e. The highest peak is seen on the 11th. However, this month presents a heavily strong variability with high intermittency and irregularity. During January of 2020, several more peaks are seen, especially at the end of the month during the transition to February.

Figures VI.9c and VI.9f show a clear difference between the information length $\mathcal{L}(t)$ of the respective months. A month with higher fluctuations will have a higher value at the end of the $\mathcal{L}(t)$ monthly calculation. Thus, the difference between August and January of 2020, since both months are highly fluctuating. The same difference is observed in the final values between July and February of 2019. Similarly, this indicator shows a higher variability for summer and winter of 2020 compared to 2019.

Forecasting Results

Now, as a proof of concept, We utilise the probabilistic properties of the KE observables to make predictions in the values of $\mathcal{L}$ and Γ. As we have discussed in Algorithm 3, the proposed short-term, hour-ahead probabilistic forecast based on LSTM incorporating uses a normalised PMF. Besides, the prediction has an hour-rolling horizon that is being updated with every new estimated value $\hat{x}$ of the KE time series. Here, we test Algorithm 3 using the data of January 2018.

The *a posteriori* multimodal PMFs evolution for the LSTM process are shown in Figure VI.10a. Note that Figure VI.10 shows only the second half of the month since the other half of the data have been used for the LSTM training. As a result, we forecast the value of Γ only for the second half of the month. In this regard, Figure VI.10b shows the forecasted $\Gamma^2(t)$ and $\mathcal{L}(t)$ metrics. Here, we note that the variability is maintained with various gradients during the month. The highest predicted variability (abrupt event) value is observed during the day 26, however, the general variability values are similar, meaning the same KE trend, a high effort of the system to maintain the heavy consumption since January is in the winter period.

Finally, to quantify the forecasting error, the Root Mean Square Error (RMSE) between the prediction and the observed data is used as a forecasting index. The results of the index are shown in Figure VI.10c. Although the model gives the highest error of 15%, the forecast data perform significantly well having an RMSE of 4.33%.

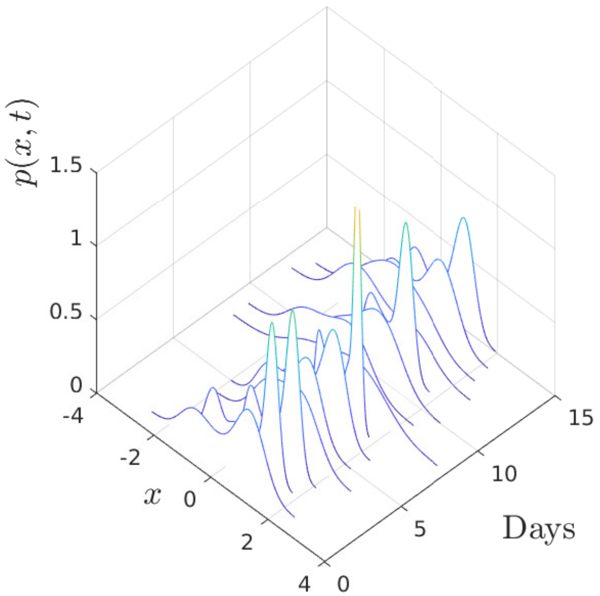

(a) Predicted PMF evolution for the second half of January 2018.

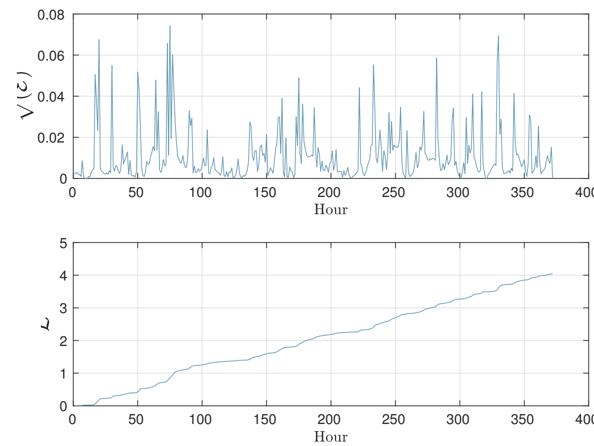

(b) Predicted Information Rate $\Gamma^2(t)$ and information Length $\mathcal{L}(t)$ for the second half of January 2018.

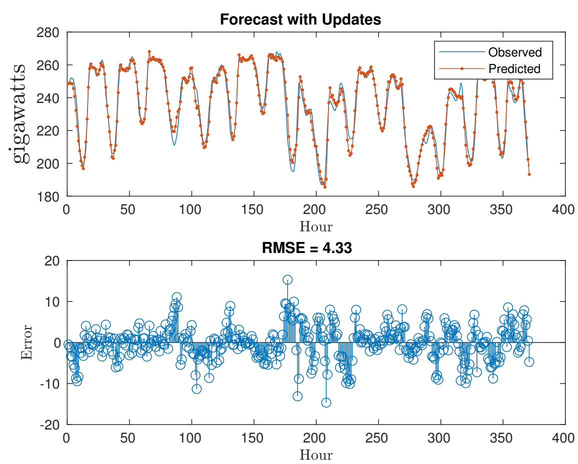

(c) Prediction vs observed data error.

Figure VI.10: Analysis of the Prediction of Information Length using Algorithm 3 where the first half of January 2018 has been used to train the NN and the second half of the month is predicted.

VI.4.2 *Case study discussion*

The potential growth of non-synchronous generation in power systems worldwide is potentially leading to a KE reduction in the system requiring a deep understanding of the trends and fluctuations within months, hours or seasons. The development and application of new metrics can help to design or adjust the generators or controllers with the ability to respond to a peak seasonal demand. To this end, we utilise the IL metric to the behaviour of the KE during the year. Specifically, we measure the time series fluctuations showing the potential[8] of IL to detect extreme and abrupt events in the system. A clear advantage of the proposed technique is that the availability of specific demand or generation profiles is not required. However, patterns or aggregated annual energy consumption data of the system will potentially help to clarify further detailed aspects when using the proposed metric. This aspect is constrained to availability since such data might require security clearance from TSOs point of view. As the implementation of KE by TSOs is a recently developed monitoring system, the collection of further data will be needed to perform a more exhaustive analysis.

Although, operating at full capacity for long periods of time is unusual for a TSO, anticipatory behaviour and innovative tools that contribute to gain insights on the system are needed to incorporate more flexibility to support grid planning for future irregular or rare events. Moreover, KE analysis, as a relatively new power systems topic, requires further understanding to provide operator planning tools that quantify, and extract relevant data.

It is important to underline that traditional statistical analysis should not be understood as erroneous but as complementary to the probabilistic metrics presented in this paper. Both can provide relevant information metrics of the KE periodic variations.

Nonetheless, as we have shown, the IL metric can track the variability through the time series evolution via time-dependent PMFs. This gives the IL metric an advantage over traditional statistical analysis. For the KE annual cases, we consider it more valuable to understand the day-by-day variability since a TSO could use this for its day-ahead operations. Even though we have analysed the highest and lowest variability months of the KE data per year, the proposed metric can be used within other ranges of time.

Chapter concluding remarks

Through this chapter, we have introduced algorithms to compute and forecast the IL from time series. The algorithms have been applied to a case study in electric power systems. The application uses IL to study the annual Kinetic Energy time series in the NPS during 2018, 2019, and 2020. In the study, we identify the variability along the seasons and evaluate the months where the KE fluctuations have abrupt events and the minimum variability. Besides, The IL metric enables us to detect daily gradient variations that are otherwise difficult to measure for a TSO. Additionally, the proposed forecasting algorithm uses the metric to predict the future KE fluctuations in an hour-ahead horizon, enabling TSOs to adjust the generator's settings accordingly.

Future work will investigate other possible probabilistic and dynamic metrics to measure power system-related signals with highly intermittent big data. For instance, we plan to use information length to measure the information flow between the elements in the system by considering its causality properties [16]. Finally, regarding this application, future work will also focus on studying the practicality of the forecasting algorithm presented here by comparing its performance with other well-assessed forecasting techniques.

[8] As the information rate is the maximum speed that every observable in the system can take (for further details, see [75]), its value would massively increase in the event of a real sudden (and possibly catastrophic) change in the system. Clearly, the prediction of its value would be subject to the error of the implemented forecasting method.

VII

Conclusions

VII.1 Concluding remarks

The present work has explored the connection between three major areas of research, namely, information geometry, stochastic thermodynamics and control engineering. From information geometry and via the Laplace assumption, we defined the concept of IL as a measure of the distance traversed by the PDF resulting from a general multivariate stochastic dynamical system. In the same fashion, IL was related to stochastic thermodynamic relations via the value of entropy rate $\dot{S}$, creating a physical relation between the length of a path in a statistical manifold (labelled by the elements of the mean vector $\boldsymbol{\mu}$ and covariance matrix $\boldsymbol{\Sigma}$) and the entropy production.

While IL defines the length of the path that the PDF takes over time, it comes from the integration of the information rate Γ value. Such quantity was also presented as a way to quantify abrupt changes in stochastic dynamics. Considering a case study of a non-autonomous second-order SDE, simulations showed that Γ was able to predict abrupt changes in the covariance matrix which were artificially induced via an impulse-like function over the noise amplitude. Furthermore, information rate was able to measure perturbations which do not affect entropy in comparison to entropy-based measures such as information flow. In the same context, the thesis also presented different information-based correlation measures that can be applied to quantify the effects of perturbations over the multiple variables of an SDE while describing the interconnection structure within the system's variables. The proposed correlation coefficients were compared against the classical Pearson and mutual information coefficients, again, proving its advantage when detecting perturbations which do not affect the entropy of the system because information geometric measures also depend on the mean value vector $\boldsymbol{\mu}$ dynamics.

Inspired by possible applications to optimal mass transport and energy efficiency design, the work additionally presented the computation of IL's geodesic to obtain the minimum information variability evolution of the stochastic dynamics. The geodesic is obtained via the MPC algorithm consisting of an on-line optimisation procedure. Hence, the algorithm would permit us to obtain a minimum information variability path in real-time. In the results, we showed the effects that MPC has on the closed-loop stochastic thermodynamics indicating that the algorithm produces entropy to maintain the system out of equilibrium in a desired state while reducing the entropy rate. Comparing the MPC results with the previous study of IL geodesic in the O-U process [64], we concluded that the MPC method does not give us a hyperbolic behaviour in the variance of the O-U process as the analytical solution presented in [64].

Finally, we explored the application of IL diagnostics to problems where the data are given in the form of time series. Specifically, we considered a case study of the kinetic energy variability of the Nordic power system. The results showed that IL and information rate can help us to identify the variability along the seasons and evaluate the months where the kinetic energy fluctuations have abrupt events. In the same study, we proposed a forecasting algorithm that uses the IL metric to predict future kinetic energy fluctuations in an hour-ahead horizon, enabling the power system manager to adjust energy generation settings accordingly.

In this manner, we consider that the presented research was able to propose starting points in the pursuit of creating integrated automatic systems whose final purpose is to produce dynamics with minimum statistical variability while giving a diagnosis of entropic measurements and perturbation effects.

VII.2 Future work

As part of future work, we plan integrating our results with current machine learning methods (ML) to enhance the performance of any autonomous system. For example, let us consider the illustration shown in Figure VII.1, where a mechanism (in this case an android) has the task of balancing a bar by placing it at an angle of 90° with the vertical while obtaining feedback information through a camera. Present literature proposes techniques such as reinforcement learning [173] or active inference [174] to process feedback information which we may combine with IL to infer the actions that will allow us to achieve our goal.

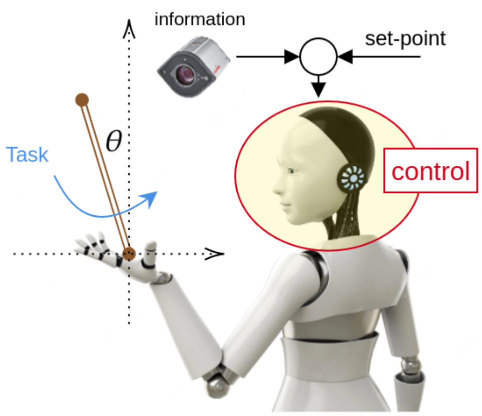

Figure VII.1: Information-based autonomous system. An android receives information via a sensor (in this case a camera) to infer which actions to take in order to balance a bar by placing it at an angle of 0° or 180° with the vertical, depending on how you orient the axis.

Another example of future work where our results can be combined with ML methods lies on detecting perturbations in data-driven systems. Specifically, we can improve the forecasting and computation of IL from time series presented in VI since computing information geometry from time series improves the performance of decision making systems, autonomous robots (as in the previous example), or mathematical modelling.

Finally, our results can be extended to any stochastic process by applying histograms instead of kernel density estimators in our algorithms. For instance, we can modify the MPC method to create histograms from the SDE solution in a parallelised computational process. Then, from the histograms, we compute a prediction of the IL to solve the optimisation and control problem.

Bibliography

[1] James Ladyman, James Lambert, and Karoline Wiesner. What is a complex system? *European Journal for Philosophy of Science*, 3:33–67, 2013.

[2] Hiroki Sayama. *Introduction to the modeling and analysis of complex systems*. Open SUNY Textbooks, 2015.

[3] Adrian-Josue Guel-Cortez, César-Fernando Méndez-Barrios, Eun-jin Kim, and Mihir Sen. Fractional-order controllers for irrational systems. *IET Control Theory & Applications*, 15(7):965–977, 2021.

[4] Maxwell JD Ramstead, Dalton AR Sakthivadivel, Conor Heins, Magnus Koudahl, Beren Millidge, Lancelot Da Costa, Brennan Klein, and Karl J Friston. On bayesian mechanics: A physics of and by beliefs. *arXiv preprint arXiv:2205.11543*, 2022.

[5] Lancelot Da Costa, Karl Friston, Conor Heins, and Grigorios A Pavliotis. Bayesian mechanics for stationary processes. *Proceedings of the Royal Society A*, 477(2256):20210518, 2021.

[6] Adrian-Josue Guel-Cortez and Eun-jin Kim. Information length analysis of linear autonomous stochastic processes. *Entropy*, 22(11):1265, 2020.

[7] Adrian-Josue Guel-Cortez and Eunjin Kim. Information geometric theory in the prediction of abrupt changes in system dynamics. *Entropy*, 23(6):694, 2021.

[8] Harold R Chamorro, Adrian Guel-Cortez, Eun-jin Kim, Francisco Gonzalez-Longatt, Alvaro Ortega, and Wilmar Martinez. Information length quantification and forecasting of power systems kinetic energy. *IEEE Transactions on Power Systems*, 2022.

[9] Adrian-Josue Guel-Cortez and Eun-Jin Kim. Relations between entropy rate, entropy production and information geometry in linear stochastic systems. *Journal of Statistical Mechanics: Theory and Experiment*, 2023(3):033204, 2023.

[10] Adrian-Josue Guel-Cortez, Eun-jin Kim, and Mohamed W Mehrez. Minimum information variability in linear langevin systems via model predictive control. *Available at SSRN 4214108*, 2022.

[11] Adrian-Josue Guel-Cortez and Eun-jin Kim. Information geometry control under the laplace assumption. In *Physical Sciences Forum*, volume 5, page 25. Multidisciplinary Digital Publishing Institute, 2022.

[12] Adrian-Josue Guel-Cortez and Eun-jin Kim. A fractional-order model of the cardiac function. In *Chaotic Modeling and Simulation International Conference*, pages 273–285. Springer, 2020.

[13] Adrian-Josue Guel-Cortez and Eun-jin Kim. Model reduction and control design of a multi-agent line formation of mobile robots. In *International Conference on Applied Science and Advanced Technology*, pages 197–207. Springer, 2021.

[14] Adrián-Josué Guel-Cortez, César-Fernando Méndez-Barrios, Diego Torres-García, and Liliana Félix. Further remarks on irrational systems and their applications. In *Computer Sciences & Mathematics Forum*, volume 4, page 5. MDPI, 2022.

[15] Adrian-Josue Guel-Cortez, Eun-jin Kim, and Harold-R. Chamorro. Parameter estimation of fractional-order systems via evolutionary algorithms and the extended fractional kalman filter. In *The International Conference on Fractional Differentiation and its Applications (ICFDA 2023)*. Ajman University, 2023.

[16] Eun-jin Kim and Adrian-Josue Guel-Cortez. Causal information rate. *Entropy*, 23(8):1087, 2021.

[17] Shankar Sastry. *Nonlinear systems: analysis, stability, and control*, volume 10. Springer Science & Business Media, 2013.

[18] Don S Lemons. An introduction to stochastic processes in physics, 2003.

[19] Peter S Maybeck. *Stochastic models, estimation, and control*. Academic press, 1982.

[20] Albert Einstein. *Investigations on the Theory of the Brownian Movement*. Courier Corporation, 1956.

[21] Ioannis Karatzas and Steven Shreve. *Brownian motion and stochastic calculus*, volume 113. Springer Science & Business Media, 2012.

[22] W Moon and JS Wettlaufer. On the interpretation of stratonovich calculus. *New Journal of Physics*, 16(5):055017, 2014.

[23] Luca Peliti and Simone Pigolotti. *Stochastic Thermodynamics: An Introduction*. Princeton University Press, 2021.

[24] Timothy Sauer. Numerical solution of stochastic differential equations in finance. In *Handbook of computational finance*, pages 529–550. Springer, 2012.

[25] Andreas Rössler. Runge–kutta methods for itô stochastic differential equations with scalar noise. *BIT Numerical Mathematics*, 46(1):97–110, 2006.

[26] AJ Roberts. Modify the improved euler scheme to integrate stochastic differential equations. *arXiv preprint arXiv:1210.0933*, 2012.

[27] Jack Karush. On the chapman-kolmogorov equation. *The Annals of Mathematical Statistics*, 32(4):1333–1337, 1961.

[28] Alexander S. Poznyak. 10 - markov processes. In Alexander S. Poznyak, editor, *Advanced Mathematical Tools for Automatic Control Engineers: Stochastic Techniques*, pages 263–286. Elsevier, Oxford, 2009.

[29] George Adomian. Stochastic systems. 1983.

[30] Hannes Risken. Fokker-planck equation. In *The Fokker-Planck Equation*, pages 63–95. Springer, 1996.

[31] Richard Lockhart. Lecture notes in Mathematical Statistics, 2000.

[32] Christopher B. Croke. Introduction to the Fourier transform, 2002.

[33] Erik Cheever. Notes on Linear Physical Systems Analysis, 2005.

[34] Y. D. Chong. Multi-Dimensional Fourier Transforms, 2021.

[35] Alan V Oppenheim, John Buck, Michael Daniel, Alan S Willsky, Syed Hamid Nawab, and Andrew Singer. *Signals & systems*. Pearson Educación, 1997.

[36] Steven Jenks. Introduction to kramers equation, 2006.

[37] A. Zee. *Quantum field theory in a nutshell*. Princenton University Press, 2nd edition, 2010.

[38] C.-T. Chen. *Linear system theory and design*, volume 7. Oxford University Press, 2013.

[39] James Ward Brown and Ruel V Churchill. *Complex variables and applications*. McGraw-Hill, 2009.

[40] A-J Guel-Cortez, Mihir Sen, and Bill Goodwine. Closed form time response of an infinite tree of mechanical components described by an irrational transfer function. In *2019 American Control Conference (ACC)*, pages 5828–5833. IEEE, 2019.

[41] André C Marreiros, Stefan J Kiebel, Jean Daunizeau, Lee M Harrison, and Karl J Friston. Population dynamics under the laplace assumption. *Neuroimage*, 44(3):701–714, 2009.

[42] Frank Nielsen. An elementary introduction to information geometry. *Entropy*, 22(10):1100, 2020.

[43] Udo Seifert. Stochastic thermodynamics: From principles to the cost of precision. *Physica A: Statistical Mechanics and its Applications*, 504:176–191, 2018.

[44] Kent W Mayhew. Entropy: An ill-conceived mathematical contrivance? *Physics Essays*, 28(3):352–357, 2015.

[45] James Sethna. *Statistical mechanics: entropy, order parameters, and complexity*, volume 14. Oxford University Press, USA, 2021.

[46] Enrico Fermi. *Thermodynamics By Enrico Fermi*. Dover publications, 1936.

[47] Mike Glazer and Justin Wark. Statistical mechanics: a survival guide, 2002.

[48] Leonid M Martyushev. Entropy and entropy production: Old misconceptions and new breakthroughs. *Entropy*, 15(4):1152–1170, 2013.

[49] Edwin T Jaynes. Information theory and statistical mechanics. ii. *Physical review*, 108(2):171, 1957.

[50] Thomas Cailleteau. Jaynes & shannon's constrained ignorance and surprise. *arXiv preprint arXiv:2107.05008*, 2021.

[51] Eun-jin Kim. Information geometry, fluctuations, non-equilibrium thermodynamics, and geodesics in complex systems. *Entropy*, 23(11):1393, 2021.

[52] Ilya Prigogine. Time, structure, and fluctuations. *Science*, 201(4358):777–785, 1978.

[53] Tânia Tomé and Mário J de Oliveira. Entropy production in irreversible systems described by a fokker-planck equation. *Physical Review E*, 82(2):021120, 2010.

[54] Tânia Tomé. Entropy production in nonequilibrium systems described by a fokker-planck equation. *Brazilian journal of physics*, 36:1285–1289, 2006.

[55] Kaare Brandt Petersen, Michael Syskind Pedersen, et al. The matrix cookbook. *Technical University of Denmark*, 7(15):510, 2008.

[56] Ariel Caticha. Entropic physics. probability, entropy and the foundations of physics, 2022.

[57] NN Cencov. Statistical decision rules and optimal inference, transl. math. monographs, vol. 53. *Amer. Math. Soc., Providence-RI*, 1981.

[58] Ariel Caticha. Lectures on probability, entropy, and statistical physics. *arXiv preprint arXiv:0808.0012*, 2008.

[59] Ariel Caticha et al. Entropic inference and the foundations of physics. *Brazilian Chapter of the International Society for Bayesian Analysis-ISBrA, Sao Paulo, Brazil*, 2012.

[60] Shun-ichi Amari and Hiroshi Nagaoka. *Methods of information geometry*, volume 191. American Mathematical Soc., 2000.

[61] Schuyler B. Nicholson, Luis Pedro García-Pintos, Adolfo del Campo, and Jason R. Green. Time–information uncertainty relations in thermodynamics. 16(12):1211–1215.

[62] Eunjin Kim. Information geometry and non-equilibrium thermodynamic relations in the over-damped stochastic processes. *Journal of Statistical Mechanics: Theory and Experiment*, 2021(9):093406, 2021.

[63] E. Kim. Investigating information geometry in classical and quantum systems through information length. *Entropy*, 20(8), 2018.

[64] Eun-jin Kim, UnJin Lee, James Heseltine, and Rainer Hollerbach. Geometric structure and geodesic in a solvable model of nonequilibrium process. *Physical Review E*, 93(6):062127, 2016.

[65] SB Nicholson and Eun-jin Kim. Investigation of the statistical distance to reach stationary distributions. *Physics Letters A*, 379(3):83–88, 2015.

[66] Eun-jin Kim and Rainer Hollerbach. Signature of nonlinear damping in geometric structure of a nonequilibrium process. *Physical Review E*, 95(2):022137, 2017.

[67] James Heseltine and Eun-jin Kim. Comparing information metrics for a coupled ornstein–uhlenbeck process. *Entropy*, 21(8):775, 2019.

[68] Eun-jin Kim and Rainer Hollerbach. Geometric structure and information change in phase transitions. *Physical Review E*, 95(6):062107, 2017.

[69] Eun-jin Kim, James Heseltine, and Hanli Liu. Information length as a useful index to understand variability in the global circulation. *Mathematics*, 8(2):299, 2020.

[70] Rainer Hollerbach, Eun-jin Kim, and Lothar Schmitz. Time-dependent probability density functions and information diagnostics in forward and backward processes in a stochastic prey–predator model of fusion plasmas. *Physics of Plasmas*, 27(10):102301, 2020.

[71] DS Tracy and KC Jinadasa. Expectations of products of random quadratic forms. *Stochastic Analysis and Applications*, 4(1):111–116, 1986.

[72] Jan R Magnus and Heinz Neudecker. *Matrix differential calculus with applications in statistics and econometrics*. John Wiley & Sons, 2019.

[73] D. Inman. Critical damping. In S. Braun, editor, *Encyclopedia of Vibration*, pages 314–319. Elsevier, Oxford, 2001.

[74] James Heseltine and Eun-jin Kim. Novel mapping in non-equilibrium stochastic processes. *Journal of Physics A: Mathematical and Theoretical*, 49(17):175002, 2016.

[75] Sosuke Ito and Andreas Dechant. Stochastic time evolution, information geometry, and the cramér-rao bound. *Physical Review X*, 10(2):021056, 2020.

[76] Xin Min Yang, Xiao Qi Yang, and Kok Lay Teo. A matrix trace inequality. *Journal of Mathematical Analysis and Applications*, 263(1):327–331, 2001.

[77] Khalid Shebrawi and Hussien Albadawi. Trace inequalities for matrices. *Bulletin of the Australian Mathematical Society*, 87(1):139–148, 2013.

[78] Rajnikant Patel and Mitsuhiko Toda. Trace inequalities involving hermitian matrices. *Linear algebra and its applications*, 23:13–20, 1979.

[79] P Falb and William Wolovich. Decoupling in the design and synthesis of multivariable control systems. *IEEE transactions on automatic control*, 12(6):651–659, 1967.

[80] Eduardo D Sontag. *Mathematical control theory: deterministic finite dimensional systems*, volume 6. Springer Science & Business Media, 2013.

[81] Giuseppe Pesce, Philip H Jones, Onofrio M Maragò, and Giovanni Volpe. Optical tweezers: theory and practice. *The European Physical Journal Plus*, 135(12):1–38, 2020.

[82] John Bechhoefer. *Control Theory for Physicists*. Cambridge University Press, 2021.

[83] Eduardo F Camacho and Carlos Bordons Alba. *Model predictive control*. Springer science & business media, 2013.

[84] Philipp Schwartenbeck, Thomas FitzGerald, Ray Dolan, and Karl Friston. Exploration, novelty, surprise, and free energy minimization. *Frontiers in psychology*, page 710, 2013.

[85] Pablo Lanillos, Cristian Meo, Corrado Pezzato, Ajith Anil Meera, Mohamed Baioumy, Wataru Ohata, Alexander Tschantz, Beren Millidge, Martijn Wisse, Christopher L Buckley, et al. Active inference in robotics and artificial agents: Survey and challenges. *arXiv preprint arXiv:2112.01871*, 2021.

[86] Manuel Baltieri and Christopher L Buckley. Pid control as a process of active inference with linear generative models. *Entropy*, 21(3):257, 2019.

[87] PC De Vries, MF Johnson, B Alper, P Buratti, TC Hender, HR Koslowski, V Riccardo, JET-EFDA Contributors, et al. Survey of disruption causes at jet. *Nuclear fusion*, 51(5):053018, 2011.

[88] Julian Kates-Harbeck, Alexey Svyatkovskiy, and William Tang. Predicting disruptive instabilities in controlled fusion plasmas through deep learning. *Nature*, 568(7753):526–531, 2019.

[89] Eun-jin Kim. Investigating information geometry in classical and quantum systems through information length. *Entropy*, 20(8):574, 2018.

[90] Eun-jin Kim, Quentin Jacquet, and Rainer Hollerbach. Information geometry in a reduced model of self-organised shear flows without the uniform coloured noise approximation. *Journal of Statistical Mechanics: Theory and Experiment*, 2019(2):023204, 2019.

[91] Mikhail Prokopenko, Fabio Boschetti, and Alex J Ryan. An information-theoretic primer on complexity, self-organization, and emergence. *Complexity*, 15(1):11–28, 2009.

[92] Massimo Franceschetti and Paolo Minero. Elements of information theory for networked control systems. In *Information and Control in Networks*, pages 3–37. Springer, 2014.

[93] Thomas M Cover. *Elements of information theory*. John Wiley & Sons, 1999.

[94] Eun-jin Kim and Rainer Hollerbach. Time-dependent probability density functions and information geometry of the low-to-high confinement transition in fusion plasma. *Physical Review Research*, 2(2):023077, 2020.

[95] Armen E Allahverdyan, Dominik Janzing, and Guenter Mahler. Thermodynamic efficiency of information and heat flow. *Journal of Statistical Mechanics: Theory and Experiment*, 2009(09):P09011, 2009.

[96] Jordan M Horowitz and Henrik Sandberg. Second-law-like inequalities with information and their interpretations. *New Journal of Physics*, 16(12):125007, 2014.

[97] B Roy Frieden. *Science from Fisher information*, volume 974. Citeseer, 2004.

[98] Christian Van den Broeck et al. Stochastic thermodynamics: A brief introduction. *Phys. Complex Colloids*, 184:155–193, 2013.

[99] Sergio Ciliberto. Experiments in stochastic thermodynamics: Short history and perspectives. *Physical Review X*, 7(2):021051, 2017.

[100] Anna Zaremba and Tomaso Aste. Measures of causality in complex datasets with application to financial data. *Entropy*, 16(4):2309–2349, 2014.

[101] Aditi Kathpalia and Nithin Nagaraj. Measuring causality. *Resonance*, 26(2):191–210, 2021.

[102] X San Liang and Richard Kleeman. Information transfer between dynamical system components. *Physical review letters*, 95(24):244101, 2005.

[103] X San Liang. Information flow and causality as rigorous notions ab initio. *Physical Review E*, 94(5):052201, 2016.

[104] Pablo Zegers. Fisher information properties. *Entropy*, 17(7):4918–4939, 2015.

[105] Alexander Ly, Maarten Marsman, Josine Verhagen, Raoul PPP Grasman, and Eric-Jan Wagenmakers. A tutorial on fisher information. *Journal of Mathematical Psychology*, 80:40–55, 2017.

[106] Steven Jenks and Statistical Mechanics II. Introduction to kramers equation. *Drexel University, Philadelphia*, 2006.

[107] Terry Bossomaier, Lionel Barnett, Michael Harré, and Joseph T Lizier. Transfer entropy. In *An introduction to transfer entropy*, pages 65–95. Springer, 2016.

[108] Lionel Barnett, Adam B Barrett, and Anil K Seth. Granger causality and transfer entropy are equivalent for gaussian variables. *Physical review letters*, 103(23):238701, 2009.

[109] Won Sang Chung and Hassan Hassanabadi. Modified dirac delta function and modified dirac delta potential in the quantum mechanics. *The European Physical Journal Plus*, 137(1):151, 2022.

[110] Tyrone E Duncan. On the calculation of mutual information. *SIAM Journal on Applied Mathematics*, 19(1):215–220, 1970.

[111] Nga Nguyen Thi Thanh, Khanh Nguyen Kim, Son Ngo Hong, and Trung Ngo Lam. Entropy correlation and its impacts on data aggregation in a wireless sensor network. *Sensors*, 18(9):3118, 2018.

[112] Nathan D Cahill. Normalized measures of mutual information with general definitions of entropy for multimodal image registration. In *International workshop on biomedical image registration*, pages 258–268. Springer, 2010.

[113] William H Press, Saul A Teukolsky, William T Vetterling, and Brian P Flannery. *Numerical recipes 3rd edition: The art of scientific computing*. Cambridge university press, 2007.

[114] Nicolas Veyrat-Charvillon and François-Xavier Standaert. Mutual information analysis: how, when and why? In *International Workshop on Cryptographic Hardware and Embedded Systems*, pages 429–443. Springer, 2009.

[115] Wentian Li. Mutual information functions versus correlation functions. *Journal of statistical physics*, 60(5):823–837, 1990.

[116] Andreia Dionisio, Rui Menezes, and Diana A Mendes. Mutual information: a measure of dependency for nonlinear time series. *Physica A: Statistical Mechanics and its Applications*, 344(1-2):326–329, 2004.

[117] Dedy Rahman Wijaya, Riyanarto Sarno, and Enny Zulaika. Information quality ratio as a novel metric for mother wavelet selection. *Chemometrics and Intelligent Laboratory Systems*, 160:59–71, 2017.

[118] Adrián Josué Guel-Cortez, César-Fernando Méndez-Barrios, Emilio Jorge González-Galván, Gilberto Mejía-Rodríguez, and Liliana Félix. Geometrical design of fractional pdμ controllers for linear time-invariant fractional-order systems with time delay. *Proceedings of the Institution of Mechanical Engineers, Part I: Journal of Systems and Control Engineering*, 233(7):815–829, 2019.

[119] Steven L Brunton and J Nathan Kutz. *Data-driven science and engineering: Machine learning, dynamical systems, and control*. Cambridge University Press, 2022.

[120] Claudius Gros. Generating functionals for guided self-organization. In *Guided self-organization: inception*, pages 53–66. Springer, 2014.

[121] Mikhail Prokopenko. *Guided self-organization: Inception*, volume 9. Springer Science & Business Media, 2013.

[122] George N Saridis. *Entropy in control engineering*, volume 12. World Scientific, 2001.

[123] Sebastian Deffner and Marcus VS Bonança. Thermodynamic control—An old paradigm with new applications. *EPL (Europhysics Letters)*, 131(2):20001, 2020.

[124] Murti V Salapaka. Control of optical tweezers. *Encyclopedia of Systems and Control*, pages 361–368, 2021.

[125] Mario Annunziato and Alfio Borzi. Optimal control of probability density functions of stochastic processes. *Mathematical Modelling and Analysis*, 15(4):393–407, 2010.

[126] Mario Annunziato and Alfio Borzì. A fokker–planck control framework for multidimensional stochastic processes. *Journal of Computational and Applied Mathematics*, 237(1):487–507, 2013.

[127] Arthur Fleig and Roberto Guglielmi. Optimal control of the fokker–planck equation with space-dependent controls. *Journal of Optimization Theory and Applications*, 174(2):408–427, 2017.

[128] M Soledad Aronna and Fredi Tröltzsch. First and second order optimality conditions for the control of fokker-planck equations. *ESAIM: Control, Optimisation and Calculus of Variations*, 27:15, 2021.

[129] P Salamon, JD Nulton, G Siragusa, A Limon, D Bedeaux, and S Kjelstrup. A simple example of control to minimize entropy production. 2002.

[130] Schuyler B Nicholson, Adolfo del Campo, and Jason R Green. Nonequilibrium uncertainty principle from information geometry. *Physical Review E*, 98(3):032106, 2018.

[131] Keiji Miura. An introduction to maximum likelihood estimation and information geometry. *Interdisciplinary Information Sciences*, 17(3):155–174, 2011.

[132] Lai-Yung Leung and Gerald R North. Information theory and climate prediction. *Journal of Climate*, 3(1):5–14, 1990.

[133] Gavin E Crooks. Measuring thermodynamic length. *Physical Review Letters*, 99(10):100602, 2007.

[134] Shane W. Flynn, Helen C. Zhao, and Jason R. Green. Measuring disorder in irreversible decay processes. *The Journal of Chemical Physics*, 141(10):104107, 2014.

[135] Schuyler B Nicholson, Luis Pedro Garcia-Pintos, Adolfo del Campo, and Jason R Green. Time–information uncertainty relations in thermodynamics. *Nature Physics*, 16(12):1211–1215, 2020.

[136] Karl J Åström and Tore Hägglund. Pid control. *IEEE Control Systems Magazine*, 1066, 2006.

[137] Steven L Brunton and J Nathan Kutz. *Data-driven science and engineering: Machine learning, dynamical systems, and control*. Cambridge University Press, 2019.

[138] Michel Fliess and Cédric Join. Model-free control. *International Journal of Control*, 86(12):2228–2252, 2013.

[139] Jay H Lee. Model predictive control: Review of the three decades of development. *International Journal of Control, Automation and Systems*, 9(3):415–424, 2011.

[140] Mohamed W Mehrez, Karl Worthmann, Joseph PV Cenerini, Mostafa Osman, William W Melek, and Soo Jeon. Model predictive control without terminal constraints or costs for holonomic mobile robots. *Robotics and Autonomous Systems*, 127:103468, 2020.

[141] Bjørn Andreas Kristiansen, Jan Tommy Gravdahl, and Tor Arne Johansen. Energy optimal attitude control for a solar-powered spacecraft. *European Journal of Control*, 2021.

[142] Tobias Salesch, Jonas Gesenhues, Moriz Habigt, Mare Mechelinck, Marc Hein, and Dirk Abel. Model based optimization of a novel ventricular assist device. *at-Automatisierungstechnik*, 69(7):619–631, 2021.

[143] Joel A E Andersson, Joris Gillis, Greg Horn, James B Rawlings, and Moritz Diehl. CasADi – A software framework for nonlinear optimization and optimal control. *Mathematical Programming Computation*, 11(1):1–36, 2019.

[144] A. Bemporad. Hybrid Toolbox - User's Guide, 2004. http://cse.lab.imtlucca.it/~bemporad/hybrid/toolbox.

[145] Brian DO Anderson and John B Moore. *Optimal control: linear quadratic methods*. Courier Corporation, 2007.

[146] Jan Gieseler, Juan Ruben Gomez-Solano, Alessandro Magazzù, Isaac Pérez Castillo, Laura Pérez García, Marta Gironella-Torrent, Xavier Viader-Godoy, Felix Ritort, Giuseppe Pesce, Alejandro V Arzola, et al. Optical tweezers—from calibration to applications: a tutorial. *Advances in Optics and Photonics*, 13(1):74–241, 2021.

[147] P. Salamon, J. D. Nulton, G. Siragusa, A. Limon, D. Bedeaux, and S. Kjelstrup. A simple example of control to minimize entropy production. 27(1):45–55, 2002.

[148] Maximilian Behr, Peter Benner, and Jan Heiland. Solution formulas for differential sylvester and lyapunov equations. *Calcolo*, 56(4):1–33, 2019.

[149] Finn Lindgren, David Bolin, and Håvard Rue. The spde approach for gaussian and non-gaussian fields: 10 years and still running. *arXiv preprint arXiv:2111.01084*, 2021.

[150] Radek Erban, Jonathan Chapman, and Philip Maini. A practical guide to stochastic simulations of reaction-diffusion processes. *arXiv preprint arXiv:0704.1908*, 2007.

[151] Jianqing Fan and James S Marron. Fast implementations of nonparametric curve estimators. *Journal of computational and graphical statistics*, 3(1):35–56, 1994.

[152] Vadim Utkin and Hoon Lee. Chattering problem in sliding mode control systems. In *International Workshop on Variable Structure Systems, 2006. VSS'06.*, pages 346–350. IEEE, 2006.

[153] I. The MathWorks. Nonlinear programming solver, 2022.

[154] Alexander Reutlinger, Dominik Hangleiter, and Stephan Hartmann. Understanding (with) toy models. *The British Journal for the Philosophy of Science*, 69(4):1069–1099, 2018.

[155] Jürgen Ackermann. *Robust control: Systems with uncertain physical parameters*. Springer Science & Business Media, 2012.

[156] Song Hi Lee and Raymond Kapral. Friction and diffusion of a brownian particle in a mesoscopic solvent. *The Journal of chemical physics*, 121(22):11163–11169, 2004.

[157] Karl P Hadeler, Thomas Hillen, and Frithjof Lutscher. The langevin or kramers approach to biological modeling. *Mathematical Models and Methods in Applied Sciences*, 14(10):1561–1583, 2004.

[158] V Balakrishnan. Diffusion in an external potential. In *Elements of Nonequilibrium Statistical Mechanics*, pages 168–190. Springer, 2021.

[159] Riyaz Ahamed Ariyaluran Habeeb, Fariza Nasaruddin, Abdullah Gani, Ibrahim Abaker Targio Hashem, Ejaz Ahmed, and Muhammad Imran. Real-time big data processing for anomaly detection: A survey. *International Journal of Information Management*, 45:289–307, 2019.

[160] Forough Hassanibesheli, Niklas Boers, and Jürgen Kurths. Reconstructing complex system dynamics from time series: a method comparison. *New Journal of Physics*, 22(7):073053, 2020.

[161] Alan V Oppenheim, John R Buck, and Ronald W Schafer. *Discrete-time signal processing. Vol. 2*. Upper Saddle River, NJ: Prentice Hall, 2001.

[162] Alan V Oppenheim. Applications of digital signal processing. *Englewood Cliffs*, 1978.

[163] James Heseltine and Eunjin Kim. Comparing Information Metrics for a Coupled Ornstein–Uhlenbeck Process. 21(8):775.

[164] Cetin K Koç. Analysis of sliding window techniques for exponentiation. *Computers & Mathematics with Applications*, 30(10):17–24, 1995.

[165] Adrian W Bowman and Adelchi Azzalini. *Applied smoothing techniques for data analysis: the kernel approach with S-Plus illustrations*, volume 18. OUP Oxford, 1997.

[166] S Haykin. *Neural Networks and Learning Machines*. Number v. 10 in Neural networks and learning machines. Prentice Hall, 2009.

[167] Y. Hua, Z. Zhao, R. Li, X. Chen, Z. Liu, and H. Zhang. Deep learning with long short-term memory for time series prediction. *IEEE Communications Magazine*, 57(6):114–119, 2019.

[168] MathWorks. Time series forecasting using deep learning, 2021.

[169] Paul Denholm, Trieu Mai, Richard Wallace Kenyon, Benjamin Kroposki, and Mark O'Malley. Inertia and the power grid: A guide without the spin. Technical report, National Renewable Energy Lab.(NREL), Golden, CO (United States), 2020.

[170] Theresa Schneider. Factsheet transmission system operators, 2015.

[171] Bálint Hartmann, István Vokony, and István Táczi. Effects of decreasing synchronous inertia on power system dynamics—overview of recent experiences and marketisation of services. *International Transactions on Electrical Energy Systems*, 29(12):e12128, 2019.

[172] The European comission establishing a guideline on electricity transmission system operation. COMMISSION REGULATION (EU) 2017/1485, 2017.

[173] Jens Kober, J Andrew Bagnell, and Jan Peters. Reinforcement learning in robotics: A survey. *The International Journal of Robotics Research*, 32(11):1238–1274, 2013.

[174] Pablo Lanillos and Marcel van Gerven. Neuroscience-inspired perception-action in robotics: applying active inference for state estimation, control and self-perception. *arXiv preprint arXiv:2105.04261*, 2021.